

Very Distant Radio Galaxies: Search Techniques and Emission Line Properties

PROEFSCHRIFT

ter verkrijging van de graad van Doctor
aan de Universiteit Leiden
op gezag van de Rector Magnificus Dr. W. A. Wagenaar
hoogleraar in de Faculteit der Sociale Wetenschappen
volgens besluit van het College voor Promoties
te verdedigen op woensdag 8 november 2000
te klokke 14.15 uur

door

Carlos Albert Gilberte De Breuck

geboren te Sint-Niklaas, België op 3 februari 1973

Promotiecommissie:

Promotor : Prof. dr. G.K. Miley
Co-promotores : Dr. H.J.A. Röttgering
Dr. W.J.M. van Breugel (IGPP/LLNL, Livermore, Californië)
Referent : Prof. Dr. R.T. Schilizzi
Overige Leden : Prof. dr. A.G. de Bruyn (R.U. Groningen / N.F.R.A. Dwingeloo)
Prof. dr. M. Franx
Dr. P. van der Werf

Aan mijn ouders

Contents	viii
1 Introduction and Summary	1
1.1 Historical background	1
1.2 The new role of radio galaxies at high redshift	3
1.2.1 The discovery of radio-quiet galaxies at high redshift	4
1.2.2 High redshift radio galaxies: tracers of massive forming galaxies and clusters	4
1.3 Outline of this thesis	6
1.4 Outlook	8
2 A Sample of 669 Ultra Steep Spectrum Radio Sources to Find High Redshift Radio Galaxies	9
2.1 Introduction	10
2.2 Description of the Radio Surveys	12
2.2.1 WENSS	13
2.2.2 Texas	13
2.2.3 NVSS	17
2.2.4 FIRST	17
2.2.5 MRC	17
2.2.6 PMN	17
2.3 USS Samples	18
2.3.1 Survey combination issues	19
2.3.2 Sample definition	21
2.3.3 Discussion	22
2.4 Radio Observations	26
2.4.1 VLA observations and data reduction	26
2.4.2 ATCA observations and data reduction	27
2.4.3 Results	27
2.4.4 Notes on individual sources	28
2.4.5 Radio spectra and spectral curvature	30
2.4.6 Radio source properties	31
2.4.7 Identifications	32

2.5	Conclusions	36
	Appendix A Source Lists	38
	Appendix B Radio Maps	54
	Appendix C Radio Spectra	54
3	Optical and Near-IR Imaging of Ultra Steep Spectrum Radio Sources	55
3.1	Introduction	56
3.2	Observations and Data Reduction	57
3.2.1	Optical Imaging	59
3.2.2	Near-IR Imaging	60
3.2.3	Astrometry	62
3.2.4	Photometry	64
3.3	Results	68
3.3.1	Notes on individual sources	68
3.3.2	Magnitude and color distributions	72
3.3.3	Surface brightness profiles	74
3.3.4	Correlations with source parameters	75
3.3.5	Radio-near-IR alignment	77
3.4	The Hubble $K - z$ diagram	78
3.4.1	The $K - z$ diagram for radio galaxies	79
3.4.2	Comparison with the $K - z$ diagram of radio-quiet galaxies	82
3.5	Repercussions for HzRG searches	85
3.6	Conclusions	86
4	Spectroscopy of Ultra Steep Spectrum Radio Sources	95
4.1	Introduction	95
4.2	Observations and Data Reduction	98
4.2.1	Target selection	98
4.2.2	Observations	99
4.2.3	Data reduction	102
4.3	Results	103
4.3.1	Redshifts and line parameters	103
4.3.2	Notes on individual sources	107
4.3.3	Sources without redshifts	114
4.4	Discussion	115
4.4.1	Redshift distribution of USS sources	115
4.4.2	Undetermined redshifts	117
4.4.3	TN J0936–2243: an old, red galaxy	122
4.4.4	Quasars	124
4.5	Conclusions	125

5	A Radio Galaxy at $z = 5.19$	139
5.1	Introduction	139
5.2	Source Selection	140
5.3	Observations	142
5.4	Redshift Determination	144
5.5	Discussion	145
6	VLT Spectroscopy of the $z=4.11$ Radio Galaxy TN J1338–1942	147
6.1	Introduction	148
6.2	Source selection and previous observations	149
6.3	VLT observations	151
6.4	Discussion	153
6.4.1	Ly α emission	153
6.4.2	Ly α absorption	154
6.4.3	Continuum	154
6.5	Conclusions	156
7	Discovery of an Ultra-Steep Spectrum, Highly Polarized Red Quasar at $z = 1.462$	157
7.1	Introduction	157
7.2	Observations and data reduction	159
7.2.1	Radio Observations	159
7.2.2	Lick Identification and Spectroscopy	160
7.2.3	Keck Infrared Spectroscopy	161
7.2.4	Keck Spectropolarimetry	161
7.3	Results	163
7.4	Discussion	165
7.4.1	Classification	165
7.4.2	The Origin of the Polarization	166
7.4.3	Comparison with Other Quasars	168
7.5	Conclusions	169
8	A Statistical Study of Emission Lines from High Redshift Radio Galaxies	171
8.1	Introduction	172
8.2	Sample selection	174
8.3	Determination of source parameters	175
8.3.1	Radio parameters	176
8.3.2	Spectroscopic parameters	177
8.4	Correlations between parameters	181
8.4.1	Selection effects	181
8.4.2	Statistical tests	181
8.4.3	Spearman rank analysis	182

8.4.4	Correlations influenced or caused by selection effects	183
8.4.5	Possible correlations	187
8.4.6	Probable correlations	188
8.4.7	Summary of correlation analysis	191
8.5	Emission line ratios	191
8.5.1	HzRG UV line ratios	191
8.5.2	Shock and photo-ionization models	193
8.5.3	Comparison with the observations	195
8.5.4	Diagnostic diagrams with Ly α	199
8.5.5	UV-optical diagnostic diagrams	201
8.5.6	Nitrogen overabundance	202
8.6	Discussion	204
8.6.1	Simultaneous shock and photo-ionization	204
8.6.2	Emission-line luminosity - radio power correlations	208
8.6.3	The independent behavior of Ly α	209
8.7	Conclusions	210
	Appendix A Radio galaxy sample	212
	Appendix B Spearman rank correlation coefficients	216
	References	217
	Samenvatting	225
	Curriculum Vitae	231
	Acknowledgements	232

1.1 Historical background

The cornerstone of modern observational cosmology was laid by the discovery by Hubble & Humason (1931) that the recession speed of galaxies, as measured by the redshift, is proportional to their distance. Lemaître (1927, 1931) interpreted these results as evidence for an expanding Universe, which started with a discontinuity (Big Bang), ~ 15 billion years ago (determined using present-day values). Because the speed of light is finite, the light from distant galaxies was emitted when the Universe was young. By observing galaxies at very high redshift, we can thus look back in time, and observe the ancestors of the present-day galaxies. This allows us to answer some of the most important questions in observational cosmology: how do galaxies form and evolve, and when did the first primeval galaxies appear?

The quest for the most distant galaxies has been an important topic of observational cosmology during the last half century. Before the 1950's, this search was based on optical selection techniques. However, the subject was revolutionized by the identification of one of the brightest radio sources in the sky, Cygnus A, with a galaxy at a redshift $z = 0.056$ (Baade & Minkowski, 1954). Spectroscopic identification of this galaxy was relatively straightforward due to the bright emission lines in its spectrum, which require much shorter exposure times than stellar absorption features. Minkowski (1960) used this technique to determine the redshift of the radio source 3C 295 to be $z = 0.462$. For the next 35 years, detecting galaxies with powerful radio emission remained the most efficient method for finding galaxies at high redshifts. Much of this work was done on the revised third Cambridge catalog of radio sources (3CR Bennett, 1962) by Spinrad and collaborators (e.g., Spinrad et al., 1985), who carried out optical spectroscopy at the position of the radio source, and this way often could determine a spectroscopic redshift before the host object had been identified as a galaxy by optical imaging.

One of the main reasons for the successful spectroscopy campaign of the 3CR galaxies is a selection effect which virtually ensures that they are the most luminous emission line galaxies at a given redshift. This follows directly from the strong Malmquist bias in a radio flux density limited sample: the 3CR sample contains the most powerful radio sources out to $z \sim 2.5$. The discovery that the emission line luminosity and radio power are correlated (e.g., Rawlings & Saunders, 1991; McCarthy, 1993; chapter 8 of this thesis) means that the most powerful radio sources also have the most luminous emission lines at a given redshift. The physical meaning of this correlation is probably that both the radio power and the emission lines are being powered by a massive central black hole.

By the mid-1980's, most of the 3CR radio galaxies had been identified, and new samples of radio sources had to be constructed to find more high redshift radio galaxies (HzRGs). Using complete samples with lower flux density limits was not really feasible, as such samples would include too many low redshift, low luminosity sources. Additional radio selection techniques were developed to cut down the number sources in the radio samples, while increasing the fraction of distant objects. One approach is to select sources at the peak of the radio source counts at ~ 1 Jy (Allington-Smith, 1982), combined with near-IR identifications. This sample led to the discovery of the first radio galaxy at $z > 3$ (B2 0902+34 at $z = 3.395$, Lilly, 1988).

The most successful technique, however, proved to be the selection of sources with the steepest radio spectra. This method is based on the discovery that the identification fraction of radio sources on the Palomar Observatory Sky Survey (POSS, $R \lesssim 20$) decreases with steepening radio spectral index (Tielens et al., 1979; Blumenthal & Miley, 1979), suggesting that the steepest spectrum sources are more distant. This allowed the construction of reasonably sized samples with flux densities two orders of magnitude fainter than the 3CR. These samples of ultra steep spectrum (USS) radio sources have led to the discovery of large numbers of galaxies at significant redshifts ($z > 2$), including several objects at $z > 4$ (Lacy et al., 1994; Rawlings et al., 1996), with the current record holder lying at $z = 5.19$ (Chapter 5 of this thesis).

The main explanation for the success of the empirically found relation between the radio spectral index and redshift is a simple radio k -correction effect. The integrated radio spectrum of a classical powerful radio source like Cygnus A (see Figure 1.1) is usually concave. The observed spectral index determined from two fixed observed frequencies will therefore sample a steeper part of the radio spectrum for sources at higher redshift. The relation between the observed spectral index and redshift is clearly seen in complete samples of radio sources, such as the 3C, 6C, 7C, and MRC (e.g., Blundell, Rawlings, & Willott, 1999a, chapter 2 of this thesis). The effect of this k -correction is strengthened by two other processes: (i) an increased importance of inverse Compton losses at high redshift due to the stronger cosmic microwave background (e.g., Krolik & Chen, 1991), and (ii) a steepening of the *rest-frame* radio spectral index α_{rest} with increasing redshift, resulting from the relation between radio power P and α_{rest} , and the strong Malmquist bias in flux density limited surveys. The $P - \alpha_{rest}$ relation in flux density limited surveys is present because in order to

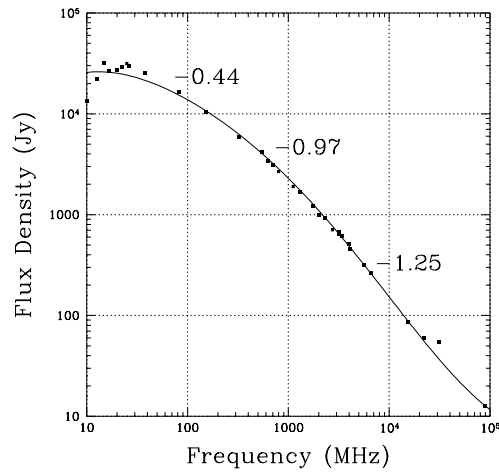


Figure 1.1: The radio spectral energy distribution of Cygnus A (e.g., Kellermann, Pauliny-Toth & Williams, 1969, and others). Note the spectral steepening with increasing frequency. If Cygnus A was located at larger distances (higher redshift), the k -correction would lead to a steeper *observed* spectral index between any two fixed frequencies in the optically thin part of the spectrum.

be powerful enough to be brighter than the flux density limit, the source requires a higher emissivity, and hence a stronger magnetic field. In turn, this leads to a lower synchrotron break frequency and more rapid synchrotron losses, resulting in a steeper radio spectrum (Krolik & Chen, 1991; Blundell, Rawlings, & Willott, 1999a).

1.2 The new role of radio galaxies at high redshift

At the start of this thesis project in 1996, radio galaxies were still the only population of galaxies detected at high redshift. The only other population of observable objects at these redshifts were quasars, which according to unification schemes (e.g., Barthel, 1989) are the same objects as radio galaxies, but seen along the radio jet axis (orientation unification), or galaxies whose nuclei are undergoing a phase of enhanced nuclear activity (time-dependent unification). Although quasars were known out to $z = 4.9$ (Schneider, Schmidt, & Gunn, 1991b), the host galaxies of these objects cannot be studied in detail because they are completely overwhelmed by the non-stellar emission from their central active galactic nucleus (AGN).

1.2.1 The discovery of radio-quiet galaxies at high redshift

A revival of interest in optically selected galaxies at high redshift occurred during the last five years. This was made possible with the commissioning of a new generation of large optical telescopes (mainly the 10m Keck telescopes on Mauna Kea), allowing such objects to be studied with unprecedented sensitivity (e.g., the optical spectroscopy of objects as faint as $I = 25$).

The breakthrough was the spectroscopic confirmation of a large population star-forming galaxies at $3 \lesssim z \lesssim 3.5$ selected using the Lyman break technique (Steidel et al., 1996). These galaxies are selected on the basis of the redshifted continuum spectral discontinuity at $(1+z) \times 912 \text{ \AA}$, and a relatively flat optical continuum longwards of redshifted Ly α . At high redshifts, hydrogen absorption from the Lyman limit and the Lyman forest causes objects to be highly attenuated in the bluer passbands (e.g., Steidel, Pettini, & Hamilton, 1995). When such Lyman-break candidates are observed in multi-slit mode with the Keck telescope, the redshifts of $\sim 15 - 20$ galaxies can be obtained simultaneously. In integration times of 1.5–3 hours, this allows typically the spectroscopic confirmation of more than 10 $z > 3$ galaxies, comparable to the *total* number of known radio galaxies at these redshifts.

To date, several hundred Lyman-break galaxies have been detected, and the Lyman-break technique has now been extended to $3.8 \gtrsim z \gtrsim 4.5$ (Steidel et al., 1999), and even beyond $z = 5$ (Weymann et al., 1998; Spinrad et al., 1998), using the extremely deep images from the Hubble deep field (Williams et al., 1996). At the same time, other optical search techniques have been successfully used to find $z > 5$ galaxies, such as narrow-band imaging of the Ly α line (e.g., Hu, McMahon, & Cowie, 1999), and serendipitous longslit searches (e.g., Dey et al., 1998; Manning et al., 2000). For a recent review of this rapidly evolving research field, see Stern & Spinrad (1999b).

1.2.2 High redshift radio galaxies: tracers of massive forming galaxies and clusters

Although radio galaxies are no longer the leading tracers of high redshift galaxies, their detailed study during the past decade have shown that they have properties which still make them unique probes of cosmic evolution. In addition, we can now compare their properties with other populations of galaxies at similarly high redshift. Radio galaxies follow a close correlation in the Hubble $K - z$ diagram (e.g., Lilly & Longair, 1984; Eales et al., 1997). This relation is maintained out to the highest redshifts observed (chapters 3 and 5 of this thesis), despite significant morphological evolution and strong k -correction effects (van Breugel et al., 1998). Because in the local Universe, the hosts of powerful radio galaxies are consistently identified with gE and cD galaxies (e.g., Matthews, Morgan, & Schmidt, 1964), this close relation in the $K - z$ diagram suggests that powerful radio sources are also hosted by the most massive galaxies at a given redshift. This relation is not unexpected, as the mass of the central super-massive black hole is assumed to be correlated with both the radio

power (e.g., Rawlings & Saunders, 1991; Willott et al., 1999), and with the total mass of the elliptical galaxy (e.g., Kormendy & Richstone, 1995; Magorrian et al., 1998).

Because the powerful radio emission points us to the most massive systems at high redshift, HzRGs are also generally more luminous and spatially extended than field galaxies at optical wavelengths, which allows them to be studied in greater detail (e.g., Pentericci, 1999b). HzRGs are also convenient beacons for over-dense regions in the early Universe, and therefore prime targets to search for high redshift proto-clusters (Pascarelle et al., 1996; Le Fevre et al., 1996; Kurk et al., 2000). Recent VLT multi-slit spectroscopy of narrow-band selected galaxies in the field surrounding the $z = 2.156$ radio galaxy PKS 1138–262 has indeed found an over-density of at least 14 galaxies within 1.5 Mpc of the radio galaxy and within 500 km s^{-1} of its systemic velocity (Pentericci et al., 2000c).

Together with high redshift quasars, HzRGs can put strong constraints on theoretical galaxy formation models. Their super-massive ($10^9\text{--}10^{10}M_{\odot}$) black holes need to be formed in the short time available since the Big Bang ($\lesssim 1 \text{ Gyr}$ at $z \simeq 5$ for all commonly considered values of the cosmological parameters). According to hierarchical theories of galaxy formation, massive galaxies were formed from mergers of smaller subunits (e.g., Kauffmann & Charlot, 1998), and it has been suggested that their central massive black holes grow in a similar hierarchical fashion (Kauffmann & Haehnelt, 2000). The detection of powerful radio emission from a radio galaxy at $z = 5.19$ (chapter 5 of this thesis), and of a luminous quasar at $z = 5.80$ (Fan et al., 2000), indicates some super-massive black holes have already formed within $\lesssim 1 \text{ Gyr}$. This may prove difficult to explain with hierarchical formation theories, and could instead favour theories invoking primordial black holes (Loeb, 1993).

Galaxies producing strong radio emission are rare, mostly because the life-time of their radio source is short compared to the age of their stellar populations. At high redshift, the age of the radio source seen in the known radio galaxies must be $< 10^7$ years (Blundell & Rawlings, 1999b). As a result, the surface density of radio galaxies at $z > 3$ is at least an order of magnitude smaller than that of Lyman-break galaxies (Stern & Spinrad, 1999b).

Selecting these galaxies at the time they are producing strong radio emission will introduce certain biases due to the influence of the radio source on their observed optical and near-IR emission. A clear manifestation of this is the discovery that the radio and optical emission in radio galaxies at $z \gtrsim 0.7$ tend to align (Chambers, Miley, & van Breugel, 1987). The origin of this aligned optical and near-IR emission probably varies from galaxy to galaxy, with the main contenders being scattered emission from an obscured central AGN (e.g., Cimatti et al., 1993), jet-induced star formation (e.g., Dey et al., 1997b), and nebular continuum emission (Dickson et al., 1995).

On the other hand, selecting galaxies solely on the basis of their radio emission has the advantage that the selection criteria are insensitive to the dust obscuration or reddening. The uncertainty in the amount of dust extinction is one of the largest

problems that prevents the optically selected Lyman-break galaxies to be used to determine the evolution of the cosmic star formation history (e.g., Steidel et al., 1999). Unlike the Lyman-break or narrow-band surveys, the radio selection is not targeted at a single redshift range, and in principle it can be used to determine redshifts out to $z \sim 17$, when the Ly α line redshifts out of the K -band.

For the above reasons, identifying and studying powerful radio galaxies at high redshifts is of great importance for observational cosmology.

1.3 Outline of this thesis

At the start of this thesis project in 1996, 104 radio galaxies were known to have $z > 2$, of which 14 were at $z > 3$, and only two at $z > 4$. It was clearly important to increase the number of HzRGs, especially at $z > 3$. Such a program was made possible by the completion of a new generation of large area radio surveys: the Westerbork Northern Sky Survey (WENSS; 325 MHz Rengelink et al., 1997), the Texas survey (Douglas et al., 1996, 365 MHz), the NRAO VLA Sky Survey (NVSS; 1.4 GHz Condon et al., 1998), and the Faint Images of the Radio Sky at Twenty centimeters (FIRST; 1.4 GHz Becker et al., 1995).

As a basis for the project reported in this thesis, we use these new radio surveys to construct a sample of 669 USS sources optimized for finding high redshift radio galaxies. This sample is more uniform than previous samples of USS sources and includes sources an order of magnitude fainter ($S_{1400} > 10$ mJy). This faint limit also allows the use of an extremely steep spectral index criterion (more stringent than before), which should increase the chance of finding the most distant radio galaxies. Because the emission line luminosity correlates with the radio power, the expected emission line fluxes at a given redshift are also fainter than in previous samples. Many of these observations are beyond the capabilities of 3–4m class telescopes, so to identify such faint objects, we required the use of the largest optical telescopes, viz. the Keck 10m and VLT 8m. To pursue this work, we took advantage of a long-standing collaboration between the AGN groups at Leiden Observatory and the University of California Lawrence Livermore National Laboratory. A large part of the optical and near-IR observations reported in this thesis were obtained with the Keck 10m telescopes during a 3-year stay by C. De Breuck as a graduate student guest at the IGPP at LLNL.

In Chapters 2, 3, and 4, we describe our radio, optical, near-IR and spectroscopic observations.

- Chapter 2 describes the selection of the USS sample, and the high resolution radio observations required to enable optical and/or near-IR identifications.
- In Chapter 3, we describe the optical and near-IR imaging of a subset of this sample. We use the Hubble $K - z$ diagram to construct a predicted redshift distribution of our sample. This peaks at $z \sim 2$, which is consistent with the

red $R - K$ colors of the identifications. We show that an additional selection based on the faintness of the K -band identification can substantially increase the efficiency of the sample for detecting radio galaxies at $z \gtrsim 3$. We find that the lower radio power of our sources causes a larger scatter in the $K - z$ relation at high redshift. We also compare the K -band magnitudes of the Lyman-break galaxies with those of the HzRGs. These results confirm that HzRGs are more than an order of magnitude more massive than field galaxies at a given redshift.

- In Chapter 4, we present optical spectroscopy of 62 USS sources, leading to the discovery of ten new radio galaxies at $z > 3$, including the most distant radio galaxy known to date at $z = 5.19$ (described in detail in Chapter 5). We also consider the possible nature of nine objects for which we could not determine the redshift, either because no spectral features or no optical emission was detected after integration times of 1 hour or more with the Keck telescope.

In Chapters 5, 6, and 7, we have selected three sources from our sample for further study.

- Chapter 5 presents the discovery of the most distant radio galaxy known to date. Until the discovery of a quasar at $z = 5.50$ (Stern et al., 2000a), this source was the most distant known AGN, the first time in history this honour was carried by a radio galaxy instead of a quasar.
- In Chapter 6, we examine the strong absorption which is often apparent in the blue side of the $\text{Ly}\alpha$ line of $z \gtrsim 3.5$ radio galaxies, using intermediate resolution spectroscopy of the $z = 4.11$ radio galaxy TN J1338–1942, obtained with the newly commissioned VLT Antu telescope. We also measure the discontinuity across the $\text{Ly}\alpha$ line due to intervening HI absorption along the cosmological line of sight. This break is clearly less pronounced than in quasars at similar redshifts, suggesting a possible selection bias in quasar samples that are selected on the basis of their optical colors.
- In Chapter 7, we present detailed observations of WN J0717+4611 at $z = 1.462$, one of the few quasars in our sample. Keck spectropolarimetry shows an unusually red optical continuum that is highly polarized (15%), with the polarization angle orthogonal to the radio jet axis. We argue that this data provides evidence that the red colour of this quasar is due to dust scattering, and that radio-selected samples of quasars might find more red quasars at cosmological redshifts.

In Chapter 8 we present a compilation of emission line data for a sample of 165 radio galaxies with the aim of studying the origin of the extended emission lines, and their relation to radio source properties. We examine the statistical significance of the 153 mutual correlations between 18 radio and spectroscopic parameters. We find evidence for an increased hydrogen abundance at $z \gtrsim 3$, both ionized and neutral.

The previously found relation between radio power and emission line luminosity for the bright emission lines is for the first time confirmed in the weaker UV emission lines. Finally, we find that although the dominating ionization mechanism in radio galaxies is photo-ionization by the central AGN, a contribution of shock ionization is required to obtain a consistent fit to the total integrated emission line spectra.

1.4 Outlook

The near-IR imaging and optical spectroscopy of our new USS sample have shown that the selection of radio sources is a powerful technique for finding massive galaxies at the highest redshifts. The lower flux limits in our sample not only allow the discovery of even higher redshift radio galaxies than previously possible, but also finds galaxies with a much larger range of radio power at a given redshift. This allows us to start disentangling the effects of radio power and cosmological evolution, which have often hampered the interpretation of the results from previous radio selected samples.

Nevertheless, there is still a difference of 2–3 magnitudes between the K -band magnitudes of radio galaxies and those of field galaxies at $z \gtrsim 2$. To make the connection between these two populations, large area radio surveys that are several orders of magnitude fainter than presently available will be needed. Such surveys could be made with next-generation radio telescopes such as LOFAR and eventually the square kilometer array (SKA). The optical and near-IR identification of these large numbers of sources would necessarily need to be a symbiosis of radio and optical selection techniques, which will become possible with new large-field optical and IR surveys (e.g., using the VLT Survey Telescope). This will allow the determination of photometric redshifts of radio sources, to be spectroscopically confirmed with current 8–10m class telescopes or future ground based 30–100m optical telescopes.

The commissioning of several new space- and ground-based telescopes and instruments enhanced by powerful adaptive optics techniques in the coming decade will enable detailed multi-spectral observations with sub-arcsecond resolution, increasing our understanding of the various components present on different scales in HzRGs. The presence of hot cluster gas (e.g., Carilli et al., 1998) and direct emission from the AGN can be detected with the Chandra and XMM-Newton X-ray telescopes. The star-forming regions will be spatially resolved in observations with the future ALMA (sub)mm-array. High-resolution optical and near-IR imaging with the Advanced Camera for Surveys (ACS) on HST will provide insight in the interaction of the radio source with the host galaxy and the morphological evolution at the earliest stages of the formation of massive galaxies.

A Sample of 669 Ultra Steep Spectrum Radio Sources to Find High Redshift Radio Galaxies

C. De Breuck, W. van Breugel, H. Röttgering, & G. Miley
2000, *A&AS*, 143, 303

Abstract

Since radio sources with Ultra Steep Spectra (USS; $\alpha \lesssim -1.30$; $S \propto \nu^\alpha$) are efficient tracers of high redshift radio galaxies (HzRGs), we have defined three samples of such USS sources using the recently completed WENSS, TEXAS, MRC, NVSS and PMN radio-surveys. Our combined sample contains 669 sources with $S_{1400} > 10$ mJy and covers virtually the entire sky outside the Galactic plane ($|b| > 15^\circ$). For our 2 largest samples, covering $\delta > -35^\circ$, we selected only sources with angular sizes $\Theta < 1'$. For 410 sources, we present radio-maps with $0''.3$ to $\sim 5''$ resolution from VLA and ATCA observations or from the FIRST survey, which allows the optical identification of these radio sources.

Comparison with spectrally unbiased samples at similar flux density levels, shows that our spectral index, flux density, and angular size selections do not affect the angular size distribution of the sample, but do avoid significant contributions by faint foreground spiral galaxies. We find that the spectral index distribution of 143,000 sources from the WENSS and NVSS consists of a steep spectrum galaxy and a flat spectrum quasar population, with the relative contribution of flat spectrum sources doubling from $S_{1400} > 0.1$ Jy to $S_{1400} > 2.5$ Jy. The identification fraction of our USS sources on the POSS ($R \lesssim 20$) is as low as 15%, independent of spectral index $\alpha < -1.30$. We further show that 85% of the USS sources that can be identified with an X-ray source are probably contained in galaxy clusters, and that $\alpha < -1.6$ sources are excellent Galactic pulsar candidates, because the percentage of these sources is four times higher in the Galactic plane.

Our sample has been constructed to start an intensive campaign to obtain a large sample of high redshift objects ($z > 3$) that is selected in a way that does not suffer from dust extinction or any other optical bias.

2.1 Introduction

Radio galaxies have now been found out to redshifts of $z = 5.19$ (Chapter 5) and radio-loud quasars out to $z = 4.72$ (Hook & McMahon, 1998). Although new optical selection techniques such as color-dropouts, deep spectroscopy of blank fields, and narrow-band Ly α imaging have now found galaxies at similar (Steidel et al., 1999) and even higher redshifts (up to $z \sim 5.75$; Dey et al., 1998; Weymann et al., 1998; Spinrad et al., 1998; Hu, McMahon, & Cowie, 1999), radio sources are still the only objects that can be selected uniformly over all redshift ranges, and in a way that does not suffer from optical biases such as dust extinction, which is known to be important at these high redshifts (e.g., Hughes, Dunlop, & Rawlings, 1997; Ivison et al., 1998a; Dickinson, 1998).

At low to moderate redshift ($z \lesssim 1$), powerful radio sources are uniquely identified with massive ellipticals (Lilly & Longair, 1984; Owen & Laing, 1989; Best, Longair & Röttgering, 1998a; McLure & Dunlop, 2000). The strongest indications that this is also true at higher redshifts comes from the near-IR Hubble $K - z$ diagram of radio galaxies which shows a remarkably close correlation from the present out to $z = 5.19$ (Lilly, 1989; Eales et al., 1997; van Breugel et al., 1998; Chapter 5). This suggests that we can use radio galaxies to study the formation and evolution of the most massive galaxies, which, by their implied star-formation history, can put important constraints on galaxy formation models, and even on cosmological parameters (e.g., Dunlop et al., 1996; Spinrad et al., 1997). Although the unification model for radio galaxies and quasars (e.g., Barthel, 1989) suggests we could also use quasars as tracers, a detailed stellar population study of quasar host galaxies is almost impossible due to the extreme luminosity of the AGN. Furthermore, samples of radio sources designed to find large quantities of quasars require additional optical selections (e.g., Gregg et al., 1996; Hook & McMahon, 1998; White et al., 2000).

Considerable effort has been spent over the last decade to find these high redshift radio galaxies (HzRGs), which has led to the discovery of more than 140 radio galaxies at redshifts $z > 2$ (see e.g., De Breuck et al., 1998 for a recent summary). However by $z > 3$, their numbers become increasingly sparse, and using flux limited radio surveys such as the 3CR ($S_{178} > 10$ Jy; Laing, Riley & Longair, 1983), or the MRC strip ($S_{408} > 0.95$ Jy; McCarthy et al., 1996), the highest redshift radio galaxy found so far is at $z \sim 3.2$ (Fig. 2.1; Rawlings, Eales, & Warren, 1990; McCarthy et al., 1996). This redshift limit arises because radio power is correlated with redshift in bright flux limited samples, and an upper limit exists in the radio luminosity. Lowering the flux limit would not only substantially increase the number of sources in these samples, but at the same time the fraction of luminous very high redshift radio galaxies would

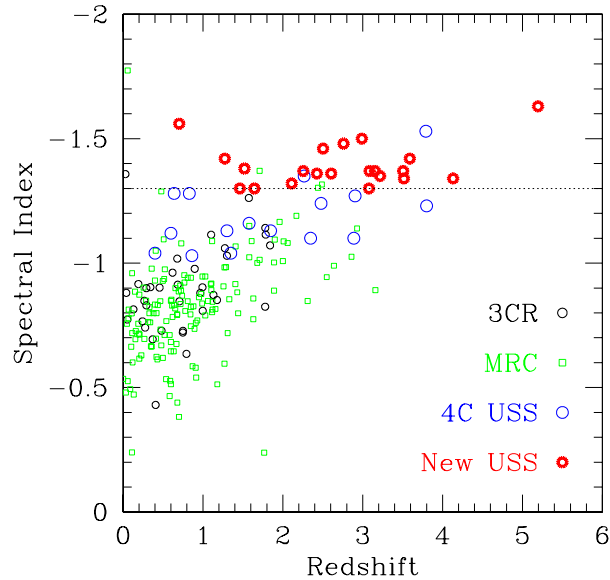


Figure 2.1: α_{1400}^{325} against z for 2 samples without spectral index selection (3CR, Spinrad et al., 1985 and MRC, McCarthy et al., 1996), and 2 USS samples (4C, Chambers et al. 1996a and our new WN/TN samples, as defined in this paper). Note that the correlation is present in the spectrally unbiased 3CR and MRC, and that the 4C and our new USS samples are finding three to five times more $z > 2$ radio galaxies than the MRC. The horizontal dotted line indicates the $\alpha_{1400}^{325} < -1.3$ cutoff used in our USS sample.

decrease (Blundell et al., 1998; Jarvis et al., 1999). This fractional decrease would arise even if there is no decrease in co-moving space density at $z \sim 2.5$. Such a redshift cutoff has been suggested by Bremer et al. (1998), but recently Jarvis et al. (1999) ruled out a break at $z \lesssim 2.5$. To efficiently find large numbers of HzRGs in acceptable observing times, it is therefore necessary to apply additional selection criteria, at the expense of completeness.

By far the most successful selection criterion has been the ultra steep spectrum criterion (e.g., Röttgering et al., 1994; Chambers et al., 1996a; Blundell et al., 1998). Selecting sources with very steep radio spectra increases dramatically the chance of finding $z > 2$ radio galaxies (Fig. 2.1). This technique is based on the results of Tielens et al. (1979) and Blumenthal & Miley (1979), who found that the identification fraction on the POSS ($R \lesssim 20$) decreases with steepening spectral index, consistent with the steeper sources being at higher redshifts. It is now getting clear that this

correlation can be explained by a combination of a K-correction of a concave radio spectrum and an increasing spectral curvature with redshift (Krolik & Chen, 1991; Carilli et al., 1999; van Breugel et al., 1999a). To further investigate the $z - \alpha$ correlation, we have calculated spectral indices using the flux densities from the WENSS (Rengelink et al., 1997) and NVSS (Condon et al., 1998) catalogs for four different samples: the flux density limited 3CR (Spinrad et al., 1985) and MRC (McCarthy et al., 1996) surveys, and the USS samples from the 4C (Chambers et al., 1996a) and the one presented in this paper. The results (Fig. 2.1) show a trend for steeper spectral index sources to have higher redshifts in flux limited, spectrally unbiased samples, confirming the empirical relation out to the highest redshifts. The efficiency of the USS criterion is clearly illustrated by the fact that the 4C USS sample (Chambers et al., 1996a) contains 50% $z > 2$ sources, and by the early spectroscopic results on the USS samples presented in this paper, which indicate that $\sim 2/3$ of our sources have $z > 2$. It is even more impressive to note that 13 of the 14 radio galaxies at $z > 3.5$ we know of have been found from samples with a steep spectral index selection¹! The limitation of this technique is that the steepest spectrum sources are rare, comprising typically only 0.5% (at $\alpha < -1.30$) of a complete low frequency sample; therefore, large and deep all sky surveys are needed to obtain a significant sample of USS sources.

With the advent of several new deep all-sky surveys (§2), it is now possible for the first time to construct a well defined all-sky USS sample with optimized selection criteria to find large numbers of $z > 3$ radio galaxies. In this paper, we describe the construction of such a sample, and present high resolution radio observations needed to determine accurate positions and morphologies. This information is essential for the optical and near-IR identifications, and subsequent optical spectroscopy of a significant sub-set of our sample, which will be described in a future papers. The organization of the paper is as follows: we describe the radio surveys we used in §2 and define our samples in §3. We present and discuss our radio observations in §4, and present our conclusions in §5.

2.2 Description of the Radio Surveys

During the past years, several all-sky radio-surveys have become available (Table 2.1), which are 1–2 orders of magnitude more sensitive than previous surveys at similar frequencies (Fig. 2.2). The combination of these new surveys allows us to define for the first time a large sample of USS sources that covers the whole sky² in both hemispheres. We list the main survey parameters in Table 2.1. In this section, we will briefly discuss the usefulness of these new radio surveys for the construction of USS samples.

¹The only exception is VLA J123642+6213 (Waddington et al., 1999), which has been identified in the HDF, but it does have a steep spectral index ($\alpha_{1400}^{8500} = -0.94$).

²To facilitate optical follow-up, we will exclude the Galactic plane at $|b| < 15^\circ$

Table 2.1: Radio Surveys

	WENSS	TEXAS	MRC
Frequency (MHz)	325	365	408
Sky region (J2000)	$\delta > +29^\circ$	$-35^\circ.7 < \delta < +71^\circ.5$	$-85^\circ < \delta < +18^\circ.5$
# of sources	229,576	67,551	12,141
Resolution	$54'' \times 54'' \text{ cosec } \delta$	$10''^a$	$2'.62 \times 2'.86 \text{ sec } (\delta - 35^\circ.5)$
Position uncertainty (strong sources)	$1''.5$	$0''.5-1''$	$8''$
RMS noise	~ 4 mJy	20 mJy	70 mJy
Flux density limit	18 mJy	150 mJy	670 mJy
Reference	Rengelink et al. (1997)	Douglas et al. (1996)	Large et al. (1981)

	NVSS	FIRST	PMN
Frequency (MHz)	1400	1400	4850
Sky region (J2000)	$\delta > -40^\circ{}^b$	$7^h 20^m < \alpha < 17^h 20^m$ $+22^\circ.2 < \delta < +57^\circ.5$ $21^h 20^m < \alpha < 3^h 20^m$ $-2^\circ.5 < \delta < +1^\circ.6$	$-87^\circ.5 < \delta < +10^\circ$
# of sources	1,689,515	437,429	50,814
Resolution	$45'' \times 45''$	$5'' \times 5''$	$4'.2$
Position uncertainty (strong sources)	$1''$	$0''.1$	$\sim 45''$
RMS noise	0.5 mJy	0.15 mJy	~ 8 mJy
Flux density limit	2.5 mJy	1 mJy	20 mJy
Reference	Condon et al. (1998)	Becker et al. (1995)	Griffith & Wright (1993)

^a The Texas interferometer has a complicated beam. However, sources with separations between $10''$ and $2'$ can be successfully modeled as doubles, and will have a single entry in the catalog. See Douglas et al. (1996) for details.

^b Some small gaps are not covered. They are listed on the NVSS homepage (1998 January 19 version).

2.2.1 WENSS

The Westerbork Northern Sky Survey (WENSS; Rengelink et al., 1997) at 325 MHz is the deepest low-frequency survey with a large sky coverage (3.14 sr). We used the WENSS to define the largest, and most complete USS sample to date, covering the entire sky North of declination 29° . We used version 1.0 of the main and polar WENSS catalogs. A small area is covered by both these catalogs; we selected only the sources from the main catalog in this overlapping area.

2.2.2 Texas

The Texas survey, made with the Texas interferometer from 1974 to 1983 (Douglas et al., 1996), covers 9.63 steradians at a frequency of 365 MHz with a limiting flux density about ten times higher than that of the WENSS. The Texas interferometer's

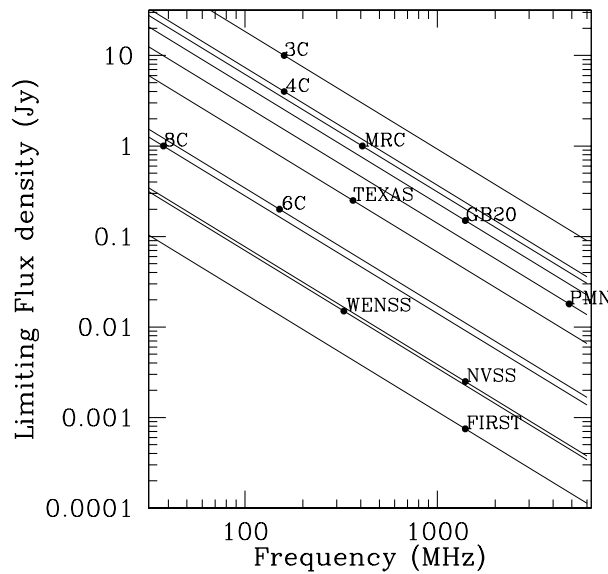


Figure 2.2: Limiting flux density plotted for all major radio surveys. Lines are of constant spectral indices of -1.3 . Note that WENSS, NVSS and FIRST have flux density limits ~ 100 times deeper than previous surveys at comparable wavelengths.

3.5 km maximum baseline provides $<1''$ positional accuracy, but its poor uv-coverage leads to irregular beamshapes and lobe-shifts, hampering accurate modeling of extended sources. A detailed discussion of these complications can be found in Douglas et al. (1996). To minimize these problems, we have selected only the 40.9% sources that are well modeled (listed with a '+++' flag in the catalog). This selection excludes primarily $S_{365} \lesssim 700$ mJy sources (Fig. 2.3), but even at $S_{365} \gtrsim 700$ mJy, one out of three sources is excluded by this criterion. Douglas et al. (1996) have calculated the completeness above flux density S of the Texas catalog (defined as the fraction of sources with true flux density greater than S which appear in the catalog) by comparing the Texas with the MRC (Large et al., 1981) and a variety of other low-frequency catalogs. They found that the completeness varies with declination (because the survey was done in declination strips over a large time span), and an expected increase in completeness at higher flux densities. In Table 2.2.2, we reproduce their completeness table, extended with the values after the '+++' selection.

To examine the reliability of the listed flux densities, and to check to what extent the '+++' selection has removed the spurious sources from the catalog, we have correlated the Texas '+++' sources with WENSS, NVSS and FIRST. In Figure 2.4, we compare

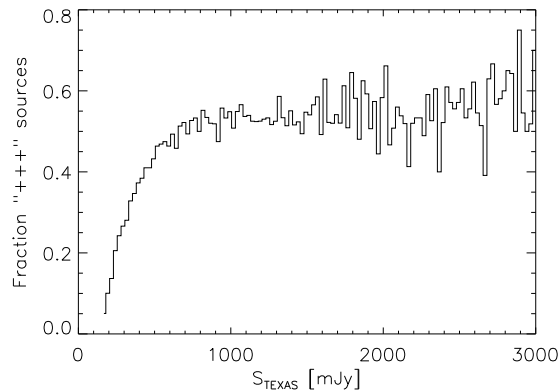


Figure 2.3: Fraction of sources with '+++' flag in the Texas catalog (see text) as a function of Texas S_{365} flux density. Note that the selection of '+++' sources excludes primarily sources with $S_{365} \lesssim 700$ mJy.

Table 2.2: Completeness of the Texas survey

Limiting flux density	all sources	'+++' sources
250 mJy	0.8	0.2
350 mJy	0.88	0.28
500 mJy	0.92	0.40
750 mJy	0.96	0.51
1 Jy	0.96	0.50

the Texas flux densities with those of the WENSS. At $S_{325} \gtrsim 500$ mJy, the ratio of the flux densities is closely distributed around 0.9. This ratio is what we expect due to the 40 MHz central frequency difference between the two surveys and assuming a spectral index $\alpha_{365}^{1400} = -0.879$ (the median of the Texas-NVSS spectral indices). At $S_{325} \lesssim 500$ mJy, the number of sources in the Texas catalog which are brighter than in WENSS catalog increases with decreasing flux density. This can be explained by the 'up-scattering' of sources near the flux limit of the Texas catalog (i.e., only sources intrinsically brighter than $S_{365} = 150$ mJy will be detected, but no $S_{365} < 150$ mJy sources with a large positive flux density measurement error). The result of this on a USS sample based on the Texas survey and correlated with a higher frequency survey (such as the NVSS), will be that with lower S_{365} , we will find more sources whose spectral indices appear steeper than they really are.

We also examined the dependence of the ratio Texas/WENSS flux density on angular

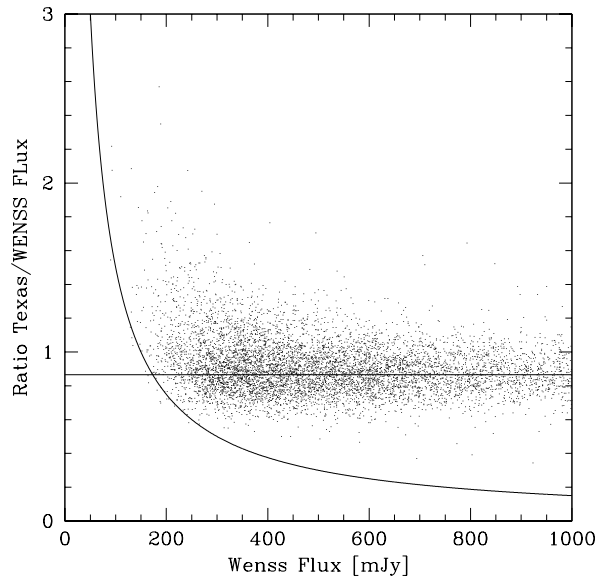


Figure 2.4: Ratio of integrated Texas over WENSS flux density against integrated WENSS flux density. Only Texas '+++' sources are plotted. The horizontal line is the expected ratio 0.865 due to the 40 MHz difference in central frequency, and assuming a spectral index of $\alpha_{365}^{1400} = -0.88$. The curved line indicates a 150 mJy flux density limit in the Texas catalog. Note the increasing amount of overestimated Texas flux densities with decreasing flux density $S_{WENSS} < 400$ mJy.

size, determined from the FIRST survey (see §2.1.4). We found no significant residual variation of the flux density ratio at sizes between $5''$ and $2'$.

In Figure 2.6b, we plot the density of NVSS sources around a Texas source (see also §2.2.5). The width of the over-density peak ($\sim 10''$) is due to the positional inaccuracies in the Texas and NVSS catalogues. However, the very broad tail of sources between $20''$ and $110''$ and the secondary peak coinciding with the fringe separation at $73''$ indicates that the '+++' selection did not remove all spurious sources from the catalog.

In summary, after the selection of '+++' sources, the Texas catalog still contains $< 5\%$ spurious sources (Douglas et al., 1996), probably due to residual lobe-shifted sources. Our comparison of the Texas flux densities with those of the WENSS survey shows that the differences are consistent with the errors quoted in the catalog. The selection of the Texas catalog with only '+++' sources is thus $>95\%$ reliable, but only $\sim 40\%$ complete.

2.2.3 NVSS

The NRAO VLA Sky Survey (NVSS; Condon et al., 1998) covers the 10.3 steradians north of -40° at 1.4 GHz, and reaches a 50 times lower limiting flux density than previous large area 1.4 GHz surveys. At the flux density levels we are using ($S_{1400} > 10$ mJy), the catalog is virtually complete. Because the NVSS resolution is comparable to that of the WENSS and Texas surveys, and its sky coverage is large, we use the NVSS to determine the spectral indices in our USS samples based on the WENSS and Texas surveys. The final NVSS catalog was not yet completed at the time of our USS sample construction. For our final sample, presented in this paper, we use the 1998 January 19 version. This version still lacks data in a small number of regions of the sky (listed on the NVSS homepage). As a result, the sky coverage of the area listed in Table 2.3.1 is only 99.77%.

2.2.4 FIRST

The Faint Images of Radio Sky at Twenty centimeters (FIRST; Becker et al., 1995) survey is currently being made with the VLA in the B-array at 1.4 GHz, and has a limiting flux density three times deeper than the NVSS. We used the 1998 February 4 version of the catalog, covering 1.45 steradians. As noted by Becker et al. (1995), the photometry for extended sources in FIRST might be less reliable than that of the NVSS, due to the $9\times$ higher resolution, which could underestimate large-scale diffuse radio emission. As the FIRST area is completely covered by the NVSS, we will consistently use NVSS flux densities for our spectral index calculation. The main advantages of FIRST over NVSS for our purposes are the much better positional accuracy ($< 0''.5$) and the higher ($5''$) resolution. This combination allows the identification of even the very faint ($R > 20$) optical counterparts of radio sources. Additionally, the fainter detection limit of the FIRST allows an extra check on the flux densities of compact sources.

2.2.5 MRC

The Molonglo Reference Catalog of radio sources (Large et al., 1981) at 408 MHz is presently the most sensitive low-frequency catalog with reasonable positional accuracy that covers the deep southern hemisphere, $\delta < -35^\circ$. We will use this catalog in combination with the PMN survey (see below) to define the first USS sample at $\delta < -40^\circ$.

2.2.6 PMN

The Parkes-MIT-NRAO (PMN) survey is a combination of 4 strips observed with the Parkes telescope at 4.85 GHz. The strips cover different parts of the sky, each with a slightly different limiting flux density. The regions are: southern ($-87.5^\circ < \delta < -37^\circ$, Wright et al., 1994), zenith ($-37^\circ < \delta < -29^\circ$, Wright et al., 1996), tropical ($-29^\circ <$

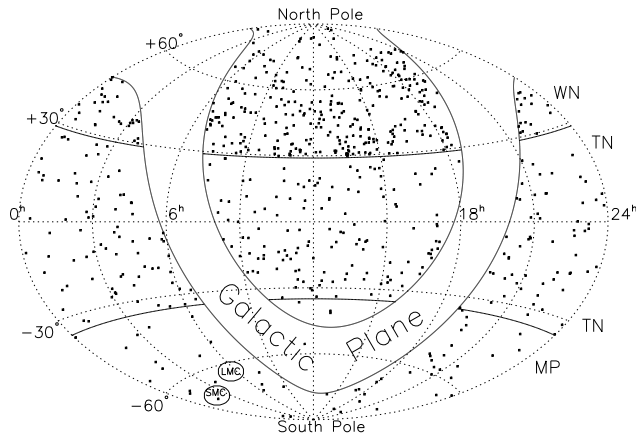


Figure 2.5: Sky coverage of our 3 USS samples. Constant declination lines denote the boundaries between our the WN and TN and between the TN and MP samples, as indicated on the right. Note the difference in source density and the exclusion of the Galactic Plane.

$\delta < -9^{\circ}5$, Griffith et al., 1994), and equatorial ($-9^{\circ}5 < \delta < +10^{\circ}$, Griffith et al., 1995). For our southern hemisphere sample, we have used the southern and zenith catalogs to find USS sources at $\delta < -30^{\circ}$.

2.3 USS Samples

Figure 2.2 shows that the surveys described above have very compatible flux density limits for defining samples of USS sources. At the same time, their sky coverage is larger and more uniform than previous surveys used for USS sample construction (Wieringa & Katgert, 1992; Röttgering et al., 1994; Chambers et al., 1996a; Blundell et al., 1998; Rengelink, 1998; Pursimo et al., 1999; Pedani & Grueff, 1999; Andernach et al., 2000). We selected the deepest low and high frequency survey available at each part of the sky. For a small region $-35^{\circ} < \delta < -30^{\circ}$ which is covered by both Texas and MRC, we used both surveys. This resulted in a more complete samples since the lower sensitivity of the PMN survey in the zenith strip (see §2.6) is partly compensated by the (albeit incomplete) Texas survey. To avoid problems with high Galactic extinction during optical imaging and spectroscopy, all regions at Galactic latitude $|b| < 15^{\circ}$ were excluded³, as well as the area within 7° of the LMC and SMC. This resulted in three USS samples that cover a total of 9.4 steradians (Fig. 2.5). We designate the USS samples by a two-letter name, using the first letter of their

³This also reduces the number of Galactic pulsars in our sample (see §4.7.2).

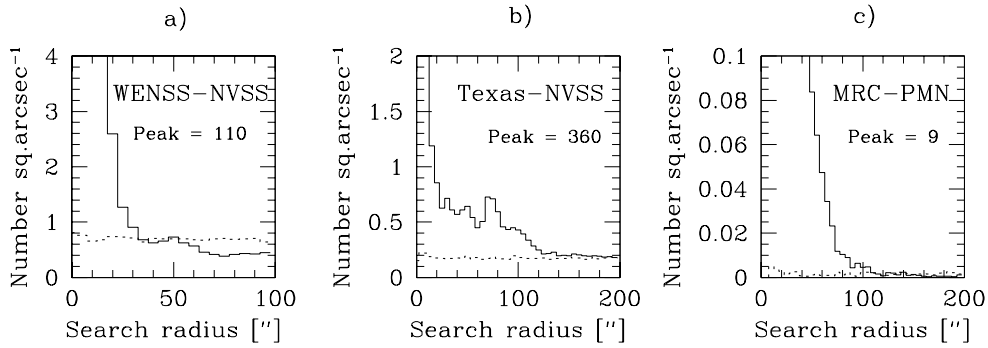


Figure 2.6: The density of sources from the high frequency catalog used in the correlation (NVSS or PMN) around sources from the low frequency catalog (WENSS, Texas or MRC) as a function of search radius. The dotted line represents the distribution of confusion sources (see text). The apparent under-density of WENSS–NVSS sources at search radii $\gtrsim 60''$ is due to the grouping of multiple component sources in the $\sim 1'$ resolution WENSS. Note the plateau and secondary peak around the $73''$ Texas fringe separation in the Texas–NVSS correlation and the much larger uncertainty in the MRC–PMN correlation.

low- and high-frequency contributing surveys. Sources from these samples are named with this 2-letter prefix followed by their IAU J2000-names using the positions from the NVSS catalog (WN and TN samples) or the MRC catalog (MP sample). We did not rename the sources after a more accurate position from our radio observations or from the FIRST survey. The sample definitions are summarized in Table 2.3.1.

2.3.1 Survey combination issues

We first discuss the problems that arise when combining radio surveys with different resolutions and positional uncertainties.

Correlation search radius

Due to the positional uncertainties and resolution differences between radio surveys, in general the same source will be listed with slightly different positions in the catalogs. To empirically determine the search radius within which to accept sources in 2 catalogs to be the same, we compared the density of objects around the position listed in the low-frequency survey (which has lower resolution) with the expected number of random correlations in each sample (\equiv confusion sources). To determine this number as a function of distance from the position in the most accurate catalog, we created a

Table 2.3: USS samples

Sample	Sky Area $ b > 15^\circ$	Density sr^{-1}	Spectral Index	SR ^a	Flux Limit mJy	C ^b	R ^b	# of Sources
WN	$29^\circ < \delta < 75^\circ$ ^c	151	$\alpha_{1400} \leq -1.30$	10''	$S_{1400} > 10$	96%	90%	343
TN	$-35^\circ < \delta < 29^\circ$ ^c	48 ^d	$\alpha_{1400} \leq -1.30$	10''	$S_{1400} > 10$	97% ^d	93%	268
MP	$\delta < -30^\circ$	26	$\alpha_{408} \leq -1.20$	80''	$S_{408} > 700$ $S_{4850} > 35$	100%	100%	58

^a SR=search radius

^b C=completeness and R=reliability accounting only for scattering across the spectral index limit (see §3.3.1).

^c coverage is only 99.7% because some small patches of sky we not covered at the time of writing. They are listed on the NVSS homepage (1998 January 19 version).

^d Because we selected only problem free sources from the Texas survey, the effective completeness of the TN sample is $\sim 30\%$.

random position catalog by shifting one of the input catalogs by 1° in declination, and made a correlation with this shifted catalog. The density of sources as a function of distance from the un-shifted catalog then represents the expected number of confusing sources as a function of radial distance. In Figure 2.6, we plot for each of our three samples the observed density around these sources with this confusing distribution over-plotted. The correlation search radius should thus be chosen at a distance small enough for the density of confusion sources to be negligible.

We decided to adopt the radius where the density of real sources is at least ten times higher than the density of confusion sources as the search radius for our sample construction, except for the WN sample (would be $15''$) where we chose the same radius as for the TN sample ($10''$). The later was done for consistency between both samples. Because of the five times lower resolution and source densities in the MRC and PMN surveys, the search radius of the MP sample is eight times larger. Summarized, the search radii we used are $10''$ for WN and TN, and $80''$ for MP.

Angular size

In order to minimize errors in the spectral indices due to different resolutions and missing flux on large angular scales in the composing surveys, we have only considered sources which are not resolved into different components in the composing surveys. Effectively, this imposes an angular size cutoff of $\sim 1'$ to the WN, $\sim 2'$ to the TN sample and $\sim 4'$ to the MP sample. We deliberately did not choose a smaller angular size cutoff (as e.g., Blundell et al. (1998) did for the 6C* sample), because (1) higher resolution angular size information is only available in the area covered by the FIRST survey, and (2) even a $15''$ cutoff would only reduce the number of sources by 30%, while it would definitely exclude several HzRGs from the sample. For example, in the 4C USS sample (Chambers et al., 1996b), three out of eight $z > 2$ radio galaxies have angular sizes $> 15''$.

We think that our $\sim 1'$ angular size cutoff will exclude almost no HzRGs, because the largest angular size for $z > 2$ radio galaxies in the literature is $53''$ (4C 23.56 at $z = 2.479$; Chambers et al., 1996a; Carilli et al., 1997), while all 45 $z > 2.5$ radio galaxies with good radio maps are $< 35''$ (Carilli et al., 1997). Although the sample of known $z > 2$ radio galaxies is affected by angular size selection effects, very few HzRGs larger than $1'$ would be expected.

The main incompleteness of our USS sample stems from the spectral index cutoff and the flux limit (§3.2). However, our flux limit ($S_{1400}=10$ mJy) is low enough to break most of the redshift-radio power degeneracy at $z > 2$. To achieve this with flux limited samples, multiple samples are needed (e.g., Blundell, Rawlings, & Willott, 1999a).

2.3.2 Sample definition

WENSS-NVSS (WN) sample

A correlation of the WENSS and NVSS catalogs with a search radius of $10''$ centered on the WENSS position (see §3.1.1) provides spectral indices for $\sim 143,000$ sources. Even with a very steep $\alpha_{325}^{1400} \leq -1.30$ spectral index criterion, we would still have 768 sources in our sample. To facilitate follow-up radio observations, and to increase the accuracy of the derived spectral indices (see §3.3.1), we have selected only NVSS sources with $S_{1400} > 10$ mJy. Because the space density of the highest redshift galaxies is low, it is important not to limit the sample area (see e.g., Rawlings et al., 1998) to further reduce the number of sources in our sample. Because the NVSS has a slightly higher resolution than the WENSS ($45''$ compared to $54'' \times 54'' \text{ cosec } \delta$), some WENSS sources have more than one associated NVSS source. We have rejected the 11 WN sources that have a second NVSS source within one WENSS beam. Instead of the nominal WENSS beam ($54'' \times 54'' \text{ cosec } \delta$), we have used a circular $72''$ WENSS beam, corresponding to the major axis of the beam at $\delta = 48^\circ$, the position that divides the WN sample into equal numbers to the North and South. The final WN sample contains 343 sources.

Texas-NVSS (TN) sample

Because the Texas and NVSS both have a large sky-coverage, the area covered by the TN sample includes 90% of the WN area. In the region $\delta > 29^\circ$, we have based our sample on the WENSS, since it does not suffer from lobe-shift problems and reaches ten times lower flux densities than the Texas survey (§2.2). In the remaining 5.28 steradians South of declination $+29^\circ$, we have spectral indices for $\sim 25,200$ sources. Again, we used a $10''$ search radius (see §3.1.1), and for the same reason as in the WN sample we selected only NVSS sources with $S_{1400} > 10$ mJy. Combined with the $\alpha_{365}^{1400} \leq -1.30$ criterion, the number of USS TN sources is 285. As for the WN sample, we further excluded sources with more than one $S_{1400} > 10$ mJy NVSS source within $60''$ around the TEXAS position, leaving 268 sources in the final TN sample.

We remind (see §2.2) that the selection of the TEXAS survey we used is only $\sim 40\%$ complete with a strong dependence on flux density. Using the values from table 2, we estimate that the completeness of our TN sample is $\sim 30\%$.

MRC-PMN (MP) sample

In the overlapping area, we preferred the TN over the MP sample for the superior positional accuracies and resolutions of both Texas and NVSS compared to MRC or PMN. Because the MRC survey has a low source density, we would have only 13 MP sources with $\alpha_{408}^{4850} \leq -1.30$. We therefore relaxed this selection criterion to $\alpha_{408}^{4850} \leq -1.20$, yielding a total sample of 58 sources in the deep South ($\delta < -30^\circ$).

2.3.3 Discussion

Spectral index errors

We have listed the errors in the spectral indices due to flux density errors in the catalogs in Tables A.1 to A.3. The WN and TN samples have the most accurate spectral indices: the median spectral index errors are $\Delta\bar{\alpha}_{325}^{1400} = 0.04$ for WN sources and $\Delta\bar{\alpha}_{365}^{1400} = 0.04$ ($S_{365} > 1$ Jy) to 0.07 ($S_{365} > 150$ mJy) for TN sources. For the MP sample, $\Delta\bar{\alpha}_{408}^{4850} \approx 0.1$, with little dependence on flux density ($S_{408} > 750$ mJy). Because our sample selects the sources in the steep tail of the spectral index distribution (Fig. 2.7 and 2.8), there will be more sources with an intrinsic spectral index flatter than our cutoff spectral index that get scattered into our sample by measurement errors than there will be sources with intrinsic spectral index steeper than the cutoff that get scattered out of our sample.

Following the method of Rengelink (1998), we fitted the steep tail between $-1.60 < \alpha < -1.0$ with a Gaussian function. For each of our three samples, we generated a mock sample drawn from this distribution, and added measurement errors by convolving this true spectral index distribution with a Gaussian distribution with as standard deviation the mean error of the spectral indices. The WN mock sample predicts that 13 $\alpha_{325}^{1400} < -1.30$ sources get scattered out of the sample while 36 $\alpha_{325}^{1400} > -1.30$ sources get scattered into the USS sample. Thus, the WN sample is 96% complete and 90% reliable. For the TN sample, we expect to lose 7 $\alpha_{365}^{1400} < -1.30$ sources⁴, and have 18 contaminating $\alpha_{365}^{1400} > -1.30$ sources. The completeness is thus 97% and the reliability 93%. For the MP sample, this spectral index scattering is negligible, because there are too few sources in the steep spectral index tail.

Our reliability and completeness are significantly better than the values of $\sim 75\%$ and $\sim 50\%$ of Rengelink (1998) because (1) our spectral indices are more accurate because they were determined from a wider frequency interval than the 325–610 MHz used by Rengelink (1998), and (2) our sample has a steeper cutoff spectral index, where the

⁴only due to the spectral index cutoff, the sample has more important incompleteness factors; see §2.2

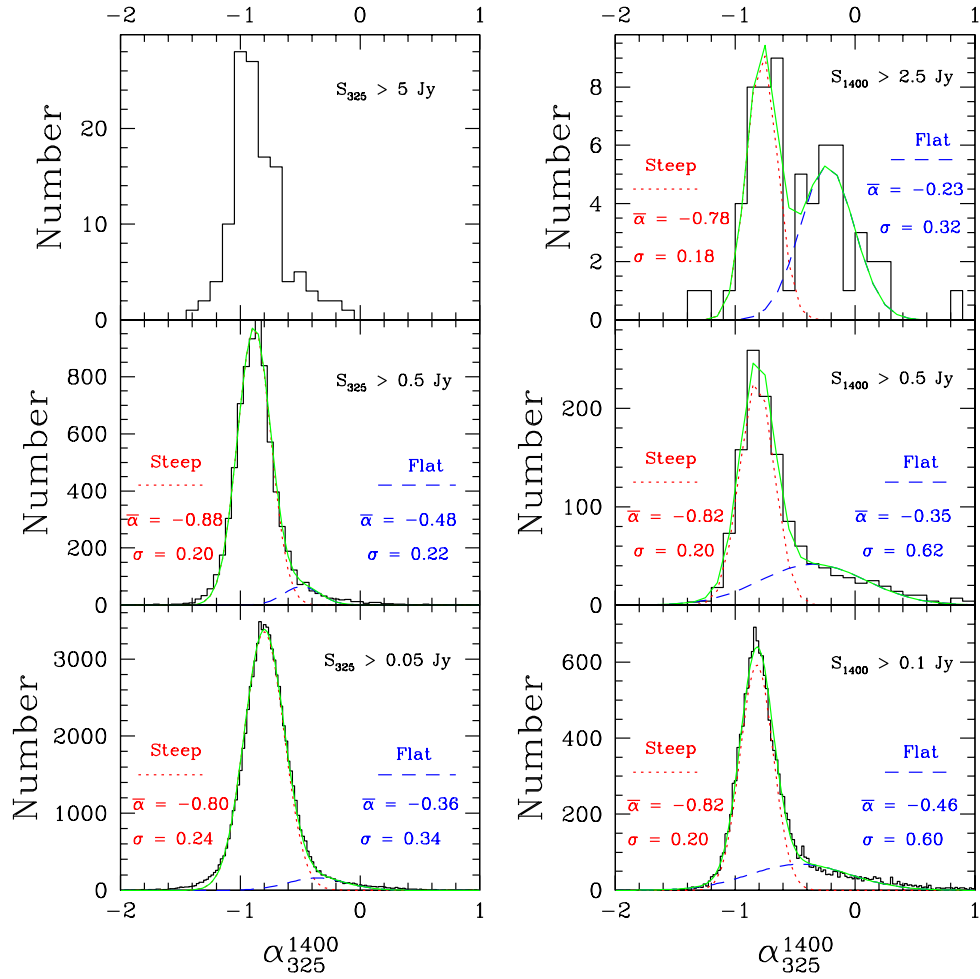


Figure 2.7: Spectral index distributions from the WENSS-NVSS correlation. The left and right panels show the variation with 325 MHz and 1.4 GHz flux density. A low frequency selected sample is more appropriate to study the steep-spectrum population. The parameters of a two-component Gaussian fit (dotted line = steep, dashed line = flat) are shown in each panel. The solid line is the sum of both Gaussians.

spectral index distribution function contains fewer sources and has a shallower slope, leading to fewer sources that can scatter in or out of the sample.

Spectral index distributions

Using the 143,000 spectral indices from the WENSS-NVSS correlation, we examined the flux density dependence of the steep and flat spectrum sources. Selecting sources with $S_{325} > 50$ mJy or $S_{1400} > 100$ mJy assures that we will detect all sources with $\alpha_{325}^{1400} > \frac{\ln(S_{NVSS}^{lim}/50)}{\ln(325/1400)} = -1.82$ or $\alpha_{325}^{1400} < \frac{\ln(S_{WENSS}^{lim}/100)}{\ln(325/1400)} = 0.82$ respectively, where $S_{NVSS}^{lim} = 3.5$ mJy and $S_{WENSS}^{lim} = 30$ mJy are the lowest flux densities where the NVSS and WENSS are complete (Condon et al., 1998; Rengelink et al., 1997). The results shown in Figure 2.7 therefore reflect only the effect of a different selection frequency. Two populations are present in both the S_{325} and S_{1400} selected distributions. The peaks of the steep and flat populations at $\bar{\alpha}_{325}^{1400} \approx -0.8$ and $\bar{\alpha}_{325}^{1400} \approx -0.4$ do not show significant shifts over three orders of magnitude in flux density. This is consistent with the results that have been found at 4.8 GHz (Witzel et al., 1979; Machalski & Ryś, 1981; Owen, Condon, & Ledden, 1983), with the exception that their $\bar{\alpha}_{1400}^{4800} \approx 0.0$ for the flat spectrum component is flatter than the $\bar{\alpha}_{325}^{1400} \approx -0.4$ we found. However, we find that the relative contribution of the flat spectrum component increases from 25% at $S_{1400} > 0.1$ Jy to 50% at $S_{1400} > 2.5$ Jy.

Because the steep- and flat-spectrum populations are best separated in the $S_{1400} > 2.5$ Jy bin, we have searched the literature for identifications of all 58 $S_{1400} > 2.5$ Jy sources to determine the nature of both populations. All but one (3C 399, Martel et al., 1998) of the objects outside of the Galactic plane ($|b| > 15^\circ$) were optically identified. Of the 30 steep spectrum ($\alpha_{325}^{1400} < -0.6$) sources, two thirds were galaxies, while the rest were quasars. Half of the flat spectrum ($\alpha_{325}^{1400} > -0.6$) sources were quasars, 20% blazars, and 30% galaxies. Figure 2.7 therefore confirms that the steep and flat spectral index populations are dominated by radio galaxies and quasars respectively. We also find that while the relative strength between the steep and flat spectrum populations changes due to the selection frequency, the median spectral index and width of the population does not change significantly over three orders in magnitude of flux density. Even fainter studies would eventually start to get contamination from the faint blue galaxy population (see e.g., Windhorst et al., 1985).

Consistency of the three USS samples

We compare the spectral index distributions of our three USS samples in logarithmic histograms (Fig. 2.8). The distributions are different in two ways. First, the WENSS-NVSS correlation contains nine times more sources than the Texas-NVSS, and 14 times more than the MRC-PMN correlation. Second, the shapes of the distributions are different: while the steep side of the TN sample coincides with that of the WN, its flat end part falls off much faster. The effect is so strong that it even shifts the TN

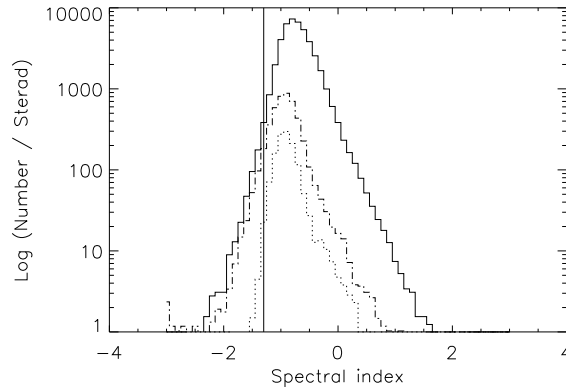


Figure 2.8: Logarithmic spectral index distribution for WENSS-NVSS (full line), Texas-NVSS (dot-dash line) and MRC-PMN (dotted line). The vertical line indicates the -1.3 cutoff used in our spectral index selection. Note the difference in number density and the sharper fall-off on the flat-end part of the TN and MP compared to the WN.

peak steep-wards by ~ 0.15 . For the MP sample, the same effect is less pronounced, though still present.

Both effects are due to the different flux density limits of the catalogs. The deeper WENSS catalog obviously contains more sources than the TEXAS or MRC catalogs, shifting the distributions vertically in Figure 2.2. The relative 'shortage' of flat spectrum sources in the Texas-NVSS and MRC-PMN correlations can be explained as follows. A source at the flux density limit in both WENSS and NVSS would have a spectral index of $\alpha_{325}^{1400} = -1.3$, while for Texas and NVSS this would be $\alpha_{365}^{1400} = -1.7$ (see Fig. 2.2). Faint NVSS sources with spectral indices flatter than these limits will thus more often get missed in the TEXAS catalog than in the WENSS catalog. This effect is even strengthened by the lower completeness at low flux densities of the Texas catalog. However, very few USS sources will be missed in either the WENSS-NVSS or Texas-NVSS correlations⁵. The parallel slope also indicates that the USS sources from both the WENSS-NVSS and Texas-NVSS correlations were drawn from the same population of radio sources. We therefore expect a similar efficiency in finding HzRGs from both samples.

The MP sample has been defined using a spectral index with a much wider frequency difference. However, the observed ATCA 1.420 GHz flux densities can be used to construct α_{408}^{1420} . An 'a posteriori' selection using $\alpha_{408}^{1420} \leq -1.30$ from our ATCA observations (see §4.2) would keep $\sim 60\%$ of the MP sources in a WN/TN USS sample.

⁵The TN sample will have more spurious sources at low flux density levels; see §2.2

Table 2.4: Radio Observations

UT Date	Telescope	Config.	Frequency	Resolution	# of sources
1996 October 28	VLA	A	4.86 GHz	0''.3	90 WN, 25 TN
1997 January 25	VLA	BnA	4.86 GHz	0''.6	29 TN
1997 March 10	VLA	BnA	4.885 GHz	0''.6	8 TN
1997 December 15	ATCA	6C	1.420 GHz	6'' × 6'' cosec δ	41 MP, 32 TN
1998 August 12+17	VLA	B	4.86 GHz	1''.0	151 WN

2.4 Radio Observations

Of all the major radio surveys described in §2, only FIRST has sufficient positional accuracy and resolution for the optical identification of $R > 20$ objects. We present FIRST maps of 139 WN and 8 TN sources in Appendix B.

Outside the area covered by FIRST, we have observed all the remaining WN sources, 30% of the TN sample, and 71% of the MP sources at 0''.3 to 5'' resolution using the Very Large Array (VLA; Napier, Thompson & Ekers, 1983) and Australia Telescope Compact Array (ATCA; Frater, Brooks & Whiteoak, 1992) telescopes. A log of the radio observations is given in Table 2.4. We observed targets for our VLA runs on the basis of declination (A-array for $\delta > 0^\circ$ and BnA-array for $\delta < 0^\circ$) and sky coverage of the WN and TN samples, which were still incomplete at the time of the 1996 observations. We observed all WN, and most TN sources with the VLA, and all MP sources with the ATCA. We observed TN sources between $-31^\circ < \delta < -10^\circ$ with either VLA or ATCA, depending on the progress of the NVSS at the time of the observations.

2.4.1 VLA observations and data reduction

We observed all sources in the standard 4.86 GHz C-band with a 50 MHz bandwidth, resulting in a resolution of $\sim 0''.3$ in the A-array and $\sim 1''$ in the BnA-array. We spent 5 minutes on each source, implying a theoretical rms level of 75 μ Jy, or a ratio of total integrated signal over map noise of 110 for the weakest sources, assuming no spectral curvature beyond 1.4 GHz. We performed calibration and data editing in *AITPS*, the Astronomical Image Processing System from NRAO. We used 3C286 as the primary flux calibrator in all runs. Comparison of the flux density of 3C48 with the predicted values indicated the absolute flux density scale was accurate up to 2%. We observed nearby (within 15°) secondary flux calibrators every 15 to 20 minutes to calibrate the phases. After flagging of bad data, we spilt the uv-data up into separate data sets for imaging and self-calibration in DIFMAP, the Caltech difference mapping program (Sheppard et al., 1997). We used field sizes of 164'' (A-array) or 256'' (BnA-array) with pixel scales of 0''.08 / pixel (A-array) or 0''.25 / pixel (BnA-array). Even the smallest field of view is still four times larger than the resolution of the NVSS, so all

components of an unresolved NVSS source will be covered.

We cleaned each source brighter than the 5σ level, followed by a phase-only self-calibration. We repeated the latter for all sources in the field of a source. Next, we made a new model from the (self-calibrated) uv-data, and subsequently cleaned to the level reached before. The last stage in the mapping routine was a deep clean with a 1% gain factor over the entire field. Most of the resulting maps have noise levels in the range 75 to 100 μJy , as expected.

2.4.2 ATCA observations and data reduction

We used the ATCA in the 6C configuration, which has a largest baseline of 6km. We observed at a central frequency of 1.384 GHz, which was selected to avoid local interference. We used 21 of the 30 frequency channels that had high enough signal, which resulted in an effective central frequency of 1.420 GHz, with a 84 MHz bandwidth. In order to obtain a good uv-coverage, we observed each source eight to ten times for three minutes, spread in hour angle. The primary flux calibrator was the source 1934-648; we used secondary flux calibrators within 20° of the sources to calibrate the phases. We performed editing and calibration in *ALPS*, following standard procedures. We made maps using the automated mapping/self-calibration procedure MAPIT in *ALPS*. The resulting 1.420 GHz maps (see Appendix B) have noise levels of ~ 5 mJy.

2.4.3 Results

Of all 343 WN sources, 139 have FIRST maps (Appendix B). All remaining 204 sources were observed, and 141 were detected. The remaining 30% were too faint at 4.86 GHz to be detected in 5 min snapshots, because their high frequency spectral index steepens more than expected, or they were over-resolved. Because they are significantly brighter, all the observed 89 TN and 41 MP sources were detected. We present contour maps of all the detections in Appendix B and list the source parameters in Tables A.1 to A.3.

We have subdivided our sources into 5 morphological classes, using a classification similar to that used by Röttgering et al. (1994). Note that this classification is inevitably a strong function of the resolution, which varies by a factor of 20 between the VLA A-array and the ATCA observations.

We have determined the source parameters by fitting two-dimensional Gaussian profile to all the components of a source. The results are listed in Tables A.1 to A.3 which contain:

Col 1: Name of the source in IAU J2000 format. The 2-letter prefix indicates the sample: WN: WENSS–NVSS, TN: Texas–NVSS, MP: MRC–PMN.

Col 2: The integrated flux density from the low-frequency catalog.

- Col 3:** The integrated flux density at the intermediate frequency, determined from the NVSS for WN and TN, or from the 1.420 GHz ATCA observations for the MP sample.
- Col 4:** The integrated flux density at 4.86 GHz, determined from the VLA observations for WN and TN, and from the PMN survey for the MP sample.
- Col 5:** The lower frequency two-point spectral index. This is the spectral index used to define the WN and TN samples.
- Col 6:** The higher frequency two-point spectral index. This is the spectral index used to define the MP sample.
- Col 7:** Morphological classification code: single (S), double (D), triple (T) and multiple (M) component sources, and irregularly shaped diffuse (DF) sources.
- Col 8:** Largest angular size. For single component sources, this is the de-convolved major axis of the elliptical Gaussian, or, for unresolved sources (preceded with <), an upper limit is given by the resolution. For double, triple and multiple component sources, this is the largest separation between their components. For diffuse sources this is the maximum distance between the source boundaries defined by three times the map rms noise.
- Col 9:** De-convolved position angle of the radio structure, measured North through East
- Col 10 – 11:** J2000 coordinates, determined from the map with position code listed in col. 12. The positions in the VLA and ATCA maps have been fitted with a single two-dimensional elliptical Gaussian. For double (D) sources, the geometric midpoint is given; for triples (T) and multiples (M), the core position is listed. For diffuse (DF) sources we list the center as determined by eye.
- Col 12:** Position code, indicating the origin of the morphological and positional data in column 7 to 11: A=ATCA, F=FIRST, M=MRC, N=NVSS, and V=VLA.

2.4.4 Notes on individual sources

WN J0043+4719: The source $18''$ north of the NVSS position is not detected in the NVSS. This is therefore not a real USS source because the NVSS flux density was underestimated.

WN J0048+4137: Our VLA map probably doesn't go deep enough to detect all the flux of this source.

WN J0727+3020: The higher resolution FIRST map shows that both components of this object are indeed identified on the POSS, even though the NVSS position is too far off to satisfy our identification criterion.

WN J0717+4611: Optical and near-IR spectroscopy revealed this object as a red quasar at $z = 1.462$ (Chapter 7).

WN J0725+4123: The extended POSS identification suggest this source is located in a galaxy cluster.

WN J0829+3834: The NVSS position of this unresolved source is $7''$ (3σ) from the FIRST position, which itself is only at $2''$ from the WENSS position.

WN J0850+4830: The difference with the NVSS position indicates that our VLA observations are not deep enough to detect a probable north-eastern component.

WN J0901+6547: This $38''$ large source is over-resolved in our VLA observations, and probably even misses flux in the NVSS, and is therefore not a real USS source.

WN J1012+3334: The bend morphology and bright optical sources to the east indicate this object is probably located in a galaxy cluster.

WN J1101+3520: The faint FIRST component $20''$ north of the brighter Southern component is not listed in the FIRST catalog, but is within $1''$ of a faint optical object. This might be the core of a $70''$ triple source.

WN J1152+3732: The distorted radio morphology and bright, extended POSS identification suggest this source is located in a galaxy cluster.

WN J1232+4621: This optically identified and diffuse radio source suggest this source is located in a galaxy cluster.

WN J1314+3515: The diffuse radio source appears marginally detected on the POSS.

WN J1329+3046A,B, WN J1330+3037, WN J1332+3009 & WN J1333+3037: The noise in the FIRST image is almost ten times higher than average due to the proximity of the $S_{1400}=15$ Jy source 3C 286.

WN J1330+5344: The difference with the NVSS position indicates that our VLA observations are not deep enough to detect a probable south-eastern component.

WN J1335+3222: Although the source appears much like the hotspot of a larger source with the core $90''$ to the east, no other hotspot is detected in the FIRST within $5'$.

WN J1359+7446: The extended POSS identification suggests this source is located in a galaxy cluster.

WN J1440+3707: The equally bright galaxy $30''$ south of the POSS identification suggests that this source is located in a galaxy cluster.

WN J1509+5905: The difference with the NVSS position indicates that our VLA observations are not deep enough to detect a probable western component.

WN J1628+3932: This is the well studied galaxy NGC 6166 in the galaxy cluster Abell 2199 (e.g., Zabludoff et al., 1993).

WN J1509+5905: The difference with the NVSS position indicates that our VLA observations are not deep enough to detect a probable west-south-western component.

WN J1821+3601: The source $35''$ south-west of the NVSS position is not detected in the NVSS. This is therefore not a real USS source because the NVSS flux density was underestimated.

WN J1832+5354: The source $19''$ north-east of the NVSS position is not detected in the NVSS. This is therefore not a real USS source because the NVSS flux density was underestimated.

WN J1852+5711: The extended POSS identification suggests this source is located in a galaxy cluster.

WN J2313+3842: The extended POSS identification suggests this source is located in a galaxy cluster.

TN J0233+2349: This is probably the north-western hotspot of a $35''$ source, with the south-eastern component barely detected in our VLA map.

TN J0309-2425: We have classified this source as a $13''$ double, but the western component might also be the core of a $45''$ source, with the other hotspot around $\alpha = 3^h 9^m 10^s, \delta = -24^\circ 25' 50''$.

TN J0349-1207: The core-dominated structure is reminiscent of the red quasar WN J0717+4611.

TN J0352-0355: This is probably the south-western hotspot of a $30''$ source.

TN J0837-1053: Given the $10''$ difference between the positions of the NVSS and diffuse VLA source, this is probably the northern component of a larger source.

TN J0408-2418: This is the $z=2.44$ source MRC 0406-244 (McCarthy et al., 1996). The bright object on the POSS is a foreground star to the north-east of the $R=22.7$ galaxy.

TN J0443-1212: Using the higher resolution VLA image, we can identify this radio source with a faint object on the POSS.

TN J2106-2405: This is the $z=2.491$ source MRC 2104-242 (McCarthy et al., 1996). The identification is an $R=22.7$ object, not the star to the north-north-west of the NVSS position.

2.4.5 Radio spectra and spectral curvature

We have used the CATS database at the Special Astronomical Observatory (Verkhodanov et al., 1997) to search for all published radio measurements of the sources in our samples. In Appendix C, we show the radio spectra for all sources with flux density information for more than two frequencies (the S_{4860} points from our VLA observations are also included). These figures show that most radio spectra have curved spectra, with flatter spectral indices below our selection frequencies, as has been seen in previous USS studies (see e.g., Röttgering et al., 1994; Blundell et al., 1998).

This low frequency flattening and high frequency steepening is obvious in the radio 'color-color diagrams' of the WN sample (Fig. 2.9). The median spectral index at low frequencies ($\nu < 325$ MHz) is -1.16 , while the median $\bar{\alpha}_{325}^{1400} = -1.38$. At higher frequencies ($\nu > 1400$ MHz), the steepening continues to a median $\bar{\alpha}_{1400}^{4850} = -1.44$. Note that the real value of the latter is probably even steeper, as 30% of the WN sources were not detected in our 4.86 GHz VLA observations, and may therefore have even more steepened high-frequency spectral indices.

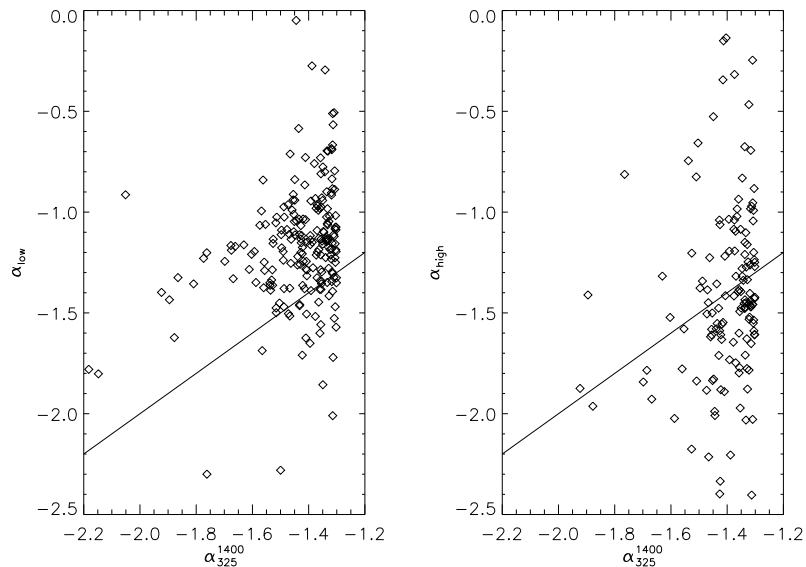


Figure 2.9: Radio “color-color” plots for the WN sample. The abscissa is the α_{325}^{1400} spectral index used to construct the sample. The ordinates are the low-frequency spectral indices determined from the 8C (38 MHz, Rees, 1990) or 6C (151 MHz, Hales, Baldwin & Warner, 1993) and the 325 MHz WENSS (left panel), and the high frequency spectral index determined between the 1.4 GHz NVSS and our 4.86 GHz VLA observations (right panel). The line in each panel indicates a straight power law spectrum. Note the unequal number of points on either side of these lines, indicating substantial spectral curvature.

2.4.6 Radio source properties

Radio source structure and angular size

In Table 2.5, we give the distribution of the radio structures of the 410 USS sources for which we have good radio-maps. At first sight, all three our samples have basically the same percentage of resolved sources, but the similar value for the MP sample is misleading, as it was observed at much lower resolution.

Our results are different from the USS sample of Röttgering et al. (1994), which contains only 18% unresolved sources at comparable resolution ($1''.5$). To check if this effect is due to the fainter sources in our sample, we compared our sample with the deep high resolution VLA observations of spectrally unbiased sources (Oort, 1988; Coleman & Condon, 1985). The resolution of our observations is significantly better

Table 2.5: Radio Structure Distribution

Morphology	USS Samples			
	WN	TN	MP	Combined
Single	157 (56±4%)	43 (48±7%)	23 (56±12%)	223 (54±4%)
Double	81 (29±3%)	28 (31±6%)	16 (39±10%)	125 (31±3%)
Triple	22 (8±2%)	9 (10±3%)	0 (0± 0%)	31 (8±1%)
Multiple	2 (1±1%)	4 (5±2%)	0 (0± 0%)	6 (1±1%)
Diffuse	18 (6±2%)	5 (6±3%)	2 (5± 3%)	25 (6±1%)
# Observed	280	89	41	410

than the median angular size for $S_{1400} > 1$ mJy sources, allowing us to accurately determine the median angular sizes in our samples. We find that our USS sources have a constant median angular size of $\sim 6''$ between 10 mJy and 1 Jy (Fig. 2.10). This is indistinguishable from the results from samples without spectral index selection. It indicates that our USS selection of sources with $\alpha < -1.3$ and $\Theta < 1'$ does not bias the angular size distribution in the resulting sample. The 'downturn' in angular sizes that occurs at ~ 1 mJy is probably due to a different radio source population, which consist of lower redshift sources in spiral galaxies (see e.g., Coleman & Condon, 1985; Oort, et al., 1987; Benn et al., 1993). By selecting only sources with $S_{1400} > 10$ mJy, we have avoided "contamination" of our sample by these foreground sources.

We have searched for further correlations between spectral index or spectral curvatures and angular size or flux density, but found no significant results, except for a trend for more extended sources to have lower than expected 4.86 GHz flux densities, but this effect can be explained by missing flux at large scales in our VLA observations.

2.4.7 Identifications

POSS

We have searched for optical identifications of our USS sources on the digitized POSS-I. We used the likelihood ratio identification criterion as described by e.g., de Ruiter et al. (1977). In short, this criterion compares the probability that a radio and optical source with a certain positional difference are really associated with the probability that this positional difference is due to confusion with a field object (mostly a foreground star), thereby incorporating positional uncertainties in both radio and optical positions. The ratio of these probabilities is expressed as the likelihood ratio LR . In the calculation, we have assumed a density of POSS objects $\rho = 4 \times 10^{-4} \text{ ''}^{-2}$, independent of galactic latitude b . We have adopted a likelihood ratio cutoff $\mathcal{L} = 1.0$, slightly

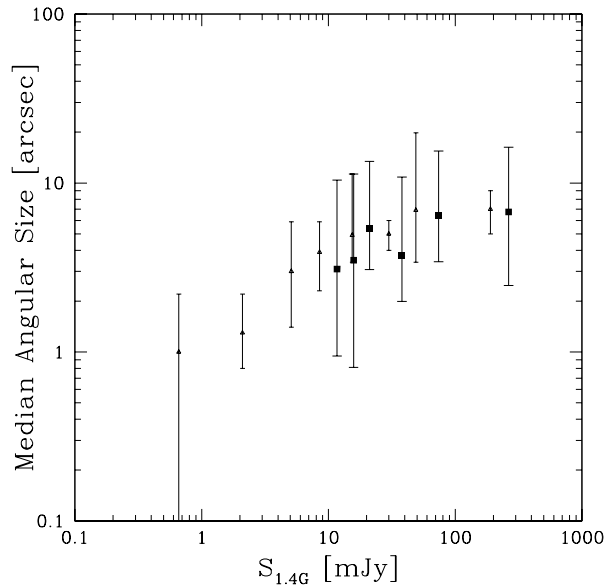


Figure 2.10: Median angular size for the flux density limited, spectrally unbiased WSRT samples of Oort (1988) (open triangles), and for our combined USS samples (filled squares). The sources have been binned in equal number bins, and errors represent the 35% and 65% levels of the distribution. Note that our USS selection does not affect the value of the median, and that our USS samples also exclude sources that fall below the break at $S_{1400} \lesssim 10$ mJy.

lower than the values used by de Ruiter et al. (1977) and Röttgering et al. (1994). We list sources with $LR > 1.0$ for our USS samples in Tables A.4 to A.6. We have included four WN sources (WN J0704+6318, WN J1259+3121, WN J1628+3932 and WN J2313+3842), two TN sources (TN J0510-1838 and TN J1521+0741) and four MP sources (MP J0003-3556, MP J1921-5431, MP J1943-4030 and MP J2357-3445) as identifications because both their optical and radio morphologies are diffuse and overlapping, making it impossible to measure a common radio and optical component, while they are very likely to be associated.

Figure 2.11 shows the identification fraction of USS sources on the POSS ($R \lesssim 20$). Because the distributions for the WN and TN are very similar, we have combined both samples to calculate the identification fraction. Unlike the results for 4C USS (Tielens et al., 1979; Blumenthal & Miley, 1979), we do not detect a decrease of the identification fraction with steepening spectral index⁶. We interpret the constant

⁶In the Westerbork faint USS (Wieringa & Katgert, 1992) or the USS sample from Röttgering

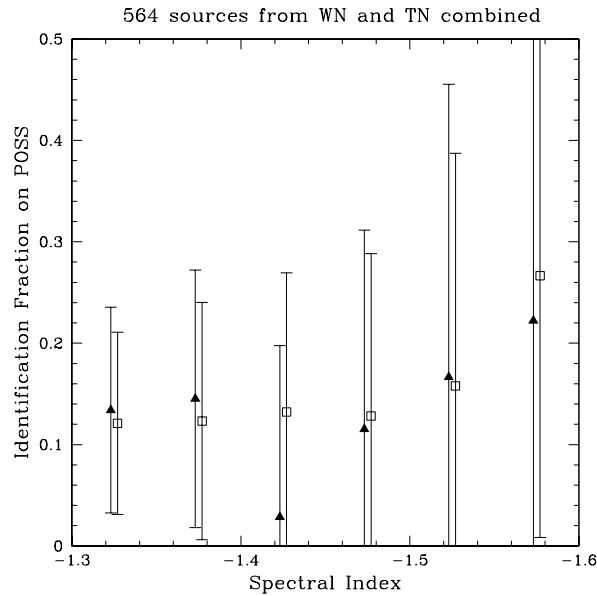


Figure 2.11: Identification fraction on the POSS as a function of spectral index for the combined WN and TN sample. Note the absence of a further decrease in the identification fraction with steepening spectral index.

$\sim 15\%$ identification fraction from our sample as a combined population of foreground objects, primarily consisting of clusters (see next section). Our extremely steep spectral index criterion would then selected only radio galaxies too distant to be detected on the POSS ($R \gtrsim 20.0$).

Literature

Using the NASA Extragalactic Database (NED), the SIMBAD database and the W³Browse at the High Energy Astrophysics Science Archive Research Center, we have searched for known optical and X-ray identifications of sources in our samples (see Appendices A.7 to A.9). Of the bright optical ($R \lesssim 20$) identifications, only one source is a known as a K0-star, three (TN J0055+2624, TN J0102–2152, and TN J1521+0742) are “Relic radio galaxies” (Komissarov & Gubanov, 1994; Giovannini, Tordi & Feretti, 1999), while all others are known galaxy clusters.

et al. (1994), there is also a decrease in the identification fraction, even at limiting magnitudes of $R = 22.5$ and $R = 23.7$, indicating that this trend continues out to fainter magnitudes and radio fluxes

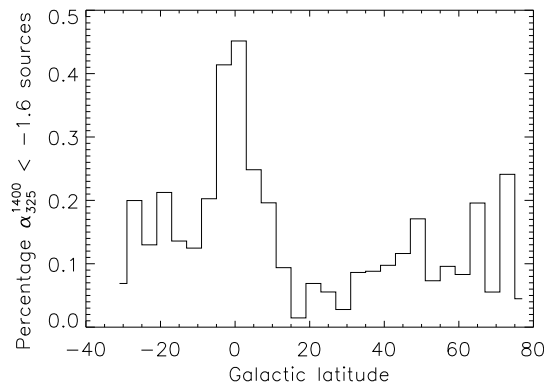


Figure 2.12: Percentage of $\alpha_{325}^{1400} < -1.60$ radio sources from a WENSS–NVSS correlation as a function of Galactic latitude. Note the clear peak near the Galactic plane, indicating that these $\alpha_{325}^{1400} < -1.60$ objects might well be Galactic pulsars.

All optical cluster identifications, except MP J1943-4030, are also detected in the ROSAT All-Sky survey Bright Source Catalogue (RASS-BSC; Voges et al., 1999). Conversely, of the 23 X-ray sources, seven are known galaxy clusters, and three known galaxies. The remaining 13 sources are good galaxy cluster candidates because they either show a clear over-density of galaxies on the POSS (eight sources), or they have low X-ray count rates (< 0.02 counts s^{-1}), suggesting that these might be more distant galaxy clusters too faint to be detected on the POSS. We conclude that probably $>3\%$ of our USS sources are associated with galaxy clusters, and that the combined USS + X-ray selection is an efficient (up to 85%) selection technique to find galaxy clusters⁷. Three of our USS sources (WN J2313+4253, TN J0630-2834 and TN J1136+1551) are previously known pulsars (Kaplan et al., 1998). It is worth noting that two out of nine sources in our USS samples with $\alpha < -2$ are known pulsars. Because Lorimer et al. (1995) found the median spectral index of pulsars to be ~ -1.6 , we examined the distribution of spectral indices as a function of Galactic latitude. In figure 2.12, we plot the percentage of $\alpha_{325}^{1400} < -1.60$ pulsar candidates as a function of Galactic latitude. The four times higher density near the Galactic plane strongly suggests that the majority of these $\alpha_{325}^{1400} < -1.60$ sources are indeed pulsars, which are confined to our Galaxy. A sample of such $\alpha_{325}^{1400} < -1.60$ sources at $|b| < 15^\circ$ would be an efficient pulsar search method.

We also note that no known quasars are present in our sample. Preliminary results

⁷In the RASS-BSC, only 14% of the extra-galactic sources are identified with galaxy clusters (Voges et al., 1999).

from our optical spectroscopy campaign (De Breuck et al. 1998b, 2000) indicate that $\sim 10\%$ of our sample are quasars. We interpret this lack of previously known quasars as a selection bias in quasar samples against USS sources.

At $R \gtrsim 20$, all five USS sources with known redshift are HzRGs, indicating a selection of sources without detections on the POSS strongly increases our chances of finding HzRGs.

2.5 Conclusions

We have constructed three spatially separated samples of USS sources containing a total of 669 objects. High-resolution radio observations of more than half of these show that the median size is $\sim 6''$, independent of 1.4 GHz flux density, which is consistent with results of similar resolution surveys of samples without spectral index selection. The absence of a downturn in angular size at the lowest fluxes indicates that we do not include significant numbers of spiral galaxies in our sample. A USS sample fainter than ours would therefore include more of these foreground sources, and be less efficient to find HzRGs.

The identification fraction on the POSS is $\sim 15\%$, with no clear dependence on spectral index, indicating that the HzRGs in the sample are all too distant to be detected, and the POSS detections consist of different classes of objects. A correlation of our USS samples with X-ray catalogs showed that at least 85% of the X-ray identifications seem to be galaxy clusters known from the literature or by inspection of the POSS. We conclude that (1) the majority of the 'non HzRG' USS sources in our sample are clusters, and (2) the combined selection of USS and X-ray sources is an extremely efficient technique to select galaxy clusters.

The above results indicate that up to 85% of our USS sample might be HzRGs. To identify these objects, we have started an intensive program of R- and K-band imaging on 3–10m class telescopes. Initial results from optical spectroscopy indicate that 2/3 are indeed $z > 2$ radio galaxies (De Breuck et al., 1998), and K-band imaging of optically undetected ($R > 25$) sources (see e.g., , van Breugel et al., 1999a) has already lead to the discovery of the first radio galaxy at $z > 5$ (Chapter 5).

Acknowledgements

We are grateful for the excellent help provided by the staff of the VLA and ATCA observatories, with special thanks to Chris Carilli and Greg Taylor (NRAO), and Ray Norris and Kate Brooks (ATNF) for help in with observation planning and data reduction. We thank Hien “Napkin” Tran for his comments on the manuscript. The VLA is a facility of the National Radio Astronomy Observatory, which is operated by Associated Universities Inc. under cooperative agreement with the National Science Foundation. The Australia Telescope is funded by the Commonwealth of Australia for operation as a National Facility managed by CSIRO. The authors made use of the database CATS (Verkhodanov et al., 1997) of the Special Astrophysical Observa-

tory, the NASA/IPAC Extragalactic Database (NED) which is operated by the Jet Propulsion Laboratory, California Institute of Technology, under contract with the National Aeronautics and Space Administration, and the High Energy Astrophysics Science Archive Research Center Online Service, provided by the NASA/Goddard Space Flight Center. Work performed at the Lawrence Livermore National Laboratory is supported by the DOE under contract W7405-ENG-48.

Appendix A Source Lists

Table A.1: WN sample

Name	S325 mJy	S1400 mJy	S4850 mJy	c ₃₂₅ ¹⁴⁰⁰	α ₁₄₀₀ ⁴⁸⁵⁰	Str	LAS	PA	h	m	s	δJ2000 o	l	b	Pos
WN J0000+4654	204±9	21.1±1.4	2.97±0.13	-1.55±0.06	-1.58±0.06	D	3.6	173	00 00 28.88	+46 54 40.7	V				
WN J0007+3641	447±18	28.8±1.7	2.51±0.11	-1.88±0.05	-1.96±0.06	S	1.7	67	00 07 02.92	+36 41 55.9	V				
WN J0007+4615	144±7	16.9±0.5	...	-1.47±0.04	00 07 15.05	+46 15 40.8	N				
WN J0016+4311	105±6	15.7±1.5	...	-1.30±0.08	00 16 40.63	+43 11 03.5	V				
WN J0029+3439	288±12	40.9±2.0	44.76±1.05	-1.34±0.04	0.07±0.04	DF	12.8	80	00 29 01.61	+34 39 34.7	N				
WN J0034+4142	84±6	11.0±0.5	2.50±0.12	-1.39±0.05	-1.19±0.05	D	23.7	154	00 34 29.21	+41 42 09.5	V				
WN J0034+3238	120±9	16.4±0.5	...	-1.36±0.04	00 34 56.36	+32 38 36.4	N				
WN J0038+7859	109±6	15.1±0.5	1.30±0.09	-1.35±0.04	-1.97±0.06	S	2.5	159	00 38 01.96	+78 59 51.5	N				
WN J0040+3857	127±7	17.5±0.5	3.13±0.14	-1.36±0.04	-1.38±0.04	S	1.4	31	00 40 56.23	+38 57 30.0	V				
WN J0043+4719†	99±6	14.2±1.3	41.81±1.01	-1.33±0.08	0.87±0.08	T	18.5	157	00 43 53.13	+47 19 48.3	V				
WN J0048+4137*	277±11	34.5±1.9	1.75±0.10	-1.43±0.05	-2.40±0.06	S	2.5	17	00 48 46.34	+41 37 20.8	V				
WN J0059+3958	152±7	11.4±1.4	...	-1.77±0.09	00 59 51.07	+39 58 46.5	N				
WN J0112+4039	111±7	15.4±0.5	...	-1.35±0.05	01 12 26.31	+40 39 30.1	N				
WN J0117+3715	165±8	22.5±0.6	6.62±0.21	-1.36±0.04	-0.98±0.03	S	1.4	71	01 17 10.02	+37 15 16.3	V				
WN J0121+4305	389±16	50.8±2.5	...	-1.39±0.04	01 21 10.71	+43 05 18.3	N				
WN J0135+3303	94±6	12.1±0.5	10.22±0.28	-1.40±0.06	-0.14±0.04	T	1.8	18	01 35 07.24	+33 03 47.4	V				
WN J0137+3250	177±9	23.8±1.6	16.06±0.40	-1.37±0.06	-0.32±0.06	T	27.9	104	01 36 59.85	+32 50 40.7	V				
WN J0155+8036	338±14	38.0±0.9	6.87±0.21	-1.50±0.03	-1.38±0.03	D	4.6	159	01 55 43.77	+80 36 48.1	V				
WN J0207+3655	118±6	17.5±1.4	...	-1.31±0.07	02 07 22.59	+36 55 16.0	N				
WN J0231+3600	303±13	45.2±2.2	7.66±0.22	-1.30±0.04	-1.43±0.05	D	14.8	59	02 31 11.48	+36 00 26.6	V				
WN J0240+3526	79±5	10.2±0.5	...	-1.40±0.06	02 40 31.10	+35 26 55.1	N				
WN J0303+3733	1071±43	127.9±5.7	17.32±0.43	-1.46±0.04	-1.61±0.04	D	4.4	3	03 03 29.01	+37 33 41.6	V				
WN J0303+3639	117±6	17.1±0.5	...	-1.32±0.05	03 03 29.87	+36 29 56.1	N				
WN J0305+3525	110±6	15.8±1.3	3.74±0.15	-1.33±0.07	-1.16±0.07	S	1.9	64	03 05 47.42	+35 25 13.4	V				
WN J0310+3644	289±11	24.2±0.6	2.45±0.12	-1.70±0.03	-1.84±0.05	S	2.0	118	03 10 54.80	+36 44 02.5	V				
WN J0315+3757	95±5	13.3±0.5	4.74±0.17	-1.35±0.05	-0.83±0.04	S	1.7	53	03 15 17.29	+37 57 05.0	V				
WN J0323+3738	205±9	22.8±1.5	8.11±0.25	-1.51±0.06	-0.83±0.06	DF	9.7	100	03 23 38.24	+37 38 39.3	V				
WN J0343+7540	118±6	12.5±1.6	...	-1.54±0.09	03 43 39.77	+75 40 43.2	N				
WN J0346+3039	286±12	35.6±1.9	4.95±0.18	-1.39±0.04	-1.39±0.04	S	0.4	89	03 46 42.60	+30 39 51.0	V				
WN J0352+3143	154±7	21.8±1.5	...	-1.34±0.06	-1.59±0.05	03 52 24.49	+31 43 03.1	N				
WN J0359+3000	88±6	12.1±0.5	...	-1.36±0.06	03 59 12.86	+30 00 51.7	N				
WN J0528+6549	96±6	10.6±2.4	1.08±0.09	-1.51±0.16	-1.84±0.19	S	1.9	108	05 28 46.07	+65 49 57.3	V				
WN J0533+7205	117±7	17.4±1.6	2.42±0.12	-1.30±0.08	-1.59±0.08	D	2.9	140	05 33 38.64	+73 05 52.7	V				
WN J0538+7348	132±7	18.1±0.5	3.20±0.14	-1.36±0.04	-1.39±0.04	S	2.1	113	05 38 25.59	+73 48 39.6	V				
WN J0559+6926	87±5	12.9±0.5	1.88±0.13	-1.31±0.06	-1.55±0.06	S	0.3	85	05 59 06.04	+69 26 37.8	V				
WN J0610+6611	98±6	12.5±1.9	1.19±0.09	-1.41±0.11	-1.89±0.14	S	2.2	114	06 10 08.59	+66 11 43.1	V				
WN J0617+5012	196±9	26.5±0.7	6.80±0.23	-1.37±0.04	-1.09±0.03	D	3.4	11	06 17 39.37	+50 12 54.7	V				
WN J0625+5708	71±4	10.3±0.5	1.54±0.10	-1.32±0.07	-1.53±0.06	D	7.3	18	06 25 01.67	+57 08 26.1	V				
WN J0627+7311	470±19	61.9±2.9	4.00±0.17	-1.39±0.04	-2.20±0.05	S	<	0	06 27 03.64	+73 11 54.2	V				
WN J0633+6024	115±6	13.4±2.8	2.07±0.11	-1.47±0.15	-1.50±0.17	S	2.2	118	06 33 19.70	+60 24 37.1	V				
WN J0633+4653	3661±146	520.1±22.8	80.88±1.74	-1.34±0.04	-1.50±0.04	T	4.0	19	06 33 52.18	+46 53 40.5	V				
WN J0641+4325	154±7	15.6±0.5	...	-1.57±0.04	06 41 08.23	+43 25 00.3	N				
WN J0646+3912	166±8	20.5±2.4	...	-1.43±0.09	06 46 34.97	+39 12 00.3	N				
WN J0648+4309	215±9	30.4±1.7	5.00±0.19	-1.34±0.08	-1.45±0.05	DF	1.5	151	06 48 01.10	+43 09 47.8	V				
WN J0648+4137	91±5	10.9±1.5	1.69±0.11	-1.46±0.11	-1.50±0.12	S	13.2	94	06 48 14.58	+41 37 18.8	V				
WN J0650+4106	393±16	53.5±1.2	15.04±0.41	-1.37±0.03	-1.02±0.03	DF	3.0	26	06 50 41.66	+41 06 36.1	V				
WN J0653+4434	115±6	13.1±0.5	...	-1.46±0.07	06 53 23.84	+44 34 55.4	N				
WN J0656+5301	137±7	18.7±1.5	...	-1.36±0.05	...	D	56.1	88	06 56 38.40	+53 01 18.1	F				
WN J0658+4444	407±17	50.6±2.4	13.91±0.35	-1.43±0.04	-1.04±0.04	S	1.7	73	06 58 27.43	+44 44 16.4	V				
WN J0702+4448	147±7	17.0±0.5	...	-1.48±0.04	...	S	7.8	119	07 02 16.79	+44 48 56.7	F				

Name	S ₃₂₅ mJy	S ₁₄₀₀ mJy	S ₄₈₅₀ mJy	c ₃₂₅ 1400	α ₁₄₀₀ 4850	Str	LAS //	PA o	h m	s	δ _{J2000} o	′	″	Pos
WN J0711+4242	140±6	16.0±0.5	...	-1.49±0.04	...	S	3.3	17	07 11	40.25	+42 42 05.6	F
WN J0715+4655	89±6	10.4±0.5	1.86±0.13	-1.47±0.06	-1.38±0.07	S	0.2	114	07 15	02.03	+46 55 26.3	V
WN J0716+5107	204±9	28.4±0.7	4.54±0.18	-1.85±0.04	-1.47±0.04	D	1.2	8	07 16	40.50	+51 07 04.7	V
WN J0717+4611*	724±29	107.8±4.8	45.30±1.00	-1.80±0.04	-0.70±0.04	T	6.2	16	07 17	58.49	+46 11 39.1	V
WN J0720+5140	95±6	11.6±0.5	...	-1.44±0.05	...	S	3.2	101	07 20	00.20	+51 40 28.5	F
WN J0720+5758	93±7	18.9±0.5	2.37±0.12	-1.80±0.05	-1.42±0.05	S	2.0	109	07 20	09.56	+57 58 32.9	V
WN J0721+3324	313±13	36.8±1.9	2.35±0.13	-1.47±0.05	-2.21±0.06	DF	2.0	143	07 21	56.85	+33 24 53.8	V
WN J0725+4123*	272±12	35.5±1.9	...	-1.89±0.05	...	S	8.3	156	07 25	57.08	+41 23 05.1	F
WN J0727+3020*	93±6	12.8±1.9	...	-1.86±0.11	...	D	34.8	103	07 27	48.50	+30 21 00.7	F
WN J0736+6845	84±5	12.4±0.5	...	-1.31±0.06	07 36	36.42	+68 45 56.8	N
WN J0737+7146	79±5	10.3±0.5	...	-1.40±0.07	07 37	09.93	+71 46 29.3	N
WN J0740+6319	254±11	26.1±1.7	...	-1.56±0.05	07 40	27.01	+63 19 55.2	N
WN J0741+5611	313±13	44.4±1.0	7.08±0.24	-1.34±0.03	-1.48±0.03	S	0.5	20	07 41	15.38	+56 11 35.9	V
WN J0747+3654	289±12	36.8±0.8	...	-1.41±0.03	...	S	2.1	2	07 47	29.38	+36 54 38.1	F
WN J0747+4527	138±7	19.1±2.2	...	-1.85±0.09	...	S	3.5	109	07 47	29.56	+45 27 16.3	F
WN J0751+3300	98±7	11.5±0.5	1.90±0.12	-1.47±0.05	-1.44±0.06	S	0.4	139	07 51	48.04	+33 00 07.1	V
WN J0756+5010	204±9	29.9±0.7	...	-1.31±0.04	...	S	1.7	93	07 56	24.63	+50 10 12.5	V
WN J0801+7134	120±6	18.5±2.3	...	-1.50±0.13	08 01	18.68	+71 34 01.6	N
WN J0809+6624	257±11	32.2±2.3	...	-1.42±0.06	08 09	19.28	+66 24 09.5	N
WN J0810+4948	146±7	18.1±1.4	2.16±0.13	-1.43±0.07	-1.74±0.08	S	< 0.3	0	08 10	34.92	+49 48 37.5	V
WN J0812+3424	160±8	19.9±1.4	...	-1.43±0.06	...	D	6.6	58	08 12	14.43	+34 24 09.3	F
WN J0813+4828	184±9	23.3±1.7	15.20±0.40	-1.42±0.06	-0.32±0.06	D	0.9	173	08 13	38.10	+48 28 41.5	V
WN J0819+5628	95±6	11.7±0.5	...	-1.43±0.06	08 19	33.65	+56 28 38.1	F
WN J0829+3834*	112±6	12.7±1.3	...	-1.49±0.08	...	S	1.6	0	08 29	17.35	+38 34 52.6	F
WN J0830+3018	109±6	13.9±1.2	...	-1.41±0.07	...	S	3.5	89	08 30	36.91	+30 18 11.8	F
WN J0834+4820	128±7	17.9±0.5	3.65±0.18	-1.85±0.04	-1.27±0.04	S	0.4	99	08 34	25.85	+48 20 00.8	V
WN J0835+3439	143±7	19.1±1.3	...	-1.88±0.06	...	D	58.0	168	08 35	22.92	+34 39 49.8	F
WN J0842+3540	110±6	15.0±0.5	...	-1.86±0.04	...	S	1.1	0	08 42	10.82	+35 40 42.2	F
WN J0842+3101	76±5	10.5±3.6	...	-1.86±0.24	08 42	16.35	+31 01 11.6	N
WN J0843+3723	290±13	35.8±1.9	...	-1.43±0.05	...	S	1.1	5	08 43	02.09	+37 23 18.1	F
WN J0850+4830*	192±9	18.9±1.4	1.53±0.13	-1.59±0.06	-2.02±0.09	S	0.3	52	08 50	56.50	+48 30 46.2	V
WN J0852+3311	179±8	24.6±1.5	...	-1.86±0.05	...	D	6.1	13	08 52	50.55	+33 11 41.0	F
WN J0901+6547†	140±7	19.0±0.5	71.60±1.57	-1.37±0.04	1.07±0.03	D	37.6	117	09 01	27.69	+65 47 25.8	V
WN J0901+3151	135±8	20.1±1.4	...	-1.30±0.06	...	D	20.1	109	09 01	48.50	+31 51 59.4	F
WN J0903+3246	112±6	15.5±0.5	...	-1.35±0.04	09 03	44.81	+32 46 02.0	N
WN J0911+6306	118±5	12.9±1.3	...	-1.52±0.08	09 11	34.24	+63 06 21.7	N
WN J0913+6104	297±12	33.8±1.8	...	-1.49±0.05	09 13	05.21	+61 04 11.7	N
WN J0915+3133	127±5	18.6±0.6	2.99±0.13	-1.32±0.04	-1.47±0.04	S	2.3	127	09 15	09.29	+81 33 34.1	V
WN J0920+5544	142±7	13.5±1.2	...	-1.61±0.07	...	D	8.9	129	09 20	46.78	+55 44 21.8	F
WN J0923+4602	107±5	12.1±0.5	...	-1.49±0.06	...	D	21.6	172	09 23	10.44	+46 02 59.0	F
WN J0928+6003	119±6	11.0±0.5	2.14±0.11	-1.53±0.05	-1.32±0.06	S	3.4	128	09 28	44.58	+60 03 01.7	V
WN J0930+4358	118±7	12.0±0.5	...	-1.57±0.05	...	S	3.1	88	09 30	12.14	+43 58 27.2	F
WN J0930+3207	218±9	31.1±1.7	...	-1.33±0.05	...	S	11.7	58	09 30	53.32	+32 07 20.8	V
WN J0939+6323	268±11	39.7±2.0	10.86±0.29	-1.31±0.05	-1.04±0.05	T	30.3	27	09 39	54.89	+63 23 31.9	F
WN J0940+3838	108±6	11.8±1.6	...	-1.52±0.10	09 40	26.15	+38 38 35.0	N
WN J0946+6726	632±25	84.7±3.7	40.19±0.88	-1.38±0.04	-0.60±0.04	T	44.8	114	09 46	44.25	+67 26 41.8	V
WN J0948+6305	731±29	90.5±1.9	14.46±0.38	-1.43±0.03	-1.48±0.03	D	3.1	134	09 48	40.83	+63 05 42.0	V
WN J0952+5153	211±10	16.1±1.3	...	-1.76±0.06	...	S	2.7	166	09 52	49.14	+51 53 05.0	F
WN J0955+6023	103±6	10.9±1.6	4.32±0.15	-1.54±0.11	-0.75±0.12	DF	3.1	129	09 55	30.01	+60 23 17.1	V
WN J1002+5512	119±5	17.7±0.5	...	-1.30±0.05	...	S	10.4	58	10 02	39.24	+55 12 55.5	F

Name	S ₃₂₅ mJy	S ₁₄₀₀ mJy	S ₄₈₅₀ mJy	c ₃₂₅ 1400	α ₁₄₀₀ 4850	Str	LAS //	PA	h m	s	δ _{J2000} °	Pos
WN J1003+4448	84±5	13.9±2.0	...	-1.31±0.11	...	DF	17.2	93	10 03 30.22	+44 48 16.2	F	
WN J1012+3334*	168±8	16.4±1.6	...	-1.59±0.07	...	D	22.1	6	10 12 00.43	+33 35 00.9	F	
WN J1013+3254	102±7	14.2±0.5	...	-1.85±0.05	...	S	< 0.3	89	10 13 06.54	+32 54 33.2	F	
WN J1014+7407	170±8	21.8±0.6	3.76±0.14	-1.41±0.04	-1.41±0.04	S	2.2	150	10 14 15.75	+74 07 56.2	V	
WN J1015+3038	285±12	38.0±1.9	...	-1.38±0.04	...	D	12.8	151	10 15 08.92	+30 38 02.0	F	
WN J1015+7432	146±7	21.4±0.6	...	-1.31±0.05	10 15 52.48	+74 32 20.0	N	
WN J1018+3634	137±7	17.7±1.4	...	-1.32±0.06	10 18 03.13	+36 34 43.2	F	
WN J1019+5244	85±5	10.5±0.4	...	-1.43±0.06	...	D	16.5	145	10 19 20.59	+52 44 33.2	F	
WN J1022+3308	90±5	10.1±0.4	...	-1.50±0.05	...	S	7.8	136	10 22 37.44	+33 08 43.6	F	
WN J1026+2943	81±6	12.0±1.2	...	-1.31±0.08	...	S	11.9	20	10 26 12.04	+29 43 48.0	F	
WN J1029+4838	118±8	17.2±1.4	2.80±0.16	-1.32±0.07	-1.46±0.08	S	2.0	131	10 29 32.98	+48 38 09.0	V	
WN J1030+5415	223±10	29.2±1.6	...	-1.39±0.05	10 30 42.94	+54 15 35.9	F	
WN J1036+3936	153±7	16.7±0.5	...	-1.52±0.04	...	T	17.5	107	10 36 21.29	+39 36 59.4	F	
WN J1038+4229	816±33	114.0±5.1	...	-1.35±0.04	...	S	1.2	3	10 38 41.04	+42 29 51.5	F	
WN J1041+5559	193±9	25.2±0.6	6.96±0.22	-1.39±0.04	-1.04±0.03	D	11.2	119	10 41 29.64	+55 59 23.5	V	
WN J1043+3953	95±8	13.9±0.5	...	-1.32±0.05	...	S	< 0.3	79	10 43 32.24	+39 53 46.8	F	
WN J1052+4826	1089±41	154.2±6.8	...	-1.31±0.04	10 52 53.05	+48 26 33.8	F	
WN J1053+5424	467±20	66.4±1.4	7.94±0.25	-1.34±0.03	-1.70±0.03	D	10.0	108	10 53 36.31	+54 24 42.1	V	
WN J1055+3047	342±14	39.0±2.0	...	-1.49±0.05	...	S	7.1	147	10 55 18.52	+30 47 23.2	F	
WN J1057+3156	221±10	22.2±1.5	...	-1.57±0.06	...	T	28.7	20	10 57 56.56	+31 56 21.0	F	
WN J1057+3007	276±12	39.5±2.0	...	-1.33±0.05	...	D	24.6	90	10 57 57.45	+30 07 02.9	F	
WN J1058+3506	205±10	24.0±1.5	...	-1.47±0.05	...	S	1.3	126	10 58 14.74	+35 06 40.9	F	
WN J1058+7003	82±4	10.5±0.5	...	-1.41±0.06	10 58 34.95	+70 03 17.6	N	
WN J1059+4341	99±8	12.3±1.6	...	-1.43±0.10	...	D	29.1	66	10 59 43.88	+43 41 05.2	F	
WN J1101+3520*	120±7	17.5±2.1	...	-1.32±0.09	...	S	8.1	1	11 01 14.35	+35 20 12.7	F	
WN J1111+3311	92±6	13.3±0.5	...	-1.32±0.05	...	S	6.7	16	11 11 40.79	+33 12 00.9	F	
WN J1115+5016	232±10	33.9±0.8	5.47±0.22	-1.32±0.03	-1.46±0.04	D	0.2	117	11 15 06.87	+50 16 23.9	V	
WN J1117+5251	1489±57	198.7±8.7	...	-1.36±0.04	...	D	9.5	6	11 17 24.37	+52 51 54.6	F	
WN J1122+3239	143±7	19.5±1.4	...	-1.36±0.06	...	S	4.2	89	11 22 33.53	+32 39 40.9	F	
WN J1123+3141	623±25	74.0±3.3	...	-1.46±0.04	...	T	25.8	83	11 23 55.85	+31 41 26.1	F	
WN J1124+3228	263±11	38.9±0.9	...	-1.31±0.03	...	S	5.7	165	11 24 34.17	+32 28 19.6	F	
WN J1126+8318	175±8	25.8±1.6	...	-1.31±0.05	11 26 26.48	+83 18 23.8	N	
WN J1128+4822	280±12	29.9±0.7	...	-1.53±0.03	...	S	1.2	171	11 28 05.19	+48 22 56.9	F	
WN J1128+6416	257±11	31.0±1.7	3.20±0.17	-1.45±0.05	-1.82±0.06	S	0.8	116	11 28 12.10	+64 16 25.3	V	
WN J1130+4911	134±6	18.9±1.5	...	-1.34±0.07	...	T	37.0	145	11 30 17.53	+49 11 17.7	F	
WN J1139+3048	819±33	119.6±5.3	...	-1.32±0.04	...	D	9.0	40	11 39 14.34	+30 48 50.7	F	
WN J1139+3706	139±8	16.7±1.4	...	-1.45±0.07	...	S	3.5	32	11 39 43.04	+37 06 55.7	F	
WN J1141+6924	81±5	11.8±0.5	...	-1.32±0.07	11 41 09.71	+69 24 16.3	N	
WN J1148+5116	148±7	20.5±1.7	...	-1.35±0.07	...	D	6.7	50	11 48 01.92	+51 16 29.6	F	
WN J1148+6233	98±5	14.1±0.5	1.37±0.09	-1.33±0.05	-1.88±0.06	S	2.4	144	11 48 44.42	+62 33 24.6	V	
WN J1148+3519	114±7	13.9±1.7	...	-1.44±0.09	...	D	20.0	7	11 48 54.29	+35 19 10.1	F	
WN J1151+4486	78±5	11.1±0.5	...	-1.34±0.06	...	D	15.1	20	11 51 16.80	+44 36 10.0	F	
WN J1152+3732*	414±17	17.1±1.4	...	-2.18±0.06	...	S	15.0	119	11 52 36.34	+37 32 43.9	F	
WN J1154+5415	153±7	19.1±0.5	1.05±0.10	-1.42±0.04	-2.33±0.08	S	< 0.3	0	11 54 18.97	+54 15 11.4	V	
WN J1203+8350	132±6	18.5±0.5	...	-1.35±0.04	12 03 30.63	+83 50 37.1	N	
WN J1204+5014	94±5	11.3±1.7	...	-1.45±0.11	12 04 31.11	+50 14 49.8	N	
WN J1206+3136	167±9	22.2±1.5	...	-1.38±0.06	...	D	16.6	53	12 06 48.10	+31 36 50.9	F	
WN J1208+4301	162±8	13.9±1.4	...	-1.68±0.08	...	T	8.0	27	12 08 42.77	+43 01 42.3	F	
WN J1216+4446	191±8	13.6±0.5	...	-1.81±0.04	...	S	6.1	98	12 16 46.84	+44 46 51.3	F	
WN J1218+3143	1906±76	261.5±12.4	...	-1.31±0.04	...	S	5.6	65	12 18 31.47	+31 43 41.7	F	

Name	S ₃₂₅ mJy	S ₁₄₀₀ mJy	S ₄₈₅₀ mJy	α_{325}	α_{1400}	α_{4850}	Str	LAS //	PA °	α_J m	δ_J m	δ_J s	δ_J 0	δ_J 1	δ_J 2	Pos
WN J1219+4644	140±8	20.9±0.6	2.84±0.14	-1.30±0.04	-1.30±0.04	-1.39±0.05	S	0.2	157	12 19 31.78	+46 44 49.6	+46 44 49.6				V
WN J1223+4256	116±6	17.2±0.5	...	-1.31±0.06	S	4.3	179	12 23 11.82	+42 56 57.3	+42 56 57.3				F
WN J1224+4956	145±7	21.4±1.6	...	-1.31±0.06	T	39.6	66	12 24 21.03	+49 56 49.2	+49 56 49.2				F
WN J1224+5436	790±31	69.1±1.5	6.30±0.20	-1.67±0.03	-1.62±0.03	-1.62±0.03	D	0.9	16	12 24 52.35	+54 36 39.9	+54 36 39.9				V
WN J1226+4836	155±8	17.0±0.5	...	-1.51±0.04	S	4.8	115	12 26 22.45	+48 36 39.6	+48 36 39.6				F
WN J1232+4621*	133±6	19.8±1.8	...	-1.30±0.07	DF	12.5	156	12 32 39.79	+46 21 48.1	+46 21 48.1				F
WN J1242+3915	549±22	78.4±1.7	...	-1.33±0.03	-1.33±0.03	-1.33±0.03	D	11.2	51	12 42 53.09	+39 15 48.6	+39 15 48.6				F
WN J1247+6121	109±5	15.4±2.4	...	-1.30±0.11	12 47 45.31	+61 21 23.3	+61 21 23.3				N
WN J1249+4043	160±7	22.8±1.4	...	-1.33±0.05	D	37.0	80	12 49 27.43	+40 43 49.3	+40 43 49.3				F
WN J1258+3212	182±12	19.9±1.5	...	-1.52±0.06	S	6.7	131	12 58 23.62	+32 12 42.4	+32 12 42.4				F
WN J1258+5041	230±11	28.8±2.0	...	-1.42±0.05	T	44.9	58	12 58 50.96	+50 41 42.3	+50 41 42.3				F
WN J1259+3121	268±11	34.0±1.8	...	-1.41±0.06	DF	20.6	1	12 59 51.96	+31 21 05.6	+31 21 05.6				F
WN J1300+5311	157±7	19.2±0.5	2.70±0.16	-1.44±0.04	-1.58±0.05	-1.58±0.05	S	0.3	7	13 00 36.25	+53 11 52.4	+53 11 52.4				V
WN J1302+3206	383±16	54.0±1.2	...	-1.34±0.03	S	4.7	102	13 02 03.07	+32 06 35.6	+32 06 35.6				F
WN J1303+8024	165±7	22.2±0.6	5.05±0.18	-1.37±0.03	-1.19±0.04	-1.19±0.04	D	4.1	145	13 03 33.92	+80 24 42.2	+80 24 42.2				V
WN J1303+5437	145±7	15.4±1.4	...	-1.54±0.07	D	16.5	88	13 03 45.48	+54 37 28.9	+54 37 28.9				F
WN J1306+4726	100±7	13.1±0.5	...	-1.39±0.05	S	10.2	40	13 06 35.99	+47 26 10.1	+47 26 10.1				F
WN J1310+5706	112±6	15.9±0.5	...	-1.52±0.04	S	4.2	99	13 10 22.96	+57 06 57.9	+57 06 57.9				F
WN J1310+3820	69±4	10.3±1.5	...	-1.30±0.12	S	4.4	18	13 10 24.08	+38 20 44.1	+38 20 44.1				F
WN J1312+6646	291±12	41.6±0.9	8.56±0.24	-1.33±0.03	-1.27±0.03	-1.27±0.03	D	6.3	118	13 12 45.59	+66 46 36.1	+66 46 36.1				V
WN J1314+3649	286±11	36.4±0.8	...	-1.41±0.03	S	1.3	90	13 14 17.86	+36 49 14.6	+36 49 14.6				F
WN J1314+3515*	169±7	20.2±1.7	...	-1.45±0.07	DF	34.2	47	13 14 25.00	+35 15 53.9	+35 15 53.9				F
WN J1315+4337	149±8	16.3±0.5	...	-1.52±0.04	S	1.3	152	13 15 19.05	+43 37 57.1	+43 37 57.1				F
WN J1321+3311	141±8	19.0±0.6	...	-1.37±0.04	D	14.7	63	13 21 13.55	+33 11 31.2	+33 11 31.2				F
WN J1323+4713	106±5	14.9±0.5	...	-1.34±0.04	S	2.5	139	13 23 08.31	+47 13 10.7	+47 13 10.7				F
WN J1327+5341	196±9	27.4±0.7	...	-1.35±0.04	S	0.6	162	13 27 12.77	+53 41 20.6	+53 41 20.6				F
WN J1327+5332	163±7	20.5±0.6	2.70±0.17	-1.42±0.04	-1.61±0.06	-1.61±0.06	D	0.3	89	13 27 37.86	+53 32 10.8	+53 32 10.8				V
WN J1329+3046*	86±5	11.7±1.7	...	-1.37±0.11	S	1.6	6	13 29 31.75	+30 46 13.6	+30 46 13.6				F
WN J1329+3046*	88±5	12.1±2.0	...	-1.36±0.13	S	3.6	129	13 29 55.12	+30 46 51.2	+30 46 51.2				F
WN J1330+6505	74±6	10.5±0.5	2.34±0.12	-1.34±0.06	-1.21±0.06	-1.21±0.06	S	1.8	5	13 30 02.77	+85 04 59.3	+85 04 59.3				V
WN J1330+3037*	496±20	64.5±2.9	...	-1.40±0.04	D	25.5	140	13 30 53.67	+30 37 59.1	+30 37 59.1				F
WN J1330+3604	103±5	15.1±0.5	...	-1.31±0.05	D	9.6	0	13 30 56.83	+36 04 01.6	+36 04 01.6				F
WN J1330+5344*	525±21	71.0±3.2	8.10±0.29	-1.37±0.04	-1.74±0.05	-1.74±0.05	DF	2.5	173	13 30 58.90	+53 44 07.8	+53 44 07.8				V
WN J1331+2937	93±5	12.5±1.3	3.44±0.13	-1.37±0.09	-1.04±0.09	-1.04±0.09	S	2.7	40	13 31 21.58	+29 37 12.6	+29 37 12.6				V
WN J1332+3009*	239±10	35.3±2.0	...	-1.31±0.05	D	39.2	161	13 32 45.73	+30 09 59.9	+30 09 59.9				F
WN J1333+3037*	423±17	21.5±0.6	...	-2.04±0.03	S	0.4	179	13 33 21.20	+30 37 35.1	+30 37 35.1				F
WN J1333+4913	149±7	22.2±0.6	4.78±0.23	-1.30±0.04	-1.22±0.04	-1.22±0.04	T	5.4	40	13 33 56.42	+49 13 27.1	+49 13 27.1				V
WN J1335+3222*	150±7	18.3±1.4	...	-1.44±0.06	D	8.8	85	13 35 35.44	+32 22 48.7	+32 22 48.7				F
WN J1336+3820	116±6	15.6±0.5	...	-1.37±0.04	D	3.4	61	13 36 40.88	+38 20 02.2	+38 20 02.2				F
WN J1337+3149	142±7	19.6±1.9	...	-1.36±0.08	D	35.2	21	13 37 02.46	+31 49 49.2	+31 49 49.2				F
WN J1337+3401	109±8	14.3±0.5	...	-1.39±0.04	S	3.5	56	13 37 10.50	+34 01 26.8	+34 01 26.8				F
WN J1339+5320	104±5	13.9±0.5	1.80±0.15	-1.38±0.05	-1.63±0.07	-1.63±0.07	D	0.1	138	13 39 59.25	+53 20 07.8	+53 20 07.8				V
WN J1341+4953	153±8	16.4±1.4	...	-1.53±0.07	D	16.0	160	13 41 25.70	+49 53 41.8	+49 53 41.8				F
WN J1346+6736	107±6	14.5±0.5	2.82±0.16	-1.37±0.04	-1.32±0.05	-1.32±0.05	S	<0.3	0	13 46 37.02	+67 36 21.7	+67 36 21.7				V
WN J1347+3033	341±14	42.4±2.2	...	-1.43±0.05	D	37.3	151	13 47 16.09	+30 33 07.6	+30 33 07.6				F
WN J1352+4259	1213±48	173.9±7.7	...	-1.33±0.04	D	12.1	19	13 52 28.39	+42 59 18.1	+42 59 18.1				F
WN J1353+3336	107±6	15.9±1.9	...	-1.31±0.09	13 53 07.46	+33 36 24.6	+33 36 24.6				N
WN J1355+3848	204±8	25.6±0.6	...	-1.42±0.03	S	2.3	59	13 55 29.50	+38 48 11.1	+38 48 11.1				F
WN J1359+7446*	214±9	12.9±0.5	1.26±0.10	-1.62±0.05	-1.87±0.07	-1.87±0.07	S	2.5	12	13 59 16.90	+74 46 42.6	+74 46 42.6				V
WN J1400+4348	178±7	20.2±1.5	...	-1.49±0.06	S	6.4	93	14 00 51.84	+43 48 07.2	+43 48 07.2				F

Name	S ₃₂₅ mJy	S ₁₄₀₀ mJy	S ₄₈₅₀ mJy	c ₃₂₅ 1400	α ₁₄₀₀ 4850	Str	LAS //	PA o	h m	α _{J2000} o	δ _{J2000} o	Pos
WN J1403+3109	328±13	46.7±2.2	...	-1.85±0.04	...	S	11.0	25	14 03 39.47	+31 09 11.4	F	
WN J1410+4615	103±5	14.2±1.4	...	-1.86±0.08	...	S	4.4	79	14 10 48.17	+46 15 57.5	F	
WN J1416+3821	94±6	18.1±0.5	...	-1.85±0.05	...	D	7.6	14	14 16 13.21	+38 21 56.7	F	
WN J1418+4546	186±8	17.9±0.5	2.70 ± 0.14	-1.60±0.04	-1.62 ± 0.05	S	0.5	18	14 18 38.40	+45 46 38.4	V	
WN J1420+6735	382±15	33.1±1.7	1.22 ± 0.08	-1.67±0.05	-2.65 ± 0.07	S	2.0	173	14 20 03.34	+67 35 07.5	V	
WN J1420+4126	128±6	18.7±0.6	...	-1.82±0.04	...	S	5.3	65	14 20 50.23	+41 26 26.1	F	
WN J1421+3103	110±5	18.6±0.5	...	-1.43±0.05	...	S	4.4	127	14 21 07.69	+31 03 03.9	F	
WN J1422+3452	163±7	10.7±1.3	...	-1.86±0.09	...	S	13.3	151	14 22 05.17	+34 52 14.4	F	
WN J1422+4212	256±10	35.4±1.8	...	-1.86±0.05	...	S	5.1	164	14 22 44.38	+42 12 00.2	F	
WN J1426+3522	89±5	11.5±1.6	...	-1.40±0.11	14 26 56.32	+35 22 34.7	N	
WN J1431+3015	101±5	14.3±1.5	...	-1.84±0.09	...	D	28.9	158	14 31 17.77	+30 15 00.2	F	
WN J1431+7317	129±6	17.9±1.3	4.65 ± 0.19	-1.85±0.06	-1.08 ± 0.07	D	11.2	47	14 31 28.01	+73 17 29.7	V	
WN J1433+3044	144±6	16.7±1.3	...	-1.48±0.06	...	D	14.5	100	14 33 56.51	+30 44 25.5	F	
WN J1435+3523	160±7	22.3±1.6	...	-1.85±0.06	...	S	8.0	64	14 35 53.99	+35 24 06.8	F	
WN J1436+6319	3507±140	514.0±22.4	64.84 ± 1.39	-1.81±0.04	-1.67 ± 0.04	D	3.8	154	14 36 37.28	+63 19 13.9	V	
WN J1437+7409	111±5	16.4±0.5	1.32 ± 0.11	-1.81±0.05	-2.02 ± 0.07	S	< 0.3	0	14 37 35.89	+74 09 22.2	V	
WN J1439+3729	142±7	17.1±0.5	...	-1.45±0.04	...	D	7.2	157	14 39 49.99	+37 29 03.4	F	
WN J1440+3707*	219±9	16.7±1.3	...	-1.76±0.06	...	S	7.4	61	14 40 03.63	+37 07 27.4	F	
WN J1444+4114	97±5	18.2±1.4	...	-1.87±0.09	...	D	30.1	151	14 44 27.65	+41 14 38.3	F	
WN J1444+4112	109±6	13.1±0.5	...	-1.45±0.05	...	D	12.6	96	14 44 48.82	+41 12 25.5	F	
WN J1447+5423	97±6	18.3±0.5	...	-1.86±0.05	...	S	11.0	174	14 47 54.36	+54 23 25.2	F	
WN J1450+3534	95±5	10.2±0.4	...	-1.53±0.05	...	S	3.3	62	14 50 20.69	+35 34 46.5	F	
WN J1451+3649	254±10	29.8±2.3	...	-1.47±0.06	...	T	50.7	101	14 51 11.62	+36 49 34.4	F	
WN J1454+3210	264±11	37.6±0.9	...	-1.83±0.03	...	S	3.0	22	14 54 11.64	+32 10 16.8	F	
WN J1459+6405	339±14	40.0±3.6	...	-1.46±0.07	14 59 33.34	+64 05 58.0	N	
WN J1459+4947	175±8	18.7±0.5	...	-1.53±0.04	...	S	3.0	109	14 59 43.19	+49 47 15.9	F	
WN J1500+3613	390±16	52.9±2.5	...	-1.87±0.04	...	S	2.2	76	15 00 09.01	+36 13 25.8	F	
WN J1502+4756	221±9	19.1±1.5	...	-1.68±0.06	...	D	12.3	37	15 02 03.58	+47 56 34.7	F	
WN J1508+5839	122±6	12.5±0.5	1.37 ± 0.09	-1.56±0.05	-1.78 ± 0.06	D	35.2	128	15 08 08.17	+68 39 13.3	V	
WN J1509+5905*	752±30	107.3±4.6	8.60 ± 0.26	-1.83±0.04	-2.03 ± 0.04	DF	1.8	74	15 09 32.34	+59 05 24.5	V	
WN J1525+3010	145±7	17.2±0.5	...	-1.46±0.04	...	S	1.2	123	15 25 01.21	+30 10 30.2	F	
WN J1525+5130	94±5	10.7±0.5	2.02 ± 0.13	-1.49±0.06	-1.84 ± 0.06	S	0.8	7	15 25 12.93	+51 30 06.1	V	
WN J1528+6317	332±14	40.0±2.0	20.80 ± 0.52	-1.45±0.04	-0.63 ± 0.05	DF	6.0	121	15 28 06.47	+63 17 40.2	V	
WN J1529+3454	124±6	18.0±0.5	...	-1.54±0.05	...	S	2.3	35	15 29 41.52	+34 54 31.3	F	
WN J1537+3402	83±5	11.6±0.5	...	-1.85±0.05	...	S	1.7	31	15 37 50.57	+34 02 33.3	F	
WN J1543+3512	231±10	23.6±1.5	...	-1.56±0.05	...	D	9.2	0	15 43 29.49	+35 12 29.7	F	
WN J1546+3935	155±7	13.7±0.5	...	-1.66±0.04	...	D	8.5	102	15 46 41.95	+39 35 52.7	F	
WN J1546+3005	92±6	15.0±0.5	...	-1.84±0.05	...	S	2.3	144	15 46 57.65	+30 05 38.1	F	
WN J1550+3830	229±10	32.9±1.7	...	-1.83±0.05	...	S	4.2	178	15 50 19.42	+38 30 14.8	F	
WN J1552+3715	546±22	27.3±1.6	...	-2.05±0.05	...	D	18.6	120	15 52 07.07	+37 15 07.1	F	
WN J1555+4011	359±14	50.9±2.4	...	-1.84±0.04	...	S	1.1	90	15 55 02.50	+40 11 58.2	F	
WN J1558+7028	114±6	15.7±0.5	1.68 ± 0.11	-1.86±0.11	-1.80 ± 0.12	S	2.1	38	15 58 37.92	+70 28 11.2	V	
WN J1559+6110	130±6	16.3±1.3	3.47 ± 0.14	-1.84±0.06	-1.34 ± 0.07	S	0.3	20	15 59 50.65	+61 10 57.8	V	
WN J1559+5926	116±6	16.3±1.3	41.70 ± 0.92	-1.89±0.07	...	D	31.0	60	15 59 54.42	+59 26 35.3	V	
WN J1604+5505	142±7	20.7±0.6	...	-1.82±0.04	...	S	1.1	15	16 04 21.91	+55 05 45.4	F	
WN J1606+6346	130±6	19.0±0.6	5.60 ± 0.19	-1.82±0.04	-0.88 ± 0.04	D	5.6	14	16 06 12.44	+63 47 06.1	V	
WN J1606+4142	83±5	12.3±0.5	...	-1.81±0.05	...	S	3.2	145	16 06 30.58	+41 42 10.8	F	
WN J1609+5725	70±5	10.2±0.5	2.13 ± 0.11	-1.82±0.07	-1.26 ± 0.06	S	1.7	60	16 09 28.14	+57 25 02.8	V	
WN J1618+5736	238±10	33.5±1.8	6.38 ± 0.20	-1.83±0.05	-1.34 ± 0.05	S	2.1	102	16 18 07.35	+57 36 11.7	V	
WN J1622+3447	156±7	21.1±0.6	...	-1.87±0.04	...	S	1.6	0	16 22 10.93	+34 47 44.6	F	

Name	S ₃₂₅ mJy	S ₁₄₀₀ mJy	S ₄₈₅₀ mJy	α_{325} 1400	α_{1400} 4850	Str	LAS //	PA °	α_J 2000 h m s	δ_J 2000 ° ' "	Pos
WN J1623+5213	166±7	19.8±0.6	...	-1.46±0.12	16 23 01.71	+82 13 17.4	N
WN J1624+4202	75±5	11.0±1.7	...	-1.31±0.14	...	D	24.4	19	16 24 37.86	+42 02 10.5	F
WN J1627+5430	146±7	20.9±0.6	...	-1.33±0.04	...	S	1.6	176	16 27 24.09	+54 30 55.2	F
WN J1628+3932	26737±1069	3680.7±35.1	...	-1.36±0.03	...	M	48.8	77	16 28 38.56	+39 33 00.1	F
WN J1633+7351	75±5	10.1±1.3	23.88±0.55	-1.37±0.11	0.69±0.11	DF	21.8	90	16 33 07.45	+73 51 38.1	V
WN J1645+4413	185±6	18.9±0.6	...	-1.35±0.04	...	S	1.1	56	16 45 00.50	+44 13 42.1	F
WN J1704+3839	335±14	34.5±1.8	...	-1.56±0.05	...	D	23.8	145	17 04 00.50	+38 39 56.7	F
WN J1713+3656	116±6	14.8±0.5	...	-1.41±0.04	...	S	1.1	169	17 13 55.63	+36 56 34.5	F
WN J1714+7031	182±6	14.2±1.4	0.95±0.09	-1.53±0.08	-2.18±0.11	S	2.4	46	17 14 35.18	+70 31 30.7	V
WN J1714+5251	262±11	37.9±2.0	...	-1.32±0.05	...	D	26.6	80	17 14 37.93	+52 51 30.1	F
WN J1717+3828	368±15	35.8±2.0	...	-1.60±0.05	...	M	33.6	156	17 17 16.22	+38 28 16.5	F
WN J1718+5823	1098±44	133.2±2.7	11.26±0.32	-1.44±0.03	-1.98±0.03	S	0.3	107	17 18 18.51	+58 23 21.8	V
WN J1723+5822	85±6	10.4±0.5	2.27±0.11	-1.46±0.06	-1.23±0.06	S	4.7	103	17 23 01.98	+58 22 44.0	V
WN J1723+6844	105±6	15.7±1.3	...	-1.30±0.07	17 23 05.64	+68 44 17.7	N
WN J1731+4640	200±9	15.7±0.5	...	-1.74±0.04	...	D	11.6	106	17 31 46.10	+46 40 03.1	F
WN J1731+4654	323±13	42.0±2.1	...	-1.40±0.05	...	S	1.9	176	17 31 59.63	+46 54 00.2	F
WN J1732+6757	85±5	11.9±0.5	2.31±0.11	-1.35±0.05	-1.32±0.05	D	1.5	178	17 32 30.61	+67 57 02.5	V
WN J1733+4037	80±5	11.2±2.0	...	-1.35±0.13	17 33 31.13	+40 37 00.6	N
WN J1734+4527	87±5	11.0±0.5	...	-1.42±0.06	...	D	10.4	174	17 34 07.58	+45 27 25.6	F
WN J1734+3606	69±3	10.2±3.2	3.12±0.13	-1.31±0.22	-0.95±0.25	S	2.1	137	17 34 24.13	+36 06 38.8	V
WN J1736+6502	183±8	27.4±1.6	4.40±0.16	-1.34±0.05	-1.47±0.06	D	16.0	159	17 36 37.50	+65 02 28.7	V
WN J1739+5309	78±5	11.3±0.5	...	-1.32±0.06	...	S	7.3	114	17 39 28.39	+53 09 41.8	F
WN J1749+5659	124±7	15.9±1.6	...	-1.41±0.08	17 49 21.19	+56 59 59.6	N
WN J1749+6248	104±6	13.3±0.5	2.69±0.12	-1.41±0.05	-1.22±0.05	S	1.7	48	17 49 27.04	+62 48 54.0	V
WN J1752+2949	185±6	16.9±0.5	2.29±0.14	-1.42±0.04	-1.61±0.05	S	3.2	102	17 52 56.67	+29 49 28.3	V
WN J1801+3336	186±6	11.6±0.5	1.26±0.12	-1.69±0.05	-1.78±0.08	S	2.5	34	18 01 07.26	+33 36 40.4	V
WN J1802+3948	1102±44	157.3±6.8	27.67±0.62	-1.33±0.04	-1.40±0.04	T	19.2	13	18 02 31.65	+66 28 59.6	V
WN J1804+5547	173±8	22.9±1.7	...	-1.38±0.06	18 04 15.35	+55 47 16.3	N
WN J1804+3048	182±8	27.7±0.7	5.88±0.18	-1.33±0.04	-1.25±0.03	S	2.0	84	18 04 42.01	+30 48 45.0	V
WN J1806+6332	188±7	17.7±0.5	...	-1.41±0.04	18 06 23.66	+63 32 07.9	N
WN J1807+5027	483±19	71.4±3.3	11.67±0.31	-1.31±0.04	-1.46±0.04	D	3.7	173	18 07 07.39	+50 27 25.8	V
WN J1807+6628	76±5	10.9±1.4	1.20±0.11	-1.33±0.10	-1.78±0.13	S	0.3	103	18 07 29.75	+66 28 33.4	V
WN J1810+6635	115±8	14.1±0.5	2.62±0.12	-1.44±0.04	-1.36±0.05	S	1.6	15	18 10 28.41	+66 35 15.1	V
WN J1811+6008	160±7	17.8±0.5	7.87±0.24	-1.50±0.04	-0.66±0.03	DF	3.5	31	18 11 18.38	+60 08 42.9	V
WN J1813+4847	92±5	12.1±0.5	...	-1.39±0.06	18 13 16.68	+48 47 50.1	N
WN J1814+5009	120±7	16.7±0.5	...	-1.35±0.05	18 14 01.40	+50 09 58.0	N
WN J1815+3656	124±6	17.3±0.6	2.96±0.14	-1.34±0.04	-1.43±0.05	S	1.6	48	18 15 23.11	+36 56 00.9	V
WN J1816+3840	186±8	27.3±1.6	...	-1.31±0.05	18 16 26.11	+38 40 53.0	N
WN J1818+7042	1624±65	199.6±8.8	30.50±0.74	-1.44±0.04	-1.51±0.04	D	1.4	10	18 18 04.24	+70 42 59.5	V
WN J1818+3852	105±6	12.6±0.5	1.29±0.09	-1.45±0.05	-1.84±0.07	S	2.6	64	18 18 42.17	+38 52 20.4	V
WN J1818+3428	167±7	23.7±0.6	5.68±0.18	-1.34±0.04	-1.15±0.03	T	7.5	103	18 18 47.90	+34 28 24.0	V
WN J1818+6144	149±6	11.1±1.0	1.11±0.10	-1.31±0.06	-2.40±0.09	S	1.6	11	18 18 50.55	+61 44 18.4	V
WN J1819+3122	77±5	10.5±0.5	...	-1.36±0.06	18 19 28.60	+31 22 19.3	N
WN J1819+6213	106±6	12.7±0.5	0.47±0.08	-1.45±0.05	-2.66±0.14	S	1.6	41	18 19 52.26	+62 13 58.0	V
WN J1820+5711	186±7	20.3±1.5	...	-1.30±0.06	18 20 51.14	+57 11 06.5	N
WN J1821+3602	3396±136	99.0±4.2	233.33±4.90	-2.42±0.04	0.69±0.04	T	35.0	55	18 21 02.20	+36 02 15.7	V
WN J1821+3601 ¹	151±6	10.2±1.5	105.26±2.53	-1.85±0.11	1.88±0.12	D	34.9	55	18 21 22.59	+36 01 03.3	V
WN J1829+6914	207±9	13.0±1.3	2.25±0.12	-1.90±0.08	-1.41±0.09	S	1.8	22	18 29 05.68	+69 14 06.1	V
WN J1829+4919	98±6	14.2±0.5	7.95±0.24	-1.32±0.06	-0.47±0.04	D	12.5	173	18 29 33.74	+49 19 55.6	V
WN J1829+5945	346±14	50.4±2.4	8.82±0.25	-1.32±0.04	-1.40±0.04	S	1.7	26	18 29 57.26	+59 45 03.2	V

Name	S ₃₂₅ mJy	S ₁₄₀₀ mJy	S ₄₈₅₀ mJy	α ₃₂₅ 1400	α ₄₈₅₀	Str	LAS //	PA °	h m	s	δ _{J2000} °	l b	Pos
WN J1830+6422	76±3	10.3±0.5	...	-1.31±0.07	18 30	45.82	+64 22 26.3	N	
WN J1832+3354†	226±10	28.7±1.6	23.82±0.59	-1.41±0.05	-0.15±0.05	D	19.4	56	18 32	41.16	+33 54 34.0	V	
WN J1836+5210	191±9	24.2±1.5	3.54±0.15	-1.41±0.05	-1.55±0.06	S	1.4	10	18 36	23.22	+52 10 28.4	V	
WN J1839+4710	176±8	22.8±1.6	...	-1.40±0.06	18 39	14.54	+47 10 59.4	V	
WN J1843+5932	998±40	148.2±6.6	30.87±0.70	-1.31±0.04	-1.26±0.04	T	7.7	64	18 43	31.70	+59 32 59.3	V	
WN J1847+5423	108±6	15.8±1.3	6.67±0.23	-1.32±0.07	-0.69±0.07	DF	2.9	67	18 47	04.03	+54 23 06.6	V	
WN J1852+5711*	387±16	53.4±2.5	...	-1.36±0.04	18 52	08.35	+57 11 42.7	V	
WN J1857+7411	160±7	19.0±0.6	...	-1.43±0.04	18 57	03.60	+74 11 31.2	N	
WN J1859+5900	98±6	11.7±0.5	1.64±0.12	-1.46±0.06	-1.56±0.07	S	0.5	171	18 59	40.34	+59 00 36.8	V	
WN J1859+5416	81±4	10.1±1.6	2.70±0.14	-1.43±0.12	-1.06±0.13	S	1.7	17	18 59	57.65	+54 16 21.8	V	
WN J1907+8532	69±4	10.2±0.4	...	-1.31±0.05	19 07	26.54	+85 32 35.2	N	
WN J1911+6342	185±10	23.3±1.5	3.37±0.14	-1.42±0.05	-1.56±0.06	S	1.8	7	19 11	49.54	+63 42 08.6	V	
WN J1912+8627	126±7	18.8±1.2	2.55±0.13	-1.30±0.05	-1.61±0.07	S	2.4	178	19 12	06.26	+86 27 10.1	V	
WN J1917+6635	75±5	11.2±0.5	2.37±0.12	-1.30±0.06	-1.25±0.06	S	1.9	152	19 17	35.50	+66 35 38.5	V	
WN J1917+7149	280±12	40.4±2.1	...	-1.33±0.05	19 17	56.11	+71 49 19.7	N	
WN J1923+6047	83±5	12.4±0.5	2.56±0.13	-1.30±0.06	-1.27±0.05	D	2.4	91	19 23	33.18	+60 47 56.8	V	
WN J1925+5203	199±9	27.5±1.7	4.30±0.16	-1.36±0.05	-1.49±0.06	D	8.6	52	19 25	16.97	+52 03 34.4	V	
WN J1925+5742	100±6	14.5±0.5	1.58±0.11	-1.32±0.06	-1.78±0.06	S	2.0	9	19 25	22.22	+57 42 27.3	V	
WN J1926+5710	136±7	20.2±0.6	4.55±0.18	-1.31±0.04	-1.20±0.04	S	1.8	161	19 26	43.85	+57 10 00.5	V	
WN J1927+6436	661±26	80.3±3.5	6.62±0.21	-1.44±0.04	-2.01±0.04	D	20.1	120	19 27	22.83	+64 36 02.6	V	
WN J1944+6552	1367±55	147.2±6.5	19.45±0.47	-1.53±0.04	-1.63±0.04	S	1.8	165	19 44	23.99	+65 52 23.8	V	
WN J1953+7052	75±7	10.3±0.5	3.22±0.15	-1.36±0.07	-0.94±0.05	D	14.4	150	19 53	21.10	+70 52 19.8	V	
WN J1954+7011	460±19	63.4±2.9	...	-1.36±0.04	19 54	30.53	+70 11 33.5	N	
WN J2044+7044	311±13	41.7±0.9	7.18±0.22	-1.38±0.03	-1.42±0.03	D	1.3	83	20 44	57.80	+70 44 03.8	N	
WN J2052+6925	113±6	16.1±1.3	...	-1.33±0.07	20 52	33.78	+69 25 09.3	N	
WN J2053+6849	108±5	15.8±0.5	2.59±0.13	-1.32±0.05	-1.45±0.05	S	2.8	13	20 53	38.68	+68 48 54.7	V	
WN J2139+3125	249±10	28.0±0.7	...	-1.50±0.04	21 39	32.31	+31 25 18.7	N	
WN J2146+3330	105±6	10.8±0.5	...	-1.56±0.05	21 46	55.47	+33 30 01.7	N	
WN J2147+3137	215±9	25.4±1.6	...	-1.46±0.05	21 47	35.21	+31 37 58.9	N	
WN J2158+3424	183±8	25.3±0.7	4.48±0.17	-1.35±0.04	-1.39±0.04	T	7.9	163	21 58	54.14	+34 24 47.8	V	
WN J2213+3411	320±13	29.8±2.2	...	-1.63±0.06	22 13	12.48	+34 11 42.8	N	
WN J2219+2951	151±10	13.2±0.5	...	-1.67±0.04	22 19	28.65	+39 51 57.4	N	
WN J2221+3800	99±6	14.4±0.5	2.18±0.11	-1.32±0.05	-1.52±0.05	S	1.4	5	22 21	49.53	+38 00 38.4	V	
WN J2222+3305	232±10	30.4±1.7	3.53±0.14	-1.39±0.05	-1.73±0.05	S	1.4	13	22 22	15.19	+33 05 44.1	V	
WN J2245+3937	204±8	15.5±1.3	5.65±0.21	-1.76±0.07	-0.81±0.07	DF	4.0	168	22 45	02.74	+39 37 27.9	V	
WN J2250+4131	128±7	15.2±1.4	2.03±0.11	-1.46±0.07	-1.62±0.09	S	1.5	25	22 50	51.16	+41 31 16.4	V	
WN J2313+4053	101±6	11.3±1.4	...	-1.50±0.09	23 13	06.34	+40 53 40.6	N	
WN J2313+4253	94±7	13.4±1.5	3.41±0.14	-1.33±0.09	-1.10±0.10	S	1.4	13	23 13	08.62	+42 53 13.0	V	
WN J2313+3842*	304±13	13.2±2.6	...	-2.15±0.14	23 13	47.75	+38 42 26.2	N	
WN J2319+4251	321±14	40.2±2.9	3.88±0.14	-1.42±0.06	-1.88±0.07	S	1.5	20	23 19	47.25	+42 51 09.2	V	
WN J2337+3421	84±4	12.4±1.3	...	-1.31±0.09	23 37	23.43	+34 21 51.5	N	
WN J2338+4047	115±6	16.9±0.5	5.06±0.18	-1.31±0.04	-0.97±0.04	D	15.7	8	23 38	11.10	+40 47 19.6	V	
WN J2350+3631	196±8	22.8±0.6	2.20±0.11	-1.47±0.04	-1.88±0.04	DF	2.7	165	23 50	25.69	+36 31 27.6	V	

† Not a real USS source; see notes
* See notes

Table A. 2. TN sample

Name	S ₃₆₅ mJy	S ₁₄₀₀ mJy	S ₄₈₅₀ mJy	c ₃₆₅ ¹⁴⁰⁰	α ₁₄₀₀ ⁴⁸⁵⁰	Str	LAS	PA	h	v	s	δJ ₂₀₀₀ o	l	b	Pos
TN J0008-0912	638 ± 64	100.3 ± 4.4	...	-1.38 ± 0.08	00.08	52.43	...	-09 12 01.4	N
TN J0018+1904	498 ± 30	84.5 ± 3.8	...	-1.32 ± 0.06	00.18	07.35	...	+19 04 50.0	N
TN J0026+1501	241 ± 26	39.4 ± 2.0	...	-1.35 ± 0.09	00.26	03.31	...	+15 01 29.2	N
TN J0027+0059	735 ± 55	98.0 ± 4.4	...	-1.50 ± 0.07	00.27	39.36	...	+00 59 53.6	N
TN J0033-2731	512 ± 41	66.1 ± 3.0	...	-1.52 ± 0.07	00.33	24.28	...	-27 31 48.1	N
TN J0037+2629	442 ± 35	70.8 ± 3.2	...	-1.36 ± 0.07	00.37	10.05	...	+26 29 42.3	N
TN J0038-1540	471 ± 33	63.9 ± 1.4	10.8 ± 0.6	-1.49 ± 0.07	-1.43 ± 0.05	D	3.2	18	00.38	47.19	...	-15 40 06.6	N
TN J0040+1417	435 ± 41	71.1 ± 1.5	...	-1.35 ± 0.07	00.40	37.04	...	+14 17 14.6	N
TN J0041+1250	451 ± 65	71.0 ± 3.3	21.0 ± 1.1	-1.38 ± 0.11	-0.98 ± 0.06	D	10.7	103	00.41	31.27	...	+12 50 32.3	N
TN J0042+2649	484 ± 57	69.6 ± 3.2	...	-1.44 ± 0.09	00.42	32.46	...	+26 49 06.2	N
TN J0055+2624	8670 ± 457	1375.5 ± 56.2	...	-1.37 ± 0.05	00.55	50.38	...	+26 24 35.8	N
TN J0102-1055	775 ± 41	110.4 ± 4.9	16.4 ± 0.9	-1.45 ± 0.05	-1.63 ± 0.06	D	1.5	136	01 01	59.99	...	-10 55 56.0	N
TN J0102-2152	1900 ± 88	168.3 ± 6.7	...	-1.80 ± 0.05	01 02	41.09	...	-21 52 30.2	N
TN J0114-0333	367 ± 36	54.7 ± 2.6	12.9 ± 0.7	-1.42 ± 0.08	-1.16 ± 0.06	T	2.4	146	01 14	42.50	...	-03 33 58.8	N
TN J0119-2054	522 ± 60	87.8 ± 4.0	...	-1.33 ± 0.09	01 19	47.65	...	-20 54 46.8	N
TN J0121+1320	348 ± 33	57.3 ± 2.7	8.4 ± 0.5	-1.34 ± 0.08	-1.55 ± 0.06	S	0.3	89	01 21	42.74	...	+13 20 58.3	N
TN J0154+0044	465 ± 29	78.6 ± 3.6	...	-1.32 ± 0.06	01 54	38.48	...	+00 44 37.7	N
TN J0156+1619	437 ± 45	62.9 ± 2.9	...	-1.44 ± 0.09	01 56	18.01	...	+16 19 52.5	N
TN J0201-1302	360 ± 33	57.0 ± 2.7	11.0 ± 0.6	-1.37 ± 0.08	-1.32 ± 0.06	S	< 1.3	0	02 01	15.80	...	-13 02 19.4	N
TN J0205+2242	381 ± 26	60.4 ± 2.8	8.8 ± 0.5	-1.37 ± 0.06	-1.55 ± 0.06	D	2.7	148	02 05	10.69	...	+22 42 50.2	N
TN J0208+1305	403 ± 61	68.3 ± 3.1	...	-1.32 ± 0.12	02 08	32.45	...	+13 05 53.0	N
TN J0215+2651	431 ± 49	69.3 ± 3.2	...	-1.36 ± 0.09	02 15	45.31	...	+26 51 12.3	N
TN J0218+0844	395 ± 32	61.8 ± 1.3	8.8 ± 0.5	-1.38 ± 0.06	-1.66 ± 0.05	S	0.4	169	02 18	25.56	...	+08 44 31.3	N
TN J0230-0255	573 ± 56	90.1 ± 4.0	22.5 ± 1.2	-1.38 ± 0.08	-1.12 ± 0.06	M	6.7	156	02 30	21.97	...	-02 55 05.1	N
TN J0230-2001	380 ± 33	57.8 ± 2.7	...	-1.40 ± 0.07	02 30	45.73	...	-20 01 19.0	N
TN J0235+2349*	1075 ± 86	176.8 ± 7.8	43.5 ± 2.3	-1.34 ± 0.07	-1.13 ± 0.06	DF	4.0	116	02 33	10.32	...	+23 49 52.2	N
TN J0234-1215	451 ± 46	64.2 ± 2.9	...	-1.45 ± 0.08	02 34	57.31	...	-12 15 21.7	N
TN J0243+1405	395 ± 51	58.4 ± 1.3	26.2 ± 1.4	-1.42 ± 0.10	-0.64 ± 0.05	T	3.1	126	02 43	10.52	...	+14 05 36.9	N
TN J0244+0327	542 ± 62	84.8 ± 3.8	...	-1.38 ± 0.09	02 44	53.97	...	+03 27 46.8	N
TN J0245+2700	388 ± 53	54.0 ± 2.5	...	-1.47 ± 0.11	02 45	22.27	...	+27 00 06.3	N
TN J0250+0130	275 ± 25	39.1 ± 2.0	...	-1.45 ± 0.08	02 50	20.94	...	+01 30 24.9	N
TN J0254-1039	421 ± 60	68.1 ± 3.1	25.5 ± 1.4	-1.36 ± 0.11	-0.79 ± 0.06	D	11.7	129	02 54	59.89	...	-10 39 49.2	N
TN J0256-2717	1045 ± 70	177.9 ± 7.4	...	-1.32 ± 0.06	02 56	51.44	...	-27 17 56.5	N
TN J0301+0155	3950 ± 180	402.7 ± 17.3	...	-1.70 ± 0.05	03 01	38.49	...	+01 55 14.9	N
TN J0306+0524	909 ± 76	155.1 ± 6.3	...	-1.32 ± 0.07	03 06	08.10	...	+05 24 23.8	N
TN J0309-2425*	483 ± 53	62.6 ± 2.9	14.8 ± 0.9	-1.52 ± 0.09	-1.16 ± 0.06	D	12.9	23	03 09	09.26	...	-24 25 11.7	N
TN J0310+0814	593 ± 67	96.8 ± 4.3	...	-1.35 ± 0.09	03 10	37.37	...	+08 14 59.2	N
TN J0311-2553	1102 ± 66	174.1 ± 7.5	...	-1.37 ± 0.06	03 11	47.40	...	-25 53 21.1	N
TN J0312-2622	442 ± 41	46.4 ± 2.3	...	-1.38 ± 0.08	03 12	34.19	...	-26 22 23.9	N
TN J0316-0815	1850 ± 82	305.1 ± 13.4	42.2 ± 2.2	-1.38 ± 0.05	-1.59 ± 0.05	T	3.2	34	03 16	18.59	...	-08 15 54.8	N
TN J0321+1631	1084 ± 85	175.7 ± 7.7	...	-1.35 ± 0.07	03 21	36.86	...	+16 31 55.8	N
TN J0327-0948	281 ± 30	39.0 ± 2.0	...	-1.47 ± 0.09	03 27	00.55	...	-09 48 05.2	N
TN J0344+1803	297 ± 22	50.7 ± 2.4	...	-1.32 ± 0.07	03 44	00.12	...	+19 03 53.1	N
TN J0344-2029	538 ± 71	74.0 ± 1.6	19.2 ± 1.1	-1.48 ± 0.11	-1.08 ± 0.05	D	6.5	42	03 44	37.88	...	-20 29 03.8	N
TN J0349-1207*	460 ± 61	77.5 ± 3.5	23.3 ± 1.3	-1.32 ± 0.11	-0.97 ± 0.06	T	9.4	101	03 49	49.22	...	-12 07 10.6	N
TN J0351-1947	642 ± 86	111.4 ± 4.9	...	-1.30 ± 0.11	03 51	33.13	...	-19 47 10.5	N
TN J0352-0355*	681 ± 63	114.9 ± 4.8	13.5 ± 0.8	-1.32 ± 0.08	-1.65 ± 0.06	DF	...	0	03 52	32.04	...	-03 55 47.2	N
TN J0355+0440	2015 ± 119	262.0 ± 11.5	...	-1.52 ± 0.05	03 55	12.79	...	+04 40 41.0	N
TN J0356-3028	1030 ± 65	167.5 ± 7.3	34.1 ± 1.8	-1.35 ± 0.06	-1.28 ± 0.06	D	3.1	86	03 56	45.54	...	-30 28 36.9	N
TN J0401-0156	1001 ± 65	172.8 ± 7.1	...	-1.31 ± 0.06	04 01	08.43	...	-01 56 08.9	N

Name	S ₃₆₅ mJy	S ₁₄₀₀ mJy	S ₄₈₅₀ mJy	α_{365}^{1400}	α_{1400}^{4850}	Str	LAS //	PA o	α_{J2000} h m s	δ_{J2000} o / /	Pos
TN J0402+1007	478±54	74.6±3.4	13.4±0.8	-1.38±0.08	-1.38±0.08	D	0.8	67	04 02 34.44	+10 07 14.9	V
TN J0404-0541	666±69	114.1±5.1	...	-1.31±0.09	04 04 09.66	-05 41 07.3	N
TN J0408-2418*	3881±172	647.7±28.1	...	-1.33±0.05	04 08 51.38	-24 18 15.5	N
TN J0410+1019	1185±88	166.9±3.4	26.5±1.4	-1.46±0.06	-1.26±0.05	S	0.2	109	04 10 40.52	+10 19 13.6	V
TN J0429-2118	561±58	95.5±4.3	...	-1.32±0.08	04 29 39.79	-21 18 01.7	N
TN J0431+0725	175±24	30.4±0.7	...	-1.30±0.10	04 31 54.21	+07 25 13.8	N
TN J0433+0717	229±27	33.1±1.8	...	-1.44±0.10	04 33 05.61	+07 17 55.2	N
TN J0435-0736	358±71	47.0±2.0	16.6±0.9	-1.51±0.15	-0.84±0.06	T	11.9	59	04 35 32.20	-07 36 12.3	V
TN J0437+0259	410±54	71.1±3.3	...	-1.30±0.10	04 37 33.04	+02 59 06.2	N
TN J0443-1212*	412±59	56.8±2.7	14.6±0.8	-1.47±0.11	-1.09±0.06	M	20.2	25	04 43 53.72	-12 12 46.7	V
TN J0452-1737	747±73	118.1±2.5	23.7±1.3	-1.37±0.07	-1.29±0.05	D	2.4	176	04 52 26.66	-17 37 54.0	V
TN J0510-1838	6801±325	641.3±25.6	...	-1.76±0.05	...	D	36.1	63	05 10 32.30	-18 38 41.4	A
TN J0515-3410	589±52	97.4±4.4	...	-1.34±0.07	05 15 18.86	-34 10 09.5	N
TN J0517-0641	285±30	40.0±0.9	6.8±0.4	-1.46±0.08	-1.43±0.05	S	1.0	0	05 17 36.89	-06 41 14.6	V
TN J0525-1832	549±73	86.4±3.9	24.1±1.3	-1.38±0.11	-1.02±0.06	T	8.1	172	05 25 54.85	-18 32 32.5	V
TN J0547-0706	2552±156	362.6±16.0	...	-1.45±0.06	05 47 27.57	-07 06 35.0	N
TN J0549-2459	427±55	58.0±1.3	...	-1.49±0.10	...	S	23.5	8	05 49 28.61	-24 59 15.2	A
TN J0551-0756	473±71	68.5±3.2	...	-1.44±0.12	05 51 30.37	-07 56 17.5	N
TN J0552-0433	1618±83	269.7±11.8	37.7±2.0	-1.33±0.05	-1.56±0.06	D	4.3	152	05 52 14.38	-04 33 28.8	V
TN J0553-2033	887±80	148.0±6.2	...	-1.33±0.07	05 53 37.24	-20 33 07.6	N
TN J0558-1858	425±54	73.4±3.4	...	-1.31±0.10	05 58 39.43	-13 58 45.5	N
TN J0559-3406	773±69	123.5±5.4	...	-1.36±0.07	...	S	4.6	8	05 59 14.30	-34 06 51.0	A
TN J0602-2741	810±54	117.2±5.2	20.7±1.2	-1.44±0.06	-1.39±0.06	T	4.3	88	06 02 41.32	-27 41 10.1	V
TN J0630-2834	343±29	14.3±0.5	...	-2.36±0.07	...	S	13.5	2	06 30 49.49	-28 34 40.4	A
TN J0634-3232	394±63	67.7±3.1	...	-1.31±0.12	06 34 17.10	-32 32 34.1	N
TN J0729+2436	1062±87	68.9±3.1	...	-2.03±0.07	...	D	19.4	72	07 29 28.65	+24 36 26.2	F
TN J0733+1753	291±45	46.1±2.3	...	-1.37±0.12	07 33 17.53	+17 53 28.4	N
TN J0805+2738	987±79	153.0±6.7	...	-1.39±0.07	...	T	71.3	119	08 05 15.50	+27 38 01.2	F
TN J0806+0401	560±53	92.1±2.0	...	-1.34±0.07	08 06 32.25	+04 01 37.7	N
TN J0812+0915	277±46	43.4±2.2	...	-1.38±0.13	08 12 16.84	+09 15 43.7	N
TN J0818-0741	381±48	59.3±2.8	...	-1.38±0.10	08 18 51.89	-07 41 48.2	N
TN J0831+0046	451±55	72.8±3.3	...	-1.36±0.10	08 31 39.92	+00 46 56.5	N
TN J0831+0851	567±53	83.8±3.8	98.3±5.2	-1.42±0.08	0.13±0.06	DF	3.0	2	08 31 52.74	+08 51 14.1	V
TN J0837-1053*	450±81	69.2±3.1	11.6±0.7	-1.39±0.14	-1.43±0.06	D	23.5	11	08 37 41.62	-10 53 46.0	V
TN J0855-0000	416±57	65.9±3.0	13.8±0.8	-1.37±0.11	-1.26±0.06	D	3.8	85	08 55 57.26	-00 00 58.2	V
TN J0856-1510	469±68	70.0±3.2	3.7±0.3	-1.41±0.11	-2.01±0.07	S	1.0	14	08 56 12.44	-15 10 35.7	V
TN J0902+1809	491±37	55.5±2.6	...	-1.62±0.07	09 02 00.00	+18 09 03.4	N
TN J0906-0701	839±101	142.5±5.8	...	-1.40±0.09	09 06 40.23	-07 01 12.4	N
TN J0910-2228	465±32	55.3±2.6	4.0±0.3	-1.58±0.06	-2.11±0.07	S	2.0	0	09 10 34.15	-22 28 47.4	V
TN J0914+1119	343±53	49.5±1.1	...	-1.44±0.12	09 14 30.81	+11 19 08.0	N
TN J0919+1845	522±50	80.0±4.0	...	-1.31±0.08	09 19 33.25	+18 45 51.2	N
TN J0920-0712	760±53	100.4±4.5	16.3±0.9	-1.51±0.06	-1.46±0.06	S	1.4	135	09 20 22.43	-07 12 17.6	V
TN J0920-1405	842±88	133.6±5.5	...	-1.37±0.08	09 20 37.77	-14 05 56.3	N
TN J0924-2201	656±72	73.3±1.5	8.6±0.5	-1.63±0.08	-1.72±0.05	D	1.2	74	09 24 19.62	-22 01 41.5	V
TN J0936+0422	6025±362	992.0±42.5	...	-1.34±0.05	09 36 32.02	+04 22 10.7	N
TN J0936-2243	488±63	69.1±3.2	18.5±1.0	-1.45±0.10	-1.06±0.06	D	8.1	77	09 36 32.53	-22 43 04.9	V
TN J0941-1628	1810±115	304.4±13.4	64.7±3.8	-1.33±0.06	-1.24±0.06	D	1.9	175	09 41 07.43	-16 28 02.5	V
TN J0946-0306	238±24	38.2±2.0	...	-1.36±0.09	09 46 00.88	-03 06 26.2	N
TN J0954-1635	1531±98	260.0±11.4	...	-1.32±0.06	09 54 52.80	-16 35 35.1	N
TN J0956-1500	505±49	68.9±1.5	...	-1.48±0.07	09 56 01.46	-15 00 21.6	N

Name	S ₃₆₅ mJy	S ₁₄₀₀ mJy	S ₄₈₅₀ mJy	c ₃₆₅ 1400	α ₁₄₀₀ 4850	Str	LAS //	PA °	h m s	α _{J2000} °	δ _{J2000} °	Pos
TN J0658-1103	431 ± 63	70.6 ± 3.2	...	-1.35 ± 0.11	09 58 21.84	-11 03 47.5	N	
TN J1000+0549	410 ± 55	67.3 ± 3.1	...	-1.34 ± 0.11	10 00 44.68	+05 49 31.1	N	
TN J1002+2225	343 ± 41	54.2 ± 2.6	12.2 ± 0.7	-1.37 ± 0.10	-1.20 ± 0.06	D	11.2	10	10 02 54.08	+22 25 21.9	V	
TN J1026-2116	399 ± 29	61.5 ± 1.3	8.5 ± 0.5	-1.39 ± 0.06	-1.59 ± 0.05	S	1.0	0	10 26 22.37	-21 16 07.7	V	
TN J1028+1114	459 ± 56	79.7 ± 3.6	...	-1.30 ± 0.10	10 28 24.31	+11 14 52.4	N	
TN J1031+0259	416 ± 62	60.0 ± 1.3	...	-1.44 ± 0.11	10 31 13.36	+02 59 05.3	N	
TN J1033-1339	981 ± 75	153.8 ± 6.8	26.0 ± 1.4	-1.38 ± 0.07	-1.43 ± 0.06	S	2.0	107	10 33 10.70	-13 39 52.0	V	
TN J1043-1718	578 ± 70	91.0 ± 3.9	18.9 ± 1.0	-1.38 ± 0.10	-1.26 ± 0.06	D	34.7	63	10 43 19.42	-17 18 53.5	V	
TN J1043+2404	439 ± 34	52.0 ± 2.5	...	-1.59 ± 0.07	...	S	3.7	90	10 43 43.28	+24 04 47.3	F	
TN J1045+1852	348 ± 27	53.6 ± 1.2	...	-1.39 ± 0.06	10 45 42.63	+18 32 37.5	N	
TN J1049-1258	818 ± 56	112.2 ± 5.0	17.2 ± 0.9	-1.48 ± 0.06	-1.50 ± 0.06	M	10.1	104	10 49 06.22	-12 58 18.3	V	
TN J1053-1518	383 ± 62	63.7 ± 2.9	...	-1.33 ± 0.13	10 53 44.52	-15 18 29.8	N	
TN J1056-0400	449 ± 57	57.2 ± 2.7	...	-1.53 ± 0.10	10 56 52.64	-04 00 15.9	N	
TN J1102+1029	3713 ± 224	633.6 ± 27.8	...	-1.32 ± 0.06	11 02 17.47	+10 29 08.0	N	
TN J1102-1651	688 ± 68	112.5 ± 5.0	20.2 ± 1.1	-1.35 ± 0.08	-1.38 ± 0.06	D	3.0	70	11 02 47.13	-16 51 34.4	V	
TN J1112-2948	663 ± 51	101.0 ± 4.5	16.6 ± 0.9	-1.40 ± 0.07	-1.45 ± 0.06	D	9.1	119	11 12 23.86	-29 48 06.4	V	
TN J1114-2221	389 ± 53	64.9 ± 3.0	...	-1.33 ± 0.11	11 14 04.82	-22 21 26.6	N	
TN J1117-1409	785 ± 69	134.5 ± 5.9	...	-1.31 ± 0.07	11 17 23.00	-14 09 09.5	N	
TN J1118-2612	514 ± 44	62.3 ± 2.9	...	-1.57 ± 0.07	11 18 54.08	-26 12 20.6	N	
TN J1121-1155	332 ± 65	50.1 ± 2.4	...	-1.41 ± 0.15	11 21 32.75	-11 55 03.2	N	
TN J1121+1706	1156 ± 83	196.8 ± 8.4	...	-1.32 ± 0.06	11 21 39.89	+17 06 14.8	N	
TN J1123-2154	407 ± 64	50.6 ± 2.4	8.5 ± 0.5	-1.55 ± 0.12	-1.43 ± 0.06	S	0.8	29	11 23 10.15	-21 54 05.3	V	
TN J1125-0342	354 ± 52	61.4 ± 2.9	...	-1.30 ± 0.11	11 25 57.41	-03 42 04.0	N	
TN J1133-2715	2938 ± 125	447.9 ± 9.2	...	-1.40 ± 0.04	11 33 31.53	-27 15 22.9	N	
TN J1136+1551	384 ± 33	21.7 ± 0.6	...	-2.14 ± 0.07	11 36 03.28	+15 51 06.7	N	
TN J1136+0610	698 ± 50	118.8 ± 5.3	...	-1.32 ± 0.06	11 36 38.91	+06 10 26.8	N	
TN J1139+0935	508 ± 58	87.3 ± 3.9	...	-1.31 ± 0.09	11 39 22.75	+09 35 26.1	N	
TN J1146-1052	843 ± 79	120.9 ± 5.4	...	-1.44 ± 0.08	...	S	8.8	1	11 46 07.21	-10 52 08.6	A	
TN J1148-0901	571 ± 67	80.4 ± 3.7	...	-1.46 ± 0.09	...	S	< 6.0	5	11 48 39.80	-09 01 48.8	A	
TN J1149+1844	457 ± 39	77.6 ± 1.6	...	-1.32 ± 0.07	11 49 36.78	+18 44 21.5	N	
TN J1151-3013	435 ± 28	52.7 ± 1.2	7.0 ± 0.4	-1.57 ± 0.05	-1.62 ± 0.05	S	1.0	0	11 51 59.42	-30 13 40.8	V	
TN J1156-3105	317 ± 48	48.3 ± 2.3	...	-1.40 ± 0.12	11 56 25.60	-31 05 40.0	A	
TN J1159-1629	324 ± 34	52.9 ± 1.2	10.4 ± 0.6	-1.35 ± 0.08	-1.30 ± 0.05	D	1.4	38	11 59 53.25	-16 29 48.2	V	
TN J1204+1630	804 ± 56	129.7 ± 5.8	...	-1.36 ± 0.06	12 04 20.48	+16 30 49.5	N	
TN J1210+1738	397 ± 50	68.1 ± 3.2	...	-1.31 ± 0.10	12 10 36.00	+17 38 27.8	N	
TN J1216+1944	546 ± 44	91.7 ± 4.1	...	-1.33 ± 0.07	12 16 01.76	+19 44 43.3	N	
TN J1216-2850	870 ± 43	145.2 ± 6.4	...	-1.33 ± 0.05	...	S	< 7.0	163	12 16 17.38	-28 50 48.7	A	
TN J1220+0604	491 ± 61	65.1 ± 3.0	...	-1.50 ± 0.10	12 20 07.82	+06 04 16.5	N	
TN J1221-2646	1403 ± 82	217.1 ± 9.5	...	-1.39 ± 0.05	...	S	8.3	162	12 21 42.91	-26 46 37.7	A	
TN J1227-2255	271 ± 27	44.0 ± 2.2	...	-1.35 ± 0.08	...	S	< 7.0	158	12 27 47.23	-22 55 35.1	A	
TN J1239+1005	830 ± 89	79.3 ± 1.7	...	-1.75 ± 0.08	12 39 02.08	+10 05 49.2	N	
TN J1239+1043	569 ± 63	87.1 ± 3.8	...	-1.40 ± 0.09	12 39 31.67	+10 43 22.9	N	
TN J1239-0319	1629 ± 74	277.3 ± 12.2	...	-1.32 ± 0.05	12 39 38.91	-03 19 03.2	N	
TN J1245-1127	518 ± 62	88.0 ± 4.0	...	-1.32 ± 0.10	12 45 02.47	-11 27 25.9	N	
TN J1247+1547	405 ± 44	70.1 ± 3.2	...	-1.30 ± 0.09	12 47 04.84	+15 47 38.9	N	
TN J1251-2714	609 ± 53	96.5 ± 4.3	...	-1.37 ± 0.07	...	S	< 7.0	158	12 51 14.86	-27 14 19.9	A	
TN J1256-0911	457 ± 38	76.4 ± 3.5	...	-1.33 ± 0.07	12 56 19.48	-09 11 24.8	N	
TN J1303-3349	2431 ± 108	360.8 ± 7.7	...	-1.42 ± 0.14	13 03 02.67	-33 49 15.5	N	
TN J1306-0436	331 ± 57	55.2 ± 2.6	...	-1.33 ± 0.13	13 06 36.11	-04 36 17.4	N	
TN J1313-0459	369 ± 34	58.1 ± 2.7	...	-1.38 ± 0.08	13 13 34.37	-04 59 30.0	N	

Name	S ₃₆₅ mJy	S ₁₄₀₀ mJy	S ₄₈₅₀ mJy	c ₃₆₅ 1400	α ₁₄₀₀ 4850	Str	LAS	PA	h	α _{J2000} m, s	δ _{J2000} °, ′, ″	Pos
TN J1317+0339	395 ± 62	39.8 ± 2.0	...	-1.71 ± 0.12	13 17 48.12	+03 39 12.3	N	
TN J1323+2604	564 ± 60	97.3 ± 2.0	...	-1.31 ± 0.08	13 23 32.43	-26 04 04.7	N	
TN J1326+2330	523 ± 33	83.2 ± 3.8	...	-1.37 ± 0.06	13 26 25.24	-23 30 23.5	N	
TN J1327+1437	788 ± 68	115.0 ± 5.1	...	-1.43 ± 0.07	13 27 23.63	+14 37 00.4	N	
TN J1336+2450	368 ± 71	51.3 ± 2.5	...	-1.45 ± 0.15	...	M	54.4	100	13 36 15.12	+24 50 05.4	F	
TN J1338+1942	718 ± 63	122.9 ± 5.4	22.1 ± 1.2	-1.31 ± 0.11	-1.34 ± 0.06	S	1.4	152	13 38 26.06	-19 42 30.1	V	
TN J1339+0114	349 ± 51	59.5 ± 1.3	...	-1.32 ± 0.07	13 39 55.28	-01 14 10.8	N	
TN J1340+2723	827 ± 93	137.8 ± 6.1	24.8 ± 1.4	-1.33 ± 0.09	-1.38 ± 0.06	DF	1.7	0	13 40 29.38	+27 23 25.0	V	
TN J1346+1004	363 ± 59	49.6 ± 2.4	...	-1.48 ± 0.13	13 46 16.84	-10 04 57.2	N	
TN J1351+1328	662 ± 54	93.8 ± 4.2	...	-1.45 ± 0.07	13 51 54.72	+13 28 38.1	N	
TN J1352+0800	554 ± 88	95.6 ± 4.3	...	-1.31 ± 0.12	13 52 55.32	-08 00 14.1	N	
TN J1353+2302	403 ± 38	59.5 ± 1.3	23.3 ± 1.3	-1.42 ± 0.07	-0.75 ± 0.05	DF	2.5	44	13 53 42.26	+23 02 50.9	N	
TN J1358+2003	227 ± 42	35.0 ± 1.8	...	-1.39 ± 0.14	13 58 29.63	+20 03 13.4	N	
TN J1403+1223	396 ± 69	65.8 ± 3.0	...	-1.34 ± 0.14	...	S	30.6	169	14 03 37.33	-12 23 57.3	A	
TN J1408+0855	694 ± 73	114.3 ± 5.1	...	-1.34 ± 0.09	14 08 18.46	-08 55 38.5	N	
TN J1411+0824	542 ± 71	76.1 ± 3.5	...	-1.46 ± 0.10	14 11 53.33	-08 24 02.9	N	
TN J1412+2548	452 ± 59	78.0 ± 3.6	...	-1.31 ± 0.10	14 12 51.27	-25 48 05.5	N	
TN J1418+2256	527 ± 59	82.0 ± 3.7	...	-1.38 ± 0.07	...	S	7.6	148	14 18 16.65	-22 56 58.6	A	
TN J1428+2425	411 ± 34	69.1 ± 1.5	...	-1.33 ± 0.07	...	S	1.0	0	14 28 10.20	+24 25 11.3	F	
TN J1438+2334	564 ± 69	96.5 ± 4.2	...	-1.31 ± 0.10	...	D	21.1	157	14 38 56.52	+23 34 25.6	F	
TN J1439+3226	622 ± 65	90.7 ± 1.9	...	-1.43 ± 0.08	14 39 02.87	-32 26 46.6	N	
TN J1449+1440	464 ± 50	80.3 ± 3.7	...	-1.30 ± 0.09	14 49 02.50	+14 40 42.2	N	
TN J1451+2351	595 ± 44	98.2 ± 4.2	...	-1.38 ± 0.07	...	D	12.6	109	14 51 10.71	+23 51 38.8	F	
TN J1452+1113	344 ± 55	53.9 ± 2.6	...	-1.38 ± 0.13	...	S	< 7.5	2	14 52 04.88	-11 13 35.7	A	
TN J1452+2013	291 ± 40	43.4 ± 1.0	...	-1.42 ± 0.11	14 52 22.63	+20 13 09.8	N	
TN J1453+1106	833 ± 56	144.9 ± 6.4	...	-1.30 ± 0.06	14 53 21.97	+11 06 04.9	N	
TN J1454+0017	1309 ± 88	214.8 ± 9.2	...	-1.34 ± 0.06	14 54 40.87	+00 17 41.9	N	
TN J1459+2730	321 ± 40	52.5 ± 2.5	...	-1.35 ± 0.10	...	S	6.5	143	14 59 34.96	-27 30 08.3	A	
TN J1506+2728	360 ± 58	60.7 ± 1.3	15.9 ± 0.9	-1.32 ± 0.12	-1.07 ± 0.05	15 06 35.41	+27 28 55.6	V	
TN J1513+2417	504 ± 33	83.6 ± 3.7	...	-1.34 ± 0.06	15 13 31.67	-24 17 55.3	N	
TN J1513+1801	534 ± 36	85.3 ± 3.9	...	-1.36 ± 0.06	...	S	< 7.5	4	15 13 55.31	-18 01 07.9	A	
TN J1515+2651	352 ± 44	58.0 ± 2.7	...	-1.34 ± 0.10	...	S	6.5	9	15 15 59.29	-26 51 14.9	A	
TN J1520+1410	478 ± 55	66.0 ± 1.4	...	-1.47 ± 0.09	15 20 53.36	+14 10 45.5	N	
TN J1521+0741	1777 ± 123	105.6 ± 4.5	...	-2.10 ± 0.06	15 21 50.75	+07 41 41.1	N	
TN J1522+2540	464 ± 63	54.1 ± 2.6	...	-1.60 ± 0.11	...	S	8.2	10	15 22 23.28	-25 40 07.1	A	
TN J1524+0642	479 ± 55	82.9 ± 1.7	...	-1.30 ± 0.09	15 24 06.39	+06 42 15.9	N	
TN J1531+3234	522 ± 59	80.6 ± 3.6	...	-1.39 ± 0.09	...	S	4.8	27	15 31 33.59	-32 34 01.7	A	
TN J1547+2218	427 ± 62	72.4 ± 3.3	...	-1.32 ± 0.11	15 47 49.65	-22 18 25.6	N	
TN J1556+2759	612 ± 56	66.4 ± 3.1	...	-1.65 ± 0.08	15 56 43.63	-27 59 43.1	N	
TN J1559+1727	575 ± 71	97.4 ± 4.3	...	-1.32 ± 0.10	15 59 34.08	-17 27 41.6	N	
TN J1604+0248	345 ± 33	46.8 ± 1.0	...	-1.49 ± 0.07	16 04 59.59	-02 48 47.9	N	
TN J1621+2043	539 ± 48	61.4 ± 2.9	...	-1.62 ± 0.08	16 21 06.18	+20 43 36.4	N	
TN J1628+1604	602 ± 44	55.5 ± 2.6	...	-1.77 ± 0.07	16 28 19.16	+16 04 00.0	N	
TN J1634+2222	4714 ± 214	808.2 ± 35.4	...	-1.31 ± 0.05	16 34 49.79	-22 22 12.7	N	
TN J1637+1931	482 ± 40	36.8 ± 0.9	...	-1.83 ± 0.07	...	S	10.8	6	16 37 44.80	-19 31 24.8	A	
TN J1646+1328	608 ± 63	102.5 ± 4.6	...	-1.32 ± 0.09	16 46 51.67	-13 28 49.1	N	
TN J1652+1339	328 ± 33	56.5 ± 1.3	...	-1.31 ± 0.08	16 52 24.29	-13 39 04.3	N	
TN J1653+1156	1181 ± 60	197.0 ± 8.7	...	-1.30 ± 0.05	16 53 52.81	-11 55 59.2	N	
TN J1656+1521	587 ± 79	93.9 ± 4.2	...	-1.36 ± 0.11	16 56 03.77	-15 21 33.3	N	
TN J1701-0101	999 ± 55	172.3 ± 7.6	...	-1.31 ± 0.05	17 01 37.58	-01 01 13.6	N	

Name	S ₃₆₅ mJy	S ₁₄₀₀ mJy	S ₄₈₅₀ mJy	α ₃₆₅ 1400	α ₁₄₀₀ 4850	Str	LAS //	PA °	h m s	δ _{J2000} ° ' "	Pos
TN J1701+0262	356±38	57.1±2.7	...	-1.36±0.09	17 01 54.89	+02 52 13.4	N
TN J1702-0811	436±38	69.9±3.2	...	-1.36±0.07	17 02 04.71	-08 11 07.5	N
TN J1702+2015	322±48	43.4±2.1	...	-1.49±0.12	17 02 23.02	+20 15 34.2	N
TN J1702-0145	808±74	135.6±6.0	...	-1.38±0.08	17 02 43.11	-01 45 54.0	N
TN J1707-1120	425±72	54.2±2.6	...	-1.59±0.13	17 07 51.37	-11 20 21.0	N
TN J1710-0826	445±74	69.2±3.2	...	-1.38±0.13	17 10 20.36	-08 26 40.3	N
TN J1714+2226	285±48	43.3±1.0	...	-1.40±0.42	...	S	1.6	38	17 14 53.42	+22 26 18.5	F
TN J1821+2433	1416±95	227.5±4.7	...	-1.36±0.05	18 21 37.07	+24 33 13.8	N
TN J1855-3430	654±85	87.8±3.8	...	-1.49±0.10	18 55 24.12	-34 30 27.7	N
TN J1905-3520	799±75	131.3±5.4	...	-1.34±0.08	19 05 22.67	-35 20 50.9	N
TN J1932-1931	5676±335	813.6±35.5	...	-1.45±0.05	19 32 07.22	-19 31 49.7	N
TN J1941-1952	1194±103	183.0±3.8	...	-1.40±0.07	...	S	7.9	164	19 41 00.07	-19 52 14.0	A
TN J1953-0541	478±83	59.0±2.8	...	-1.56±0.13	19 53 27.04	-05 41 28.5	N
TN J1954-1207	657±67	102.8±4.6	...	-1.38±0.08	...	S	< 7.0	177	19 54 24.15	-12 07 48.7	A
TN J2007-1316	777±46	115.4±5.2	...	-1.49±0.06	...	S	7.2	174	20 07 53.23	-13 16 43.6	A
TN J2008-1344	798±71	132.3±2.7	...	-1.34±0.07	...	S	8.2	176	20 08 07.48	-13 44 17.8	A
TN J2009-3040	409±65	65.3±3.0	...	-1.36±0.12	...	S	< 7.0	144	20 09 48.13	-30 40 07.0	A
TN J2014-2115	348±33	48.0±1.1	...	-1.47±0.07	...	D	56.4	11	20 14 31.96	-21 14 36.7	A
TN J2021+0839	880±72	145.4±6.4	...	-1.34±0.07	20 21 33.11	+08 39 09.2	N
TN J2028+0811	455±58	74.8±1.6	...	-1.34±0.10	20 28 37.12	+08 11 21.4	N
TN J2028-1934	814±88	134.4±5.8	...	-1.34±0.09	...	S	19.2	169	20 28 48.57	-19 34 03.2	A
TN J2029-0858	396±34	47.2±2.3	...	-1.56±0.07	20 29 49.60	-08 58 48.5	N
TN J2034-2735	510±70	67.4±1.5	...	-1.51±0.10	...	S	< 8.0	163	20 34 15.74	-27 35 45.6	A
TN J2042+1354	281±45	42.0±1.0	...	-1.41±0.12	20 42 07.25	+13 54 16.6	N
TN J2048-0618	881±99	150.7±6.6	...	-1.31±0.09	20 48 06.24	-06 18 40.5	N
TN J2049-2223	823±86	126.1±5.6	...	-1.40±0.08	...	D	95.0	97	20 49 43.04	-22 22 56.3	A
TN J2051-0527	377±79	54.7±1.2	...	-1.44±0.16	20 51 13.39	-05 27 06.1	N
TN J2051+0133	391±33	66.6±3.1	...	-1.39±0.07	20 51 32.31	+01 33 34.9	N
TN J2052-0555	321±35	41.5±0.9	...	-1.52±0.08	20 52 49.63	-05 55 49.1	N
TN J2102+2158	483±52	73.5±1.6	...	-1.40±0.08	21 02 52.80	+21 58 35.1	N
TN J2103-1917	1410±109	228.6±10.1	...	-1.35±0.07	21 03 42.81	-19 17 47.7	N
TN J2106-2405*	2232±150	366.3±15.9	...	-1.34±0.06	21 06 58.42	-24 05 04.2	N
TN J2107+0933	476±56	68.0±3.1	...	-1.45±0.09	21 07 10.61	+09 33 32.5	N
TN J2108+0249	573±41	65.8±3.1	...	-1.61±0.06	21 08 26.75	+02 49 46.3	N
TN J2113+0111	553±68	90.8±4.1	...	-1.34±0.10	21 13 50.43	+01 11 22.3	N
TN J2125+2013	352±45	51.9±2.5	...	-1.40±0.10	21 25 51.74	+20 13 39.8	N
TN J2133+1629	1737±123	283.4±12.4	...	-1.35±0.06	21 33 29.32	+16 29 19.4	N
TN J2134+0946	351±47	48.0±2.3	...	-1.46±0.11	21 34 42.85	+09 46 56.6	N
TN J2136+0947	426±60	66.9±3.1	...	-1.38±0.11	21 36 36.29	+09 47 22.8	N
TN J2147-0645	382±63	57.3±2.7	...	-1.41±0.13	21 47 57.13	-06 45 48.8	N
TN J2155-2109	449±87	77.2±1.6	...	-1.31±0.15	21 55 50.80	-21 09 30.0	N
TN J2158-2516	1225±59	200.9±8.9	...	-1.34±0.05	21 58 11.14	-25 16 01.5	N
TN J2201-2822	703±54	120.5±5.1	...	-1.31±0.07	22 01 22.84	-28 22 14.0	N
TN J2204+1621	381±42	57.3±2.7	...	-1.41±0.09	22 04 14.18	+16 21 43.7	N
TN J2205-3201	430±60	65.7±3.1	...	-1.40±0.11	22 05 27.56	-32 01 23.9	N
TN J2217-1913	321±34	40.5±2.0	...	-1.54±0.09	22 17 28.22	-19 13 21.1	N
TN J2219-1648	301±53	32.0±0.8	...	-1.67±0.13	22 19 40.06	-16 48 03.1	N
TN J222-2817	528±59	91.7±1.9	...	-1.32±0.05	22 32 57.25	-29 17 56.5	N
TN J2237-0242	727±48	125.0±2.6	...	-1.31±0.08	22 37 22.60	-02 42 23.0	N
TN J2239-0429	3607±177	571.4±24.9	...	-1.41±0.05	22 39 32.85	-04 29 33.9	N

Name	S ₃₆₅ mJy	S ₁₄₀₀ mJy	S ₄₈₅₀ mJy	l ₄₀₀ α ₃₆₅	l ₄₀₀ α ₄₈₅₀	Str	LAS //	PA o	h m	s	α _{J2000} o	l /	b /	Pos
TN J2245+0007	297 ± 53	61.6 ± 1.1	...	-1.30 ± 0.13	22	45	44.89	+00 07 11.3	...	N
TN J2251-1634	561 ± 64	60.6 ± 1.3	...	-1.64 ± 0.09	22	51	14.06	-16 34 03.2	...	N
TN J2251-1034	862 ± 72	138.8 ± 5.9	...	-1.36 ± 0.07	22	51	22.01	-10 34 18.0	...	N
TN J2252-1618	397 ± 60	51.6 ± 2.5	...	-1.52 ± 0.12	22	52	20.15	-16 18 14.9	...	N
TN J2253-2156	425 ± 72	59.3 ± 2.8	...	-1.47 ± 0.13	22	53	17.03	-21 56 38.0	...	N
TN J2301+0555	484 ± 62	74.1 ± 3.3	...	-1.40 ± 0.10	23	01	18.11	+05 55 01.0	...	N
TN J2303-0251	405 ± 56	66.5 ± 3.1	...	-1.34 ± 0.11	23	03	55.67	-02 51 08.6	...	N
TN J2310+1358	1497 ± 102	251.9 ± 5.2	...	-1.33 ± 0.05	23	10	52.32	+13 58 20.5	...	N
TN J2312-0040	293 ± 25	45.5 ± 1.0	...	-1.39 ± 0.07	23	12	46.80	-00 40 53.0	...	N
TN J2312-0208	1295 ± 80	194.8 ± 8.6	...	-1.41 ± 0.06	23	12	55.71	-02 08 39.9	...	N
TN J2314+2053	386 ± 27	46.8 ± 2.3	5.9 ± 0.4	-1.57 ± 0.06	-1.67 ± 0.07	S	0.3	129	23	14	56.04	+20 53 37.4	...	Y
TN J2320+1222	1566 ± 93	264.3 ± 5.4	...	-1.32 ± 0.05	23	20	07.79	+12 22 06.6	...	N
TN J2333-1508	504 ± 68	70.2 ± 3.3	...	-1.47 ± 0.11	23	33	06.99	-15 08 12.8	...	N
TN J2335+0634	507 ± 58	84.3 ± 3.8	...	-1.33 ± 0.09	23	35	06.42	+06 34 38.8	...	N
TN J2350-1321	419 ± 35	56.1 ± 1.2	...	-1.50 ± 0.06	23	50	15.92	-13 21 16.0	...	N
TN J2352+0814	498 ± 50	71.0 ± 3.2	...	-1.45 ± 0.08	23	52	10.44	+08 14 50.0	...	N
TN J2352+0450	398 ± 59	60.5 ± 2.8	...	-1.40 ± 0.12	23	52	32.20	+04 50 30.1	...	N
TN J2352-3139	573 ± 87	85.8 ± 3.8	29.0 ± 1.5	-1.41 ± 0.12	-0.87 ± 0.06	T	21.1	170	23	52	46.79	-31 39 36.9	...	Y

† Not a real USS source; see notes

* See notes

Table A. 8. MP sample

Name	S ₄₀₈ mJy	S ₁₄₂₀ mJy	S ₄₈₅₀ mJy	l ₄₀₈ α ₄₀₈	l ₄₀₈ α ₄₈₅₀	Str	LAS //	PA o	h m	s	α _{J2000} o	l /	b /	Pos
MP J0003-3556	2440 ± 80	...	103.0 ± 13.0	00	03	13.11	-35 56 33.8	...	M
MP J0028-5523	1910 ± 80	389 ± 38	86.0 ± 9.0	-1.25 ± 0.05	-1.25 ± 0.05	S	3.7	57	00	28	53.76	-55 23 28.5	...	A
MP J0100-6403	1410 ± 150	247 ± 24	56.0 ± 7.0	-1.40 ± 0.11	-1.30 ± 0.07	S	4.2	100	01	00	32.42	-64 03 13.6	...	A
MP J0103-3225	2390 ± 80	...	93.0 ± 13.0	01	03	17.10	-32 25 53.3	...	M
MP J0114-3302	1590 ± 90	396 ± 39	76.0 ± 12.0	-1.11 ± 0.14	-1.23 ± 0.07	D	22.0	119	01	14	37.06	-33 02 10.2	...	A
MP J0118-6331	1040 ± 90	264 ± 26	50.0 ± 7.0	-1.10 ± 0.09	-1.23 ± 0.07	S	4.1	48	01	18	07.54	-63 31 43.2	...	A
MP J0130-8352	950 ± 50	159 ± 15	23.0 ± 5.0	-1.43 ± 0.11	-1.50 ± 0.09	S	3.2	66	01	30	07.45	-83 52 29.6	...	A
MP J0141-4421	1400 ± 60	295 ± 29	56.0 ± 9.0	-1.25 ± 0.10	-1.30 ± 0.07	D	29.9	95	01	41	13.57	-44 21 10.8	...	A
MP J0141-6941	3986 ± 320	755 ± 75	179.0 ± 11.0	-1.33 ± 0.09	-1.25 ± 0.04	D	16.1	153	01	41	55.18	-69 41 33.1	...	A
MP J0155-8521	830 ± 70	...	38.0 ± 5.0	01	55	16.98	-85 21 07.4	...	M
MP J0202-5425	820 ± 70	186 ± 18	41.0 ± 8.0	-1.19 ± 0.09	-1.21 ± 0.09	D	14.5	5	02	02	56.25	-54 25 13.3	...	A
MP J0211-5146	900 ± 40	160 ± 16	43.0 ± 8.0	-1.38 ± 0.08	-1.23 ± 0.08	S	11.1	50	02	11	44.92	-51 46 47.0	...	A
MP J0249-4145	1100 ± 50	242 ± 24	48.0 ± 9.0	-1.21 ± 0.08	-1.27 ± 0.08	S	8.2	49	02	49	10.08	-41 45 36.3	...	A
MP J0339-4018	3610 ± 140	759 ± 75	174.0 ± 13.0	-1.25 ± 0.09	-1.22 ± 0.03	S	5.6	33	03	39	48.18	-40 18 22.1	...	A
MP J0340-6507	1640 ± 50	383 ± 38	81.0 ± 8.0	-1.17 ± 0.10	-1.22 ± 0.04	D	14.0	18	03	40	44.92	-65 07 07.3	...	A

Table A.3: MP sample

Name	S_{408} mJy	S_{1420} mJy	S_{4850} mJy	α_{408}	α_{1420}	α_{4850}	Str	LAS	PA	h	v	w	δ_{J2000} °	ρ "/	Pos
MP J0446-3305	1910±100	448±44	82.0±12.0	-1.16 ± 0.10	-1.27±0.06	-1.27±0.06	D	55.8	6	04 46 00.21	-83 05 18.3	...	A
MP J0449-5449	906±70	200±20	46.0±8.0	-1.20 ± 0.09	-1.20±0.08	-1.20±0.08	S	4.3	56	04 49 04.66	-54 49 10.1	...	A
MP J0601-3926	2270±320	451±45	97.0±10.0	-1.29 ± 0.08	-1.27±0.07	-1.27±0.07	S	6.2	43	06 01 00.77	-39 26 18.1	...	A
MP J0605-5036	1040±70	358±35	43.0±8.0	-0.85 ± 0.10	-1.29±0.08	-1.29±0.08	D	9.4	105	06 05 47.25	-50 36 41.7	...	A
MP J0618-7340	750±50	...	25.0±6.0	...	-1.37±0.10	-1.37±0.10	06 18 47.54	-73 40 40.8	...	M
MP J0648-7118	1000±50	300±30	42.0±7.0	-0.96 ± 0.09	-1.28±0.07	-1.28±0.07	S	2.5	45	06 48 37.38	-71 18 26.4	...	A
MP J0731-6621	870±40	...	40.0±7.0	...	-1.24±0.07	-1.24±0.07	07 31 47.00	-66 21 30.3	...	M
MP J0839-7359	1450±60	...	69.0±7.0	...	-1.23±0.04	-1.23±0.04	DF	08 39 33.38	-73 59 37.4	...	M
MP J1033-3418	5590±250	...	268.0±22.0	...	-1.23±0.04	-1.23±0.04	10 33 13.04	-34 18 48.4	...	M
MP J1119-3631	2440±70	542±54	113.0±14.0	-1.21 ± 0.10	-1.24±0.05	-1.24±0.05	S	4.8	166	11 19 21.81	-36 31 39.5	...	A
MP J1208-3403	4650±210	...	198.0±18.0	...	-1.28±0.04	-1.28±0.04	12 08 39.17	-34 03 10.7	...	M
MP J1250-4026	6030±180	...	299.0±18.0	...	-1.21±0.03	-1.21±0.03	12 50 05.68	-40 26 28.7	...	M
MP J1250-4119	1350±60	167±16	63.0±9.0	-1.67 ± 0.09	-1.24±0.06	-1.24±0.06	S	7.4	123	12 50 46.49	-41 19 35.7	...	A
MP J1355-7806	1690±90	...	44.0±6.0	...	-1.47±0.06	-1.47±0.06	DF	13 55 35.57	-78 06 43.7	...	M
MP J1657-7423	1080±50	...	50.0±7.0	...	-1.24±0.06	-1.24±0.06	16 57 44.73	-74 23 09.3	...	M
MP J1710-7343	910±70	47±4	26.0±6.0	-2.37 ± 0.10	-1.44±0.10	-1.44±0.10	S	...	149	17 10 17.73	-73 43 19.1	...	A
MP J1733-8342	4630±210	...	198.0±12.0	...	-1.27±0.03	-1.27±0.03	17 33 55.38	-83 42 48.0	...	M
MP J1755-6916	1580±90	486±48	71.0±7.0	-0.94 ± 0.09	-1.25±0.05	-1.25±0.05	D	0.5	90	17 55 30.23	-69 16 49.8	...	A
MP J1758-6738	3090±140	478±47	112.0±9.0	-1.47 ± 0.09	-1.33±0.04	-1.33±0.04	D	31.2	119	17 58 51.25	-67 38 30.5	...	M
MP J1821-7457	2190±110	...	77.0±7.0	...	-1.35±0.04	-1.35±0.04	18 21 59.83	-74 57 47.5	...	M
MP J1909-7755	900±70	182±18	41.0±6.0	-1.28 ± 0.09	-1.25±0.07	-1.25±0.07	D	27.9	81	19 09 57.19	-77 56 01.5	...	A
MP J1912-5349	1110±70	441±44	56.0±8.0	-0.74 ± 0.09	-1.21±0.06	-1.21±0.06	D	17.0	45	19 12 20.77	-53 49 01.3	...	A
MP J1921-6217	2110±40	400±40	79.0±8.0	-1.33 ± 0.08	-1.33±0.04	-1.33±0.04	S	3.4	113	19 21 03.06	-62 17 25.2	...	A
MP J1921-5431	4590±210	...	66.0±8.0	...	-1.71±0.05	-1.71±0.05	19 21 52.92	-54 31 51.8	...	M
MP J1929-3732	3260±110	806±80	135.0±12.0	-1.12 ± 0.09	-1.29±0.04	-1.29±0.04	S	3.7	14	19 29 08.51	-37 32 48.8	...	A
MP J1940-4236	1340±70	...	64.0±9.0	...	-1.23±0.06	-1.23±0.06	19 40 58.04	-42 36 49.5	...	M
MP J1942-5553	2120±110	385±38	74.0±8.0	-1.37 ± 0.08	-1.36±0.05	-1.36±0.05	S	6.7	176	19 42 06.97	-55 53 32.6	...	A
MP J1943-4030	4400±140	...	163.0±12.0	...	-1.36±0.03	-1.36±0.03	DF	19 43 52.33	-40 30 10.9	...	M
MP J1953-4852	860±30	143±14	42.0±8.0	-1.44 ± 0.09	-1.22±0.08	-1.22±0.08	S	4.7	115	19 53 39.88	-48 52 13.8	...	A
MP J2002-5252	2730±130	411±41	76.0±9.0	-1.52 ± 0.09	-1.45±0.05	-1.45±0.05	S	4.5	29	20 02 22.89	-52 52 51.8	...	A
MP J2003-8340	1600±80	253±25	67.0±6.0	-1.48 ± 0.09	-1.28±0.04	-1.28±0.04	S	3.5	106	20 03 30.73	-83 41 00.0	...	A
MP J2017-5747	1860±160	287±28	79.0±8.0	-1.50 ± 0.08	-1.28±0.05	-1.28±0.05	S	11.8	28	20 17 48.11	-57 47 11.9	...	A
MP J2045-6018	11160±340	2105±210	447.0±24.0	-1.34 ± 0.09	-1.30±0.02	-1.30±0.02	D	41.6	44	20 45 21.82	-60 18 51.5	...	A
MP J2048-5750	2810±130	494±49	137.0±10.0	-1.39 ± 0.09	-1.22±0.03	-1.22±0.03	S	5.7	18	20 48 36.64	-57 50 47.6	...	A
MP J2126-5439	1180±80	282±28	57.0±8.0	-1.15 ± 0.12	-1.22±0.06	-1.22±0.06	D	17.1	147	21 26 53.65	-54 39 36.0	...	A
MP J2204-5831	900±70	148±14	44.0±8.0	-1.45 ± 0.08	-1.22±0.08	-1.22±0.08	S	10.5	11	22 04 05.48	-58 31 38.3	...	A
MP J2222-4723	910±70	509±50	45.0±9.0	-0.47 ± 0.09	-1.21±0.09	-1.21±0.09	D	9.1	148	22 22 53.71	-47 23 12.1	...	A
MP J2226-7654	900±60	203±20	35.0±6.0	-1.19 ± 0.09	-1.31±0.07	-1.31±0.07	S	4.1	107	22 26 56.90	-76 54 48.0	...	A
MP J2229-3824	8210±210	...	412.0±23.0	...	-1.21±0.02	-1.21±0.02	22 29 46.94	-38 24 02.9	...	M
MP J2308-6423	1750±90	301±30	39.0±7.0	-1.41 ± 0.09	-1.54±0.08	-1.54±0.08	D	14.3	7	23 08 45.21	-64 23 33.3	...	A
MP J2313-4243	1390±60	...	58.0±9.0	...	-1.28±0.07	-1.28±0.07	23 13 58.76	-42 43 38.1	...	M
MP J2352-6154	1450±40	311±31	69.0±8.0	-1.23 ± 0.10	-1.23±0.05	-1.23±0.05	D	56.1	148	23 52 55.52	-61 54 06.9	...	A
MP J2357-3445	8700±350	...	117.0±14.0	...	-1.74±0.05	-1.74±0.05	23 57 01.09	-34 45 38.9	...	M

Table A.4: WN POSS identifications

Name	S_{1400} mJy	α_{325}^{1400}	LAS "	LR ^a
WN J0029+3439	40.9	-1.34	12.8	4
WN J0121+4305	50.8	-1.39	...	7
WN J0315+3757	13.3	-1.35	1.7	15
WN J0559+6926	12.9	-1.31	0.3	5
WN J0641+4325	15.6	-1.57	...	196
WN J0725+4123	35.5	-1.39	8.3	183
WN J0756+5010	29.9	-1.31	1.7	127
WN J0830+3018	13.9	-1.41	3.5	27
WN J0835+3439	19.1	-1.38	58.0	25
WN J0923+4602	12.1	-1.49	21.6	17
WN J0952+5153	16.1	-1.76	2.7	194
WN J0955+6023	10.9	-1.54	3.1	1
WN J1014+7407	21.8	-1.41	2.2	148
WN J1026+2943	12.0	-1.31	11.9	136
WN J1030+5415	29.2	-1.39	6.1	16
WN J1052+4826	154.2	-1.31	10.0	38
WN J1124+3228	38.9	-1.31	5.7	101
WN J1130+4911	18.9	-1.34	37.0	19
WN J1141+6924	11.8	-1.32	...	1
WN J1148+5116	20.5	-1.35	6.7	1
WN J1152+3732	17.1	-2.18	15.0	160
WN J1232+4621	19.8	-1.30	12.5	43
WN J1258+5041	28.8	-1.42	44.9	4
WN J1259+3121	34.0	-1.41	20.6	0
WN J1330+6505	10.5	-1.34	1.8	21
WN J1353+3336	15.9	-1.31	...	3
WN J1400+4348	20.2	-1.49	6.4	29
WN J1403+3109	45.7	-1.35	11.0	148
WN J1410+4615	14.2	-1.36	4.4	42
WN J1440+3707	16.7	-1.76	7.4	182
WN J1459+4947	18.7	-1.53	3.0	47
WN J1558+7028	15.7	-1.36	2.1	3
WN J1624+4202	11.0	-1.31	24.4	182
WN J1628+3932	368.1	-1.36	48.8	0
WN J1717+3828	35.8	-1.60	33.6	141
WN J1752+2949	16.9	-1.42	3.2	3
WN J1801+3336	11.6	-1.69	2.5	2
WN J1815+3656	17.6	-1.34	1.6	195
WN J1819+6213	12.7	-1.45	1.6	123
WN J1852+5711	53.4	-1.36	...	145
WN J1927+6436	80.3	-1.44	20.1	6
WN J1944+6552	147.2	-1.53	1.8	147
WN J2146+3330	10.8	-1.56	...	5
WN J2147+3137	25.4	-1.46	...	32
WN J2313+3842	11.3	-1.50	...	0
WN J2313+4053	40.2	-1.42	1.5	36

^a Likelihood Ratio, see text**Table A.5: TN POSS identifications**

Name	S_{1400} mJy	α_{365}^{1400}	LAS "	LR ^a
TN J0244+0327	84.8	-1.38	...	7
TN J0245+2700	54.0	-1.47	...	31
TN J0250+0130	39.1	-1.45	...	15
TN J0256-2717	177.9	-1.32	...	127
TN J0301+0155	402.7	-1.70	...	21
TN J0433+0717	33.1	-1.44	...	30
TN J0443-1212	56.8	-1.47	20.2	162
TN J0510-1838	641.3	-1.76	36.1	0
TN J0729+2436	68.9	-2.03	19.4	129
TN J0812+0915	43.4	-1.38	...	38
TN J0818-0741	59.3	-1.38	...	97
TN J0958-1103	70.6	-1.35	...	182
TN J1043+2404	52.0	-1.59	3.7	168
TN J1053-1518	63.7	-1.33	...	2
TN J1117-1409	134.5	-1.31	...	128
TN J1220+0604	65.1	-1.50	...	189
TN J1239+1005	79.3	-1.75	...	181
TN J1245-1127	88.0	-1.32	...	146
TN J1326-2330	83.2	-1.37	...	190
TN J1408-0855	114.3	-1.34	...	161
TN J1418-2256	82.0	-1.38	7.6	85
TN J1513-2417	83.6	-1.34	...	3
TN J1521+0741	105.6	-2.10	...	0
TN J1531-3234	80.6	-1.39	4.8	173
TN J1547-2218	72.4	-1.32	...	7
TN J1556-2759	66.4	-1.65	...	9
TN J1628+1604	55.5	-1.77	...	154
TN J1646-1328	102.5	-1.32	...	120
TN J1701+0252	57.1	-1.36	...	19
TN J1707-1120	54.2	-1.53	...	86
TN J1710-0826	69.2	-1.38	...	9
TN J1953-0541	59.0	-1.56	...	71
TN J2028+0811	74.8	-1.34	...	33
TN J2155-2109	77.2	-1.31	...	185
TN J2335+0634	84.3	-1.33	...	189

^a Likelihood Ratio, see text**Table A.6: MP UKST identifications**

Name	S_{408} mJy	α_{408}^{4850}	LAS "	LR ^a
MP J0003-3556	2440	-1.28	...	0
MP J0103-3225	2290	-1.29	...	88
MP J0618-7340	750	-1.37	...	8
MP J1033-3418	5590	-1.23	...	82
MP J1250-4026	1350	-1.24	7.4	131
MP J1921-5431	4590	-1.71	...	0
MP J1943-4030	4400	-1.36	...	0
MP J2313-4243	1390	-1.28	...	96
MP J2357-3445	8700	-1.74	...	0

^a Likelihood Ratio, see text

Table A.7: WN identifications from the literature

Name	z	R [mag]	F_X^a	Identification	Reference
WN J0633+4653	...	23.6	...	4C +46.12	Chambers et al. (1996a)
WN J0648+4309	...	23.0	...	B3 0644+432	Wieringa & Katgert (1992)
WN J0658+4444	...	23.4	...	B3 0654+448	Wieringa & Katgert (1992)
WN J0717+4611	1.462	21.6	...	B3 0714+462	Chapter 7
WN J0725+4123	0.1137	1RXS J072600.0+4	Voges et al. (1999)
WN J0923+4602	0.0242	1WGA J0923.1+460	White, Giommi & Angelini (1994)
WN J0952+5153	0.214	...	0.2413	ZwCl 0949.6+5207	Voges et al. (1999)
WN J1148+5116	0.0508	1RXS J114802.7+5	Voges et al. (1999)
WN J1152+3732	0.0192	1WGA J1152.5+373	White, Giommi & Angelini (1994)
WN J1259+3121	...	16.2	...	NGP9 F323-0140639	Odewahn & Aldering (1996)
WN J1332+3009	...	19.8	...	NGP9 F324-0235590	Odewahn & Aldering (1996)
WN J1352+4259	...	21.7	...	4C +43.31	Vigotti et al. (1989)
WN J1359+7447	0.07485	1RXS J135916.0+7	Voges et al. (1999)
WN J1400+4348	...	8.2	...	HD122441	SIMBAD
WN J1410+4615	SHK 010	Shakhbazian (1973)
WN J1436+6319	4.261	24.1	...	4C +63.20	Lacy et al. (1994)
WN J1440+3707	0.07944	1RXS J144005.4+3	Voges et al. (1999)
WN J1628+3932	0.031	13.1	4.5	NGC 6166	Zabludoff et al. (1993)
WN J1736+6502	...	22.2	...	8C 1736+650	Lacy et al. (1993)
WN J1829+6913	0.05765	1RXS J182903.8+6	Voges et al. (1999)
WN J1852+5711	0.1466	1RXS J185209.4+5	Voges et al. (1999)
WN J1944+6552	0.1118	1RXS J194423.1+6	Voges et al. (1999)
WN J2319+4251	0.1255	1RXS J231947.4+4	Voges et al. (1999)

^a F_X is the number of X-ray counts s^{-1} as listed in the cited catalogs.

Table A.8: TN identifications from the literature

Name	z	R [mag]	F_X^a	Identification	Reference
TN J0055+2624	0.1971	ABELL 85	Giovannini, Tordi & Feretti (1999)
TN J0102-2152	0.0604	ABELL 133	Komissarov & Gubanov (1994)
TN J0245+2700	0.0782	1RXS J024521.0+2	Bade et al. (1998)
TN J0256-2717	0.480	19.2	...	MRC 0254-27	McCarthy et al. (1996)
TN J0301+0155	0.170	...	0.2053	ZwCl 0258.9+0142	Crawford et al. (1995)
TN J0408-2418	2.440	22.7	...	MRC 0406-244	McCarthy et al. (1996)
TN J0510-1838	...	19.5	0.00314	1RXS J051032.4-1	Voges et al. (1999)
TN J0630-2834	0.00314	1WGA J0630.8-283	White, Giommi & Angelini (1994)
TN J0729+2436	0.1752	1RXS J072927.4+2	Voges et al. (1999)
TN J0936-2243	1.339	23.0	...	3C 222	Heckman et al. (1994)
TN J0958-1103	0.153	...	1.64	ABELL 0907	McCarthy et al. (1996)
TN J1521+0742	0.045	14.5	1.64	NGC 5920	Komissarov & Gubanov (1994)
TN J2106-2405	2.491	22.7	...	MRC 2104-242	McCarthy et al. (1996)
TN J2239-0429	...	18.8	...	4C -04.85	Röttgering et al. (1995a)
TN J2320+1222	...	22.0	...	MRC 2317+120	Röttgering et al. (1995a)

^a F_X is the number of X-ray counts s^{-1} as listed in the cited catalogs.

Table A.9: MP identifications from the literature

Name	z	R [mag]	F_X^a	Identification	Reference
MP J0003-3556	0.0497	13.2	0.5206	ABELL 2717	Collins et al. (1995)
MP J0103-3225	...	19.0	...	IRAS F01009-3241	Condon et al. (1995)
MP J1250-4026	0.000595	1RXP J125006-402	Voges et al. (1999)
MP J1943-4030	...	17.3	...	ABELL 3646	Abell et al. (1989)
MP J2313-4243	0.0564	14.6	2.024	ABELL S1101	Stoeke et al. (1991)
MP J2357-3445	0.0490	13.7	2.27	ABELL 4059	Postman & Lauer (1995)

^a F_X is the number of X-ray counts s^{-1} as listed in the cited catalogs.

Appendix B Radio Maps

FITS-files of the VLA and ATCA radio maps are available from:
<ftp://cdsarc.u-strasbg.fr/cats/J/A+AS/143/303/>

Postscript figures are available from:
<http://www.edpsciences.fr/articles/astro/full/2000/08/ds1811/node10.html>

Appendix C Radio Spectra

Postscript figures are available from:
<http://www.edpsciences.fr/articles/astro/full/2000/08/ds1811/node10.html>

Optical and Near-IR Imaging of Ultra Steep Spectrum Radio Sources

C. De Breuck, W. van Breugel, S. A. Stanford, H. Röttgering, G. Miley,
& D. Stern, in preparation

Abstract

We present 83 optical R - or I -band and 86 near-IR K -band images of ultra steep spectrum (USS) radio sources. The fraction of sources identified in the optical images is $\sim 50\%$ ($R \lesssim 24$), while in the near-IR images, $>94\%$ are detected at $K \lesssim 22$. The mean K -magnitude is $\bar{K} = 19.26$ within a $2''$ diameter aperture. The distribution of $R - K$ colors indicates that at least $1/3$ of the objects observed are extremely red objects (EROs, $R - K > 5$). The major axis of the identifications in K -band are preferentially oriented along the radio axis and are mostly compact, resembling those of previously observed $z < 3$ radio galaxies.

The 22 sources with spectroscopic redshifts and K -band magnitudes obey the $K - z$ found from previous radio samples, but with a larger scatter. We argue that this scatter is due to a dependence of K -magnitude on the radio power, with the highest radio power sources inhabiting the most massive host galaxies. We present a composite $K - z$ diagram of radio-loud and radio-quiet galaxies, selected from the HDF-North and the Hawaii surveys. Out to $z \lesssim 1$, the radio-loud galaxies trace the bright envelope of the radio quiet galaxies, while at $z \gtrsim 1$, the radio-loud galaxies are $\gtrsim 2$ magnitudes brighter. This strongly suggests that radio galaxies pinpoint the most massive systems out to the highest known redshifts, probably due to the mutual correlation of the mass of the galaxy and the radio power on the mass of the central black hole.

3.1 Introduction

High redshift radio galaxies (HzRGs) provide some of the best opportunities to study the spatially resolved emission in galaxies out the highest redshifts ($z = 5.19$; Chapter 5). Although they are no longer the only class of galaxies studied at cosmological redshifts (e.g., Steidel et al., 1999), they are still amongst the most massive galaxies at these redshifts. The best evidence that HzRGs are indeed massive galaxies comes from observations of the host galaxies of powerful radio sources at lower redshift ($z \lesssim 1$), which show them to be uniquely identified with massive ellipticals (e.g., Best, Longair & Röttgering, 1998a; McLure & Dunlop, 2000), and from the tight correlation in the Hubble $K - z$ diagram for powerful radio sources out to $z \sim 5$ (e.g., Eales et al., 1997; van Breugel et al., 1998; Lacy, Bunker, & Ridgway, 2000). Because HzRGs are more luminous and larger than field galaxies at similar redshifts, detailed studies of their optical and near-IR morphologies can be carried out. For example, deep K -band imaging by van Breugel et al. (1998; hereafter vB98) has indicated a morphological evolution in the host galaxies of the most powerful radio sources: at $z \gtrsim 3$, they display faint, large-scale morphologies, often surrounded by multiple components aligned with the radio source, while at $z \lesssim 3$, they appear as a single, compact structure without radio-aligned components. In the rest-frame UV, this alignment is even more pronounced, and it occurs in the vast majority of $z \gtrsim 0.7$ powerful radio galaxies (e.g., Chambers, Miley, & van Breugel, 1987). A variety of physical mechanisms has been proposed to explain the nature of this alignment effect. The most viable ones include (i) star-formation induced by shocks associated with the radio jet propagation outward from the central AGN (e.g., Dey et al., 1997b; Bicknell et al., 2000), (ii) scattering of light from an obscured nucleus by dust or electrons (e.g., Cimatti et al., 1993), and (iii) nebular continuum emission from warm line emitting clouds (e.g., Dickson et al., 1995). High-resolution optical and near-IR HST observations of HzRGs indicate that the aligned light is probably a mixture of these proposed components (Pentericci et al., 1999a, 2000b).

To examine the influence of radio sources on the galaxy formation process, it is important to obtain a large sample of HzRGs, covering a range in redshift and radio power. Despite several intensive search campaigns during the last two decades, the number of known HzRGs is still quite small: fewer than 20 radio galaxies are known with $z > 3$. Further, because the HzRGs were discovered from flux limited radio samples, there is a strong artificial dependence of radio power on redshift in the samples of known HzRGs. To find more radio galaxies at the highest redshifts and with lower radio power, we constructed a sample of ultra steep spectrum (USS, $\alpha < -1.30$; $S \propto \nu^\alpha$) radio sources drawn from new radio surveys that reach flux densities levels more than an order of magnitude fainter than before. USS sources have been successfully used for two decades to find HzRGs (Blumenthal & Miley, 1979). This technique mainly makes use of a “radio k -correction” effect: at higher redshift, an increasingly steeper part of the generally concave radio spectrum shifts to the fixed observing frequencies of the large radio surveys.

Table 3.1: Observing Runs

Run	UT Date	Telescope	Instrument	photometric?	
L3	1996 apr 19	Lick 3m	Kast	no	1''8
L6	1996 nov 11	Lick 3m	Kast	yes	1''3
L7	1997 jan 7-9	Lick 3m	Kast	no	2''-3''
E2	1997 mar 5-6	ESO 3.6m	EFO SC1	yes	1''3
E3	1997 apr 9-11	ESO 3.6m	EFO SC1	yes	1''4
W4	1997 may 1-2	WHT 4.2m	Prime-focus	yes	0''9
L8	1997 may 6-7	Lick 3m	Kast	yes	1''7
L9	1997 jun 6-8	Lick 3m	Kast	yes	1''1-2''
L10	1997 aug 8	Lick 3m	Kast	no	1''2-1''5
K4	1997 sep 10-11	Keck 10m	NIRC	yes	0''4-0''5
C1	1998 feb 16	CTIO 4m	CIRIM	yes	0''5
K7	1998 apr 18-19	Keck 10m	NIRC	yes	0''4-0''6
L13	1998 aug 23-24	Lick 3m	Kast	yes	1''3
C2	1998 sep 1-4	CTIO 4m	CIRIM	part	0''6-1''
L15	1998 oct 18-19	Lick 3m	Kast	part	1''0-1''3
K9	1998 dec 19-20	Keck 10m	LRIS	yes	0''7
W5	1999 may 17-19	WHT 4.2m	Prime-focus	yes	1''0
K10	1999 may 22-23	Keck 10m	NIRC	yes	0''3-0''4
K12	1999 sep 23-24	Keck 10m	NIRC	no ^a	0''4-0''7
P1	1999 oct 13	Palomar 60''	CCD13	yes	0''9
K13	2000 jan 30	Keck 10m	NIRC	yes	0''6

^a Affected by instrumental problems, see §3.2.1.1

In Chapter 2, we defined our sample based on several new, large radio surveys. We also presented VLA and ATCA radio images of 410 sources, which provide morphological information and the accurate positions needed to identify the optical or near-IR counterparts. In this chapter, we present the optical and/or near-IR imaging of a sub-sample of 128 sources. We shall use the near-IR magnitudes to obtain redshift estimates based on the Hubble $K - z$ diagram. In Chapter 4, we present optical spectroscopy of 46 sources from this imaged sub-sample, including 34 sources with spectroscopic redshifts.

The layout of this Chapter is as follows. In §3.2, we describe the optical and near-IR observations and data reduction, paying special attention to the astrometry. We present the results and discuss the morphologies of the near-IR identifications and the Hubble $K - z$ diagram in §3.3. We discuss the expected redshift distribution from our sample in §3.4. Our conclusions are given in §3.5.

3.2 Observations and Data Reduction

We obtained the optical and near-IR images described in this chapter at five different observatories between 1996 April and 2000 January. Table 3.1 gives an overview of the 21 successful imaging observing sessions. We use a consecutive numbering scheme for each session in the project, counting also the runs where we did not obtain any data, or only spectroscopic data (see Chapter 4). Table 3.2 gives a journal of the observations, and Table 3.3 gives an overview of the instrumental setups.

Table 3.2: Journal of imaging observations

Source	z	Session	Band	$t_{exp}(s)$	Source	z	Session	Band	$t_{exp}(s)$
WN J0000+4054	...	K12	K	780	WN J1123+3141	3.217	L3	r_S	2700
WN J0007+3641	...	L13	r_S	600	K10	K_S	1920
WN J0034+4142	...	L13	r_S	3000	TN J1146-1052	...	W5	R	600
WN J0040+3857	2.605	K12	K	1020	TN J1148-0901	...	W5	R	600
MP J0100-6403	...	L15	r_S	2700	TN J1151-3013	...	E3	R	900
TN J0102-1055	...	C2	K	1800	K10	K_S	1920
MP J0114-3302	...	K12	K	780	TN J1159-1629	...	E3	R	600
MP J0117+3715	...	C2	K	1920	WN J1224+5436	...	W5	R	600
WN J0121+1320	3.516	K12	K	840	K10	K	1920
MP J0130-8352	...	L7	r_S	1800	WN J1242+3915	2.131	L7	r_S	3840
WN J0137+3250	...	K4	K_S	3840	K7	K_S	960
MP J0141-6941	...	C2	K	1920	WN J1258+3212	...	L9	r_S	3300
WN J0155+8036	...	L15	r_S	3600	K13	K'	1260
TN J0201-1302	...	K12	K	1920	WN J1314+3649	...	W4	R	600
MP J0202-5425	...	L15	r_S	2100	K7	K	960
TN J0205+2242	3.506	K12	K	1560	WN J1333+3037	1.213	W4	R	600
TN J0218+0844	...	C2	K	3840	TN J1338-1942	4.11	E3	R	600
WN J0231+3600	3.079	L7	r_S	1980	K7	K	3840
MP J0249-4145	...	K4	K_S	1920	WN J1355+3848	...	W4	R	600
WN J0303+3733	2.506	L10	r_S	900	K10	K_S	1920
WN J0305+3525	...	K9	I	720	WN J1420+6735	...	W5	R	600
WN J0310+3644	...	C2	K	840	K10	K	1920
MP J0340-6507	...	L15	r_S	3000	WN J1421+3103	...	W5	R	600
WN J0346+3039	...	K9	I	960	TN J1428+2425	...	K10	K_S	1920
WN J0359+3000	...	K12	K	2280	WN J1433+3044	...	W4	R	600
TN J0402+1007	...	K12	K	900	K7	K_S	960
TN J0410+1019	...	C2	K	960	WN J1450+3534	...	W5	R	600
MP J0449-5449	...	K12	K_S	600	K10	K	1920
TN J0452-1737	2.256	L13	r_S	3000	WN J1500+3613	...	L9	r_S	1800
TN J0517-0641	...	K12	K_S	540	TN J1506+2728	...	K10	K_S	1920
WN J0528+6549	...	L7	r_S	2280	WN J1525+3010	...	W4	R	600
WN J0538+7348	...	K4	K_S	1920	K7	K	1020
TN J0552-0433	...	K12	K	1320	WN J1529+3454	...	W5	R	600
MP J0601-3926	...	C2	K	720	WN J1543+3512	0.703	W4	R	600
WN J0610+6611	...	L7	r_S	1800	WN J1546+3005	...	W4	R	600
WN J0617+5012	3.153	K4	K_S	960	WN J1546+3935	...	W4	R	600
WN J0633+4653	...	E2	R	600	WN J1550+3830	...	L9	r_S	1200
WN J0716+5107	...	K13	K	1920	K10	K	1920
WN J0717+4611	1.462	L15	r_S	3000	WN J1555+4011	...	K10	K_S	960
WN J0741+5611	...	K13	K	1920	WN J1604+5505	...	K10	K_S	1920
WN J0747+3654	2.092	E2	R	600	TN J1634-2222	...	E3	R	60
WN J0813+4828	1.274	C1	K_S	3840	WN J1645+4413	...	K10	K_S	960
TN J0837-1053	...	K13	K'	1920	WN J1718+5823	...	L13	r_S	3600
TN J0855-0000	...	L6	r_S	2550	WN J1731+4640	...	K10	K_S	1860
TN J0856-1510	...	K4	K_S	2880	WN J1731+4654	...	L10	r_S	900
TN J0910-2228	...	L15	r_S	3600	K10	K_S	840
TN J0920-0712	2.760	L15	r_S	3300	MP J1755-6916	2.551	C2	K	2880
TN J0924-2201	5.19	K13	K'	1920	MP J1758-6738	2.026	C2	K	1560
TN J0936-2243	1.479	L6	r_S	900	WN J1802+3948	...	L13	r_S	3600
TN J0941-1628	1.644	L7	r_S	2400	WN J1804+3048	...	K10	K_S	960
WN J0948+6305	...	K7	K	1500	WN J1818+3852	...	K10	K	1920
WN J1015+3038	0.54	L7	r_S	900	WN J1818+6144	...	K10	K	960
TN J1026-2116	...	K13	K'	1260	WN J1829+5945	...	L13	r_S	660
TN J1033-1339	2.425	L7	r_S	2700	WN J1830+6422	...	L13	r_S	3900
TN J1043-1718	...	K7	K_S	1920	WN J1836+5210	...	K10	K_S	960
TN J1049-1258	...	E2	R	600	WN J1859+5900	...	W5	R	600
WN J1053+5424	...	E2	R	900	WN J1859+5416	...	W5	R	600
WN J1055+3047	...	E3	R	900	WN J1911+6342	3.590	K10	K	960
TN J1102-1651	2.111	K13	K'	3360	WN J1917+6635	...	K10	K	960
TN J1112-2948	3.09	E3	R	900	MP J1929-3732	0.748	C2	K	2880
WN J1115+5016	2.54	E3	R	300	TN J1941-1952	...	K12	K	840
TN J1123-2154	4.109	E3	R	900	TN J1954-1207	...	K10	K	960
...	...	K7	K_S	960	MP J2003-8340	1.169	C2	K	3840
...	...	K7	K_S	960	TN J2007-1316	...	K12	K_S	780
...	...	K7	K_S	960	TN J2008-1344	...	P1	R	900
...	...	K7	K_S	960	TN J2009-3040	...	K10	K	1440
...	...	K7	K_S	960	TN J2028-1934	...	P1	R	900
...	...	K7	K_S	960	K12	K_S	1320
...	...	K7	K_S	960	WN J2044+7044	...	L15	r_S	3300
...	...	K7	K_S	960	K10	K_S	1560
...	...	K7	K_S	960	MP J2045-6018	1.464	C2	K	2460
...	...	K7	K_S	960	MP J2048-5750	1.262	C2	K	2880
...	...	K7	K_S	960	MP J2126-5439	...	C2	K	2880
...	...	K7	K_S	960	WN J2213+3411	...	L13	r_S	3900
...	...	K7	K_S	960	K12	K_S	1560
...	...	K7	K_S	960	WN J2221+3800	...	P1	R	900
...	...	K7	K_S	960	WN J2222+3305	...	L15	r_S	600
...	...	K7	K_S	960	MP J2226-7654	...	C2	K	1680
...	...	K7	K_S	960	WN J2250+4131	...	K12	K	1560
...	...	K7	K_S	960	WN J2313+4053	2.99	L15	r_S	120
...	...	K7	K_S	960	WN J2313+4253	...	K12	K	1080
...	...	K7	K_S	960	TN J2314+2053	...	L10	r_S	840
...	...	K7	K_S	960	K12	K_S	1800
...	...	K7	K_S	960	MP J2352-6154	...	C2	K	3840

Table 3.3: Observational setup

Telescope	Instrument	Filter	FOV ^a	Pixel scale
Keck	LRIS	<i>I</i>	6'×7.8'	0''.212 ± 0''.001
WHT	PFIP+EEV42	<i>R</i>	8'×16'	0''.236 ± 0''.001
	PFIP+LOR2	<i>R</i>	9'×9'	0''.2631 ± 0''.0006
ESO 3.6m	EFOSC1	<i>R</i>	5'.2×5'.2	0''.6075 ± 0''.0007
Lick 3m	Kast	<i>r_S</i>	145''×145''	0''.789 ± 0''.0035
Palomar 60''	CCD13	<i>R</i>	12'.9×12'.9	0''.3786 ± 0''.0005
Keck	NIRC	<i>K, K_S, K'</i>	38''.4×38''.4	0''.1516 ± 0''.0016
CTIO 4m	CIRIM	<i>K, K_S</i>	54''×54''	0''.219 ± 0''.007

^a Field of view of a single exposure; the combined images might be significantly larger due to the dithering applied.

3.2.1 Optical Imaging

Observations

Lick 3m We used the Kast imaging spectrograph (Miller & Stone, 1994) at the Lick Observatory Shane 3m telescope on Mount Hamilton to obtain images in the “Spinrad night-sky” filter. This yields red magnitudes in the *r_S* system, which can be related to commonly used photometric systems as determined by Djorgovski (1985)¹. The field of view of Kast is ∼145'' square, but there is substantial circular vignetting in all corners. To enlarge the field of view and reduce the chance that the object falls on a bad pixel on the CCD, we dithered the individual exposures by ∼15''. We limited the exposure times of the individual exposures to 3–5 minutes to avoid extensive saturation of bright stars in the field.

ESO 3.6m To identify the radio source for spectroscopic observations, we took 10–15 minute images with the ESO faint object spectrograph and camera (EFOSC1; Savaglio, Benetti, & Pasquini, 1997) on the ESO 3.6m telescope at La Silla. If an object was not detected in 15 min, we did not attempt to obtain a spectrum. We observed a large number of these optical “blank fields” in *K*– band with NIRC on Keck II (see §3.2.2.1).

¹The transformation from Spinrad night-sky *r_s* into Johnson *VR* is $(r_S - R) = -0.004 - 0.072(V - R) + 0.073(V - R)^2$.

WHT On two occasions, we used the prime focus imaging platform (PFIP; Carter & Bridges, 1995) at the William Herschel Telescope at La Palma to obtain deep R-band images of USS sources. During the 1997 May run, we used the LORAL CCD, while during the 1999 May run, we used the EEV12 CCD. This resulted in slightly different pixel scales and fields of view (see Table 3.3).

Keck We obtained I -band images of 3 USS sources with the Low Resolution Imaging Spectrometer (LRIS; Oke et al., 1995) on the Keck II telescope on Mauna Kea. The main use of these deep images was to determine accurate positions and offsets from nearby brighter stars ($I \lesssim 18$) to set up the spectroscopic observations during the same observing session.

Data Reduction

For all the imaging data, we performed standard data reductions consisting of over-scan bias correction, and flat fielding using a median sky flat, constructed for each individual night from the non-saturated science exposures.

To correct for the circular edges of the Lick images before registering them, we constructed a filter image from the flat-field frame, filtering out all pixels at $\lesssim 96\%$ of the median central flat-field value. Failure to do so would lead to a strongly increased noise pattern in the outer regions of the registered image. To register the dithered Lick images, we first determined the relative position-shifts between the images using the task “registar” from the IRAF DIMSUM² package. Finally, we combined all individual image frames using integer pixels shifts, which avoids degrading of the resolution due to re-sampling of the pixels.

We calibrated the images using observations from several standard stars obtained during the same night. After including the zero-point uncertainty and the fitting uncertainties given by the `phot` routine, we estimate that the photometric scale is accurate up to ~ 0.2 magnitude. We used the IRAF task `phot` to determine fixed aperture magnitudes. We used a $4''$ diameter aperture for the optical images, because the seeing was often not sufficiently good to justify using a smaller aperture. For images obtained under non-photometric conditions, we used a value of the photometric zero-point determined from previous observations; these magnitudes (indicated with † in Table 3.4) should be considered as indicative only.

3.2.2 Near-IR Imaging

Observations

We used near-IR cameras at the Keck and CTIO observatories to observe sources in both the northern and southern hemispheres. At each observatory, we employed

²DIMSUM is the Deep Infrared Mosaicing Software package, developed by P. Eisenhardt, M. Dickinson, A. Stanford, and J. Ward, which is available as a contributed package in IRAF.

Table 3.4: Optical photometry of USS sources

Name	<i>z</i>	Obs. session	Filter	Mag 4''	Name	<i>z</i>	Obs. session	Filter	Mag 4''
WN J0007+3641	...	L13	<i>r_S</i>	21.6	TN J1112-2948	3.09	E2	<i>R</i>	21.5
WN J0034+4142	...	L13	<i>r_S</i>	>24.5	WN J1115+5016	2.54	L7	<i>r_S</i>	>24
WN J0040+3857	2.606	L15	<i>r_S</i>	23.3:†	TN J1123-2154	4.109	E2	<i>R</i>	>24.5
TN J0121+1320	3.516	L7	<i>r_S</i>	>24	WN J1123+3141	3.217	L7	<i>r_S</i>	21.3
WN J0137+3250	...	L15	<i>r_S</i>	23.2†	TN J1146-1052	...	W5	<i>R</i>	23.5
WN J0155+8036	...	L15	<i>r_S</i>	22.3†	TN J1148-0901	...	W5	<i>R</i>	24.2
TN J0205+2242	3.506	L7	<i>r_S</i>	>24	TN J1151-3013	...	E3	<i>R</i>	>24
TN J0218+0844	...	L10	<i>r_S</i>	>22.5	TN J1159-1629	...	E2	<i>R</i>	23.4
WN J0231+3600	3.079	K9	<i>I</i>	25.0	WN J1224+5436	...	W5	<i>R</i>	24.4
WN J0303+3733	2.506	L13	<i>r_S</i>	23.2	WN J1242+3915	2.131	L7	<i>r_S</i>	23.6
WN J0305+3525	...	K9	<i>I</i>	>25	WN J1258+3212	...	L9	<i>r_S</i>	>24
WN J0310+3644	...	K9	<i>I</i>	23.0	WN J1314+3649	...	W4	<i>R</i>	>26
WN J0359+3000	...	L13	<i>r_S</i>	>23.5	WN J1333+3037	1.213	W4	<i>R</i>	22.5
TN J0402+1007	...	L7	<i>r_S</i>	>24	TN J1338-1942	4.11	E3	<i>R</i>	23.0
TN J0452-1737	2.256	L7	<i>r_S</i>	>23	WN J1355+3848	...	W4	<i>R</i>	>25
TN J0517-0641	...	E2	<i>R</i>	24.0	WN J1420+6735	...	W5	<i>R</i>	>25
WN J0538+7348	...	L15	<i>r_S</i>	>24	WN J1433+3044	...	W4	<i>R</i>	>25
TN J0552-0433	...	E2	<i>R</i>	22.9	WN J1450+3534	...	W5	<i>R</i>	24.1
WN J0617+5012	3.153	W3	<i>R</i>	>24	WN J1500+3613	...	L9	<i>r_S</i>	22.3
WN J0633+4653	...	L15	<i>r_S</i>	22.9:†	WN J1525+3010	...	W4	<i>R</i>	25.3
WN J0716+5107	...	L15	<i>r_S</i>	>23.5	WN J1529+3454	...	W5	<i>R</i>	24.1
WN J0717+4611	1.462	L6	<i>r_S</i>	21.4	WN J1543+3512	0.703	W4	<i>R</i>	21.2
WN J0741+5611	...	L7	<i>r_S</i>	>24	WN J1546+3935	...	W4	<i>R</i>	... ^a
WN J0747+3654	2.992	L7	<i>r_S</i>	>23†	WN J1546+3005	...	W4	<i>R</i>	22.4
WN J0813+4828	1.274	L7	<i>r_S</i>	23.9	WN J1550+3830	...	L9	<i>r_S</i>	22.8
WN J0837-1053	...	E2	<i>R</i>	>24.5	TN J1634-2222	...	E3	<i>R</i>	>23
TN J0855-0000	...	E2	<i>R</i>	>24.5	WN J1718+5823	...	L13	<i>r_S</i>	23.0
TN J0856-1510	...	E3	<i>R</i>	>23.5	WN J1731+4654	...	L10	<i>r_S</i>	>23†
TN J0910-2228	...	E3	<i>R</i>	23.0	WN J1802+3948	...	L13	<i>r_S</i>	>24
TN J0920-0712	2.760	E3	<i>R</i>	22.4	WN J1829+5945	...	L13	<i>r_S</i>	>23
TN J0924-2201	5.19	E3	<i>R</i>	>24	WN J1830+6422	...	L13	<i>r_S</i>	>24
TN J0936-2243	1.479	E3	<i>R</i>	>24	WN J1850+5900	...	W5	<i>R</i>	22.9
TN J0941-1628	1.644	E2	<i>R</i>	23.0	WN J1850+5416	...	W5	<i>R</i>	20.3
WN J0948+6305	...	L15	<i>r_S</i>	22.2†	TN J2008-1344	...	P1	<i>R</i>	>23
WN J1015+3038	0.54	L8	<i>r_S</i>	21.4	TN J2028-1934	...	P1	<i>R</i>	>23
TN J1026-2116	...	E3	<i>R</i>	>24	WN J2044+7044	...	L15	<i>r_S</i>	>24
TN J1033-1339	2.425	E3	<i>R</i>	>24	WN J2213+3411	...	L13	<i>r_S</i>	>24
TN J1043-1718	...	E3	<i>R</i>	>24	WN J2221+3800	...	P1	<i>R</i>	>23
TN J1049-1258	...	E3	<i>R</i>	23.4	WN J2222+3305	...	L15	<i>r_S</i>	21.6†
WN J1053+5424	...	L7	<i>r_S</i>	>24	WN J2313+3842	...	L15	<i>r_S</i>	15.8†
WN J1055+3047	...	L7	<i>r_S</i>	22.8	TN J2314+2053	...	L10	<i>r_S</i>	>23
TN J1102-1651	2.111	E2	<i>R</i>	23.7					

† Estimated from non-photometric conditions.

^a Nearby bright star prohibits measurement.

NOTE: Uncertain values are indicated with a colon.

a non-redundant 16-point dithering pattern. The integration times and specific K -band filter (K , K_S or K') were adapted to the expected magnitudes and sky conditions. We first describe the site-specific details, and next describe the data reduction procedure.

Keck The objects that remained undetected after optical imaging constitute excellent candidates for the highest redshift radio galaxies. We observed these objects with the near-infrared camera (NIRC; Mathews & Soifer, 1994) on the Keck I telescope on Mauna Kea. NIRC contains a 256×256 InSb array with a pixel scale of $0''.151$ pixel⁻¹. Depending upon the sky conditions (as measured from the sky counts during the observations), we used either a standard K , a K_S or a K' filter. We used typical integration times of 60 s comprising 3 co-additions of 20 s per pointing, in a 16-point non-redundant dithering pattern.

The NIRC requires a $R \lesssim 18$ guide star to be placed in an offset guider. To achieve

this, we often needed to rotate the target field. In some cases, we also had to shift the field by several arcseconds in order to place the guide star on the guider camera. As a result, the images obtained have to be rotated back to orient them in the usual North up, East left orientation, and the objects are not always perfectly centered in the registered frames. Bright stars in the frames display electronic 'bleeding trails', for which we do not attempt to correct in the final images.

The data from the 1999 September observing session (K12) were severely affected by instrumental problems due to accidental illumination of one corner of the detector. This decreased the gain down to $<10\%$ of the normal value over more than a third of the detector array. During this session, we adapted our dithering pattern such as to avoid placing the identification in this affected areas. These areas are clearly visible in the finding charts. The measured counts of the objects in the relevant corners are severely attenuated by this problem, a factor that should be taken into account if the resulting images are being used as finding charts.

CTIO For the southernmost sources from our USS sample, we used the CIRIM camera with the tip-tilt system on the CTIO Blanco 4m telescope at Cerro Tololo in the f/14 focal ratio. The detector is a 256×256 HgCdTe NICMOS 3 array. Typical integration times were 120 s, comprising 6 co-averages of 20 s exposures per pointing, in a 16-point non-redundant dithering pattern. To improve the resolution in the images, we performed a tip-tilt correction, using a $V < 16$ reference star within 2.5 of the radio galaxy.

Data Reduction

We reduced the near-IR data using the NOAO IRAF package. After bias subtraction and flat-fielding, we sky-subtracted, registered, and summed the data using the DIMSUM near-IR data reduction package. For most images observed with excellent seeing ($\lesssim 0.5$), we block-replicated the pixels by a factor of 2 before summing the individual images.

3.2.3 Astrometry

The mean density of objects down to $R = 25$ from faint galaxy counts is $\sim 10^5 \text{ deg}^{-1} \text{ mag}^{-1}$ (Smail et al., 1995). This agrees well with the space density of $R \lesssim 24.75$ objects in the field of USS radio sources found by Röttgering et al. (1995a). Because the optical images reach similar or deeper limiting magnitudes, we can statistically expect to find an unrelated source within $\sim 11''$ from the radio position. This can lead to a number of possible mis-identifications in cases where the this confusion source falls within $\lesssim 2''$ from the radio position. One way to limit the number of mis-identifications is to use more accurate astrometry. The accuracy of an astrometric solution is dominated by 2 factors: (i) the positional uncertainty of the astrometric reference catalog with respect to the International Celestial Reference Frame (ICRF), and (ii) the accuracy

of the transformation of this astrometrical information to the images. The uncertainty in the transformation is mainly influenced by the number of objects available to solve the astrometric parameters (positional zero-points in the x- and y-directions, pixel scales, and rotation) using the positions from the astrometric reference catalog. Because the field of view of the images is generally only a few square arcminutes and we are only interested in the central \sim arcmin², we did not attempt to determine the field distortion parameters.

The uncertainties of the VLA positions with respect to the ICRF are $\lesssim 0''.2$. As we will show below, this is 2 to 3 times smaller than the uncertainty between the optical astrometry and the ICRF. In the following, therefore, we will consider only the uncertainties in the optical images. Note that this does not include the uncertainty in the predicted position of the optical/near-IR identification with respect to the radio morphology. In cases where the radio source consists of different components it is possible that the identification does not fall at the midpoint of the radio lobes, but closer to one of the lobes (see e.g., Fig. 6.1). In those cases, a visual inspection of the radio source overlaid on the optical/near-IR image often provided an unambiguous identification.

For the optical and near-IR images obtained prior to 1998, we used the astrometric solution from the digitized sky survey (DSS-I). Véron & Véron (1996) compared accurate absolute VLBI positions of 153 QSO's with positions from the DSS-I, and found the rms uncertainty of the DSS-I astrometry is $\sim 0''.6$ in both coordinates over the whole sky. In 1998, the more accurate USNO-A2.0 catalog was published (Monet et al., 1998), which is based on astrometry from the Tycho catalog (Perryman & ESA, 1997), generated from the Hipparcos mission. The astrometric uncertainty of this catalog with respect to the ICRF is more than 2 times better: $1\sigma \approx 0''.25$ (Deutsch, 1999). Provided that a good transformation of this astrometry to the object frames is possible, we can identify the radio source to within one seeing element in the optical and near-IR images.

To perform the astrometric calibration on the CCD images, we used the task "XTRAN" in the NRAO *AIPS* package. In almost all cases, the optical images were obtained before the near-IR image, because we can use the larger field of view of the optical images (see Table 3.3) to identify the field with the DSS images.

For the astrometric calibration, we only consider stellar objects in the field, because the inclusion of resolved galaxies would introduce additional uncertainties to our solution. In some cases, we had to remove some of the reference objects from our solution in order to get a better fit; these objects are most likely stars with a significant proper motion. The mean number of available reference stars in the optical images is 8 (median is 7). Table 3.3 lists the mean pixel scales and their 1σ deviations. We find that the uncertainties in the optical pixel scales are generally $\lesssim 0''.001$, with the largest uncertainties occurring in the images with the smallest field of view, viz. those obtained with the Kast imaging spectrograph at Lick.

In frames where less than 4 reference stars were available, instead of following the above procedure, we used the position of a single star as the origin of the coordinate

system, and adopted the pixel scale quoted in Table 3.3. When a second or third reference star was available, we selected the object that provided the most consistent results, or the object that was closest to the image center.

Because the field of view of the registered K -band images barely exceeds $1' \times 1'$, we rarely have sufficient stars from the DSS-I, DSS-II or the USNO-A2.0 catalog to perform the same astrometric calibration as in the optical images. We therefore translated the astrometry from the optical images, using stellar objects to $R \lesssim 24$ in common between the optical and near-IR frames. On average, 7 common objects were used to solve the astrometry in the NIRC images. For the K -band images obtained at CTIO, no optical images deeper than $R \sim 20$ were available, and the uncertainties are significantly larger. Nevertheless 6 radio galaxy identifications determined using this astrometry have been shown to be genuine, as they were all successfully detected spectroscopically with the VLT (see Chapter 4).

For 4 objects having K -band images, but lacking large field of view optical images to find reference objects, we obtained J - and K -band images using the Gemini twin-arrays infrared camera (McLean et al., 1993) at the Lick 3m telescope. In addition, R. Gal kindly obtained wide field R -band images of 3 additional objects (TN J2008–1344, TN J2028–1934, WN J2221+3800) with the Palomar 60" telescope. The astrometric solution obtained with these shallow wide-field images were translated to align the deeper K -band images.

Using the astrometric solutions, we could find unambiguous identifications within $\lesssim 1''$ of the radio positions in $>90\%$ of the optical images, and $>94\%$ of the near-IR images. In cases where there was another object within $\lesssim 2''$, we adopted as the real identification the object that was closest to the line connecting both radio lobes, or the object with the more diffuse morphology (assuming the other unresolved object to be a foreground star).

3.2.4 Photometry

We calibrated the photometry using short observations of standard stars from the UKIRT faint standard list (Casali & Hawarden, 1992) or from the list of Persson et al. (1998). For NIRC, this procedure yielded typical zeropoints of $K_0 = 25.12 \pm 0.03$, $K_{S0} = 24.75 \pm 0.03$, and $K'_0 = 25.12 \pm 0.03$ (for 1 count/second, integrated over the source). For CIRIM at the CTIO 4m, we found $K_0 = 21.73 \pm 0.05$. We estimated the uncertainties from the variation of the zeropoints determined from different standards during the same night. We did not correct for airmass variations, because we observed all of our objects with airmasses <1.7 (mean airmass 1.15), and the airmass dependence in K -band is small compared to the fitting errors described below.

Because in most cases the redshift was not known at the time of the near-IR observations, we could not predict the expected K -band magnitudes, as determined from the Hubble $K - z$ diagram (§3.4). Consequently, there is a significant range in signal to noise (S/N) in the fixed apertures of the final images, with some of the brighter

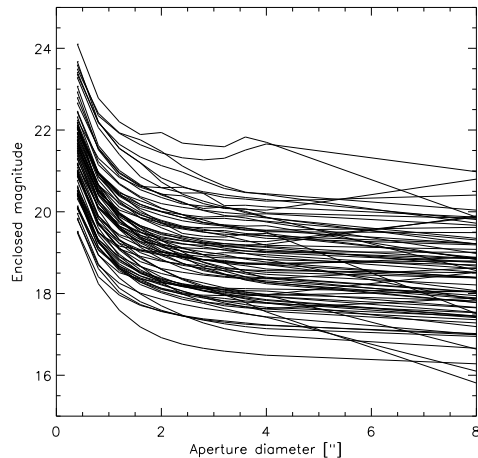


Figure 3.1: Magnitude as a function of aperture diameter. For the large majority of sources, most of the flux is enclosed in within a $2''$ aperture.

images reaching S/N levels well over 50 , while the faintest detections are only detected down to the 5σ level. As a result, the use of isophotal magnitudes is inappropriate. To determine a standard fixed aperture, we first measured the magnitude in a variety of different apertures, with diameters ranging from $0''.4$ to $8''$, using the IRAF task `phot`. Figure 3.1 shows the resulting variation of the aperture magnitudes as a function of the aperture diameter. It is clear that for the large majority of sources, most of the flux is contained within a $2''$ diameter aperture. This is also visible from the images (Fig. 3.2).

Table 3.5 therefore lists magnitudes in 3 different apertures: (i) a $2''$ aperture, which, as shown above, corresponds best to the actual size of most galaxies, (ii) a $4''$ aperture for comparison with the optical magnitudes in Table 3.4, and (iii) an $8''$ aperture for comparison with previously published K -band photometry in the literature (e.g., Eales et al., 1997, vB98). The uncertainties quoted are our best estimates, which include both the zero-point uncertainty and the fitting uncertainty given by the `phot` routine.

We did not correct the magnitudes for Galactic extinction, but list the expected extinction in the K -band in Table 3.5. We obtained these values using the NASA Extragalactic Database (NED), which are based on the $E(B - V)$ values from the extinction maps of Schlegel, Finkbeiner & Davis (1998), and converted to $A(K)$ using the extinction curve of Cardelli et al. (1989), under the assumption of $R_V = A(V)/E(B - V) = 3.1$. The $A(K)$ corrections are generally negligible compared to the uncertainties, except in a few objects which lie close to the Galactic plane.

Table 3.5: K -band Photometry and Morphology

Name	z	Obs. session	Filter	$A(K)^\alpha$	M_{27}	M_{47}	M_{87}	Size	Ellipticity	PA	Morphology
WN J0000+4654	...	K12	K	0.041	18.49±0.04	17.96±0.04	16.65±0.04	3.7/13	0.416	147°	compact
WN J0034+4142	...	K12	K	0.025	18.80±0.05	18.56±0.05	18.52±0.10	2.7/17	0.100	36°	compact
MP J0100-6403	...	C2	K	0.008	19.23±0.15	18.95±0.17	18.61±0.28	low S/N
TN J0102-1055	...	K12	K	0.010	19.45±0.06	19.03±0.07	18.86±0.12	2.7/61	0.475	149°	compact
MP J0114-3302	...	C2	K	0.009	18.59±0.11 [†]	17.94±0.10 [†]	17.66±0.18 [†]	compact
WN J0117+3715	...	K12	K	0.020	18.22±0.04	18.75±0.04	17.28±0.05	1.7/81	0.240	18°	compact
TN J0121+1320	3.516	K4	K _S	0.014	19.47±0.06	19.00±0.06	18.76±0.07	3.7/76	0.463	86°	companions
MP J0130-8352	...	C2	K	0.047	18.11±0.08 [†]	17.97±0.10 [†]	18.52±0.31 [†]	compact
MP J0141-6941	...	C2	K	0.010	16.98±0.09 [†]	17.62±0.09 [†]	17.36±0.12 [†]	compact
TN J0201-1302	...	K12	K	0.007	16.98±0.03	16.50±0.03	16.29±0.03	3.7/25	0.234	112°	elliptical
MP J0203-5425	...	C2	K	0.009	18.59±0.11	17.55±0.08	18.82±0.06	compact
MP J0246-4145	3.506	K4	K _S	0.037	19.30±0.06	19.08±0.06	18.77±0.07	2.7/17	0.194	172°	compact
WN J0346+3525	...	C2	K	0.005	>19.0	non-detection
MP J0346-6507	...	K12	K	0.094	20.84±0.11	20.12±0.10	19.87±0.16	low μ
WN J0346+3039	...	K12	K	0.163	18.68±0.08 [†]	18.28±0.08 [†]	17.78±0.12 [†]	low S/N
WN J0359+3000	...	K12	K _S	0.162	19.08±0.07	18.72±0.10	18.07±0.13	compact
TN J0402+1007	1.521	K4	K _S	0.122	17.57±0.04	17.23±0.04	16.99±0.07	1.7/09	0.183	28°	compact
TN J0410+1019	...	K12	K	0.140	18.35±0.04	17.98±0.04	17.83±0.05	2.7/61	0.224	1°	compact
MP J0449-5449	...	C2	K	0.004	18.02±0.09	17.42±0.09	16.11±0.07	compact
TN J0452-1737	2.256	K4	K _S	0.018	18.81±0.04	18.48±0.04	18.39±0.09	2.7/61	0.178	66°	compact
WN J0528+6549	...	K13	K	0.028	19.67±0.06	19.42±0.07	18.22±0.05	2.7/61	0.090	151°	compact
WN J0538+7348	...	K13	K	0.020	19.74±0.21	19.47±0.28	18.86±0.38	1.7/81	0.123	115°	compact
MP J0601-3926	...	C1	K _S	0.035	18.14±0.04	17.78±0.04	17.42±0.04	3.7/13	0.148	29°	low S/N
WN J0610+6611	...	K13	K	0.051	21.49±0.18	20.42±0.13	19.72±0.15	compact
WN J0617+5012	3.153	K4	K _S	0.025	20.35±0.08	20.05±0.08	20.81±0.30	2.7/61	0.596	174°	low μ
WN J0716+5107	...	K13	K	0.020	>22.5	non-detection
WN J0741+5611	...	K7	K	0.020	21.13±0.10	20.45±0.08	20.05±0.10	1.7/81	0.191	6°	low μ
WN J0747+3654	2.992	K13	K'	0.040	19.18±0.06	19.02±0.06	19.02±0.11	2.7/17	0.263	112°	compact
WN J0813+4828	1.274	K7	K _S	0.020	21.79/22.05	low S/N
TN J0856-1510	...	K13	K	0.022	21.94±0.22	21.71±0.30	19.88±0.15	low μ
TN J0824-2201	5.19	K7	K _S	0.021	18.62±0.06	18.32±0.05	17.96±0.07	2.7/61	0.221	16°	compact
TN J0836-2243	1.479	K7	K _S	0.010	18.40±0.06	17.78±0.04	17.19±0.04	3.7/13	0.211	129°	companions
WN J1015+3038	0.54	K7	K _S	0.035	20.41±0.10	19.76±0.11	18.98±0.13	low μ
TN J1026-2116	...	K7	K	0.027	19.62±0.06	19.15±0.06	18.96±0.07	3.7/13	0.303	113°	compact
TN J1033-1339	2.425	K10	K _S	0.022	19.31±0.05	18.37±0.05	17.90±0.05	interacting
TN J1049-1258	...	K7	K	0.004	20.74±0.12	19.86±0.09	19.21±0.11	low μ
WN J1053+5424	...	K10	K _S	0.010	19.03±0.06	18.72±0.07	18.40±0.10	1.7/81	0.113	53°	compact
WN J1055+3047	...	K7	K _S	0.010	20.10±0.09	19.54±0.09	19.22±0.14	compact
WN J1115+5016	2.54	K7	K _S	0.006	20.10±0.09	19.54±0.09	19.22±0.14	low μ
TN J1123-2154	4.109	K7	K _S	0.015	20.59±0.14	20.27±0.19	20.41±0.52	interacting
WN J1123+3141	3.217	K10	K _S	0.007	18.34±0.04	17.84±0.04	17.45±0.04	compact
TN J1151-3013	...	K10	K _S	0.018	20.00±0.08	19.77±0.09	19.31±0.12	2.7/17	0.358	170°	compact
WN J1224+5436	...	K10	K	0.005	19.40±0.05	19.14±0.06	18.97±0.07	1.7/81	0.172	3°	interacting
WN J1245+3915	2.131	K7	K _S	0.007	19.14±0.06	18.61±0.06	18.39±0.09	2.7/61	0.268	52°	companions
WN J1258+3212	...	K13	K _S	0.005	19.79±0.06	19.35±0.06	19.19±0.08	1.7/81	0.065	156°	compact
WN J1314+3649	...	K7	K	0.004	20.20±0.18	22.07±0.63	low S/N
TN J1338-1942	4.11	K7	K	0.036	20.20±0.07	19.95±0.08	19.67±0.13	3.7/13	0.374	146°	interacting
WN J1355+3848	...	K10	K _S	0.008	19.49±0.06	19.28±0.07	19.87±0.18	1.7/51	0.253	80°	compact

Name	z	Obs. session	Filter	A(K) ^a	Mag _{2'}	Mag _{4'}	Mag _{8'}	Size	Ellipticity	PA	Morphology
WN J1420+6735	...	K10	K	0.009	18.96±0.06	18.75±0.05	18.80±0.07	1.7/81	0.006	114°	compact
TN J1428+2425	...	K10	K _S	0.021	>22.1	non-detection
WN J1433+3044	...	K7	K _S	0.006	18.37±0.05	17.93±0.04	17.54±0.05	3.7/6	0.447	98°	elliptical
WN J1450+3634	...	K10	K	0.004	20.00±0.07	19.67±0.07	18.84±0.07	1.7/51	0.284	38°	compact
TN J1506+2728	...	K10	K _S	0.012	20.58±0.10	20.30±0.12	19.82±0.17	low S/N
WN J1525+3010	...	K7	K	0.007	20.08±0.08	19.51±0.09	19.49±0.18	1.7/26	0.057	44°	compact
WN J1550+3830	...	K10	K	0.004	19.15±0.05	18.84±0.05	18.70±0.08	2.7/61	0.430	155°	compact
WN J1555+4011	...	K10	K _S	0.006	18.95±0.05	18.71±0.05	18.90±0.11	1.7/81	0.198	130°	compact
WN J1604+5505	...	K10	K _S	0.003	21.45±0.18	21.67±0.38	20.98±0.51	low μ
WN J1645+4413	...	K10	K _S	0.005	18.31±0.04	18.07±0.04	17.66±0.05	3.7/13	0.481	145°	elliptical
WN J1731+4640	...	K10	K _S	0.009	19.78±0.07	19.18±0.07	19.08±0.11	1.7/51	0.182	177°	compact
WN J1731+4654	...	K10	K _S	0.009	>21.5	non-detection
MP J1755-6916	2.551	C2	K	0.027	19.08±0.13	18.28±0.12	17.87±0.17	low μ
MP J1758-6738	2.026	C2	K	0.028	19.20±0.17	18.25±0.14	17.78±0.21	low S/N
WN J1804+3048	...	K10	K _S	0.021	19.73±0.07	19.55±0.09	19.62±0.19	1.7/51	0.053	26°	compact
WN J1818+3852	...	K10	K	0.011	19.91±0.07	19.50±0.07	17.52±0.04	2.7/17	0.161	165°	compact
WN J1818+6144	...	K10	K	0.021	17.86±0.04	17.44±0.04	17.01±0.04	4.7/51	0.287	12°	elliptical
WN J1896+5210	...	K10	K ₉	0.016	18.24±0.04	17.66±0.04	17.45±0.04	2.7/61	0.545	168°	interacting
WN J1911+6342	3.590	K10	K	0.025	20.44±0.09	19.87±0.10	18.57±0.07	low μ
WN J1917+6635	...	K10	K	0.015	20.48±0.09	19.97±0.11	19.84±0.22	2.7/61	0.559	176°	low μ
MP J1929-3732	0.748	C2	K	0.122	17.59±0.08	17.14±0.07	16.96±0.09	compact
TN J1941-1952	...	K12	K	0.042	18.29±0.04	17.64±0.04	17.90±0.09	compact
TN J1954-1207	...	K10	K	0.053	20.01±0.08	19.86±0.10	19.35±0.14	compact
MP J2003-8340	1.169	C2	K	0.078	18.84±0.12	18.36±0.12	18.63±0.30	compact
TN J2007-1316	...	K12	K _S	0.044	19.03±0.06	18.84±0.08	17.85±0.08	1.7/51	0.071	44°	compact
TN J2009-3040	...	K10	K	0.066	18.26±0.04	18.12±0.04	18.05±0.05	2.7/61	0.220	37°	compact
TN J2028-1834	...	K12	K ₉	0.023	19.05±0.06	18.49±0.06	18.34±0.10	compact
WN J2044+7044	...	K10	K ₉	0.173	19.37±0.06	19.20±0.07	19.90±0.23	1.7/81	0.058	1°	compact
MP J2045-6018	1.464	C2	K	0.023	18.28±0.10	17.96±0.11	18.06±0.22	compact
MP J2048-5750	1.262	C2	K	0.025	17.57±0.07	17.22±0.07	17.02±0.09	compact
MP J2126-5439	...	C2	K	0.015	18.12±0.09†	17.77±0.09†	17.58±0.13†	compact
WN J2213+3411	...	K12	K _S	0.048	18.28±0.05	17.86±0.05	17.45±0.06	3.7/13	0.334	140°	compact
MP J2226-7654	...	C2	K	0.051	18.93±0.14†	18.39±0.14†	18.04±0.23†	compact
WN J2250+4131	...	K12	K	0.090	19.72±0.07	19.42±0.09	18.89±0.13	1.7/81	0.393	36°	compact
WN J2313+4253	...	K12	K	0.056	17.70±0.04	16.99±0.03	16.66±0.04	pulsar
TN J2314+2053	...	K12	K	0.100	19.34±0.06	18.90±0.06	18.52±0.09	2.7/61	0.277	6°	compact
MP J2352-6154	...	C2	K	0.008	19.30±0.15	18.41±0.12	18.05±0.16	interacting

^a Extinction in K-band, from HI column densities.

† Estimated from non-photometric conditions.

3.3 Results

Figure 3.2 shows $8'' \times 8''$ images of the K -band images, centered on the derived identifications (i.e., not the predicted radio position). The grey scale is from $\mu - \sigma$ to $\mu + 4\sigma$, where μ and σ are the mean and rms, as determined from a histogram of the sky-subtracted background counts, determined in a source-free region with the *AIPS* task 'IMEAN'. All images are shown in the usual orientation with North up and East to the left. Note that this required a generally non-orthogonal rotation of the NIRC images because they were obtained in an orientation that positions a guide star in the offset guider CCD (see §3.2.2.1). Table 3.6 lists the positions of the optical and near-IR identifications, with the brightest nearby offset stars.

We shall now discuss the optical and/or near-IR identification of a number of individual sources, and then consider the magnitude distribution of the sample as a whole. K -band observations of 2 sources (WN J0117+3715 and WN J1843+5932) from our USS sample have been reported by Villani & di Serego Alighieri (1999).

3.3.1 Notes on individual sources

WN J0034+4142: Although the near-IR identification does not lie at the midpoint, it falls on the line connecting both radio lobes.

WN J0117+3715: Villani & di Serego Alighieri (1999) report $K = 18.20 \pm 0.57$ in a $3''.88$ diameter aperture for this source, which is consistent with our value ($K = 17.57 \pm 0.04$ in a $4''$ diameter aperture).

TN J0121+1320: This galaxy has been spectroscopically confirmed at $z = 3.516$ (Chapter 4). The near-IR identification resembles that of a radio galaxies at $z < 3$.

MP J0202-5425: There is a bright stellar object $\sim 3''$ to the north-east of the near-IR identification, which contaminates the aperture photometry.

TN J0205+2242: This galaxy has been spectroscopically confirmed at $z = 3.506$ (Chapter 4). The near-IR identification resembles that of a radio galaxies at $z < 3$.

TN J0218+0844: The most likely optical identification is the source slightly north of the predicted radio position, although we cannot exclude the source at $\alpha_{J2000} = 2^h 18^m 25^s 57$, $\delta_{J2000} = 08^\circ 44' 27''.7$.

WN J0305+3525: The near-IR identification is an very diffuse source without a central core component.

WN J0346+3039: The near-IR photometry for this object is highly uncertain due to the problems with the detector during this run.

WN J0359+3000: The near-IR identification is uncertain because the radio position is based on the NVSS position only.

WN J0617+5012: The very faint K -band identification coincides with the southern radio lobe of a $z = 3.153$ radio galaxy (see Chapter 4).

WN J0741+5611: Our radio map is of insufficient depth to identify any of the features observed in the field of the K -band image.

Table 3.6: Astrometric data on the optical images

Source		α_{2000} h m s	δ_{2000} ° ' "	Source		α_{2000} h m s	δ_{2000} ° ' "
WN J0000+4654	Radio	00 00 28.88	+46 54 40.7	TN J0410+1019	Radio	04 10 40.52	+10 19 13.6
	IR	00 00 28.93	+46 54 40.9		IR	04 10 40.56	+10 19 13.8
	A (IR)	00 00 29.25	+46 54 53.8		A (IR)	04 10 40.38	+10 19 35.3
WN J0007+3641	Radio	00 07 02.92	+36 41 55.9	MP J0449-5449	Radio	04 49 04.66	-54 49 10.1
	Opt	00 07 02.80	+36 41 55.8		IR	04 49 04.73	-54 49 07.9
	A (opt)	00 07 04.92	+36 42 09.3		A (IR)	04 49 02.08	-54 48 38.6
WN J0034+4142	Radio	00 34 29.21	+41 42 09.5	TN J0452-1737	Radio	04 52 26.66	-17 37 54.0
	A (opt)	00 34 28.45	+41 41 33.5		A (opt)	04 52 24.94	-17 38 25.9
	IR	00 34 29.10	+41 42 15.7		IR	04 52 26.68	-17 37 54.0
	A (IR)	00 34 30.38	+41 42 06.5	TN J0517-0641	A (IR)	04 52 26.30	-17 37 35.9
WN J0040+3857	Radio	00 40 56.23	+38 57 30.0		Radio	05 17 36.89	-06 41 14.6
	Opt	00 40 56.19	+38 57 29.8		Opt	05 17 36.85	-06 41 14.5
	A (opt)	00 40 59.27	+38 57 19.8		A (opt)	05 17 38.25	-06 40 57.0
MP J0100-6403	Radio	01 00 32.42	-64 03 13.6	WN J0528+6549	Radio	05 28 46.07	+65 49 57.3
	IR	01 00 32.27	-64 03 14.4		IR	05 28 46.03	+65 49 58.0
	A (IR)	01 00 29.39	-64 03 11.4		A (IR)	05 28 44.65	+65 49 48.6
TN J0102-1055	Radio	01 01 59.99	-10 55 56.0	WN J0538+7348	Radio	05 38 25.59	+73 48 39.6
	IR	01 02 00.01	-10 55 54.5		A (opt)	05 38 18.12	+73 48 46.7
	A (IR)	01 02 00.76	-10 56 10.1		IR	05 38 25.61	+73 48 39.6
MP J0114-3302	Radio	01 14 37.06	-33 02 10.2	TN J0552-0433	A (IR)	05 38 35.39	+73 48 42.8
	IR	01 14 36.64	-33 02 11.3		Radio	05 52 14.38	-04 33 28.8
	A (IR)	01 14 35.69	-33 02 20.2		Opt	05 52 14.30	-04 33 26.9
WN J0117+3715	Radio	01 17 10.02	+37 15 16.3		A (opt)	05 52 11.68	-04 33 41.2
	IR	01 17 10.10	+37 15 16.3	MP J0601-3926	Radio	06 01 00.77	-39 26 18.1
	A (IR)	01 17 09.61	+37 15 06.2		IR	06 01 00.74	-39 26 15.5
TN J0121+1320	Radio	01 21 42.74	+13 20 58.3		A (IR)	06 01 01.67	-39 26 27.0
	A (opt)	01 21 44.53	+13 20 58.6	WN J0610+6611	Radio	06 10 08.59	+66 11 43.1
	IR	01 21 42.76	+13 20 58.1		IR	06 10 08.47	+66 11 41.9
	A (IR)	01 21 44.52	+13 20 58.5		A (IR)	06 10 09.61	+66 11 15.0
MP J0130-8352	Radio	01 30 07.46	-83 52 29.6	WN J0617+5012	Radio	06 17 39.37	+50 12 54.7
	IR	01 30 08.88	-83 52 33.0		A (opt)	06 17 38.81	+50 12 29.2
	A (IR)	01 30 08.46	-83 52 17.5		IR	06 17 39.40	+50 12 53.2
WN J0137+3250	Radio	01 36 59.85	+32 50 40.7		A (IR)	06 17 38.96	+50 12 28.3
	Opt	01 36 59.86	+32 50 38.5	WN J0633+4653	Radio	06 33 52.18	+46 53 40.5
	A (opt)	01 37 03.40	+32 51 05.9		A (opt)	06 33 50.38	+46 53 09.2
MP J0141-6941	Radio	01 41 55.18	-69 41 33.0	WN J0716+5107	Radio	07 16 40.50	+51 07 04.7
	IR	01 41 55.01	-69 41 33.1		A (opt)	07 16 39.30	+51 07 06.2
	A (IR)	01 41 56.70	-69 41 15.3		IR	07 16 40.50	+51 07 06.4
WN J0155+8036	Radio	01 55 43.77	+80 36 48.1		A (IR)	07 16 39.32	+51 07 06.6
	Opt	01 55 43.85	+80 36 50.3	WN J0717+4611	Radio	07 17 58.49	+46 11 39.1
	A (opt)	01 55 39.96	+80 36 29.2		Opt	07 17 58.47	+46 11 38.9
TN J0201-1302	Radio	02 01 15.80	-13 02 19.4		A (opt)	07 18 00.56	+46 11 24.8
	IR	02 01 15.75	-13 02 18.8	WN J0741+5611	Radio	07 41 15.38	+56 11 35.9
	A (IR)	02 01 14.26	-13 02 28.5		A (opt)	07 41 19.92	+56 11 41.6
MP J0202-5425	Radio	02 02 56.25	-54 25 13.3		A (IR)	07 41 14.89	+56 11 51.2
	IR	02 02 56.25	-54 25 13.7	WN J0747+3654	Radio	07 47 29.38	+36 54 38.1
	A (IR)	02 02 53.69	-54 25 23.7		A (opt)	07 47 32.83	+36 55 15.7
TN J0205+2242	Radio	02 05 10.69	+22 42 50.2		IR	07 47 29.37	+36 54 37.9
	A (opt)	02 05 11.70	+22 42 33.6		A (IR)	07 47 31.05	+36 54 33.7
	IR	02 05 10.71	+22 42 51.1	WN J0813+4828	Radio	08 13 38.10	+48 28 41.5
	A (IR)	02 05 11.78	+22 42 34.2		A (opt)	08 13 39.24	+48 28 12.4
TN J0218+0844	Radio	02 18 25.56	+08 44 31.3		IR	08 13 38.01	+48 28 41.0
	A (opt)	02 18 25.02	+08 43 51.5		A (IR)	08 13 36.70	+48 28 17.1
WN J0231+3600	Radio	02 31 11.48	+36 00 26.6	TN J0837-1053	Radio	08 37 41.62	-10 53 46.0
	Opt	02 31 11.13	+36 00 23.8		A (opt)	08 37 42.14	-10 54 04.8
	A (opt)	02 31 09.95	+36 00 52.0	TN J0855-0000	Radio	08 55 57.26	-00 00 58.2
MP J0249-4145	Radio	02 49 10.08	-41 45 36.3		A (opt)	08 55 56.66	-00 00 52.5
	A (IR)	02 49 10.41	-41 45 55.8	TN J0856-1510	Radio	08 56 12.44	-15 10 35.7
WN J0303+3733	Radio	03 03 26.01	+37 33 41.0		A (opt)	08 56 14.93	-15 10 44.1
	Opt	03 03 26.09	+37 33 41.0	TN J0859-1510	Radio	08 56 12.44	-15 10 35.7
	A (opt)	03 03 26.40	+37 34 10.6		A (IR)	08 56 11.20	-15 10 24.3
WN J0305+3525	Radio	03 05 47.42	+35 25 13.4	TN J0910-2228	Radio	09 10 34.15	-22 28 47.4
	A (opt)	03 05 47.74	+35 25 33.8		Opt	09 10 34.14	-22 28 46.7
	IR	03 05 47.58	+35 25 13.3		A (opt)	09 10 32.51	-22 28 26.4
	A (IR)	03 05 47.76	+35 25 33.2	TN J0920-0712	Radio	09 20 22.43	-07 12 17.6
WN J0310+3644	Radio	03 10 54.80	+36 44 02.5		Opt	09 20 22.41	-07 12 18.4
	Opt	03 10 54.77	+36 44 03.2		A (opt)	09 20 23.35	-07 12 24.4
	A (opt)	03 10 53.38	+36 44 18.7	TN J0924-2201	Radio	09 24 19.92	-22 01 41.5
MP J0340-6507	Radio	03 40 44.92	-65 07 07.3		A (opt)	09 24 20.47	-22 01 22.6
	IR	03 40 45.33	-65 07 08.0		IR	09 24 19.93	-22 01 41.4
	A (IR)	03 40 50.15	-65 07 00.7		A (IR)	09 24 20.48	-22 01 22.6
WN J0346+3039	Radio	03 46 42.60	+30 39 51.0	TN J0936-2243	Radio	09 36 32.53	-22 43 04.9
	IR	03 46 42.55	+30 39 50.7		A (opt)	09 36 31.78	-22 43 17.5
	A (IR)	03 46 43.67	+30 39 35.5		IR	09 36 32.54	-22 43 01.7
WN J0359+3000	Radio	03 59 12.86	+30 00 51.7		IR	09 36 32.60	-22 43 05.4
	A (opt)	03 59 11.44	+30 00 42.9		A (IR)	09 36 34.06	-22 43 01.3
	IR	03 59 12.89	+30 00 55.0	TN J0941-1628	Radio	09 41 07.43	-16 28 02.5
	A (IR)	03 59 11.44	+30 00 43.1		Opt	09 41 07.43	-16 28 02.6
TN J0402+1007	Radio	04 02 34.44	+10 07 14.9		A (opt)	09 41 08.81	-16 27 50.3
	A (opt)	04 02 36.56	+10 07 16.5	WN J0948+6305	Radio	09 48 40.83	+63 05 42.0
	IR	04 02 34.44	+10 07 15.1		Opt	09 48 40.82	+63 05 42.2
	A (IR)	04 02 35.13	+10 06 52.5		A (opt)	09 48 40.10	+63 05 34.0

Source		α_{2000} h m s	δ_{2000} ° ' "	Source		α_{2000} h m s	δ_{2000} ° ' "
WN J1015+3038	Radio	10 15 08.92	+30 38 02.0	TN J1338-1942	Radio	13 38 26.06	-19 42 30.1
	Opt	10 15 09.09	+30 38 02.0		Opt	13 38 26.11	-19 42 30.6
	A(opt)	10 15 08.18	+30 39 03.9		A(opt)	13 38 26.15	-19 42 12.0
	IR	10 15 08.93	+30 38 02.9		IR	13 38 26.14	-19 42 31.3
	A(IR)	10 15 07.15	+30 37 50.5		A(IR)	13 38 26.09	-19 42 11.0
TN J1026-2116	Radio	10 26 22.37	-21 16 07.7	WN J1355+3848	Radio	13 55 29.50	+38 48 11.1
	A(opt)	10 26 20.54	-21 16 28.9		A(opt)	13 55 31.42	+38 47 36.7
	IR	10 26 22.39	-21 16 07.7		IR	13 55 29.51	+38 48 12.0
	A(IR)	10 26 21.92	-21 16 19.6		A(IR)	13 55 28.04	+38 48 08.1
TN J1033-1339	Radio	10 33 10.70	-13 39 52.0	WN J1420+6735	Radio	14 20 03.34	+67 35 07.5
	A(opt)	10 33 13.54	-13 40 07.4		A(opt)	14 20 10.17	+67 35 10.7
	IR	10 33 10.67	-13 39 52.2		IR	14 20 03.26	+67 35 06.0
	A(IR)	10 33 13.05	-13 40 01.5		A(IR)	14 20 07.12	+67 34 58.8
TN J1043-1718	Radio	10 43 19.42	-17 18 53.5	TN J1428+2425	Radio	14 28 10.20	+24 25 11.3
	Opt	10 43 20.52	-17 18 44.9		A(IR)	14 28 11.91	+24 25 24.0
	A(opt)	10 43 20.52	-17 18 44.8	WN J1433+3044	Radio	14 33 56.51	+30 44 25.5
	IR	10 49 06.22	-12 58 18.3		A(opt)	14 33 54.58	+30 44 44.5
	A(opt)	10 49 09.24	-12 58 56.7		IR	14 33 56.44	+30 44 25.0
	IR	10 49 06.26	-12 58 18.9		A(IR)	14 33 55.82	+30 44 33.1
	A(IR)	10 49 06.78	-12 58 42.1	WN J1450+3534	Radio	14 50 20.69	+35 34 46.5
WN J1053+5424	Radio	10 53 36.31	+54 24 42.1		Opt	14 50 20.70	+35 34 47.1
	A(opt)	10 53 34.67	+54 24 13.0		A(opt)	14 50 19.28	+35 34 19.4
	IR	10 53 36.28	+54 24 42.3		IR	14 50 20.70	+35 34 47.1
	A(IR)	10 53 36.90	+54 24 57.9		A(IR)	14 50 19.27	+35 34 19.5
WN J1055+3047	Radio	10 55 18.52	+30 47 23.2	WN J1500+3613	Radio	15 00 09.01	+36 13 25.8
	Opt	10 55 18.65	+30 47 23.5		Opt	15 00 09.04	+36 13 27.8
	A(opt)	10 55 17.35	+30 47 58.4		A(opt)	15 00 07.69	+36 13 51.4
	IR	10 55 18.44	+30 47 23.3	TN J1506+2728	Radio	15 06 35.41	+27 28 55.6
	A(IR)	10 55 17.42	+30 47 24.9		IR	15 06 35.41	+27 28 56.0
TN J1102-1651	Radio	11 02 47.13	-16 51 34.4		A(IR)	15 06 33.89	+27 29 10.0
	Opt	11 02 47.18	-16 51 35.2		B ₁ IR	15 06 36.56	+27 28 46.8
	A(opt)	11 02 46.56	-16 51 00.9	WN J1525+3010	Radio	15 25 01.21	+30 10 30.2
	IR	11 12 23.86	-29 48 06.4		Opt	15 25 01.24	+30 10 29.7
	A(IR)	11 12 23.98	-29 48 06.6		A(opt)	15 25 01.72	+30 10 54.5
TN J1112-2948	Radio	11 12 24.54	-29 48 16.2		IR	15 25 01.23	+30 10 29.6
	Opt	11 15 06.87	+50 16 23.9		A(IR)	15 25 01.71	+30 10 54.5
	A(opt)	11 15 06.58	+50 15 47.4	WN J1529+3454	Radio	15 29 41.52	+34 54 31.3
	IR	11 15 06.90	+50 16 24.5		Opt	15 29 41.45	+34 54 29.9
	A(IR)	11 15 06.79	+50 16 39.8		A(opt)	15 29 39.06	+34 54 29.1
TN J1123-2154	Radio	11 23 10.15	-21 54 05.3	WN J1543+3512	Radio	15 43 29.49	+35 12 29.7
	A(opt)	11 23 07.98	-21 53 41.1		Opt	15 43 29.60	+35 12 27.8
	IR	11 23 10.18	-21 54 04.8		A(opt)	15 43 28.27	+35 12 15.1
	A(IR)	11 23 10.85	-21 54 03.4	WN J1546+3005	Radio	15 46 57.65	+30 05 38.1
WN J1123+3141	Radio	11 23 55.85	+31 41 26.1		Opt	15 46 57.72	+30 05 39.0
	Opt	11 23 55.70	+31 41 26.7		A(opt)	15 46 55.61	+30 05 33.8
	A(opt)	11 23 53.11	+31 41 04.7	WN J1550+3830	Radio	15 50 19.42	+38 30 14.8
	IR	11 23 55.88	+31 41 26.5		A(opt)	15 50 16.51	+38 30 35.3
	A(IR)	11 23 53.28	+31 41 04.7		IR	15 50 19.47	+38 30 13.4
TN J1146-1052	Radio	11 46 07.21	-10 52 08.6		A(IR)	15 50 20.79	+38 29 55.8
	Opt	11 46 07.26	-10 52 07.1	WN J1555+4011	Radio	15 55 02.50	+40 11 58.1
	A(opt)	11 46 08.46	-10 52 30.3		IR	15 55 02.49	+40 11 58.4
TN J1148-0901	Radio	11 48 39.90	-09 01 48.8		A(IR)	15 55 02.41	+40 11 43.8
	Opt	11 48 39.97	-09 01 49.6	WN J1604+5505	Radio	16 04 21.91	+55 05 45.4
	A(opt)	11 48 42.14	-09 01 41.3		IR	16 04 21.95	+55 05 45.4
	IR	11 51 59.42	-30 13 40.8		A(IR)	16 04 19.99	+55 05 31.0
	A(IR)	11 51 57.27	-30 14 10.6	TN J1634-2222	Radio	16 34 49.79	-22 22 12.7
	IR	11 51 59.54	-30 13 40.6		A(opt)	16 34 50.24	-22 22 29.1
	A(IR)	11 51 59.62	-30 13 48.1	WN J1645+4413	Radio	16 45 35.69	+44 13 42.1
TN J1159-1629	Radio	11 59 53.25	-16 29 48.2		IR	16 45 35.73	+44 13 43.1
	Opt	11 59 53.30	-16 29 47.9		A(IR)	16 45 37.60	+44 13 42.2
	A(opt)	11 59 51.29	-16 29 07.8	WN J1718+5823	Radio	17 18 18.51	+58 23 21.8
WN J1224+5436	Radio	12 24 52.35	+54 36 39.9		Opt	17 18 18.51	+58 23 21.8
	Opt	12 24 52.31	+54 36 40.3		A(opt)	17 18 14.16	+58 22 58.0
	A(opt)	12 24 51.92	+54 36 00.6	WN J1731+4640	Radio	17 31 46.10	+46 40 03.1
	IR	12 24 52.32	+54 36 40.1		IR	17 31 46.02	+46 40 03.4
	A(IR)	12 24 49.21	+54 36 40.2		A(IR)	17 31 48.42	+46 39 40.1
WN J1242+3915	Radio	12 42 53.09	+39 15 48.6	WN J1731+4654	Radio	17 31 59.63	+46 54 00.2
	Opt	12 42 53.00	+39 15 47.5		A(opt)	17 32 02.07	+46 53 25.2
	A(opt)	12 42 52.49	+39 15 38.9		A(IR)	17 32 02.66	+46 54 08.3
	IR	12 42 53.08	+39 15 47.6	MP J1755-6916	Radio	17 55 30.23	-69 16 49.8
	A(IR)	12 42 52.02	+39 15 30.2		IR	17 55 30.02	-69 16 51.7
WN J1258+3212	Radio	12 58 23.62	+32 12 42.4		A(IR)	17 55 30.94	-69 17 07.0
	A(opt)	12 58 25.63	+32 12 56.7	MP J1758-6738	Radio	17 58 51.25	-67 38 30.5
	IR	12 58 23.63	+32 12 40.8		IR	17 58 51.29	-67 38 27.9
	A(IR)	12 58 25.64	+32 12 56.4	WN J1802+3948	Radio	18 02 31.65	+39 48 59.6
WN J1314+3649	Radio	13 14 17.86	+36 49 14.6		A(opt)	18 02 29.76	+39 48 55.8
	A(opt)	13 14 20.39	+36 48 50.9	WN J1804+3048	Radio	18 04 42.01	+30 48 45.0
	IR	13 14 17.80	+36 49 14.6		IR	18 04 42.03	+30 48 45.4
	A(IR)	13 14 17.74	+36 48 58.9		A(IR)	18 04 42.07	+30 48 53.7
WN J1333+3037	Radio	13 33 21.20	+30 37 35.1	WN J1818+3852	Radio	18 18 42.17	+38 52 20.4
	Opt	13 33 21.20	+30 37 34.8		IR	18 18 42.02	+38 52 20.7
	A(opt)	13 33 23.15	+30 37 37.6		A(IR)	18 18 41.01	+38 52 37.0

WN J1314+3649: This is one of our faintest K -band identifications. We attempted optical spectroscopy with LRIS at Keck, but did not detect the object (see Chapter 4).

TN J1338–1942: The near-IR identification, a radio galaxy at $z = 4.11$, corresponds to the brightest component of a very asymmetric radio source. This source is described in detail Chapter 6.

TN J1428+2425: This is a rare K -band “blank field”. Although our astrometry is based on only 2 stars in common with an image taken with the Gemini camera at Lick observatory, there are no candidate identifications within $8''$.

WN J1525+3010: There appears to be a diffuse halo around the K -band identification. We have obtained a $t_{int} = 5400$ s spectrum with LRIS at Keck, but did not detect any optical emission from this source (see Chapter 4).

WN J1604+5505: The near-IR identification is a very diffuse source without a central core component.

WN J1731+4654: This is a rare K -band “blank field”. We obtained the astrometric solution by transferring a single star from the Lick image and assuming the pixel scale; comparison with 2 other stars common with the Lick image suggests this solution is accurate up to $\sim 1''$. There is a source $5''$ north of the predicted position at $\alpha_{J2000} = 17^h 31^m 59^s 68$, $\delta_{J2000} = 46^\circ 54' 05''.5$, but this falls well outside the position uncertainty from the FIRST survey.

WN J1836+5210: The optical and near-IR identifications are ambiguous between a red northern component, and a blue southern component. Table 3.6 lists the position of the red, northern component, which is slightly closer to the predicted radio position, although both sources might well be part of the same physical system.

WN J1843+5932: Villani & di Serego Alighieri (1999) detected this source with $K = 17.96 \pm 0.19$ in a $3''.28$ aperture. We did not re-observe it, and refer to their paper for a finding chart.

TN J1941–1952: The unresolved object $1''$ west of the near-IR identification is probably a foreground star, and contaminates the aperture photometry.

WN J2044+7044: This object appears compact in the K -band image. We attempted optical spectroscopy with LRIS at Keck, but did not detect any optical emission from the object (see Chapter 4).

WN J2213+3411: The near-IR identification is uncertain, because we lack a high resolution VLA map of this field. However, the NVSS map shows a source that is elongated in the same direction as the proposed identification ($52'' \times 19''$ at position angle -31°).

WN J2313+4253: This is the pulsar PSR J2313+4253.

3.3.2 Magnitude and color distributions

We identified approximately 50% of the 83 optically imaged USS sources, while in the near-IR, we found counterparts for $>94\%$ of the 86 sources observed. Of the 4 K -band non-detections, MP J0249–4145 was obtained with CIRIM at CTIO, and might well have been detected if observed down to fainter levels comparable to the

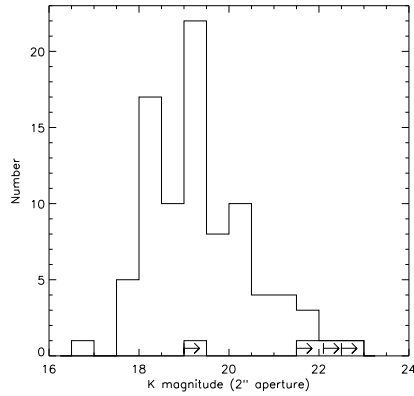


Figure 3.3: Histogram of the K -band magnitudes measured in a $2''$ diameter aperture. Non detections are indicated by arrows.

Keck data. Another non-detection, WN J0741+5611, requires more sensitive radio map to determine the possible identification. It is clear that a deep K -band survey of radio sources is much more efficient in detecting the galaxy counterparts than deep optical imaging. The offsets from brighter stars in the field of the radio galaxy allow one to accurately position the slit for spectroscopic redshift determinations. Moreover, the K -band magnitude provides an estimate of the expected redshift of the radio galaxy by means of the Hubble $K - z$ diagram (§3.4).

Because the magnitude limits of our optical imaging vary from $R \sim 23$ to $R \sim 26$, and half of the observed USS sources are not detected, we cannot construct a reliable optical magnitude distribution. Only one third of the sources are brighter than $R = 24$, implying that the mean optical magnitude is probably $R \sim 25$. This is significantly fainter than that of the USS sample of Röttgering et al. (1995a), who found that the R -band magnitude distribution in their sample peaks between $R = 22$ and $R = 23$, with 70% of the radio sources identified at $R < 24$. This difference is due to 2 main differences between the samples. First, the flatter radio spectral index cutoff ($\alpha \sim -1.2$) in their sample, which selects lower redshift objects than our optically observed sample, which has a mean (and median) spectral index of $\bar{\alpha} \simeq -1.38$. Second, their sample contains sources with radio flux densities an order of magnitude brighter than our sample.

Our optical magnitude distribution more resembles that of the sample of fainter USS sources by Wieringa & Katgert (1992), who find that half of their sources have $R > 24$. This suggests that the difference with the sample of Röttgering et al. (1995a) could also be due to the lower radio flux densities in our sample. This could lead to lower optical magnitudes, because the host galaxy absolute magnitude appears to be correlated with radio luminosity (e.g., Best, Longair & Röttgering, 1998a; Lacy,

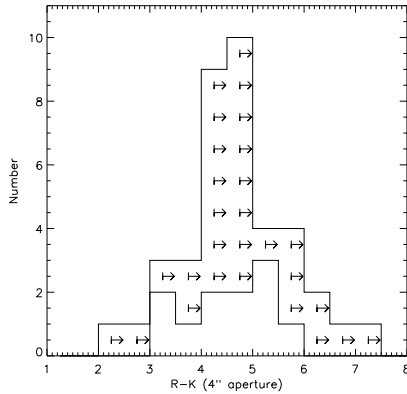


Figure 3.4: Histogram of the $R - K$ colors measured in a $4''$ diameter aperture. Non-detections in the R -band are indicated by arrows.

Bunker, & Ridgway, 2000). Such a correlation could arise if the host galaxies of the more powerful radio sources contain a greater mass of stars, and assuming that their central black holes accrete at near-Eddington rates. We return to this point in §3.4. Figure 3.3 shows the distribution of K magnitudes. The mean/median K -band magnitude is $K = 19.26/19.19$ in a $2''$ diameter aperture ($K = 18.57/18.72$ in a $4''$ aperture). The distribution appears to be slightly asymmetric, in the sense that the tail of sources with magnitudes fainter than the mean seems to be broader than the bright-end tail, which cuts off at $K = 17.5$. This may be partially due to our prior selection of objects undetected on the POSS ($R \lesssim 20$).

We can get an idea of the content of the sources in our sample from the $R - K$ color distribution shown in Figure 3.4. This histogram consists of only 37 sources, of which 27 are non-detections in the R -band. This is mostly due to the nature of our observational programme, where we assigned lower priorities in our K -band imaging campaign to those objects that had been previously detected in the R -band. From this histogram, we can conclude that at least half of the sources observed have $R - K > 4$, but given that a significant number of the upper limits are quite shallow at $R > 24$, a larger fraction of sources than the 33% might have $R - K > 5$, and can be called extremely red objects (EROs, Elston, Rieke, & Rieke, 1988).

3.3.3 Surface brightness profiles

To obtain basic morphological information, we fitted surface brightness profiles in the near-IR images of the galaxies with sufficient S/N and not having close companion objects using the STSDAS task `ellipse`. The profiles are generated by fitting elliptical isophotes to the data, with the center, ellipticity, and position angle of each ellipse allowed to vary. The iterative method used in the fitting of each ellipse is described

more fully in Jedrzejewski (1987). We fitted each source interactively, and continued fitting outward isophotes until the ellipticity or position angle started showing large variations or before nearby companions were being picked up.

We did not attempt to fit radial profiles for (i) sources observed with CIRIM at CTIO, because the seeing was too poor, (ii) sources with companion objects within $<2''$, (iii) sources fainter than $K \sim 20$ in a $2''$ diameter aperture, and (iv) sources with an obvious non-elliptical morphology (e.g., TN J1049–1258, WN J1123+3141). Excluding these sources, we retain 45 objects.

3.3.4 Correlations with source parameters

Because our sample is virtually completely identified in the K -band, we can now examine some possible correlations between the parameters determined from the near-IR images (magnitude, color, ellipticity, position angle) and other source parameters (redshift, radio power, radio spectral index, radio size, radio position angle, emission line luminosity). Chapter 2 and 4 list the radio and spectroscopic parameters, and how they were determined. Because the vB98 sample consists of well-studied objects, we added their data to our sample to search for possible correlations.

Correlations with redshift

The most obvious correlation is between redshift and K -band magnitude, the so called Hubble $K - z$ diagram, which is discussed separately in §3.4. Because we have only 10 sources with both R - and K -band detections, the present data do not allow to check the possible existence of color evolution.

Correlations between morphological parameters

The radio and near-IR morphologies do not show strong correlations, except for the tendency for the main axis of the near-IR identification and the radio position angle to be aligned. We will come back to this point in §3.3.5.

Correlations with emission line luminosities

For less than 20 sources do we have information on the emission line luminosity of $\text{Ly}\alpha$ and/or $\text{C IV } \lambda\lambda 1549$. Neither these luminosities nor their ratio appear to be correlated with any of the photometric or morphological near-IR parameters, although a weak correlation between these parameters would not be detected in such a small sample.

K -band magnitude and radio spectral index

Because we use both the steepness of the radio spectral index and the faintness of the K -band magnitude to select the highest redshift radio galaxies, it is of interest to

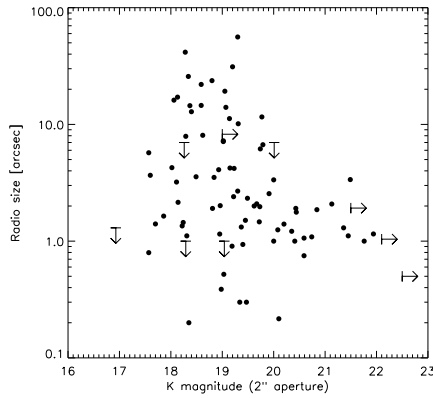


Figure 3.5: Radio largest angular size plotted against K -magnitude in a $2''$ diameter aperture. Note that all the $K > 20$ sources are $\lesssim 3''$, while the brighter sources have a large range of sizes.

examine if both parameters are correlated through their mutual redshift dependence. In our inhomogeneous sample, the low frequency spectral indices and $2''$ or $4''$ diameter aperture K -band magnitudes are correlated at the 88% significance level. However, we do not consider this number representative because of (i) the limited spectral index coverage $\alpha < -1.2$ in our sample, (ii) the incomplete K -band imaging of $<13\%$ of our sample, and (iii) the radio power dependence within our sample (see §3.4). To illustrate the importance of this third point, we note that mean/median the K -band magnitude of sources observed from our radio brightest MP sub-sample (see Chapter 2) is $\bar{K}_{MP} = 18.6$, while for our ~ 10 times fainter WN sample, $\bar{K}_{WN} = 19.4$. For these same sub-samples, the median spectral indices are $\bar{\alpha}_{MP} = -1.23$ and $\bar{\alpha}_{WN} = -1.41$.

K -band magnitude and radio size

Figure 3.5 shows the radio size plotted against K -band magnitude. The faint $K > 20$ sources are all very small ($\lesssim 3''$), while the brighter sources have a large range of radio sizes. Because the K -band imaging has an almost complete identification fraction, and the identifications of the large radio sources are unambiguous, we can exclude that the distribution in Figure 3.5 is due to selection effects.

The spectroscopic observations (see Chapter 4), concentrated on these weak sources with small radio sizes. Of the 18 $K > 20$ detections 13 were observed spectroscopically. We could determine the redshift of 7 objects, which have a mean of $\bar{z} = 3.67$, range from $z = 2.54$ to $z = 5.19$, and include the 4 highest redshift objects from our sample. For 3 objects, we did not detect any optical emission in our deep ($t_{int} = 1 - 1.5$ h) Keck spectra, while the remaining 3 objects have a faint optical continuum down to

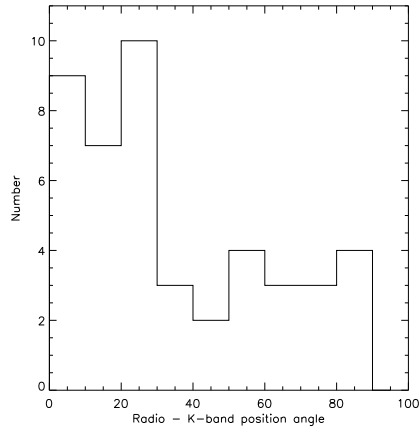


Figure 3.6: Distribution of the differences in position angle between the radio emission and the K -band emission of our USS sources, measured at the outer isophote of the ellipse fitting.

4800 Å, but no detectable emission or absorption lines. In Chapter 4, we discuss the possible nature of the objects lacking redshift determination.

Although we obtained redshifts for only 39% of the $K > 20$ objects with small radio sizes, they are significantly more distant than the other objects in our sample. This suggests that an angular size cutoff of $\lesssim 5''$ could also be used as an additional filter to select the highest redshift objects, prior to the K -band imaging. Such a cutoff has been used in several samples designed to find HzRG, such as the 6C* USS sample of Blundell et al. (1998). However, although the largest radio galaxy at $z > 4$ is 4''3 (8C 1435+635; Lacy et al., 1994), 5 out of the 16 known $3 < z < 4$ radio galaxies are $> 10''$ (Chapter 8), including 4C 41.17 at $z = 3.8$, which is as large as $13''$. It is therefore likely that applying such an angular size cutoff will also exclude a number of $z > 4$ radio galaxies, and it would also introduce additional selection effects.

3.3.5 Radio-near-IR alignment

Figure 3.6 shows a histogram of the difference in orientation between the position angle of the radio structure and the orientation of the near-IR image, as determined from the major axis of the outer fitted isophote in the K -band image. There is a clear trend for the radio and *observed* K -band morphologies to align. There are at least 2 additional objects in our sample that show an even closer correlation between the radio and near-IR morphologies: TN J1049-1258 and WN J1123+3141.

Our result is consistent with the high-resolution NICMOS H -band observations of 19 radio galaxies with $1.68 < z < 3.13$ (Pentericci et al., 2000b), which showed radio structures that are often (although with several notable exceptions) aligned with

the near-IR morphologies. In contrast, using K -band images from B2/6C sample (Eales et al., 1997) found no alignment effect, and argued that such a radio - near-IR alignment effect only occurs in the most luminous radio sources. Because our sample contains sources of similar or lower radio luminosity than the B2/6C sample, Figure 3.6 leads us to question the significance of the distribution based on only 9 objects shown in Figure 6 of Eales et al. (1997). We believe our result is more robust because (i) our sample is 5 times larger, (ii) the seeing in our observations is superior (and the pixel scale is 3 times smaller), and (iii) our limiting magnitude is ~ 2 magnitudes fainter.

Together with the previous NIRC observations of vB98 and the NICMOS observations of Pentericci et al. (2000b), our data confirm the existence of a radio-near-IR alignment effect. Because our sample contains objects over a wide redshift range, the question on the exact origin of the observed K -band emission arises. The spectroscopic redshifts of 1/4 of the objects with K -band images from our sample indicate that 1/3 are at $z < 2$, 1/3 at $2 < z < 3$ and 1/3 at $z > 3$ (Chapter 4). For the remaining objects, we estimate redshifts $1 < z < 3$, based on the Hubble $K - z$ diagram (see §3.4). Therefore, the observed K -band most likely samples rest-frame $\sim 5500 \text{ \AA}$ to $\sim 11000 \text{ \AA}$. The absence of strongly nucleated morphologies in the K -band images suggests there is no strong direct contribution from the AGN to the K -band emission. The images also do not show cone-like morphologies, which may be indicative of scattered AGN light along the radio jet axes (Chambers, Miley, & van Breugel, 1987; Cimatti et al., 1993). Stellar light therefore seems to be the most likely origin of the K -band emission. We will return to this issue in §3.4.

Without redshifts or high-resolution imaging in other wavelength bands, we cannot put any constraints on the age of this stellar population. At these large wavelengths, the stellar light in HzRGs might well be dominated by an old population, as argued on the basis of colors in the HST data of Pentericci et al. (2000b). However, a small contribution of a jet-induced young stellar population could well dominate the emission at wavelengths of $\lesssim 7000 \text{ \AA}$. Even when observed at a typical seeing of $0''.4$, we might not resolve this closely aligned component from the underlying old stellar population.

3.4 The Hubble $K - z$ diagram

Over the last 2 decades, the Hubble $K - z$ diagram has played an important role in the search for and the study of high redshift galaxies (e.g., Lilly & Longair, 1984; Eales et al., 1997, vB98). For example, the first radio galaxy discovered at $z > 3$ was selected from a radio sample on the basis of a faint $K \sim 18.5$ magnitude (Lilly, 1988). In our sample, we combine this faint K -band selection with our radio USS criterion, which provides a very efficient selection technique for finding extremely high redshift radio galaxies, and has already resulted in the discovery of the most distant radio source known to date at $z = 5.19$ (TN J0924-2201; Chapter 5).

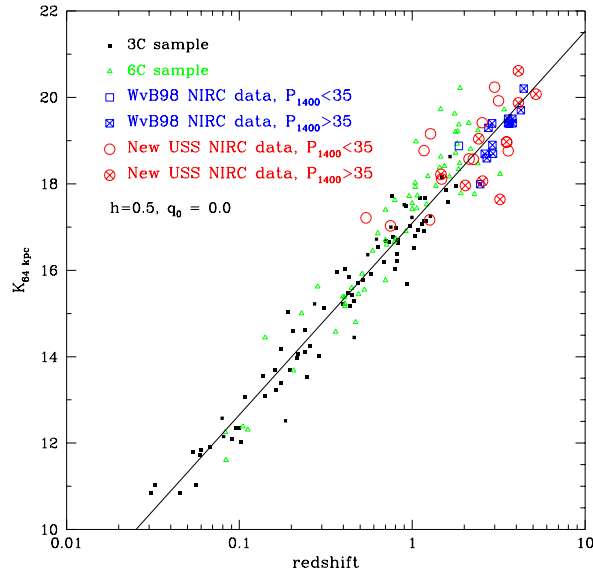


Figure 3.7: Hubble $K - z$ diagram of radio galaxies. Our new USS NIRC data are plotted in the same aperture corrected 64 kpc metric diameter magnitudes as the literature data from van Breugel et al. (1998) and Eales et al. (1997). The NIRC data of the sources with radio power $P_{1400} > 10^{35} \text{ erg s}^{-1} \text{ Hz}^{-1}$ are filled with a cross. The lines shows a linear fit to the data, but does not have a direct physical meaning.

3.4.1 The $K - z$ diagram for radio galaxies

Figure 3.7 presents a $K - z$ diagram that includes the 22 objects with K -band data and redshifts, augmented with data of 3 samples drawn from the literature: the 3C sample (Lilly & Longair, 1984; Dunlop & Peacock, 1993), the 6C/B2 sample (Eales et al., 1997), and the sample of HzRGs observed with NIRC by vB98. We followed the same photometric procedures as described in Eales et al. (1997) to ensure that all magnitudes are on the same metric system. This involves correcting the magnitudes measured in an $8''$ diameter aperture to a standard 64 kpc aperture, assuming the emission within an aperture of radius r is $\propto r^{0.35}$. This aperture correction dims the magnitudes by ~ 0.2 , with no strong dependence on redshift. As shown in Figure 3.1, the $8''$ diameter aperture is too large for most objects, but no smaller-aperture magnitudes have been published for large samples in the literature.

Our new HzRGs obey the same relation as the previous data, but have a larger scatter than the objects observed by vB98, even though the same observational setup was used in both samples. We now examine the possible reasons for this.

Contribution from emission lines. Most sources in the sample of vB98 are not subject to emission line contamination because they were observed through filters that avoid rest-frame wavelengths which include strong emission lines. Our observations could be more subject to line contamination because we used only the K - and K_S -band, mostly without prior knowledge of the spectroscopic redshift. However, the only lines that are expected to contribute significantly to the K -band magnitude are [O II] λ 3727, [O III] λ 5007, and H α (see McCarthy, 1993). This would lead to an asymmetric scatter towards brighter magnitudes around $z \sim 4.6$, 3.2, and 2.2. Only one object shows an excess magnitude at this redshift (WN J1123+3141), but this is an exceptional, complex merging system, in which enhanced star-formation may well contribute more to the K -band luminosity in the continuum than optical line emission ([O III] λ 5007). We therefore neglect this possibility.

Direct contribution from the AGN. According to unified models, the hosts of radio galaxies harbor hidden AGNs which are shielded from our direct view by thick obscuring material, while in quasars there is a direct line of sight toward the unresolved central AGN. Because the AGN emission is extremely bright relative to the emission from the stellar population in the host galaxy, even a small partially obscured contribution could have a significant influence on the total integrated K -band magnitude. However, this contribution would appear unresolved, which is not obvious in the images (see Fig. 3.2).

The low selection frequency (325 or 365 MHz) of our USS sample also tends to avoid objects which are dominated by a strong flat spectrum radio core (e.g., Blundell et al., 1998). Those objects are thought to be more Doppler boosted due to a decrease in the angle between the jet-axis and the line of sight. Such small viewing angles would increase the chance of a direct line of sight towards the central AGN, like in quasars. At $z \sim 1$, there is also observational evidence from studies of other samples of radio galaxies that the contribution of AGN emission to the K -band emission is small. The results of thermal IR observations of 3C and lower redshift radio galaxies by Simpson, Rawlings & Lacy (1999a); Simpson, Ward, & Wall (2000) show that even in the most powerful radio sources, the contribution by AGN emission to the K -band magnitude is $\lesssim 10\%$. Near-IR polarimetry observations by Leyshon & Eales (1998) indicate that scattered quasar light makes only a small contribution at near-IR wavelengths, even in sources where this contribution is important in the UV and optical.

Relation between radio power and mass of the host galaxy. Based on the observation that at $z \sim 1$, the K -band magnitudes of the stellar populations of the 3CR radio galaxies are brighter than those of the lower radio power 6C radio galaxies, Best, Longair & Röttgering (1998a) argued that the stellar masses of the more powerful radio galaxies are greater. The most powerful radio sources would possess radio beams with kinetic powers close to the Eddington limiting luminosity of a central super-massive black hole. In the likely assumption that the mass of the

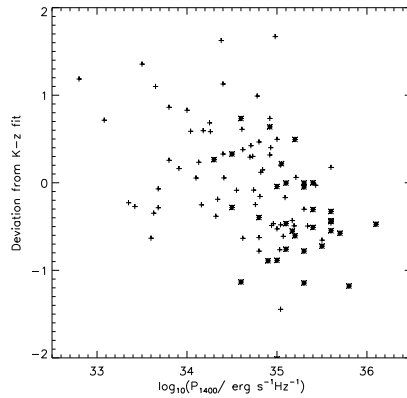


Figure 3.8: Deviation from a linear fit to the $\log_{10}(z) - K_{64kpc}$ relation plotted against radio power at 1.4 GHz, using the data from Figure 3.7. Plus-signs represent radio galaxies at $z < 2$, stars those at $z > 2$. These data show that, on average, lower luminosity radio sources have less luminous parent galaxies.

black hole scales with the mass of the host galaxy (e.g., Magorrian et al., 1998), the most powerful radio sources will contain more massive central engines together with their larger stellar mass. Additional evidence for the existence of such a relation was provided recently by Lacy, Bunker, & Ridgway (2000), who found that the *rest-frame* R -band magnitudes M_R of $z \sim 1$ radio galaxies increase with radio luminosity.

Figure 3.7 shows that the most powerful ($P_{1400} > 10^{36}$ erg s $^{-1}$ Hz $^{-1}$) radio galaxies display less scatter in the $K - z$ diagram than the lower power objects. Our USS sample is based on radio surveys that are 10 – 100 times fainter than the ones used to find the other HzRGs (see Figure 8.1), and therefore includes radio sources with a much larger range of radio luminosities, a natural explanation for the larger K vs. z scatter.

To examine this dependence quantitatively, we first fitted a linear relation to the $\log_{10}(z)$ vs. K_{64kpc} relation. This line, shown in Figure 3.7, does not have any direct physical meaning, and only serves to measure the deviation from the main trend at a certain redshift. We determined the radio power at 1.4 GHz rest-frame in a consistent way, using flux densities from the WENSS 325 MHz (Rengelink et al., 1997), Texas 365 MHz (Douglas et al., 1996), and NVSS 1.4 GHz (Condon et al., 1998); see Chapter 8 for more details. This procedure provides radio powers for 100 radio galaxies with known K -band magnitudes. Figure 3.8 shows the strong correlation between the deviation from the $K - z$ relation and radio power. The statistical significance of this correlation is $> 99.99\%$, with a Spearman rank correlation coefficient of $r = -0.50$. Considering only the 33 sources at $z > 2$, the significance drops to 87%, but as Figure 3.8 shows, the range in radio power of the $z > 2$ sources is insufficient to detect this correlation. Of course the linear fit to the $\log_{10}(z)$ vs. K_{64kpc}

relation is a serious over-simplification which may well introduce an artificial dependence in Figure 3.8. But the observation by Eales et al. (1997) at $z \sim 1$ that the 6C galaxies are on average 0.6 magnitudes fainter than the higher radio power 3C sources, and our findings from Figure 3.7 both indicate there is a real correlation between radio power and excess K -band emission.

The difference in scatter between the 2 samples observed with NIRC could also be reinforced by a spectroscopic selection effect in the sample of vB98. The redshifts of the HzRGs in the vB98 sample have been determined mostly with 3–4m class telescopes, and require bright emission lines to determine the redshift, while we performed the spectroscopy of our sample with the Keck telescope, and can determine redshifts of objects which have emission lines that are an order of magnitude fainter than before (see Chapter 4). Because radio power and emission line luminosity in HzRGs are correlated (e.g., Rawlings & Saunders, 1991; McCarthy, 1993; Chapter 8), the vB98 sample includes only objects with strong radio luminosities. This connection between the radio and emission line luminosities is most likely established through a mutual dependence on the black hole mass. This can also explain the small range in K -band magnitudes through the dependence of the host galaxy stellar mass on the same black hole mass (Best, Longair & Röttgering, 1998a; Lacy, Bunker, & Ridgway, 2000).

Assuming this radio power – host galaxy mass relation is the main determinant of the trends with radio power in the $K - z$ diagram, this would argue that the most massive galaxies at the highest redshifts can be found by selecting the most powerful radio sources.

3.4.2 Comparison with the $K - z$ diagram of radio-quiet galaxies

For almost two decades, this tight correlation in the Hubble $K - z$ diagram has been used as one of the strongest indications that radio galaxies are amongst the most massive systems at high redshift. However, this argument is based on the extrapolation from the $z \lesssim 1$ observations, where this is indeed the case. A direct comparison between the stellar populations of radio-loud and radio-quiet galaxies at $z \gtrsim 1$ has not been possible until only very recently. This situation has now changed with the availability of extremely deep imaging and spectroscopy of the Hubble Deep Field (HDF-North; Williams et al., 1996).

Dickinson et al. (2000) obtained a $t_{int} = 22.9$ h K -band image of the HDF-North using the IRIM camera at the Kitt Peak National Observatory 4m telescope in 1996 April. These images reach a formal 5σ limiting magnitude of $K = 21.92$ ($2''$ diameter aperture), which is comparable to or fainter than our NIRC HzRG images. M. Dickinson kindly provided us with a list of all 185 objects in the HDF-North with known spectroscopic redshifts, and their K -band magnitudes or limits. Because the K -band HDF-North image has much poorer resolution ($\sim 1''$ seeing) than the space-based HST images, the magnitudes of the individual objects were not measured in standard apertures. Instead, only objects detected in the HST NICMOS

F110W (J -band) and F160W (H -band) images were selected, convolved to match the ground-based K -band PSF, and then fitted to the K data. This way overlapping objects are deblended, and meaningful fluxes and limits to every object detected in the NICMOS data can be assigned, regardless of whether it can be detected or not in the ground-based K -band image. These magnitudes can be considered as approximately total magnitudes, and are calibrated to the same Vega-based photometric system, as also used for the observations of the radio-loud galaxies. The 185 spectroscopic redshifts have been compiled by M. Dickinson from identification campaigns of various groups. They are therefore a heterogeneous mix, and do not intend to be complete in any way. The highest redshift galaxy in the sample is HDF 4-473.0 at $z = 5.60$ (Weymann et al., 1998).

The HDF-North catalog contains mainly $z \gtrsim 0.3$ galaxies. To increase the number of radio-quiet galaxies at low redshifts ($z \lesssim 1$), we used the redshifts and K -band magnitudes of the Hawaii survey (Cowie et al., 1994; Songaila et al., 1994). These magnitudes were measured in a $3''$ or $3''.5$ diameter circular aperture, and then corrected to total magnitudes using an average correction determined from all bright isolated objects in the field (see Cowie et al., 1994 for details). Songaila et al. (1994) provide spectroscopic redshifts for the $K < 20$ objects. The highest redshift galaxy in this sample is at $z = 1.154$, and the list also contains a $z = 2.33$ BALQSO (Cowie et al., 1994), which we include for completeness, although it can not be directly compared with the other radio-quiet or radio-loud galaxies.

Because the 64 kpc metric apertures determined for the radio galaxies in Figure 3.7 are also our best estimated for their total magnitudes, we can now directly compare the K -band magnitudes of radio-quiet and radio-loud galaxies over the entire redshift range $0 < z < 5.2$. Figure 3.9 shows this composite Hubble $K - z$ diagram of radio-quiet and radio-loud galaxies. The most obvious difference with Figure 3.7 is the almost complete absence of a relation in the radio-quiet objects. There appears to be a deficiency of $K > 20$ objects at $z \lesssim 0.3$, but this is due to the limited survey area of the HDF, and the $K < 20$ limit of the spectroscopy of the Hawaii survey. This could also be a possible explanation for the absence of bright radio-quiet galaxies. Also note the dearth of sources in the 'redshift desert' at $1.5 \lesssim z \lesssim 2$, where no bright emission lines are observable with optical spectrographs.

Figure 3.9 shows that at $z \lesssim 1$, the radio-loud galaxies trace the bright envelope of the radio-quiet galaxies, while at $z \gtrsim 1$, they are $\gtrsim 2$ magnitudes brighter. This is some of the strongest evidence to date that powerful radio galaxies pinpoint the most massive systems out to the highest redshifts currently accessible.

Are all massive galaxies at high redshift powerful radio sources? To answer this question, a large-area spectroscopic survey of $K \sim 20$ galaxies, with follow-up radio observations would be needed. The coverage of the present optical surveys is of the order ~ 1 degree² (Hawaii survey) to 10 arcmin² (HDF), which is too small to detect statistically significant numbers of galaxies at the highest redshifts. Nevertheless, it is worth pointing out that the one $z > 4$ galaxy in the HDF that is more than a magnitude brighter than the other 6 at $z > 4$ is a $S_{1400} = 470 \mu\text{Jy}$ radio source

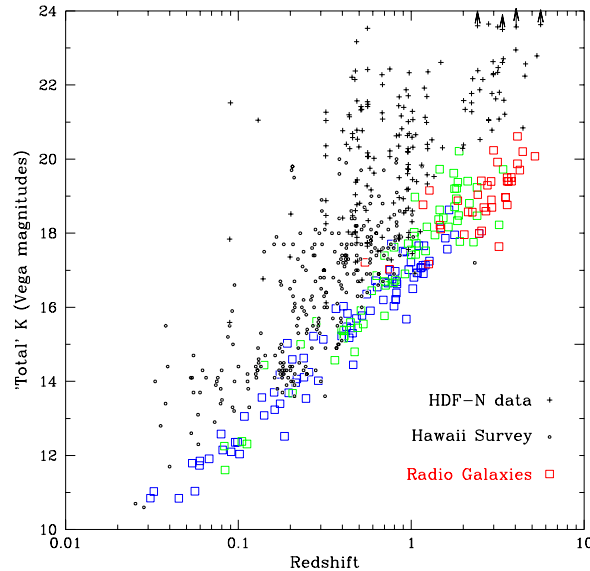


Figure 3.9: Composite Hubble $K - z$ diagram of radio-loud and radio-quiet galaxies. The radio-loud data is the same as in Figure 3.7; the radio-quiet data is taken from the HDF-North and the Hawaii survey. The radio-quiet galaxies do not show the strong correlation seen in radio-loud galaxies, and are significantly fainter than the radio-loud galaxies, which trace the bright envelope of the radio-quiet data at $z \lesssim 1$, and are 1 – 2 magnitudes brighter at $z \gtrsim 1$.

(VLA J123642+621331 at $z = 4.424$ Waddington et al., 1999). The radio power of this source is close to the FR I/FR II break, and the $0''.026$ resolution radio image of the HDF obtained with the European VLBI Network (EVN) indicates that there is an unresolved component of $220 \mu\text{Jy}$ in the source (M. Garrett et al., in preparation). Both these observations indicate that the radio emission from this source most likely originates from an AGN. At lower redshift, VLA J123644+621133 is a $z = 1.050$ FR I source (Richards et al., 1998). The $K = 16.92$ of this object is comparable to the the brightest 3C sources at these redshifts. Several other AGN in the HDF detected in deep radio and/or Chandra X-ray maps (Hornschemeier et al., 2000) inhabit fairly normal galaxies. One of the Chandra sources with a photometric $z_{\text{phot}} \simeq 2.6$ is an extremely red object with $K = 22.07$, and is probably a totally obscured AGN (M. Dickinson, private communication). Such obscured AGN at $z \lesssim 2$ might also be present in our radio selected sample (see Chapter 4).

To summarize, radio galaxies remain by far the most efficient tracers of the most massive galaxies at the highest redshifts accessible with optical spectrographs. Some of the most luminous objects at a given redshift in the optically selected surveys also

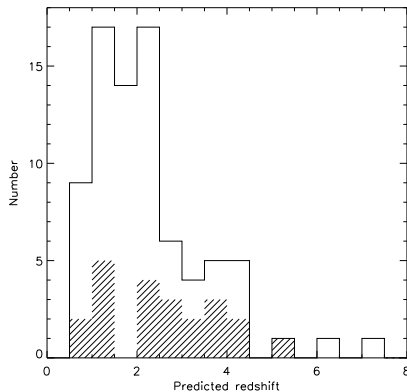


Figure 3.10: Predicted redshift distribution of the 80 objects with K -band detections. The redshifts are estimated from the $K-z$ diagram in Figure 3.7. The shaded histogram shows the distribution of the 22 objects with spectroscopic redshifts from this sample.

appear to harbour an AGN, but the present sample is too small to determine the fraction of massive galaxies that contains an AGN. Moreover, deep Chandra X-ray observations indicate that a substantial fraction of AGNs might be heavily obscured (Mushotzky et al., 2000), and might prove difficult to identify at optical or near-IR wavelengths. Because the life-time of a powerful radio source ($\sim 10^7$ y; Blundell & Rawlings, 1999b) is short compared to the Hubble time, it is likely that massive galaxies do exist during a period of radio inactivity.

3.5 Repercussions for HzRG searches

The original goal of the imaging programme was to identify our USS sources as promising high redshift radio galaxy targets for subsequent optical spectroscopy. We find that near-IR imaging is a far more efficient technique for obtaining HzRG identifications than optical imaging because it leads to an almost complete identification rate, and provides an approximate photometric redshift by means of the Hubble $K-z$ diagram. Figure 3.3 shows that the majority of the K -band images are relatively bright, suggesting a moderate average redshift for our USS sample. To examine this, we first transformed the $8''$ diameter apertures to 64 kpc metric apertures using the average correction of $K_{64kpc} = K(8'') + 0.2$. We then used the fit of the K_{64kpc} versus $\log_{10}(z)$ relation as obtained in §3.4 to determine the predicted redshift of these objects. Although this is a severe over-simplification which ignores the scatter in the $K-z$ relation, and is based on only 13% of the total number of sources in our USS sample, it can provide a first estimate of the redshift distribution of the 81 objects detected at K -band.

Figure 3.10 shows our predicted redshift distribution. The median predicted redshift from this sample is 2.06, while the mean is $\bar{z} = 2.25$. This median redshift is consistent with the compact radio morphologies in Figure 3,2 (see also vB98). Figure 3.10 also shows the distribution of the spectroscopic redshifts obtained, which has a mean/median at $z \simeq 2.5$. This difference illustrates the advantage of using an additional faint near-IR magnitude selection criterion to increase the chances for finding very high redshift radio galaxies.

The distributions in Figures 3.4 and 3.10 suggest that the majority of the sources in our sample are EROs at $0.5 \lesssim z \lesssim 2.5$ with a tail of very high redshift radio galaxies. Wide-field surveys of EROs have indeed shown that the density of ERO increases with K -band magnitude out to their completeness limit of $K \sim 19$ (e.g., Daddi et al., 2000). Because the imaging sub-sample selects objects at K -band, and a number of objects were even pre-selected to have faint R -band magnitudes, our sample includes a large number of EROs that happen to be radio-loud. This ERO population might represent more than half of our total sample, suggesting that EROs at $z \sim 1.5$ are probably important contributors to galaxy counts in steep-spectrum radio-selected samples.

3.6 Conclusions

We have obtained 83 optical images, and 85 near-IR images of sources selected from our USS sample. Our main conclusions from these observations are:

- $\sim 50\%$ of the objects are detected in the optical images down to $R \sim 24 - 25$.
- 94% of the objects are detected in the near-IR K -band down to $K \sim 22$, with a mean $\bar{K} = 19.26$ in a $2''$ diameter aperture. At least 2 of the 4 non-detections could be due to the low sensitivity of the radio maps.
- The distribution of $R - K$ colors shows that at least 1/3, and probably more, are EROs with $R - K > 5$. At least 4 objects have $R - K > 6$.
- The $K > 20$ identifications appear only associated with radio sources $\lesssim 2''$.
- The K -band morphologies show mostly compact objects typical of $z \lesssim 3$ radio galaxies.
- The major axes of the K -band morphologies, as determined from the fitting of ellipsoidal isophotes are preferentially oriented along the radio axes. This confirms the existence of a near-IR/radio alignment effect, presumably caused by a stellar population. High resolution color information would be needed to determine the age of this population.
- The 22 objects from our sample with known z and K obey the same relationship in the Hubble $K - z$ diagram as previous radio samples, but with a larger scatter.
- The scatter is dominated by the radio power, which is strongly correlated with the deviation from a linear fit to the $\log_{10}(z)$ vs. K_{64kpc} relation. This indicates that the most powerful radio sources are located in the most massive host galaxies, probably due to a mutual correlation of galaxy mass and radio power on the mass of the central

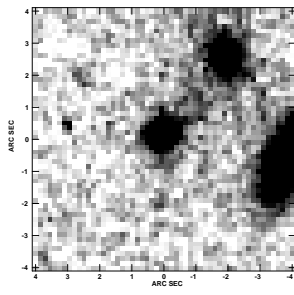
black hole. The previously known HzRGs were drawn from samples which included only the most powerful radio sources, giving rise to a tighter correlation in the $K - z$ diagram.

- A comparison between the $K - z$ relation of radio-loud and radio-quiet galaxies determined from the HDF-North and the Hawaii survey shows that the radio-loud galaxies define the luminous envelope of the K -band magnitudes at $z \lesssim 1$, while at $z \gtrsim 1$, the radio-loud galaxies are $\gtrsim 2$ magnitudes brighter. This is amongst the strongest evidence to date that radio galaxies trace the most massive forming stellar populations at high redshifts.
- Some of the brightest objects in the K -band from the optically selected surveys appear to contain AGN, suggesting that the fraction of massive galaxies containing AGN is quite high. However, a much larger K -band selected sample of high redshift galaxies would be needed to estimate this fraction.

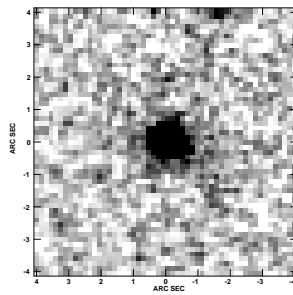
Acknowledgements

We thank Mike Brown for generously donating the half of his observing night with NIRC on Keck I on 1999 September 22 (which was not useful for his purposes as it was plagued by instrumental problems) for observations of our objects (WN J0346+3039 and WN J0359+3000). We thank Mark Dickinson for providing the catalog of redshifts and K -band magnitudes in the HDF-North, and for helpful comments on the $K - z$ diagram. We thank Roy Gal for obtaining Palomar 60'' images needed for the astrometry of a few of the fields. We are grateful for the excellent help provided by the staff of the Lick, Keck, ESO, CTIO, and WHT telescopes. We thank Philip Best for useful discussions. This research made use of the NASA/IPAC Extragalactic Database (NED) which is operated by the Jet Propulsion Laboratory, California Institute of Technology, under contract with the National Aeronautics and Space Administration. The Digitized Sky Survey was produced at the Space Telescope Science Institute under U.S. Government grant NAG W-2166. The images of these surveys are based on photographic data obtained using the Oschin Schmidt Telescope on Palomar Mountain and the UK Schmidt Telescope. The plates were processed into the present compressed digital form with the permission of these institutions. The work by C.D.B., W.v.B., and S.A.S. at IGPP/LLNL was performed under the auspices of the US Department of Energy by University of California Lawrence Livermore National Laboratory under contract W-7405-ENG-48. This work was supported in part by the Formation and Evolution of Galaxies network set up by the European Commission under contract ERB FMRX-CT96-086 of its TMR programme.

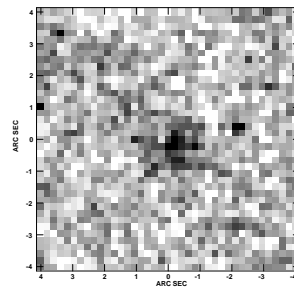
WN J0000+4654



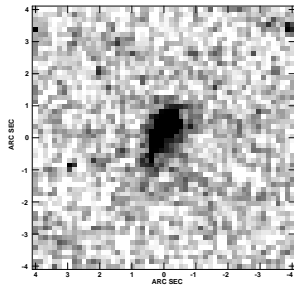
WN J0034+4142



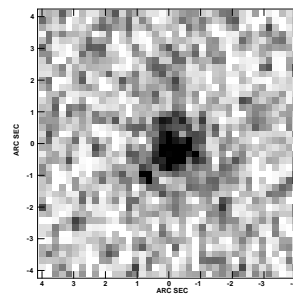
MP J0100-6403



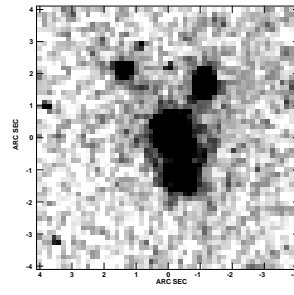
TN J0102-1055



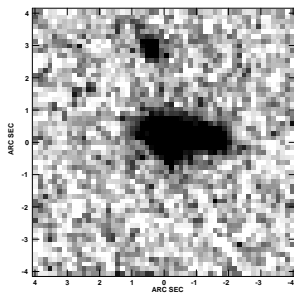
MP J0114-3302



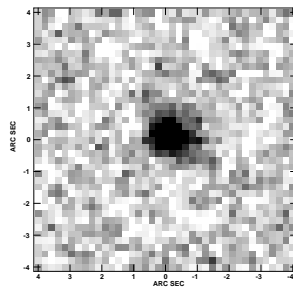
WN J0117+3715



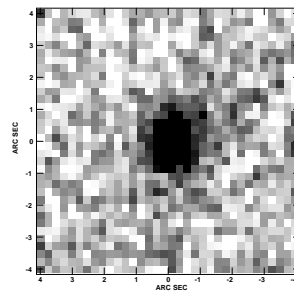
TN J0121+1320



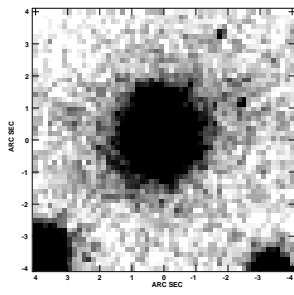
MP J0130-8352



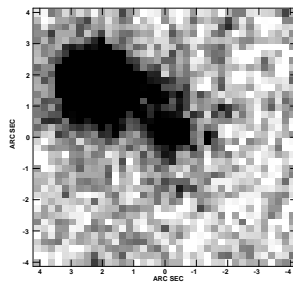
MP J0141-6941



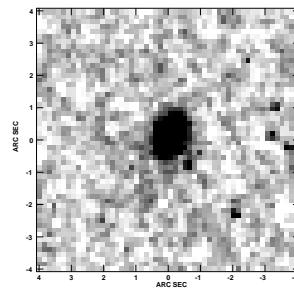
TN J0201-1302

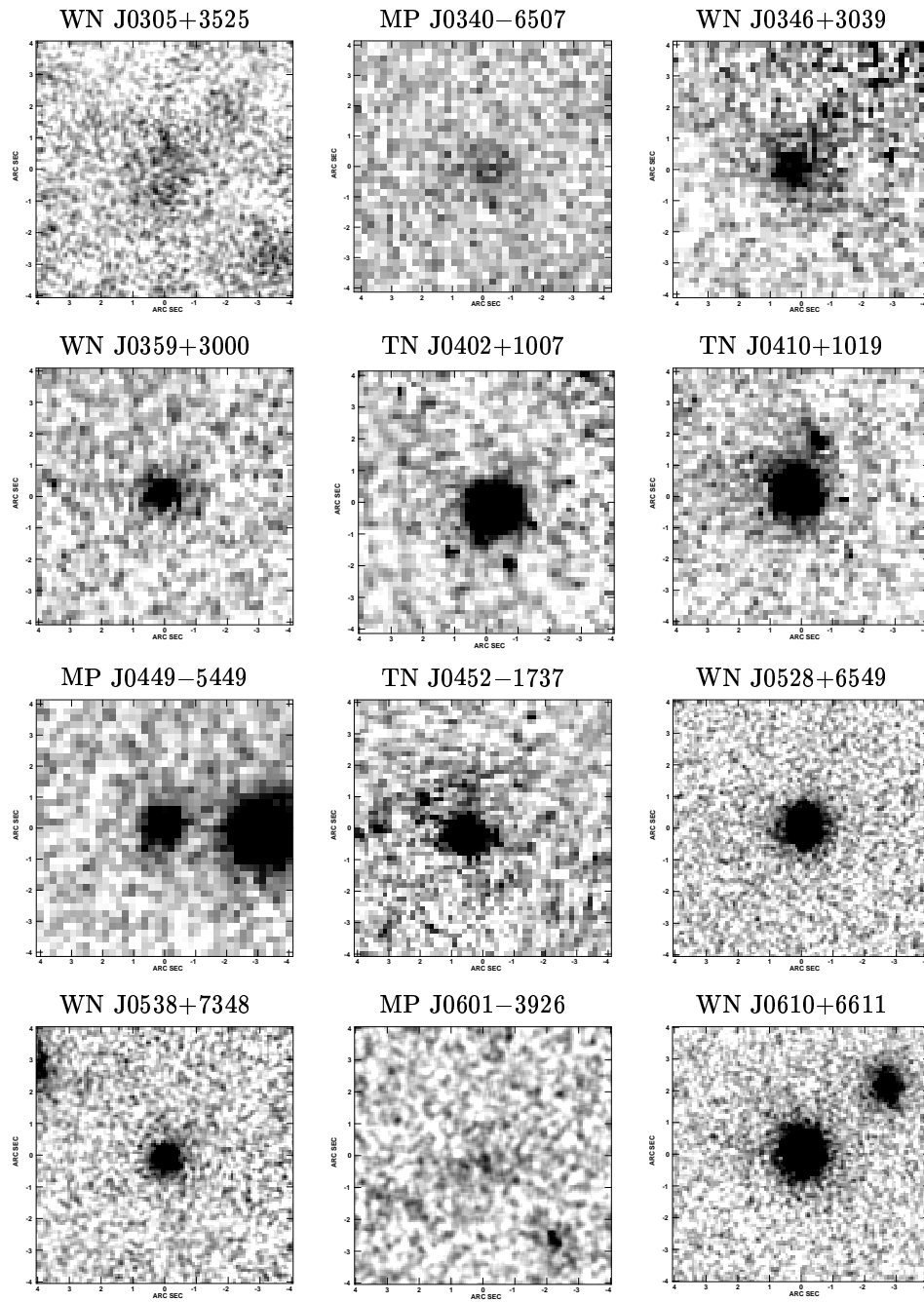


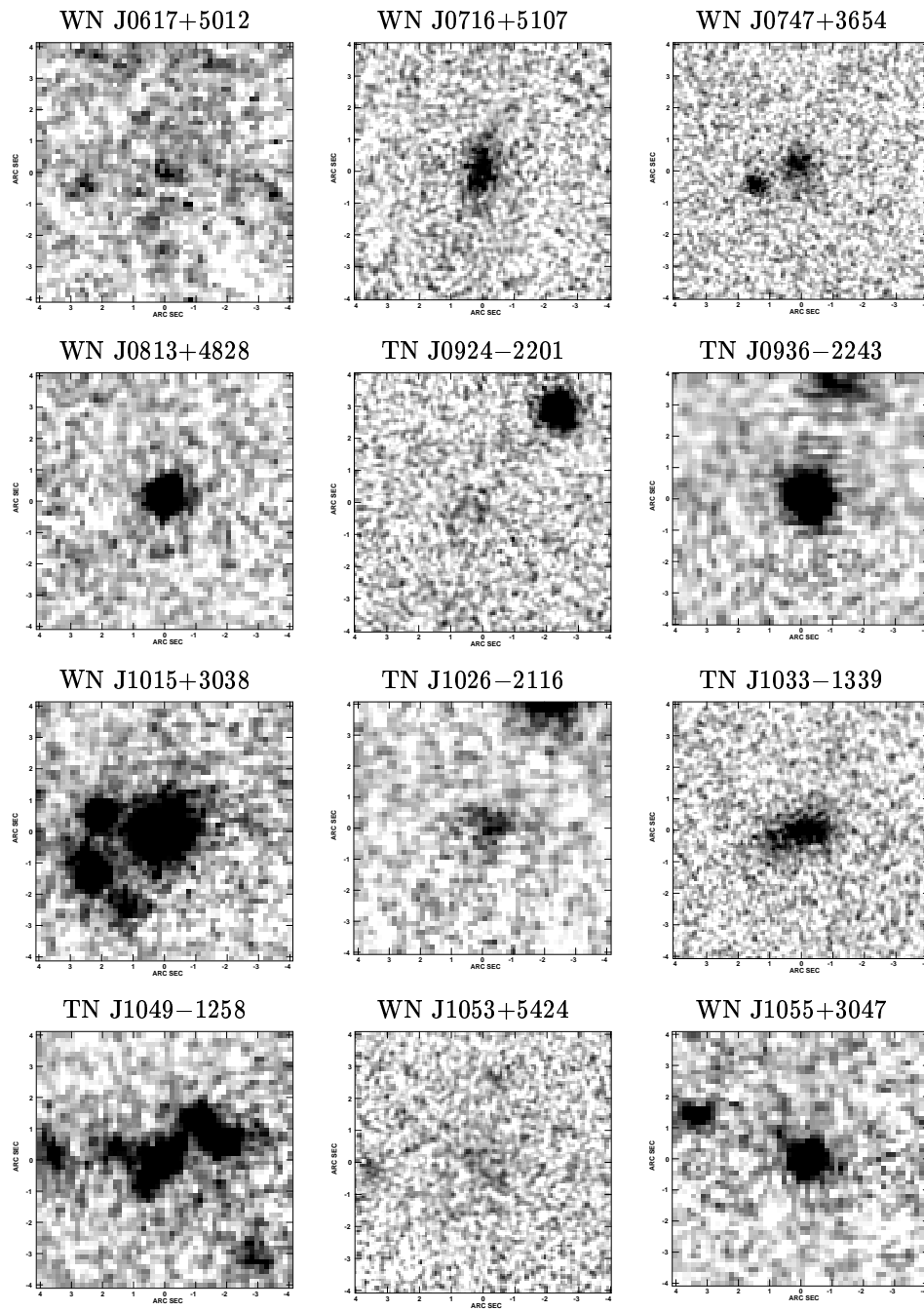
MP J0202-5425

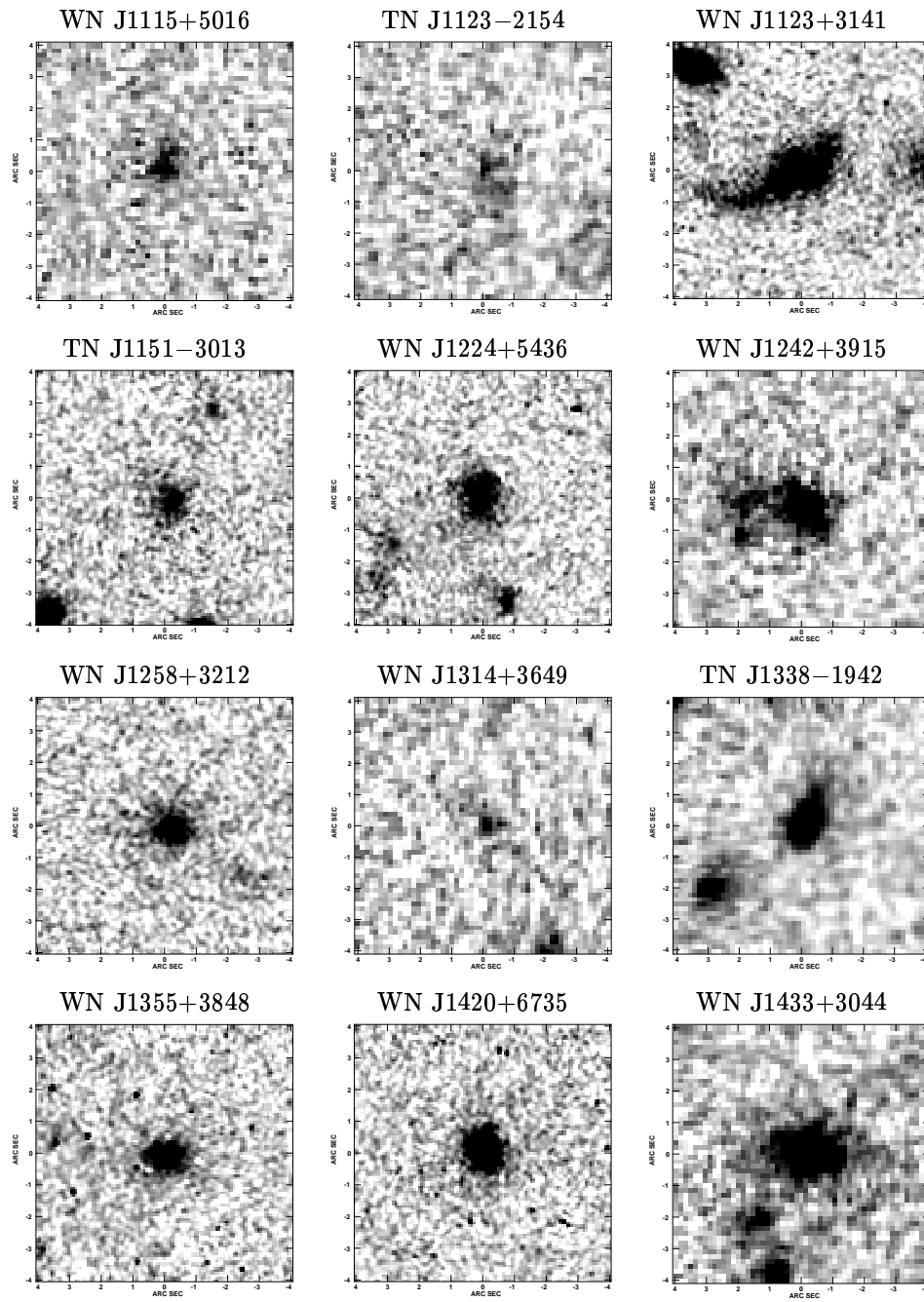


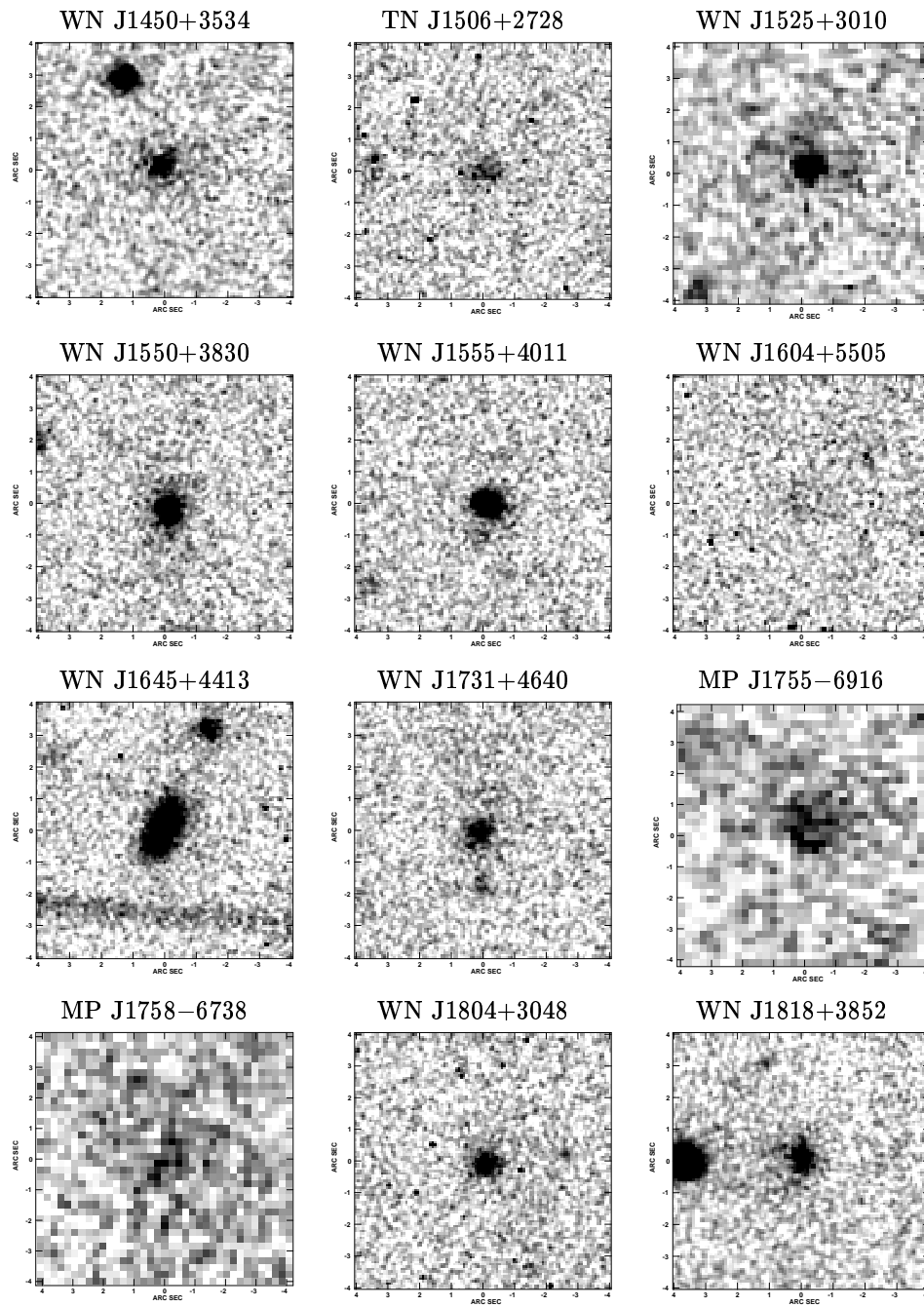
TN J0205+2242

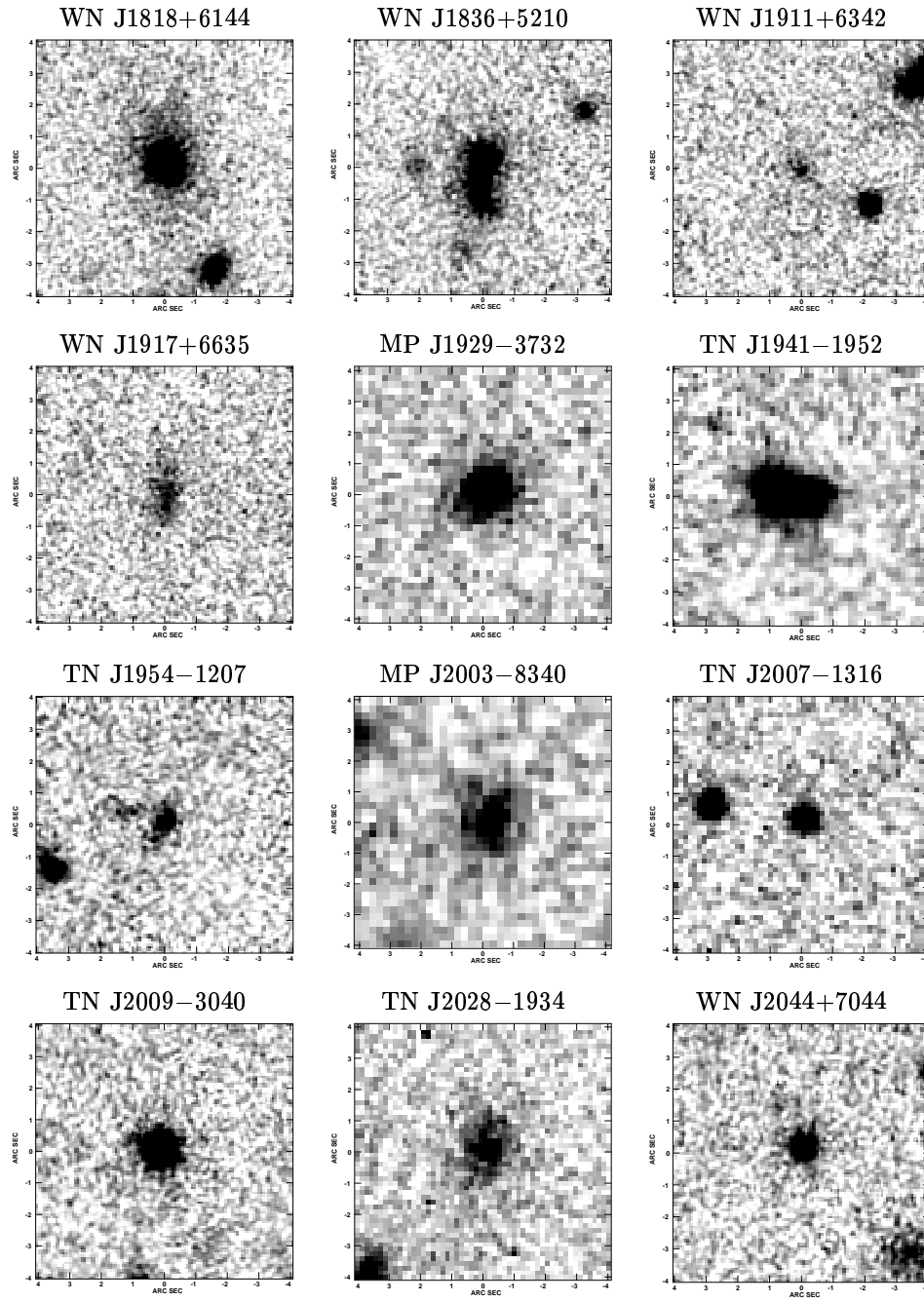












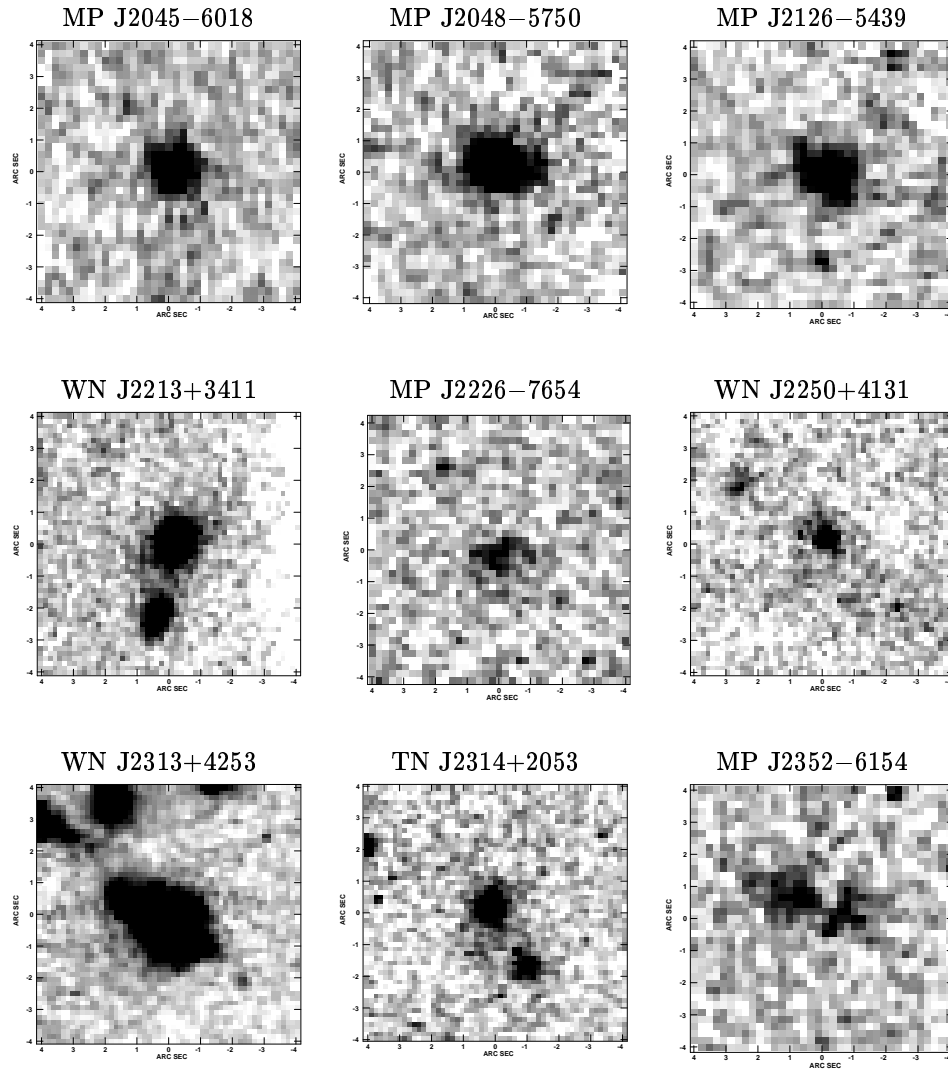


Figure 3.2: Cutout images of the 79 K -band detections. Each image is $8'' \times 8''$, and the origin is the position listed with 'O' in Table 3.6. The vector next to the name indicates the position angle of the radio source. The images are oriented North up and East left.

Spectroscopy of Ultra Steep Spectrum Radio Sources

C. De Breuck, W. van Breugel, H. Röttgering, D. Stern, G. Miley,
W. de Vries, S. A. Stanford, J. Kurk & R. Overzier 2000, AJ, submitted

Abstract

We present optical spectroscopy of 62 objects selected from several samples of ultra steep spectrum (USS) radio sources; 46 of these are from our primary catalog, consisting of sources with radio spectral indices $\alpha < -1.3$ ($S_\nu \propto \nu^\alpha$). Most are identified as narrow-lined radio galaxies with redshifts ranging from $z = 0.25$ to $z = 5.19$. Ten objects are at $z > 3$, nearly doubling the number of such sources known to date. Four of the USS radio sources are identified with quasars, of which at least three have very red spectral energy distributions. The source TN J0936–2242 is identified with an extremely red object (ERO, $R-K > 5$); both it and a close companion are at $z = 1.479$. The spectrum of the ERO closely resembles that of previously discovered radio galaxies at $z \sim 1.5$. Five sources show continuum emission, but fail to show any clear emission or absorption features, despite integrations of ~ 1 h with the Keck telescope. We suggest that these objects could be (i) radio galaxies with faint emission lines in the “redshift desert” at $1.5 \lesssim z \lesssim 2.3$, (ii) radio galaxies with an obscured AGN, which are dominated by a stellar continuum observed with insufficient S/N, or (iii) pulsars. Three radio sources identified with faint objects in the K -band images remain undetected in 50–90 min spectroscopic integrations with the Keck telescope, and are possible $z > 7$ candidates.

4.1 Introduction

The host galaxies of powerful radio sources have been identified with massive galaxies at low and intermediate redshifts (e.g., Best, Longair & Röttgering, 1998a). The close correlation in the Hubble $K - z$ diagram suggests this is also true out to the highest

redshifts (e.g., Eales et al., 1997; van Breugel et al., 1998). By studying high redshift radio galaxies (HzRGs), we can thus observe some of the largest mass concentrations on galaxy scales in the early Universe, and put constraints on galaxy formation theories. HzRGs are amongst the most luminous observable objects at very high redshift. Although unification theories of radio galaxies and quasars (e.g., Barthel, 1989) imply that we can also use quasars for such studies, radio galaxies offer a much clearer picture of the host galaxy, because of the absence of appreciable contamination from the active galactic nucleus (AGN). In radio galaxies, the cone of bright emission originating from the AGN is believed to be directed at large angles to the line of sight, and the AGN emission itself is presumed to be shielded by optically thick material. This “natural coronagraph” allows the study of the stellar populations in some HzRGs (e.g., Spinrad et al., 1997; Dey et al., 1997b; Fosbury, 2000) and investigations of the morphology of forming massive galaxies unhindered by issues of dynamic range (e.g., Pentericci et al., 1999a, 2000b).

In studying high redshift objects, a major advantage radio galaxies have over the large population of Lyman-break galaxies (e.g., Steidel et al., 1999) is that they are not selected on the basis of their optical properties, but on the basis of radio emission. In principle, a radio-selected survey with subsequent near-IR identifications can find galaxies out to $z \simeq 7$ (optical spectroscopy) or $z \simeq 16$ (near-IR spectroscopy), unrestricted to specific pass-bands, which limit optical color selection techniques. Such a continuous redshift range is important to select targets for follow-up observations that depend on atmospheric pass-bands in the near-IR or interference-free frequency ranges in the radio regime. For example, searches for associated HI 21cm line absorption are often hampered by local interference (Röttgering, de Bruyn, & Pentericci, 1999), and are only possible in limited redshift ranges. The absence of any *a priori* optical color selection also allows the discovery of objects with anomalous UV/optical spectral energy distributions, and because the radio emission is insensitive to dust absorption, radio-selected samples can provide an unbiased view with respect to the dust properties at high redshift. For example, the importance of dust at high redshift was recently shown by sub-mm observations of a large sample of HzRGs (Archibald et al., 2000), which suggest an increased detection rate at $z > 3$, even after k -correction effects are taken into account.

Previous searches for HzRGs, using 3-4m class telescopes have been difficult because the galaxies are faint ($R \gtrsim 24, K \gtrsim 20$), and fewer than 20 radio galaxies with $z > 3$ have been reported in the literature. However, with the availability of modern 8-10m class telescopes, it is now feasible to begin a systematic search for HzRGs at much fainter magnitudes than before. To start such a program, we constructed a sample of ultra steep spectrum (USS) radio sources (Chapter 2). Such sources have been used for two decades to find HzRGs. This technique mainly makes use of a “radio k -correction” effect: at higher redshift, an increasingly steeper part of the generally concave radio spectrum shifts to the fixed observing frequencies of the large radio surveys. Previous samples of USS sources have shown the efficiency of this technique in finding $z > 2$ radio galaxies: half of the $\alpha < -1.0$ ($S \propto \nu^\alpha$) sources are at $z > 2$

Table 4.1: WNR and TNR radio parameters

Name	S_{low}^a mJy	S_{1400} mJy	S_{4850} mJy	α_{325}^{1400}	α_{1400}^{4850}
TNR J0516+0637	269 ± 27	48.9 ± 1.1	8.60 ± 0.26	-1.27 ± 0.08	-1.40 ± 0.06
WNR J1338+3532	723 ± 29	131.0 ± 5.7	...	-0.71 ± 0.18	...
WNR J1356+3929	1440 ± 57	223.2 ± 9.2	...	-1.28 ± 0.04	...
TNR J1402-1510	2862 ± 53	795 ± 34	216.7 ± 4.8	-0.95 ± 0.04	-1.05 ± 0.04
WNR J1703+3739	31 ± 6	8.3 ± 0.4	...	-0.90 ± 0.11	...
TNR J2254+1857	175 ± 21	30.7 ± 1.7	7.2 ± 0.2	-1.29 ± 0.09	-1.16 ± 0.04

Name	Str ^b	LAS "	PA °	RA J2000	Dec J2000	Pos ^c
TNR J0516+0637	D	1.3	22	05 16 16.22	+06 37 18.0	V
WNR J1338+3532	D	11.6	159	13 38 15.09	+35 32 03.4	F
WNR J1356+3929	S	1.6	164	13 56 15.24	+39 29 43.7	F
TNR J1402-1510	D	15.9	80	14 02 08.66	-15 10 09.5	V
WNR J1703+3739	T	30.1	3	17 03 32.31	+37 39 00.8	F
TNR J2254+1857	D	2.7	36	22 54 53.71	+18 57 04.4	V

^a S_{325} for WNR sources, S_{365} for TNR sources.

^b Radio structure code: S=single, D=double, M=multiple morphology.

^c V=VLA observations, F=FIRST survey.

(Chambers et al., 1996a; Röttgering et al., 1997; Blundell et al., 1998). In our USS sample, which is based on several deep, large radio surveys that have recently become available, we select sources with spectral indices $\alpha < -1.30$ in order to enlarge the sample of $z > 3$ objects.

Our sample partially overlaps with the one of Kaplan et al. (2000a), who use a spectral index cutoff of $\alpha < -1.50$, also based on the 365 MHz Texas (Douglas et al., 1996) and 1.4 GHz NVSS (Condon et al., 1998) radio surveys, to study the distribution of extremely steep spectrum sources. Their sample emphasizes the contribution of pulsars, whose median spectral index is ~ -1.6 (Lorimer et al., 1995), and could represent a significant fraction of the steepest spectrum radio sources. In our sample, we have excluded the Galactic plane region ($|b| < 15^\circ$) in order to avoid large amounts of Galactic extinction; this should also reduce the number of pulsars in our sample.

Our observational campaign to find HzRGs from our sample of USS sources consists of three parts: (i) high resolution radio imaging (Chapter 2) to select sources with either compact or FR II Faranoff & Riley (1974) morphologies, and determine radio positions accurate to within $\sim 1''$; (ii) optical and near-IR imaging (Chapter 3) to identify the host galaxies of the radio sources; and (iii) optical spectroscopy, as described in this chapter. The organization of this chapter is as follows. In §4.2, we present the spectroscopic sample and describe both the observations and data reduction. The results comprise §4.3. In §4.4, we discuss the redshift distribution of the USS sources, the small population of USS quasars, and speculate on the nature of the sources lacking redshift determination. We summarize our results in §4.5. We defer a statistical analysis of the emission line regions in HzRGs to Chapter 8. Throughout, we assume $H_0 = 50 \text{ km s}^{-1} \text{ Mpc}^{-1}$, $q_0=0.5$, and $\Lambda = 0$.

Table 4.2: Sources from the Nelson (1995) USS sample

Name	RA J2000	Dec J2000	S_{4860} ^a mJy	α_{365}^{4860}	Str ^b	LAS "	PA °	z
TXS J0137+2521	01 37 06.81	+25 21 19.2	33	-1.29	D	6.9	82	2.896
TXS J1650+0955	16 50 04.83	+09 55 04.8	39	-1.25	D	19.4	56	2.509
TXS J1908+7220	19 08 23.70	+72 20 11.8	42	-1.28	T	14.4	14	3.542
TXS J2036+0256	20 36 34.78	+02 56 54.8	54	-1.37	D	3.1	34	2.129
TXS J2321+2237	23 21 42.28	+22 37 54.6	40	-1.28	D	8.1	24	2.555
TXS J2334+1545	23 34 58.30	+15 45 51.4	25	-1.38	D	6.4	133	2.481
TXS J2355-0002	23 55 35.57	-00 02 46.6	58	-1.26	T	33.8	127	2.590

^a Determined from VLA observations, except for TXS J2334+1545 and TXS J2351+1034 which were obtained from Becker, White, & Edwards (1991).

^b D=double, T=triple morphology.

4.2 Observations and Data Reduction

4.2.1 Target selection

We obtained the spectra presented in this chapter between April 1996 and April 2000. At the start of this spectroscopic campaign, our main USS sample was not finalized, as the final versions of the WENSS, Texas, NVSS and FIRST radio source catalogs were not yet published (see Chapter 2 for a description of these catalogs and our final USS sample, consisting of 669 sources). During this period, we observed objects from two other USS samples, as well as six sources that were excluded from our well-defined ($\alpha < -1.30$) USS sample when the revised flux densities in the radio survey catalogs were published. We refer to these sources using the prefix “WNR” and “TNR”, for sources removed from our WN and TN samples, respectively. We provide the final radio source parameters of these six objects in table 4.1. The entries in this table are similar to those for the sources in Chapter 2.

We selected seven sources from a sample of $\alpha_{365}^{4860} < -1.25$ sources constructed by Nelson (1995) from the 365 MHz Texas (Douglas et al., 1996) and 4.85 GHz Greenbank (Becker, White, & Edwards, 1991) surveys. In table 4.2, we reproduce from Nelson (1995) the J2000 coordinates, 4.86 GHz flux densities, spectral indices, angular sizes and position angles of the radio sources we observed spectroscopically. For completeness, we include the previously published Keck spectrum of TXS J1908+7220 (Dey, 1999). Two sources (USS J0006-0141 and PKS J1428-1502) are USS sources from the sample of Röttgering et al. (1994). We refer to that paper for details on the radio source parameters. In addition, we also present a Keck spectrum of the $z = 4.41$ radio galaxy 6C J0143+3253 (Rawlings et al., 1996), showing the C IV $\lambda\lambda$ 1549 line confirming the redshift.

All remaining sources are part of our main sample of 669 USS sources, described in Chapter 2. Here, we report spectroscopic results for 46 objects from this sample. We selected these objects mainly on the basis of observational constraints, preferentially selecting targets with the faintest K -band magnitudes, where available. We stress

Table 4.3: Spectroscopy Observing Runs

Session	UT Date	Telescope	Instrument	photometric?
K1	1995 Sep 27	Keck 10m	LRIS	yes
L4	1996 Apr 21	Lick 3m	Kast	yes
W1	1996 Jul 11–12	WHT 4.2m	ISIS	yes
E1	1996 Jul 15–16	ESO 3.6m	EFOSC1	yes
L6	1996 Nov 11	Lick 3m	Kast	yes
K2	1996 Nov 21	Keck 10m	LRIS	yes
E2	1997 Mar 5-6	ESO 3.6m	EFOSC1	yes
E3	1997 Apr 9–11	ESO 3.6m	EFOSC1	yes
K5	1997 Dec 2–3	Keck 10m	LRIS	no
K6	1998 Mar 7	Keck 10m	LRIS	yes
L15	1998 Oct 18–19	Lick 3m	Kast	yes
K9	1998 Dec 19–20	Keck 10m	LRIS	yes
V1	1999 Apr 19	VLT 8.2m	FORS1	yes
K11	1999 Jul 12	Keck 10m	LRIS	yes
K14	2000 Feb 1	Keck 10m	LRIS	yes
V2	2000 Apr 8–9	VLT 8.2m	FORS1	no?
K15	2000 May 5	Keck 10m	ESI	yes

that the spectroscopic sub-sample presented in this chapter is not necessarily representative of the entire sample of 669 sources, although we did select objects with a reasonably large spread in radio flux densities. For completeness, we include the data of three previously published objects from our USS sample, viz. the $z = 1.462$ red quasar WN J0717+4611 (Chapter 7), the $z = 4.11$ radio galaxy TN J1338–1942 (Chapter 6) and the $z = 5.19$ radio galaxy TN J0924–2201 (Chapter 5). We call the USS sample described in Chapter 2 our 'main' USS sample, while the 16 other sources originate from the commonly referred 'subsidiary' samples.

4.2.2 Observations

We obtained our spectra at five different observatories. We give an overview of the different observing sessions in table 4.3, an overview of the instrumental setups used in table 4.4, and a journal of the observations in table 4.5. We use a consecutive numbering scheme for each observing session, counting also the sessions where we did not obtain any data, or only imaging data (see Chapter 3). The R - and K -band magnitudes listed in table 4.3 are measured in a $4''$ diameter aperture are reproduced from Chapter 3, to which we refer for details on the photometry.

To acquire the faint ($20 \lesssim R \lesssim 25$) identifications of the radio galaxies in the slit of the spectrograph, we followed the same procedure at each observatory: we first centered the slit on a star visible on the Palomar Observatory Sky Survey ($R \lesssim 20$), followed by an offset to the position of the identification of the radio source, which we determined

Table 4.4: Observational setup

Telescope	Instrument	Grism/grating	λ coverage	Slit width	λ resolution
Keck	LRIS	300 ℓ mm ⁻¹	4100– 8800 Å	1''0	10 Å
		150 ℓ mm ⁻¹	4100–10000 Å	1''5	15 Å
VLT Antu	FORS1	600R	4350– 7250 Å	1''3	5.5 Å
		300V	3600– 8950 Å	1''0	12 Å
		300I	6350–10800 Å	1''0	11 Å
WHT	ISIS	R158B	3650– 6000 Å	2''5	16 Å
		R158R	6000– 8950 Å	2''5	15 Å
ESO 3.6m	EFOSC1	B300	3700– 7000 Å	2''5	20 Å
		R300	6000– 9900 Å	2''5	30 Å
Lick 3m	Kast	452/3306	3100– 6150 Å	2''0	6 Å
		300/7500	5200–10600 Å	2''0	8 Å

from the optical or K -band images presented in Chapter 3. For some of the faintest objects observed at Keck, we first acquired a fainter offset star that was within the same small field K -band image as the identification, before performing a final offset to the object. At the VLT, we used the FIMS software on the previously obtained K -band images to position the identification into the slit. We list the position angle used for each object in table 4.3. For objects with resolved radio morphologies, we oriented the slit in the direction of the radio jets. For the other objects, we either aligned the slit through possible companion objects, or used the parallactic angle (Filippenko, 1982).

Between exposures, we shifted the object by 10''–20'' along the slit to facilitate removal of fringing in the reddest parts of the CCD. During the second exposure, we performed a quick data-reduction of the first exposure, and if this yielded an unambiguous redshift, we shortened the second exposure to save observing time. We observed two or more standard stars during each night for spectrophotometric calibration, and wavelength calibration lamps either at the beginning or end of the night, or during the night at the position of the object to correct for small gravitational distortion factors on the CCD.

Lick 3m

We used the Kast double-beam imaging spectrograph (Miller & Stone, 1994) at the Lick 3m telescope on Mount Hamilton to obtain spectra of objects with $R \lesssim 22$. We used the d55 dichroic to split the light at 5500 Å. Because the seeing at Mount Hamilton is mostly poor, we consistently used a 2'' slit. The main advantage of using Kast for redshift determinations is the large continuous wavelength coverage from ~ 3150 Å to $\sim 10,000$ Å.

Table 4.5: Journal of the Spectroscopy Observations

Source	z	m_R (mag)	m_K (mag)	α_{radio}	Sample ^a	Session	t_{exp} (s)	Slit PA	Extraction width
USS J0006-0141	1.541	23	...	-1.36	Röt	E1	2700	46°	6''/4
WN J0040+3857	2.6055	>24.5	...	-1.36	DB	K9	1800	42°	2''/1
TN J0121+1320	3.516	>24	19.0	-1.34	DB	K5	3080	140°	2''/3
TXS J0137+2521	2.8970	-1.29	Nel	W1	3600	82°	3''/2
6C J0143+3253	4.41	-1.15	Raw	K1	2700	137°	2''/1
TN J0205+2242	3.5061	>24	19.0	-1.37	DB	K5	2400	156°	3''/8
WN J0231+3600	3.079	25.0	...	-1.30	DB	K9	1800	107°	2''/1
WN J0303+3733	2.506	23.2	...	-1.46	DB	K9	1200	171°	3''/4
WN J0310+3644	...	23.0	...	-1.70	DB	K9	3600	249°	1''/7
TN J0402+1007	...	>24	17.2	-1.38	DB	K9	1200	67°	1''/7
TN J0452-1737	2.256	>23	18.8	-1.37	DB	K9	1800	176°	3''/8
TNR J0516+0637	0.3568	-1.27	USSrem	E2	2700	22°	6''/1
TN J0517-0641	...	24.0	...	-1.46	DB	E2	2700	132°	...
WN J0617+5012	3.153	>24	20.4	-1.37	DB	K9	5400	10°	8''/5
WN J0717+4611	1.462	21.4	16.8	-1.30	DB	K2	3600	17°	2''/7
WN J0747+3654	2.992	>23	20.5	-1.41	DB	K14	5400	129°	1''/5
WN J0813+4828	1.274	23.9	19.0	-1.42	DB	K9	3600	132°	4''/2
TN J0910-2228	...	23.0	...	-1.58	DB	E3	1800	180°	4''/9
TN J0920-0711	2.760	22.4	...	-1.51	DB	E3	900	135°	4''/9
TN J0924-2201	5.19	>24	21.7	-1.63	DB	K9	10000	0°	1''/5
TN J0936-2243	1.479	>24	18.3	-1.45	DB	K9	3600	168°	1''/7
TN J0941-1628	1.644	23.0	...	-1.33	DB	E2	2700	3°	4''/7
WN J1015+3038	0.54	21.4	17.8	-1.38	DB	K9	1800	121°	2''/5
TN J1026-2116	...	>24	19.8	-1.39	DB	K9	3600	0°	...
TN J1033-1339	2.425	>24	19.2	-1.38	DB	E3	2700	287°	4''/3
TN J1102-1651	2.111	23.7	...	-1.35	DB	E2	2700	71°	5''/3
TN J1112-2948	3.09	21.5	...	-1.40	DB	E2	2700	299°	3''/8
WN J1115+5016	2.54	>24	19.5	-1.32	DB	K14	2700	30°	0''/8
TN J1123-2154	4.109	>24.5	20.3	-1.55	DB	K14	2400	79°	1''/3
WN J1123+3141	3.2174	21.3	17.8	-1.46	DB	L4	1800	90°	4''/7
TN J1151-3013	...	>24	19.8	-1.57	DB	E3	2700	180°	...
TN J1159-1629	...	23.4	...	-1.35	DB	E3	3600	215°	...
WN J1242+3915	2.131	23.6	18.6	-1.33	DB	K14	1800	51°	1''/5
WN J1314+3649	...	>26	22.1	-1.41	DB	K11	3600	126°	2''/1
WN J1333+3037	1.2127	22.5	...	-2.04	DB	K6	900	0°	2''/4
WNR J1338+3532	2.769	-0.71	USSrem	W1	3600	340°	3''/5
TN J1338-1941	4.11	23.0	20.0	-1.31	DB	E3,V1	2800	210°	4''/0
WNR J1356+3929	0.2525	-1.28	USSrem	W1	3600	156°	2''/6
TNR J1402-1510	0.739	-0.95	USSrem	E3	1800	260°	7''/8
PKS J1428-1502	2.349	22	...	-1.18	Röt	E1	2700	132°	9''/2
WN J1525+3010	...	25.3	19.5	-1.46	DB	K11	5400	90°	...
WN J1543+3512	0.7033	21.2	...	-1.56	DB	K6	600	0°	3''/3
TXS J1650+0955	2.510	23.5	...	-1.25	Nel	E1	2700	56°	5''/8
WNR J1703+3739	0.2561	-0.90	USSrem	W1	1800	183°	2''/6
MP J1755-6916	2.551	...	18.3	-1.25	DB	V2	1800	84°	1''/2
MP J1758-6738	2.026	...	18.3	-1.33	DB	V2	1800	237°	2''/0
WN J1836+5210	17.7	-1.41	DB	K11	1200	0°	2''/1
6C J1908+7220	3.536	21.2	16.5	-1.28	Nel	K1	3600	90°	2''/0
WN J1911+6342	3.590	...	19.9	-1.42	DB	K11	2700	0°	2''/1
WN J1917+6635	20.0	-1.30	DB	K11	3600	0°	2''/1
MP J1929-3732	0.7476	...	17.1	-1.29	DB	V2	1400	352°	3''/2
TN J1954-1207	19.9	-1.38	DB	K11	3600	36°	3''/2
MP J2003-8340	1.169	...	18.4	-1.28	DB	V2	1200	99°	1''/6
TXS J2036+0256	2.130	24	...	-1.37	Nel	E1	2700	33°	5''/2
WN J2044+7044	...	>24	19.2	-1.38	DB	K11	3000	90°	...
MP J2045-6018	1.464	...	18.0	-1.30	DB	V2	3600	37°	4''/4
MP J2048-5750	1.262	...	17.2	-1.22	DB	V2	1200	32°	2''/8
TNR J2254+1857	2.153	-1.29	USSrem	L6	3600	36°	3''/8
WN J2313+4053	2.99	-1.50	DB	L15	3600	90°	6''/3
TXS J2321+2237	2.553	-1.28	Nel	W1	3600	27°	6''/2
TXS J2334+1545	2.480	23	...	-1.38	Nel	E1	2700	133°	4''/7
TXS J2355-0002	2.587	23	...	-1.26	Nel	E1	4500	127°	4''/8

^a DB=Chapter 2; Röt=Röttgering et al. (1994); Nel=Nelson (1995); Raw=Rawlings et al. (1996);

USSrem=USS removed sources, this chapter.

NOTE: Colons denote uncertain redshifts.

WHT 4.2m

During our observing run at the William Herschel 4.2m Telescope at La Palma, we used the ISIS double beam spectrograph (Carter et al., 1994) with a dichroic splitting the light at 6100 Å and used a 2''/5 wide slit. In the blue arm, we used a recently com-

missioned LORAL1 CCD, which experienced problems with the flat-field exposures and disk storage, and consequentially lost most of the data at $\lambda < 6000 \text{ \AA}$. In the red arm, we used a TEK5 CCD and were not subject to these problems.

ESO 3.6m

To extend our spectroscopic sample into the southern hemisphere, we used the ESO faint object spectrograph and camera (EFOSC1; Savaglio, Benetti, & Pasquini, 1997) on the ESO 3.6m telescope at La Silla. We first observed each object with the B300 grating, covering $\sim 3700 \text{ \AA}$ to $\sim 7000 \text{ \AA}$ and re-observed the best high redshift candidates with the R300 grating, which covers $\sim 6000 \text{ \AA}$ to $\sim 9900 \text{ \AA}$.

VLT 8.2m

On two occasions, we used the FORS1 spectrograph (Appenzeller et al., 1997) on the ESO VLT Antu telescope. In 1999 April, we obtained a deep spectrum of the Ly α line in TN J1338–1942 (Chapter 6). In 2000 April, we observed six very southern USS sources as additional targets after the main target of the observing run reached high airmass (the main goal of this run was to detect cluster galaxies around HzRGs, see Kurk et al. 2000).

Keck 10m

To obtain deeper spectra of those objects that failed to yield redshifts on the 3-4m telescopes described above, we first obtained deep K-band images with the near infrared camera (NIRC; Mathews & Soifer, 1994) on the Keck I telescope (see Chapter 3 for details). We then determined accurate offsets from these images for deeper spectroscopy with the Low Resolution Imaging Spectrometer (LRIS; Oke et al., 1995) at the Keck II telescope on Mauna Kea. During all runs prior to 1998 December, we used the $300 \ell \text{ mm}^{-1}$ grating blazed at 5000 \AA combined with the $1''$ wide slit, which results in a resolution of $\sim 10 \text{ \AA}$ (FWHM), with a wavelength coverage from $\sim 4100 \text{ \AA}$ to $\sim 8800 \text{ \AA}$. Starting from our 1998 December run, we used the $150 \ell \text{ mm}^{-1}$ grating blazed at 7500 \AA combined with the $1''.5$ wide slit, which results in a resolution of $\sim 15 \text{ \AA}$ (FWHM) and a wavelength coverage from $\sim 4000 \text{ \AA}$ to $\sim 10,000 \text{ \AA}$, but with poor S/N at the red end.

4.2.3 Data reduction

We reduced our spectra using the NOAO IRAF package. After bias correction using the overscan region, we flat-fielded the spectra using internal lamps or dome-flats, and removed the cosmic rays using the task ‘szap’, which is based on the cosmic ray cleaning routine ‘xzap’ from the DIMSUM¹ package. For objects with only a single

¹DIMSUM is the Deep Infrared Mosaicing Software package, developed by P. Eisenhardt, M. Dickinson, A. Stanford, and J. Ward, which is available as a contributing package in IRAF.

exposure, we subtracted the sky emission using a third order polynomial interpolation along the slit at the position of the object. For those objects with more than one exposure, we subtracted one of the bracketing exposures which was shifted by $\sim 10''$ along the slit, and subtracted the residual sky contribution which is due to the variation of the sky brightness. After registration using an integer pixel shift determined from other objects along our long slit, we summed both exposures, and extracted a one-dimensional spectrum. Because most of our objects are very faint, we used the aperture that included the maximal amount of line flux for each object instead of a standard aperture (the exact values for each object are listed in table 4.5). The use of a wide aperture is justified in HzRG spectra, as the emission line regions are often very extended; the main use of our spectra is the redshift determination and relative line flux ratios between the individual emission lines. In most cases, deeper spectra are needed to study the faint continuum flux. We extracted a calibration lamp spectrum using the same aperture as that for the object, and corrected the derived wavelength solution by applying a small additional offset determined from a comparison with the wavelength of several well-resolved skylines (e.g., Osterbrock & Martel, 1992). Finally, we flux calibrated the spectra using standard star observations obtained during each observing night. We estimate our flux calibration is accurate to $\sim 20\%$, except for the objects which were observed in non-photometric conditions (see table 4.5). We include the derived line fluxes of these sources nevertheless for line-ratio studies.

4.3 Results

4.3.1 Redshifts and line parameters

We used the procedures described in Röttgering et al. (1997) to determine the central wavelength, total line flux, de-convolved widths, and rest-frame equivalent widths (with their related errors) of all the emission and absorption lines detected in our spectra. For each object, we quote a single redshift, which is an average of all the lines, weighed by the uncertainties due to the line fitting and wavelength calibration (see Röttgering et al., 1997). We present the results for the sources in our main and subsidiary USS samples (see §4.2.1) in table 4.6, and show extracted one-dimensional spectra in figure 4.8.

To determine the redshift and identify the emission and absorption lines, we compared our spectra with composite HzRG spectra (McCarthy, 1993; Stern et al., 1999a). The spectra at $z \gtrsim 2$ are generally dominated by extended Ly α with a large equivalent width ($W_{\lambda}^{rest} \sim 100\text{\AA}$; Stern et al., 1999a). The brightest confirming lines are C IV $\lambda\lambda$ 1549, He II λ 1640, C III] λ 1909, and C II] λ 2326. In some cases, we also detected N V λ 1240, O VI λ 1035 and the Si IV/O IV λ 1400 complex. In the lower redshift objects, the spectra are generally dominated by [O II] λ 3727, [O III] λ 5007, or H α . Confirming lines in these objects are [Ne IV] λ 2424, Mg II λ 2800, [Ne IV] λ 3426,

Table 4.6: Emission and absorption line parameters of sources from the WN/TN/MP USS sample.

Source	z	Line	λ_{obs} Å	$10^{-16} \times \text{Flux}$ erg/s/cm ²	Δv_{FWHM} km s ⁻¹	$W_{\lambda}^{\text{rest}}$ Å
USS 0006-0141	1.541 ± 0.006	C IV $\lambda\lambda$ 1549	3950 ± 1	5.9 ± 1.2	850 ± 300	> 118
		He II λ 1640	4181 ± 2	3.9 ± 0.8	1050 ± 400	35 ± 11
		C III] λ 1909	4862 ± 1	3.4 ± 0.5	900 ± 200	23 ± 3
		C II] λ 2326	5899 ± 1	1.0 ± 0.2	< 150	6 ± 1
		[Ne IV] λ 2424	6180 ± 3	1.7 ± 0.3	1000 ± 300	11 ± 2
WN J0040+3857	2.6055 ± 0.0005	L α	4386 ± 3	4.1 ± 0.5	2600 ± 500	> 479
		C IV $\lambda\lambda$ 1549	5585 ± 1	1.0 ± 0.5	700 ± 250	69 ± 18
		He II λ 1640	5913 ± 1	0.1 ± 0.1	< 225	9 ± 3
		C III] λ 1909	6873 ± 19	0.6 ± 0.1	2600 ± 1700	33 ± 9
TN J0121+1320	3.516 ± 0.002	L α	5500 ± 5	$178^{\dagger} \pm 50$	1350 ± 400	300 ± 100
		C IV $\lambda\lambda$ 1549	6994 ± 4	$22.1^{\dagger} \pm 2.7$	1300 ± 500	26 ± 5
		He II λ 1640	7411 ± 6	$24.9^{\dagger} \pm 3.1$	1600 ± 550	40 ± 10
		C III] λ 1909	8617 ± 8	$6.2^{\dagger} \pm 2.6$	400 ± 350	> 3
TXS J0137+2521	2.8970 ± 0.0005	L α	4738 ± 1	12.0 ± 1.2	950 ± 150	> 326
6C 0143+3253	4.413 ± 0.002	L α	6582 ± 1	6.38 ± 0.64	1350 ± 100	500 ± 150
		C IV $\lambda\lambda$ 1549	8399 ± 2	0.15 ± 0.03	300 ± 200	9 ± 3
TN J0205+2242	3.5061 ± 0.0004	L α	5479 ± 1	$792^{\dagger} \pm 79$	1300 ± 200	650 ± 100
		Si IV/ O IV	6316 ± 22	$14.1^{\dagger} \pm 2.6$	2650 ± 2050	14 ± 3
		C IV $\lambda\lambda$ 1549	6981 ± 1	$44.2^{\dagger} \pm 4.7$	850 ± 200	40 ± 7
		He II λ 1640	7392 ± 4	$30.1^{\dagger} \pm 3.7$	1100 ± 400	33 ± 8
		C III] λ 1909	8598 ± 20	$19.3^{\dagger} \pm 6.2$	< 1350	> 12
WN J0231+3600	3.079 ± 0.002	L α	4960 ± 2	1.1 ± 0.1	1950 ± 350	100 ± 25
WN J0303+3733	2.506 ± 0.002	L α	4263 ± 1	10.3 ± 1.0	1950 ± 300	550 ± 250
		Si IV/ O IV	4940 ± 63	1.3 ± 0.3
		C IV $\lambda\lambda$ 1549	5438 ± 5	1.5 ± 0.2	2000 ± 450	68 ± 15
		He II λ 1640	5749 ± 4	0.5 ± 0.1	1100 ± 400	21 ± 5
		C III] λ 1909	6687 ± 3	1.4 ± 0.2	1600 ± 400	65 ± 13
		C II] λ 2326	8140 ± 10	0.4 ± 0.1	800 ± 600	...
TN J0452-1737	2.256 ± 0.003	He II λ 1640	5348 ± 2	0.3 ± 0.1	1000 ± 400	6 ± 1
		C III] λ 1909	6212 ± 1	0.1 ± 0.1	< 250	3 ± 2
		C II] λ 2326	7587 ± 3	0.4 ± 0.1	550 ± 250	9 ± 2
TNR J0516+0637	0.3568 ± 0.0002	[O II] λ 3727	5056 ± 1	2.1 ± 0.3	500 ± 150	24 ± 3
		G-band	5819 ± 16	-2.7 ± 0.6	3000 ± 1700	...
WN J0617+5012	3.153 ± 0.002	L α	5050 ± 2	0.8 ± 0.2	1600 ± 350	> 400
WN J0717+4611	1.462 ± 0.001	C IV $\lambda\lambda$ 1549	3816 ± 2	30.2 ± 4.0	1300 ± 400	28 ± 12
		C III] λ 1909	4700 ± 2	0.9 ± 0.1	1350 ± 300	6 ± 1
		C II] λ 2326	5726 ± 2	0.4 ± 0.1	1300 ± 400	3.2 ± 0.4
		[Ne IV] λ 2424	5968 ± 2	0.6 ± 0.1	1150 ± 300	2.8 ± 0.4
		Mg II λ 2800	6900 ± 2	6.6 ± 0.6	11000 ± 500	13 ± 1
		[Ne IV] λ 3346	8242 ± 3	0.5 ± 0.3	500 ± 350	1.2 ± 0.4
		[Ne IV] λ 3426	8437 ± 2	0.7 ± 0.3	600 ± 200	1.2 ± 0.4
WN J0747+3654	2.992 ± 0.004	L α	4863 ± 3	0.78 ± 0.09	2050 ± 450	400 ± 150
		Si IV/O IV	5579 ± 19	0.13 ± 0.04	2350 ± 1250	14 ± 4
		C IV $\lambda\lambda$ 1549	6178 ± 7	0.17 ± 0.03	1350 ± 600	31 ± 11
		He II λ 1640	6541 ± 4	0.22 ± 0.04	1050 ± 600	38 ± 12
		C III] λ 1909	7625 ± 33	0.11 ± 0.05	< 2150	> 48
		C II] λ 2326	9286 ± 6	0.20 ± 0.04	850 ± 500	> 26
WN J0813+4828	1.274 ± 0.001	C III] λ 1909	4330 ± 13	0.2 ± 0.1	1500 ± 1300	1291 ± 8
		C II] λ 2326	5300 ± 9	0.4 ± 0.1	1950 ± 1150	28 ± 7
		[Ne IV] λ 2424	5510 ± 8	0.2 ± 0.1	< 1100	9 ± 4
		Mg II λ 2800	6376 ± 20	0.1 ± 0.1	< 1250	> 5
		[Ne IV] λ 3426	7795 ± 18	0.4 ± 0.2	< 1950	18 ± 8
		[O II] λ 3727	8476 ± 2	2.2 ± 0.3	800 ± 250	74 ± 15
		[Ne III] λ 3869	8798 ± 59	1.3 ± 0.4	3350 ± 2800	32 ± 10
TN J0920-0711	2.760 ± 0.003	L α	4573 ± 1	44.0 ± 4.4	2050 ± 150	350 ± 60
		Si IV/ O IV	5281 ± 8	0.6 ± 0.3	1100 ± 600	5 ± 2
		C IV $\lambda\lambda$ 1549	5831 ± 1	3.6 ± 0.5	1100 ± 200	37 ± 7
		He II λ 1640	6155 ± 1	3.0 ± 0.4	950 ± 200	29 ± 5
TN J0924-2201	5.195 ± 0.007	L α	7531 ± 9	0.35 ± 0.06	1500 ± 200	> 180

Source	z	Line	λ_{obs} Å	$10^{-16} \times \text{Flux}$ erg/s/cm ²	Δv_{FWHM} km s ⁻¹	$W_{\lambda}^{\text{rest}}$ Å
TN J0941-1628	1.644 ± 0.001	C IV λλ 1549	4095 ± 3	3.2 ± 0.5	2100 ± 600	> 140
		He II λ 1640	4331 ± 3	0.9 ± 0.2	1250 ± 450	29 ± 9
		C III] λ 1909	5051 ± 2	2.0 ± 0.3	1900 ± 400	72 ± 15
		C II] λ 2326	6149 ± 2	1.9 ± 0.2	1500 ± 250	59 ± 9
TN J1033-1339	2.425 ± 0.002	Lyα	4164 ± 1	9.8 ± 1.0	2000 ± 200	> 885
		Si IV/ O IV	4806: ± 17	4.1: ± 0.5	62000 ± 2300	...
		C IV λλ 1549	5308 ± 2	2.3 ± 0.3	1500 ± 300	140 ± 50
		He II λ 1640	5623 ± 3	0.8 ± 0.1	950 ± 200	> 128
		C III] λ 1909	6527 ± 4	0.7 ± 0.1	900 ± 250	56 ± 27
TN J1102-1651	2.111 ± 0.003	Lyα	3781 ± 1	2.7: ± 0.5	800 ± 250	> 129 :
		C IV λλ 1549	4824 ± 1	1.0 ± 0.2	700 ± 250	35 ± 11
		He II λ 1640	5090 ± 3	1.3 ± 0.2	1350 ± 400	57 ± 20
		C III] λ 1909	5927 ± 7	1.1 ± 0.2	1750 ± 550	53 ± 20
TN J1112-2948	3.09 ± 0.01	Lyα	4976 ± 1	2.9 ± 0.3	1300 ± 150	93 ± 21
		C IV λλ 1549	6307: ± 1	0.7: ± 0.1	500: ± 150	42: ± 17
		He II λ 1640	6717 ± 1	1.2 ± 0.1	800 ± 150	38 ± 8
WN J1115+5016	2.54 ± 0.01	Lyα	4323 ± 2	2.03 ± 0.21	2550 ± 400	350 ± 150
		C IV λλ 1549	5413 ± 8	-0.18 ± 0.03	1950 ± 850	-4 ± 2
		He II λ 1640	5801 ± 12	0.03 ± 0.01	1150 ± 900	3 ± 2
		C III] λ 1909	6749 ± 5	0.15 ± 0.02	2450 ± 500	26 ± 3
		C II] λ 2326	8223 ± 46	0.06 ± 0.03	<2350	>22
TN J1123-2154	4.109 ± 0.004	Lyα	6213 ± 4	0.18 ± 0.05	550 ± 350	>47
WN J1123+3141	3.2174 ± 0.0004	O VI λ 1035	4370 ± 6	4.7 ± 0.6	2550 ± 1050	22 ± 4
		Lyα	5128 ± 1	6.2 ± 0.6	400 ± 150	25 ± 3
		C IV λλ 1549	6532 ± 2	3.4 ± 0.4	900 ± 250	14 ± 2
		He II λ 1640	6917 ± 2	2.4 ± 0.3	700 ± 250	10 ± 1
WN J1242+3915	2.131 ± 0.001	C IV λλ 1549	4873 ± 38	0.09 ± 0.05
		He II λ 1640	5135 ± 2	0.36 ± 0.07	500 ± 400	32 ± 11
		C III] λ 1909	5975 ± 7	0.76 ± 0.11	2300 ± 800	85 ± 26
		C II] λ 2326	7286 ± 29	0.25 ± 0.07	2500 ± 1300	29 ± 10
WN J1333+3037	1.2127 ± 0.0006	C III] λ 1909	4219 ± 4	0.3 ± 0.1	850 ± 500	20 ± 6
		C II] λ 2326	5149 ± 6	0.4 ± 0.1	1600 ± 750	33 ± 7
		Mg II λ 2800	6190 ± 7	0.9 ± 0.1	2400 ± 800	52 ± 8
		[O II] λ 3727	8247 ± 1	3.5 ± 0.4	850 ± 150	180 ± 40
		[Ne III] λ 3869	8553 ± 5	1.1 ± 0.2	1000 ± 550	44 ± 10
WNR J1338+3532	2.769 ± 0.003	Lyα	4586 ± 1	17.8 ± 1.8	1800 ± 150	> 693
		C IV λλ 1549	5832 ± 1	1.3 ± 0.2	400 ± 150	> 2
		He II λ 1640	6189 ± 1	3.0 ± 0.3	950 ± 200	> 19
		C III] λ 1909	7196 ± 1	2.2 ± 0.3	750 ± 200	> 16
TN J1338-1941	4.11 ± 0.01	Lyα	6211 ± 1	13.63 ± 1.37	1000 ± 100	200 ± 60
		C IV λλ 1549	7899 ± 3	1.0 ± 0.1	1450 ± 350	> 237
		He II λ 1640	8382 ± 35	0.2 ± 0.1	1500 ± 900	> 37
WNR J1356+3929	0.2525 ± 0.0002	[O III] λ 5007	6272 ± 1	1.3 ± 0.2	400 ± 100	8 ± 1
		Hα	8218 ± 1	4.5 ± 0.5	500 ± 100	44 ± 6
TNR J1402-1510	0.739 ± 0.001	Mg II λ 2800	4829 ± 40	6.88 ± 1.23	7650 ± 3750	80 ± 17
		[Ne IV] λ 3426	5953 ± 1	3.2 ± 0.4	1550 ± 200	26 ± 2
		[O II] λ 3727	6475 ± 1	35.1 ± 3.5	1950 ± 100	320 ± 35
		[Ne III] λ 3869	6732 ± 1	3.8 ± 0.4	< 180	32 ± 3
		Hδ	7131 ± 3	2.2 ± 0.4	950 ± 350	14 ± 2
		Hγ	7557 ± 12	4.1 ± 0.9	1900 ± 800	30 ± 6
		Hβ	8448 ± 2	7.1 ± 1.1	750 ± 200	31 ± 5
		[O III] λ 4959	8626 ± 1	10.8 ± 1.3	400 ± 100	47 ± 6
		[O III] λ 5007	8705 ± 1	56.8 ± 5.8	1000 ± 100	400 ± 60
PKS J1428-1502	2.349 ± 0.004	Lyα	4076 ± 1	20.7 ± 2.2	2650 ± 350	> 785
		C IV λλ 1549	5189 ± 3	2.3 ± 0.4	1300 ± 450	37 ± 11
		He II λ 1640	5495 ± 4	2.3 ± 0.4	1550 ± 550	35 ± 10
		C III] λ 1909	6378 ± 3	1.0 ± 0.3	750 ± 450	18 ± 6
WN J1543+3512	0.7033 ± 0.0006	[O II]	6348 ± 2	0.8 ± 0.1	550 ± 300	22 ± 4
		CaII K	6706 ± 2	-0.4 ± 0.1	...	-11 ± 4
		Mg b	8788 ± 10	-4.3 ± 2.0	...	-61 ± 30
TXS J1650+0955	2.510 ± 0.002	Lyα	4267 ± 1	20.9 ± 2.1	1850 ± 250	...
		C IV λλ 1549	5441 ± 1	3.2 ± 0.4	1200 ± 200	36 ± 5
		He II λ 1640	5760 ± 2	2.7 ± 0.3	1700 ± 400	26 ± 3
		C III] λ 1909	6692 ± 6	1.2 ± 0.3	1350 ± 600	20 ± 5
WNR J1703+3739	0.2561 ± 0.0003	[O III] λ 5007	6291 ± 1	1.1 ± 0.2	500 ± 150	7 ± 1
		Hα	8242 ± 1	2.4 ± 0.3	400 ± 100	25 ± 4

Source	z	Line	λ_{obs} Å	$10^{-16} \times \text{Flux}$ erg/s/cm ²	Δv_{FWHM} km s ⁻¹	$W_{\lambda}^{\text{rest}}$ Å
MP J1755-6916	2.551 ± 0.004	Lya	4317 ± 1	9.0 ± 0.9	1700 ± 250	370 ± 100
		N V λ 1240	4404 ± 12	0.05 ± 0.03
		Si IV / O IV	4989 ± 2	0.21 ± 0.04	<400	10 ± 3
		C IV λ λ 1549	5505 ± 3	0.61 ± 0.08	1450 ± 400	37 ± 8
		He II λ 1640	5820 ± 6	0.39 ± 0.06	1500 ± 450	22 ± 5
		C III] λ 1909	6773 ± 4	0.57 ± 0.08	1100 ± 500	29 ± 7
MP J1758-6738	2.026 ± 0.002	C IV λ λ 1549	4688 ± 1	1.0 ± 0.1	1750 ± 300	39 ± 4
		He II λ 1640	4969 ± 2	0.60 ± 0.06	1800 ± 300	24 ± 3
		C III] λ 1909	5772 ± 2	0.42 ± 0.05	1350 ± 300	23 ± 3
6C J1908+7220	3.5356 ± 0.0003	Lya	5516 ± 0.3	9.0 ± 0.9	1200 ± 90	87 ± 9
		He II λ 1640	7437.9 ± 0.4	1.3 ± 0.1	1350 ± 70	9 ± 1
WN J1911+6342	3.590 ± 0.002	Lya	5582: ± 1	1.4: ± 0.1	1350: ± 250	220: ± 40
		C IV λ λ 1549	7109 ± 3	0.08 ± 0.01	950 ± 350	17 ± 3
		He II λ 1640	7517 ± 4	0.08 ± 0.01	1000 ± 400	40 ± 12
MP J1929-3732	0.7476 ± 0.0006	C II] λ 2326	4062 ± 3	2.05 ± 0.29	1550 ± 600	46 ± 9
		[Ne IV] λ 2424	4234 ± 1	1.75 ± 0.23	700 ± 300	42 ± 8
		O II λ 2470	4320 ± 1	0.8 ± 0.2	1300 ± 300	80 ± 20
		Mg II λ 2800	4892 ± 1	3.12 ± 0.33	1550 ± 300	61 ± 7
		[O III] λ 3047	4955 ± 1	0.43 ± 0.20	< 750	...
		[O III] λ 3133	5475 ± 2	0.93 ± 0.12	1200 ± 300	16 ± 2
		He II λ 3203	5600 ± 1	0.79 ± 0.30	< 750	...
		[Ne IV] λ 3346	5848 ± 1	2.07 ± 0.40	1150 ± 200	62 ± 9
		[Ne IV] λ 3426	5988 ± 1	4.97 ± 0.50	1100 ± 200	63 ± 6
		[O II] λ 3727	6511 ± 1	15.97 ± 1.60	1050 ± 150	200 ± 20
		[Ne III] λ 3869	6761 ± 1	9.06 ± 0.91	1100 ± 150	90 ± 9
		[Ne III] λ 3967	6934 ± 1	4.00 ± 1.20	1400 ± 300	116 ± 18
		S II λ 4071	7113 ± 2	2.45 ± 1.10	1650 ± 400	52 ± 15
		Hδ	7167 ± 3	1.48 ± 0.90	1300 ± 350	34 ± 20
		Hγ	7582 ± 1	2.50 ± 0.29	800 ± 200	33 ± 4
		He II λ 4686	8188 ± 6	2.24 ± 0.33	1150 ± 500	29 ± 4
		Hβ	8494 ± 1	7.44 ± 1.75	1300 ± 450	178 ± 25
		[O III] λ 4959	8667 ± 1	37.41 ± 3.75	850 ± 150	273 ± 31
		[O III] λ 5007	8750 ± 1	112.88 ± 11.29	1100 ± 150	850 ± 100
		MP J2003-8340	1.169 ± 0.001	[O II] λ 3727	8085 ± 2	3.28 ± 0.36
TXS J2036+0256	2.130 ± 0.001	Lya	3805 ± 1	6.8: ± 1.0	700 ± 250	...
		C IV λ λ 1549	4859 ± 12	0.6 ± 0.3	1550 ± 1100	> 12
		He II λ 1640	5131 ± 5	0.7 ± 0.2	1100 ± 800	23 ± 10
		C III] λ 1909	5965 ± 5	1.2 ± 0.3	1200 ± 650	29 ± 10
MP J2045-6018	1.464 ± 0.001	C IV λ λ 1549	3817 ± 1	5.59 ± 0.57	650 ± 300	35 ± 4
		He II λ 1640	4042 ± 1	4.72 ± 0.48	<250	33 ± 4
		C III] λ 1909	4701 ± 1	2.68 ± 0.27	850 ± 250	19 ± 2
		C II] λ 2326	5734 ± 1	0.48 ± 0.30	<200	...
		[Ne IV] λ 2424	5972 ± 1	1.72 ± 0.17	750 ± 200	13 ± 1
		O II λ 2470	6091 ± 1	0.19 ± 0.15	400 ± 150	4 ± 1
		Mg II λ 2800	6901: ± 3	0.92: ± 0.11	1350: ± 450	7: ± 1
		[O III] λ 3133	7721 ± 4	0.91 ± 0.13	900 ± 350	9 ± 1
		[Ne IV] λ 3346	8246 ± 1	1.32 ± 0.25	650 ± 150	38 ± 9
		[Ne IV] λ 3426	8444 ± 1	2.90 ± 0.30	450 ± 150	27 ± 3
MP J2048-5750	1.262 ± 0.002	[O III] λ 3133	7082 ± 17	2.61 ± 0.33	3150 ± 1450	14 ± 2
		[Ne IV] λ 3426	7748 ± 4	3.39 ± 0.38	1400 ± 350	16 ± 2
		[O II] λ 3727	8439 ± 1	46.50 ± 4.66	1500 ± 150	200 ± 20
		[Ne III] λ 3869	8750 ± 2	11.73 ± 1.20	1150 ± 200	37 ± 4
TNR J2254+1857	2.153 ± 0.002	Lya	3833 ± 2	33.0 ± 3.8	2050 ± 400	> 86
		He II λ 1640	5178 ± 21	3.2 ± 1.5	1550 ± 1250	> 25
WN J2313+4053	2.99 ± 0.01	O VI λ 1035	4005 ± 3	-26 ± 4	3300 ± 500	-33 ± 10
		Lya	4846 ± 5	330 ± 50	4100 ± 1000	350 ± 50
		Si IV / O IV	5570 ± 19	17 ± 3	4150 ± 1450	4 ± 1
		C IV λ λ 1549	6178 ± 3	164 ± 17	5100 ± 300	31 ± 3
		C III] λ 1909	7614 ± 8	66 ± 7	4850 ± 650	14 ± 1
TXS J2321+2237	2.553 ± 0.001	Lya	4320 ± 1	8.1 ± 0.8	1050 ± 200	44 ± 7
TXS 2334+1545	2.480 ± 0.003	Lya	4231 ± 3	3.1 ± 0.5	1900 ± 450	> 65
		C IV λ λ 1549	5402 ± 36	0.1 ± 0.1	< 550	> 1
		C III] λ 1909	6644 ± 15	0.8 ± 0.3	1600 ± 1200	12 ± 5
TXS J2355-0002	2.587 ± 0.003	Lya	4366 ± 1	1.2 ± 0.2	900 ± 300	27 ± 8
		N V λ 1240	4455 ± 4	0.8 ± 0.3	1200 ± 600	22 ± 8
		C IV λ λ 1549	5551 ± 2	0.3: ± 0.1	450 ± 250	6: ± 2

† Estimated from non-photometric conditions, only to be used to determine line ratios.

NOTE: Measurements affected by sky-lines are indicated with a colon. See §4.3.2 for more information.

[Ne III] λ 3869, H δ , H γ , and H β . In the low redshift objects with sufficiently bright continua, we can also detect the stellar absorption features Ca II K and H $\lambda\lambda$ 3934,3968, G-band λ 4300 and Mg I b $\lambda\lambda$ 5174, and continuum break features at 2640 Å, 2900 Å and 4000 Å.

The above line identifications yielded redshifts for 50 of the 62 objects that we observed spectroscopically. All 16 objects from the subsidiary USS samples yielded redshifts, while this was possible for 74% of the 46 objects selected from our main USS sample. This difference is most likely due to the lower average redshift and higher radio flux densities in the subsidiary samples, as compared to our main sample. In §4.3.4, we discuss the sources which defied redshift determination. Of the objects with redshifts, 94% are radio galaxies, while 6% are quasars.

4.3.2 Notes on individual sources

We now discuss the redshift determination of the individual sources. We list all sources from our main and subsidiary samples in order of right ascension. We show the extracted one-dimensional spectra in Figures 4.8 and 4.1.

USS J0006–0141, at $z = 1.541$, exhibits a classic HzRG spectrum. The shape and flux level of the continuum is uncertain due to problems with internal reflections.

WN J0040+3857, at $z = 2.606$, exhibits a classic HzRG spectrum, with the Ly α emission slightly weaker than normal. The C IV $\lambda\lambda$ 1549 line is severely affected by the strong [OI] λ 5577 Å skyline.

TN J0121+1320, at $z = 3.516$, displays a clear associated HI absorption system in the Ly α line. The observations were made in non-photometric conditions with heavy cirrus.

TXS J0137+2521, at $z = 2.897$, displays a single emission line, and no continuum emission. We identify this line as Ly α on the basis of the absence of confirming lines if the line were [O II] λ 3727.

6C J0143+3253, at $z = 4.413$, was the highest redshift radio galaxy at the time of discovery (Rawlings et al., 1996). Our Keck spectrum shows a weak C IV $\lambda\lambda$ 1549 line, confirming the redshift reported by Rawlings et al. (1996). The Ly α line shows strong blueward absorption, like the $z = 4.11$ galaxy TN J1338–1942 (Chapter 6). This source was not included in our main sample because the spectral index $\alpha_{325}^{1400} = -1.15$ does not qualify our extreme $\alpha < -1.30$ criterion.

TN J0205+2242, at $z = 3.506$, has a very luminous and extended (8'') Ly α halo. The velocity structure of the Ly α line repeats at lower S/N in C IV. The observations were made in non-photometric conditions with heavy cirrus.

WN J0231+3600, at $z = 3.079$, has a redshift based on only one emission line, which we identify with Ly α . It is extremely unlikely that the identification of this line is [O II] λ 3727, because the corresponding [O III] λ 5007 is not detected, while this line is 2.4 times brighter than [O II] λ 3727 in the composite HzRG spectrum of McCarthy (1993). The presence of a small continuum break is consistent with the identification of the line as Ly α .

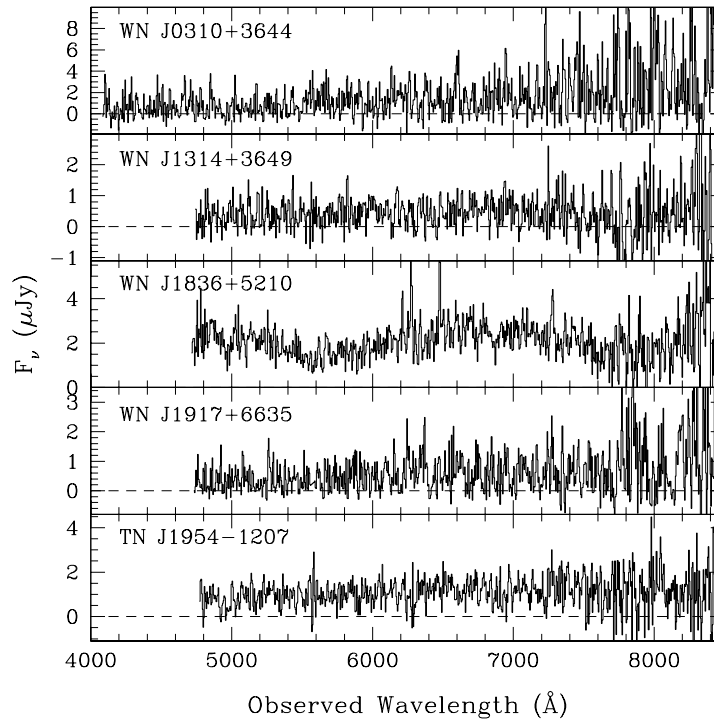


Figure 4.1: Spectra obtained with LRIS at Keck showing continuum emission, but no identifiable features. Although the spectral coverage extends out to $\sim 1\mu\text{m}$, we show only the part out to 8500 \AA because the S/N at longer wavelengths is too low to provide useful information.

WN J0303+3733, at $z = 2.504$, exhibits a classic HzRG spectrum with strong Ly α emission.

WN J0310+3644 shows continuum emission, but no emission or absorption lines (see Fig. 4.1). The high resolution radio map of Kaplan (2000b) shows a complex morphology reminiscent of a core-jet or head-tail FR-I type radio source.

TN J0402+1007 is an ERO with $R - K > 6.8$ and $K = 17.2$ in a $4''$ aperture. The optical spectrum shows a marginal detection of a broad emission line around 7074 \AA in one of the two exposures, but this needs reconfirmation (no spectrum shown). If this source would fall on the Hubble $K - z$ relation, we could identify this possible line with Mg II $\lambda 2800$ at $z = 1.52$. A near-IR H -band spectrum would be able to detect the H α line in this case.

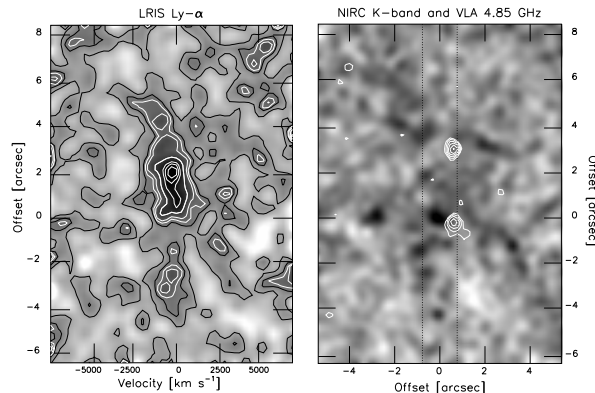


Figure 4.2: *Left*: two dimensional spectrum of the Ly α line at $z = 3.153$ of WN J0617+5012 obtained with LRIS at Keck II ($t_{int} = 90$ min), showing the “core” of the line and two faint “wings” extending 4” to the bottom at the velocity of the core and 2” to the top with blueshifts of up to 2000 km s⁻¹. *Right*: K-band image obtained with NIRC at Keck I ($t_{int} = 64$ min) with VLA 4.85 GHz radio contours overlaid (subject to an astrometric uncertainty of $\lesssim 1''$). The position of the spectroscopic slit in the left panel is indicated with dotted lines. Both panels are at the same scale and orientation (position angle 10° East of North). Note that the Ly α “core” falls in between the 3”4 double radio source, but the wings extend further out than the radio source.

TN J0452–1737, at $z = 2.256$, has a low-ionization spectrum with C II] λ 2326 stronger than the confirming He II λ 1640 and C III] λ 1909 lines. This object shows the difficulty to identify the redshift of objects in the “redshift desert” (see §4.4.2.5).

TNR J0516+0637, at $z = 0.357$, is dominated by an old stellar population. The redshift is confirmed by the presence of the 4000 Å break, and the [O II] λ 3727 emission line.

TN J0517–0641 remains undetected in our ESO 3.6m spectrum (no spectrum shown).

WN J0617+5012, at $z = 3.153$, has the faintest observed K-band flux in our sample ($K = 21.9 \pm 0.4$ in a 2” aperture). Figure 4.2 shows the region of the spectrum containing the only emission line we detect, which we interpret as Ly α at $z = 3.15$, based on its large spatial extent and equivalent width, and on the absence of confirming lines. The line consists of a brighter “core” which coincides with the region between the radio lobes, and two fainter “wings”, extending 2” (top) and 4” (bottom) beyond the radio lobes. Also note the asymmetry in the radio lobes with respect to the K-band identification. This asymmetry is also seen in TN J1338–1942 (Chapter 6), and might reflect density variations in the ambient medium of radio galaxies at the highest redshifts.

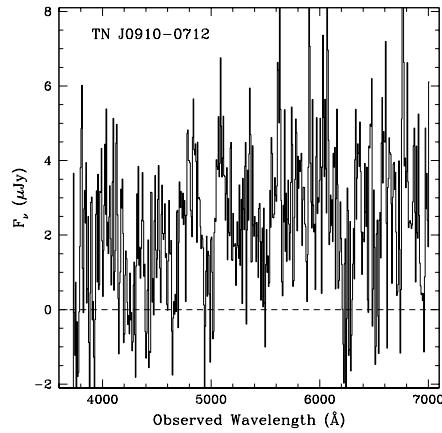


Figure 4.3: Spectrum of TN J0910–0712 obtained with EFOSC1 on the ESO 3.6m telescope showing continuum emission, but no identifiable features.

WN J0717+4611, at $z = 1.462$, is a red quasar. Keck spectro-polarimetry has given strong support for dust scattering as the origin of the redness. The object is described in detail in Chapter 7.

WN J0747+5611, at $z = 2.992$, has a weak emission-line spectrum. The blue wing of the Ly α line is strongly attenuated by associated HI absorption.

WN J0813+4828, at $z = 1.274$, exhibits the classical emission lines from a lower redshift radio galaxy. The [Ne III] λ 3869 emission falls in a region that is severely affected by fringing of the CCD.

TN J0910–2228 shows continuum emission but no emission or absorption lines in our ESO 3.6m spectrum (see Fig. 4.3). A slightly deeper spectrum with a larger spectral coverage will probably be sufficient to determine the redshift.

TN J0920–0712, at $z = 2.760$, has strong absorption at the blue side of the Ly α line. Such absorption by associated HI is often seen in HzRGs (e.g., Chapter 8), and other high-redshift galaxies (e.g., Dey et al., 1998).

TN J0924–2201, at $z = 5.19$, is the highest redshift source from our sample. It is described in detail in Chapter 5.

TN J0936–2243, at $z = 1.479$, is an object consisting of two components, one of them showing an old stellar population, and the other showing a brighter emission line spectrum. We discuss this object in greater detail in §4.4.3.

TN J0941–1628, at $z = 1.644$, displays a low ionization spectrum, which might well have an important contribution from shock ionization (see Chapter 8). Although the object is in the “redshift desert”, the emission lines are bright enough to be easily detected.

WN J1015+3038, at $z = 0.54$, is an ERO with $R - K = 5.2$ in a $4''$ diameter aperture. The source has faint optical continuum emission for an object at this redshift, but

the $K = 17.8$ is consistent with $z \sim 0.5$ in the $K - z$ diagram. The spectrum shown in figure 4.8 is smoothed by a factor of three to increase S/N. The redshift is based on the 4000 Å break and on tentative detections of an unresolved Ca II K+H doublet and Mg I b.

TN J1026–2116 remains undetected in our 1h Keck spectrum, with the possible exception of the marginal detection of an emission line at 6646 Å that requires confirmation (no spectrum shown).

TN J1033–1339, at $z = 2.427$, exhibits a classic HzRG spectrum. The shape and flux level of the continuum is uncertain due to problems with internal reflections.

TN J1102–1651, at $z = 2.111$, exhibits a classic HzRG spectrum with Ly α at the very edge of the spectrum, where the flux calibration is more uncertain.

TN J1112–2948, at $z = 3.09$, exhibits a classic HzRG spectrum. The C IV $\lambda\lambda$ 1549 emission is severely affected by the strong [OI] λ 6300 Å skyline

WN J1115+5016, at $z = 2.54$, displays a C IV $\lambda\lambda$ 1549 broad absorption line system at $z = 2.494 \pm 0.005$ that completely attenuates the C IV $\lambda\lambda$ 1549 emission. This is only the second radio galaxy showing a BAL system, after TXS J1908+7220 (Dey, 1999). The region of the spectrum where we predict the [Ne IV] λ 2424 line is affected by a cosmic ray hit in one of our exposures, so we do not attempt to fit the parameters of this line.

TN J1123–2154, at $z = 4.109$, has no continuum detected, but only one faint, slightly extended emission line, which is repeated in two individual exposures. We identify this line as Ly α on the basis of the absence of confirming [O III] λ 5007 and H α lines if the identification had been [O II] λ 3727 or [O III] λ 5007. The spectrum shown in figure 4.8 is smoothed by a factor of 3 to increase the signal to noise ratio.

WN J1123+3141, at $z = 3.217$, shows clear signs of interaction in the K -band image presented in Chapter 3. The noisy area in the spectrum around 5500 Å is due to the dichroic.

TN J1151–3013 remains undetected in our ESO 3.6m spectrum (no spectrum shown).

TN J1159–1629 remains undetected in our ESO 3.6m spectrum (no spectrum shown).

WN J1242+3915, at $z = 2.131$, is an example source in the ‘redshift desert’, where the redshift must be based on weaker emission lines.

WN J1314+3649 displays a faint continuum in our 1h Keck spectrum, but no emission or absorption lines (see Fig. 4.1).

WN J1333+3037, at $z = 1.213$, has a hint of broad Mg II λ 2800 emission, suggestive of a scattered quasar component (e.g., Tran et al., 1998).

WNR J1338+3532, at $z = 2.769$, exhibits a classic HzRG spectrum, with indications for associated HI absorption near the peak of the Ly α line. The apparent discontinuity at ~ 6000 Å is due to the dichroic.

TN J1338–1942, at $z = 4.11$, was at the time of discovery the highest redshift radio galaxy in the southern hemisphere. It has one of the most luminous Ly α halos observed. More details can be found in Chapter 6. The Ly α flux listed in table 4.6 is from VLT observations, while the C IV $\lambda\lambda$ 1549 and He II λ 1640 measurements are from the discovery ESO 3.6m spectrum, which covers a larger wavelength range.

WNR J1356+3929, at $z = 0.2525$, shows a bright continuum which is at some places severely affected by fringing in our single exposure.

TNR J1402–1510, at $z = 0.739$, shows a rich emission line spectrum and a 4000 Å continuum break.

PKS J1428–1502, at $z = 2.349$, exhibits a classic HzRG spectrum. The continuum break across Ly α is uncertain because it is at the edge of the CCD flux calibration.

WN J1525+3010 remains undetected in our deep Keck spectrum (no spectrum shown).

WN J1543+3512, at $z = 0.703$, is dominated by an old stellar population, with [O II] λ 3727 observed weakly in emission. The spectrum in appendix A is smoothed by a factor 3 to increase the S/N.

TXS J1650+0955, at $z = 2.510$, exhibits a classic HzRG spectrum. The shape and flux level of the continuum is uncertain due to problems with internal reflections.

WNR J1703+3739, at $z = 0.256$, shows a bright continuum which is at some places severely affected by fringing in our single exposure.

MP J1755–6916, at $z = 2.551$, exhibits a classic HzRG spectrum. The Ly α emission is spatially extended over $\gtrsim 7''$, and has a complex morphology.

MP J1758–6738, at $z = 2.026$, is an example source in the ‘redshift desert’, where the redshift must be based on weaker emission lines.

WN J1836+5210 displays a relatively bright continuum with several changes in the slope, but no emission or absorption lines (see Fig. 4.1).

TXS J1908+7220, at $z = 3.536$, we reproduce the deep Keck spectrum by Dey (1999) which shows the first broad absorption line system detected in a radio galaxy. This source is also known as 6C1908+72.

WN J1911+6342, at $z = 3.590$, falls at a redshift where Ly α coincides with the strong [OI] λ 5577 Å skyline. However, the high redshift is confirmed by two other emission lines and a continuum break across Ly α .

WN J1917+6635 displays a faint continuum in our 1h Keck spectrum, but no emission or absorption lines (see Fig. 4.1).

MP J1929–3732, at $z = 0.7476$, has a very rich emission line spectrum. At least 19 emission lines can be identified in our spectrum.

TN J1954–1207 displays a faint continuum in our 1h Keck spectrum, but no emission or absorption lines (see Fig. 4.1).

MP J2003–8340, at $z = 1.169$, is the southernmost source from our spectroscopic sample. We detect only a single bright emission line and continuum emission on both sides, which excludes Ly α as a possible identification. We can also exclude [O III] λ 5007 and H α on the basis of the absence of confirming lines within our observed wavelength range.

TXS J2036+0256, at $z = 2.130$, exhibits a classic HzRG spectrum. The shape and flux level of the continuum is uncertain due to problems with internal reflections.

WN J2044+7044 remains undetected in our Keck spectrum (no spectrum shown). This source has a higher galactic extinction than most others: $A(R) = 1.26$, as determined from the extinction maps of Schlegel, Finkbeiner & Davis (1998), and using the extinction curve of Cardelli et al. (1989).

MP J2045–6018, at $z = 1.464$, is an extremely luminous radio source. With $P_{408} = 2 \times 10^{36} \text{ erg s}^{-1} \text{ Hz}^{-1}$, it surpasses even the most luminous 3C sources, but not a number of radio galaxies at very high redshift, such as 8C 1435+635 at $z = 4.25$ (Lacy et al., 1994). The parameters for the Mg II λ 2800 emission are uncertain because this line coincides with atmospheric B-band. The ionization spectrum is typical of a large, powerful radio source, showing a clear dominance of photo-ionization (e.g., Best, Röttgering & Longair, 2000b, , Chapter 8). A detailed analysis of this source is deferred to a future publication.

MP J2048–5750, at $z = 1.262$, has very broad emission lines, around 1500 km s^{-1} deconvolved FWHM for [O II] λ 3727. Such line widths would be slightly higher than all other powerful radio galaxies around this redshift (e.g., Baum & McCarthy, 2000). However, this object does not appear to be a quasar, because we do not detect broad hydrogen lines (H δ , H γ , H β), and the K -band identification is slightly resolved (see Chapter 3).

TNR J2254+1857, at $z = 2.153$, shows a bright Ly α line with associated HI absorption.

WN J2313+4053, at $z = 2.99$, is the optically brightest object we observed spectroscopically. It is a quasar with a continuum slope of $\alpha = -2.2$ ($F_\nu \propto \nu^\alpha$). The broad absorption near 4000 \AA is consistent with a detached O VI λ 1035 broad absorption line (BAL) system with a velocity width of $3300 \pm 500 \text{ km s}^{-1}$ and a z offset by $36,000 \text{ km s}^{-1}$. No absorption system is seen in any other lines. A deeper spectrum would be needed to confirm the O VI λ 1035 BAL. An object that shows an O VI λ 1035 BAL but not a C IV $\lambda\lambda$ 1549 one is quite unique. Normally BALQSOs are identified by their C IV $\lambda\lambda$ 1549 BAL (Weymann et al., 1991). The significance of this discovery is that it may be the tip of the iceberg for an underdetected population of BALQSOs, ones that show BALs only from very high ionized species (O VI and above). The radio spectrum of this source is also exceptional, and shows a strong convex curvature from $\alpha_{151}^{325} = -2.28$ to $\alpha_{325}^{1400} = -1.50$.

TXS J2321+2237, at $z = 2.553$, shows the Ly α and Si IV/O IV complex; the C IV, He II and C III] lines are too weak to detect in the blue arm, which experienced technical problems (see §4.2.2.2).

TXS J2334+1545, at $z = 2.480$, has a relatively bright continuum and weak emission lines.

TXS J2353–0002, at $z = 2.587$, shows N V λ 1240 emission that is almost as bright as Ly α . Such high N V/Ly α ratios have been detected before in HzRGs (van Ojik et al., 1994; Dey, Spinrad & Dickinson, 1995, e.g.,), and have been explained by the strong attenuation of Ly α by dust. The C IV $\lambda\lambda$ 1549 line is close to the strong [OI] λ 5577 \AA skyline, and the flux might well be affected. The He II λ 1640 line is not detected. A deeper and higher resolution spectrum will be needed to confirm these high N V/C IV and N V/He II ratios, which are more likely indicative of a high nitrogen abundance (Villar-Martín et al., 1999c; Vernet et al., 1999) than of attenuation of Ly α by large amounts of dust.

Table 4.7: Attempted spectroscopic observations not yielding a redshift

Source	S_{1400} mJy	α	LAS "	m_R^a mag	m_K^a mag	run	t_{exp} s	comments
WN J0310+3644	24	-1.70	2.0	23.0 ^b	...	K9	3600	flat continuum, no lines
TN J0402+1007	75	-1.38	0.8	>24	17.2	K9	1200	undetected, possible line at 7074 Å
TN J0517-0641	40	-1.46	1.0	24.0	...	E2	2700	undetected
TN J0910-2228	55	-1.58	2.0	23.0	...	E3	1800	continuum, no lines
TN J1026-2116	62	-1.39	1.0	>24	19.8	K9	3600	undetected, possible line at 6646 Å
TN J1151-3013	53	-1.57	1.0	>24	19.8	E3	2700	undetected
TN J1159-1629	53	-1.35	1.4	23.4	...	E3	3600	undetected
WN J1314+3649	36	-1.41	1.3	>26	22.1	K11	3600	flat continuum, no lines
WN J1525+3010	17	-1.46	1.2	25.3	19.5	K11	5400	undetected
WN J1836+5210	24	-1.41	1.4	...	17.7	K11	1200	wavy continuum, no lines
WN J1917+6635	11	-1.30	1.9	...	20.0	K11	3600	flat continuum, no lines
TN J1954-1207	103	-1.38	<7	...	19.9	K11	3600	flat continuum, no lines
WN J2044+7044	42	-1.38	1.3	>24	19.2	K11	3000	undetected

^a 4" diameter aperture, see Chapter 3 for details.

^b I -band magnitude.

4.3.3 Sources without redshifts

For 35% of the spectroscopically observed sources from our main USS sample, we could not determine the redshift, because either no distinctive emission or absorption features were detected, or no emission was detected in the spectrum. In table 4.7, we list all 12 such sources with the reason for the failure of the redshift determination. We only include sources in this table that have been observed sufficiently long and under good conditions (i.e., not during twilight, heavy obscuration or bad seeing). We find that half of the spectra do not have any emission detected, but this fraction drops to a third when we consider only the deep Keck spectra. In Figure 4.1, we show the spectra where we did detect continuum emission, but no identifiable emission or absorption features.

The most obvious reason for the failure to detect any optical emission could be an incorrect offset to the object. However, we are confident this is not the case for the sources observed with the Keck telescope because (i) we used the same procedures and quality of images to determine the offsets for both the detected and undetected sources, and (ii) other objects detected along our 2'6 long slit provided us with accurate spectro-astrometry with which we could verify the proper slit placement, based on the optical and/or near-IR images of the field.

We also exclude the possibility that the identification we determined is not the host galaxy, but an optical counterpart of an individual component of the radio source because: (i) our USS sample was constructed to exclude objects $>1'$, and follow-up high resolution radio images did not show other components in the field; (ii) the position differences between the different frequency and resolution radio observations agree within $\sim 1''$ indicating we are not missing any radio source component with a significantly different radio spectrum; (iii) the identifications of the sources in table 4.7 are within $1''$ from the predicted radio positions, and do not show a different near-IR morphology or $R - K$ color than the confirmed HzRG sources; (iv) the near-IR identifications of 85 sources from our main USS sample are virtually complete, with no large position differences between the radio and near-IR positions.

We discuss the possible nature of these sources lacking redshifts in §4.4.2.

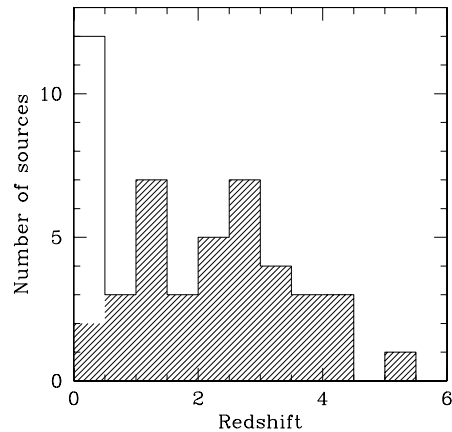


Figure 4.4: Redshift distribution of the WN/TN sources described in this chapter. The unshaded histogram includes the low-redshift cluster identifications. Note the dip at $1.5 < z < 2.5$ coinciding with the ‘redshift desert’ (see text).

4.4 Discussion

4.4.1 Redshift distribution of USS sources

Figure 4.4 shows the redshift distribution of all sources with known redshifts in our USS sample (we exclude the 12 sources observed from the other samples in this analysis). We find that the redshift distribution is roughly flat from $z = 0.5$ to $z = 4$, with a mean of $\bar{z} = 2.5$. Two features deserve special attention: (i) the peak in the lowest redshift bin, and (ii) the slight drop at $1.5 < z < 2.5$ (see also Fig. 4.5). The peak at low redshift is due to cluster sources found from the literature. We refer to our discussion in Chapter 2, where we argued that a USS sample is an efficient way to select cluster galaxies. The lack of sources at $1.5 < z < 2.5$ is probably due to the ‘redshift desert’. In this redshift range, [O II] has shifted outside of the observable spectroscopic window, while $\text{Ly}\alpha$ has not yet entered, and the redshift has to be based on weaker emission lines. We return to this issue in §4.4.2.5.

To examine the relation between our *observed* spectral index and redshift in a consistent way, we determined the spectral indices for those spectroscopically identified radio galaxies from the complete 3CR (Spinrad et al., 1985) and MRC (McCarthy et al., 1996) samples. We used spectral indices determined from the same radio surveys as in our USS sample. In practice, we determined the α_{325}^{1400} for the 3CR sources, using fluxes from the 325 MHz WENSS (Rengelink et al., 1997) and 1.4 GHz NVSS (Condon et al., 1998), and the α_{355}^{1400} from the 365 MHz Texas survey (Douglas et al., 1996) and NVSS, using a $60''$ search radius to correlate the survey catalogs. We only used the single component (‘S’-type) sources in WENSS to avoid problems due to

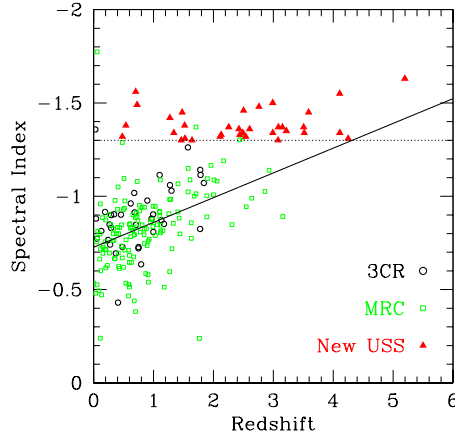


Figure 4.5: Spectral index from the 325 MHz WENSS or 365 MHz Texas and 1.4 GHz NVSS survey plotted against redshift for 36 3CR (Spinrad et al., 1985), 152 MRC (McCarthy et al., 1996), and 35 WN/TN sources. The solid line shows a linear fit to the 3CR and MRC data while the dashed horizontal line indicates the spectral index cutoff we used in our WN/TN USS samples.

different resolutions. From the Texas survey, we only used those sources that were well modeled and not subject to lobe-shift problems ('+++’ flag, see Douglas et al., 1996). The complicated beam of the Texas survey leads to problems in the determination of the fluxes for the 3CR survey (which contains many more large sources than the MRC), so we opted not to include Texas-NVSS spectral indices from the 3CR sources in our analysis.

This procedure yields spectral indices for 36 3CR and 152 MRC sources (Fig. 4.5). Inspection of figure 4.5 suggests a correlation between redshift and spectral index which we verify statistically: the Spearman rank correlation coefficient is $r_S = -0.44$, implying a $>99.99\%$ likelihood that redshift and spectral index are correlated for this sample.

To obtain an approximate estimate of the number of sources we excluded by the application of our $\alpha < -1.30$ criterion, we fitted a linear function to the $z - \alpha$ relationship (Fig. 4.5). The fit has an offset of $\alpha(z = 0) = -0.73$, and a slope of -0.13 . We stress that this fit is not well constrained, especially at $z > 2$, where few radio galaxies from flux limited samples are known. A linear fit is probably inadequate at high redshift, and the relation should probably curve up at high redshift because of effects such as (i) additional steepening of the spectra due to inverse Compton losses against the cosmological background, and (ii) a relation between the radio spectral curvature and radio power (e.g., Blundell, Rawlings, & Willott, 1999a; Carilli et al., 1999); at the highest redshifts, the most powerful radio sources are more dominant in flux density limited surveys, which would lead to a steeper rest-frame spectral index,

in addition to the steepening due to the k -correction. The combined result would be that our crude linear fit predicts spectral indices which are too flat at the highest redshifts, which would suggest that by $z \sim 4$, our sample includes roughly half of the sources that would have been in a sample without a spectral index cutoff. This number should be considered *very* tentative; a sample of high redshift sources with a much shallower spectral index cutoff would be needed to provide a more reliable measure.

The roughly constant number of $\alpha < -1.30$ sources with redshift implies that (after the preferential selection of sources with relatively faint K -band magnitudes) our sample selects as many high redshift sources as low redshift sources. This is even more remarkable because in a flux density limited survey, the fraction of radio-luminous sources at the highest redshifts decreases when the flux density limit is lowered, even in the absence of a redshift cutoff in the co-moving space density (Blundell et al., 1998; Jarvis et al., 1999). In practice, this means that, when compared to other radio selected samples, our sample is clearly more efficient in selecting sources at $z > 3$, than at $z < 3$. However, we note that our efficiency may depend to a large extent on the selection of sources with faint K -band magnitudes. A K -band imaging campaign not only increases the chances of finding very high redshift radio galaxies, but also increases the efficiency of the spectroscopic observations by providing accurate offset positions, that can be used to point the spectroscopic slit at the optimal position. To obtain such images in the optical would require much longer observing times, than the typical 16–32 min integrations we used (see Chapter 3), and the seeing will likely be poorer.

Counting the 19 previously determined redshifts from the literature (see Chapter 2 and table 4.8), we now have spectroscopic information for 65 (=10%) sources in our USS sample. The diffuse radio morphologies for 26 additional sources indicate low redshifts, these 91 sources are still insufficient to draw any firm conclusions on the co-moving space density of radio sources. For example, a sample that extends out to flatter spectral indices ($\alpha > -1.3$) would be needed to better estimate the fraction of sources excluded by our spectral index selection as a function of redshift.

4.4.2 Undetermined redshifts

We now consider the sources of which we could not determine the redshifts either because we detected no spectral features or because no optical emission was detected. For three of the non-detections, we obtained the spectra with the ESO 3.6m telescope. These sources might well be detectable with 8-10m class telescopes. For example, a 45min integration with the ESO 3.6m telescope did not detect any emission in TN J0924–2201 and TN J0936–2243, while the deeper Keck spectra were sufficient to allow the redshift determination. The only non-Keck spectrum that had a continuum detection, but no redshift (TN J0910–2228, Fig. 4.3) had a spectral coverage from 4000 Å to 7000 Å. Such a limited wavelength coverage could easily miss some of the brighter emission lines, especially when neither $\text{Ly}\alpha$ nor $[\text{O II}]$ are in this wavelength

window (from $z = 0.9$ to $z = 2.3$). In the following, we therefore consider only our deep Keck spectra with a continuous spectral coverage from 4000 \AA or 4775 \AA to $1 \text{ }\mu\text{m}$.

We note that sources with only continuum emission have been detected with 4m class telescopes in previous samples of radio sources (e.g., the 7C and 8C sample of Lacy et al. (1999), and the USS sample constructed from the WENSS survey by Rengelink et al., 1997). These authors attributed the failure to determine the redshift to a lack of sensitivity prohibiting the detection of emission lines in the $1.2 < z < 1.8$ 'redshift desert' or absorption lines in a stellar continuum dominated spectrum. It is remarkable that the latter class contains mainly compact USS sources, much like the objects in table 4.7, but they are several magnitudes brighter in the optical ($R \sim 22.5$; Rengelink, 1998).

In the following, we discuss various possibilities for the identifications for the sources in figure 4.1.

Stars

The fraction of mJy-level radio sources that are identified with the coronal magnetic activity of stars brighter than $V = 11$ is $< 0.1\%$, while this fraction decreases linearly with increasing V - magnitude (Helfand et al., 1999). Assuming that radio stars have the same spectral index distribution as extra-galactic radio sources, we therefore expect from figure 1 of Helfand et al. (1999) to find < 1 star in our USS sample, while we have already detected one bright ($V = 8.76$) star in our sample (Chapter 2). We conclude that it is unlikely that many more identifications in our sample are stars. We also exclude the possibility that the spectra are chance alignments of foreground stars, because the radial profiles from the optical or near-IR images in Chapter 3 are resolved, and our spectra in figure 4.1 do not show characteristic stellar absorption lines.

BL Lacs or un-beamed quasars

One of the main characteristics of BL Lac objects is the low equivalent width of their emission lines ($W_{\lambda}^{\text{rest}} < 5 \text{ \AA}$; Stocke et al., 1991). This would be an obvious interpretation for most of our featureless spectra. However, the radio to optical flux ratio is several orders of magnitude higher than seen in BL Lac objects (Laurent-Muehleisen et al., 1999), and we therefore reject this interpretation.

Fan et al. (1999) reported the discovery of SDSSp J53259.96-003944.1, an object at $z = 4.62$ which shows all the characteristics of a quasar (unresolved optical morphology and $M_B < -23$), except for the broad emission lines, which are missing. The absence of radio and X-ray emission, optical polarization and variability are unlike BL Lac objects, and lead to the suggestion that this object could represent a rare class of quasars without broad emission line regions. If such an object were observed at $z \lesssim 2.3$, we would not detect the Ly α break, and such an object would appear as

a featureless continuum. However, the objects with continuum detected in Table 4.7 are clearly resolved in the K -band images and are significantly fainter than SDSSp J53259.96-003944.1. They do not qualify as quasars on the basis of absolute magnitude (for $z \lesssim 2.6$) or compactness. However, if SDSSp J53259.96-003944.1 does indeed represent a rare type of AGN without broad emission line regions, very little is known about the nature of these objects, and on their radio properties. Our extreme radio spectral index selection might then preferentially select the radio loud counterparts of such objects. Nevertheless, the very steep radio to optical flux ratio and absence of an unresolved component in the near-IR images remain difficult to reconcile with a direct view of the central AGN continuum emission.

Stellar continuum dominated galaxies with obscured AGNs

Due to the extreme faintness of the identifications, the S/N of our spectra could be insufficient to identify stellar absorption features or continuum breaks at 2640 Å, 2900 Å or 4000 Å. In low-redshift objects ($z \lesssim 1$), we would expect to detect these breaks from an old stellar population within our $\gtrsim 4000$ Å wavelength coverage, such as in WN 1015+3038 or WN J1543+3512 (see appendix A). Even in the two spectra with slightly better S/N spectra (WN J1836+5210 and TN J1954–1207) do not see evidence for breaks or absorption features, suggesting that either the continuum is completely non-stellar, or the stellar population is significantly diluted by an underlying non-stellar component. In WN J0310+3644, WN J1314+3649 and WN J1917+6635, even deeper spectra would be needed to determine the possible presence of an old stellar population in the continuum emission. A strong indication for the presence of an old stellar population could come from a large $R - K$ color, but we only have one object with continuum emission that has both R - and K -band photometry. However, the distribution of $R - K$ colors of 81 sources from our USS sample shows that at least one third, and possibly more than half of the sources are EROs with $R - K > 5$. Daddi et al. (2000) argued that EROs are mainly composed of $z \gtrsim 1$ ellipticals. Our sample indeed contains at least one such object, TN J0936–2243 (see §4.4.3), and it is possible that some of the objects in table 4.7 also belong to this class of objects.

Alternatively, these objects could be dominated by a relatively young stellar population which is observed after the starburst. Such objects would not show any strong stellar emission lines, and would not yet display strong continuum breaks. Their redshift determination would then depend on weak interstellar absorption lines. The absence of the Lyman break would limit their redshift to $z < 2.9$ or $z < 2.3$ (WN J0310+3644). However, the generally large $R - K$ colors in our sample are not consistent with the expected blue continuum from the young stars.

Mushotzky et al. (2000) found that 75% of the hard X-ray background is composed of AGN, of which half have faint or even optically undetectable counterparts presumed due to an adverse orientation of the molecular torus that surrounds the active nucleus in the context of the unified schemes of AGN. Because our radio survey is also

insensitive to dust obscuration, it is therefore conceivable that our sample contains a number of such obscured AGN.

Such an obscuration would also be consistent with the second class of ERO identifications, which consists of strongly dust-reddened, star-forming AGN or starbursts (e.g., Dey et al., 1999; Smail et al., 1999). Large dust masses have been detected in HzRGs (e.g., Archibald et al., 2000). If the narrow line region were located behind a thick dust layer, this could obscure much of the emission lines. The objects in table 4.7 all have compact radio structures, and are probably still confined within the host galaxy, where the dust would be located. As a result, the narrow emission line regions could still be shielded from our view by a dust layer on the outside of the host galaxy. In larger radio sources, extending beyond the bounds of the host galaxy the radio jets could have cleared the dust away, allowing the detection of narrow emission line regions ionized by a central photo-ionizing source, or by shock ionization.

The presence of a large amount of dust should be revealed by bright sub-mm emission, which could be detected by instruments like SCUBA on the JCMT. If these objects are indeed obscured AGN, like the objects that compose the hard X-ray background, they should be detectable in sensitive X-ray surveys with Chandra or XMM-Newton. Barger et al. (2000) have made deep optical, near-IR, submillimeter, and 20cm radio observations of a deep Chandra field. Their high quality LRIS spectroscopy of 20 sources also failed to provide the redshift of six out of 19 X-ray selected objects. Two of these sources lacking redshift determination have possible submm detections. It might well be that some of our sources are very similar objects, but with ~ 1000 times brighter radio flux densities.

Intrinsically weak AGN in the redshift desert

If the object is at a redshift where only the faintest emission lines fall into the observable window, the S/N ratio might still be insufficient, despite our long integrations. The most probable redshift in this case would lie in the so-called “redshift desert” at $1.5 \lesssim z \lesssim 2.3$, where the brightest restframe optical emission lines ([O II], [O III], H α) have shifted out of the observed range, but the break across Ly α is still too blue to be observed. For most sources, except WN J1314+3649, such redshifts are low, but still consistent within the scatter of the Hubble $K - z$ diagram (e.g., van Breugel et al., 1998).

The faintest detectable emission lines in integrations of ~ 1 hour with LRIS on the Keck telescope have integrated flux densities of $\sim 1 \times 10^{-17}$ erg cm $^{-2}$ s $^{-1}$ (see also Stern et al., 1999a). At redshifts within the redshift desert, this corresponds with line luminosities in the range $\sim 1 - 4 \times 10^{41}$ erg s $^{-1}$, and radio powers in the range $\log(P_{325}/\text{erg s}^{-1} \text{ Hz}^{-1}) = 34 - 35$. Such values do fall on the extrapolations of the correlations between line luminosities and radio powers for all UV lines, except Ly α (Chapter 8).

Further evidence that we are missing a significant number of sources in this redshift range comes from the redshift distribution of our spectroscopic sub-sample (Fig. 4.4).

Although based on very incomplete data which is subject to complicated non-optical selection effects (e.g., selecting preferably objects with fainter K -band magnitudes), figure 4.4 suggests an under-representation of ~ 6 sources with redshifts in the redshift desert. We therefore consider it likely that about half of the sources lacking redshifts are intrinsically weaker AGN with redshifts $1.5 \lesssim z \lesssim 2.3$. This redshift range falls near the epoch where the co-moving space density of steep spectrum radio sources peaks or flattens off to a constant high level (Jarvis et al., 1999), so we expect to find a substantial number of radio galaxies in complete samples of radio sources. Our findings predict it will prove very difficult to obtain complete spectroscopic redshift information for samples of flux densities $\lesssim 100$ mJy.

Pulsars

The radio spectral indices of pulsars show a broad distribution with the mean at ~ -1.6 (Lorimer et al., 1995), suggesting a fraction of our USS sources could be pulsars. The detection of 3 previously known pulsars in our USS sample and the over-density of $\alpha < -1.6$ sources near the Galactic plane (Chapter 2) are strong evidence for the presence of a significant number of pulsars in our USS sample. To avoid excessive Galactic extinction, we have excluded the Galactic plane ($|b| < 15^\circ$) from our sample, which should reduce the number of Galactic pulsars in our USS sample, but it is possible that it still contains a number of pulsars, especially for objects having the steepest spectral indices.

Optical spectroscopy of pulsars has proven difficult, even with large aperture telescopes. We have found optical spectra of three pulsars in the literature: the Crab pulsar (Nasuti et al., 1996), PSR B0540-69 (Hill et al., 1997) and Geminga (Martin, Halpern, & Schiminovich, 1998). All three spectra show flat continua with possible broad absorption and emission (in the case of PSR B0540-69) features. These spectra are qualitatively similar to most of the spectra in Figure 4.7, retaining these objects as pulsar candidates. If a significant number of these indeed turn out to be pulsars, a sample of extremely steep spectrum sources (e.g., Kaplan et al., 2000a) would be an efficient pulsar search method, especially when concentrated on the Galactic plane.

Extremely high redshift objects

An intriguing possible explanation for the objects we did not detect even after integration times of 1 hour or longer with the Keck telescope is that they are at such high redshifts that even the Ly α line has redshifted out of the optical window ($z \gtrsim 7$). The $R=25.3$ detection in WN J1525+3010 excludes this object as a potential extremely high redshift galaxy, but the non-detections in R of TN J1026-2116 and WN J2044+7044 are consistent with this interpretation, although our optical imaging is too shallow, and cannot be considered as strong evidence that the R -band samples a rest-frame wavelength range below the Lyman break. We are planning near-IR spectroscopy to search for possible emission lines in these objects.

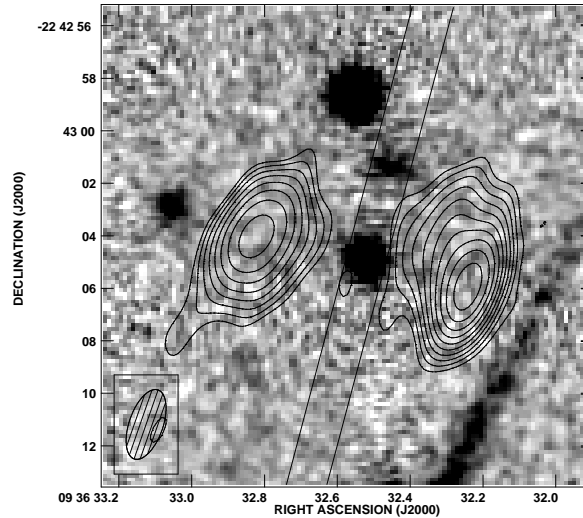


Figure 4.6: *Greyscales*: NIRC K -band image; *contours*: VLA 4.85 GHz radio image of TN J0936–2243. Contour levels are 0.24, 0.34, 0.48, 0.68, 0.96, 1.4, 1.9, 2.7, 3.8 and 5.4 mJy beam^{-1} . The VLA beam is indicated as a hatched ellipse in the lower left corner. The two parallel lines indicate the position of the $1''.5$ wide long slit used to obtain the spectra shown in figure 4.7. Note the two objects in the slit, viz. the bright identification at the midpoint of the radio lobes, and the diffuse object due north near the extension of the western radio lobe. The astrometric uncertainty in the registration of the radio and near-IR images is $<0''.4$. The dark streak in the bottom right corner is a bleed-out trail of a nearby bright star.

4.4.3 TN J0936–2243: an old, red galaxy

One of the most peculiar sources we observed spectroscopically, is TN J0936–2243. We show an overlay of our VLA radio map (see Chapter 2) on our NIRC K -band image (see Chapter 3) in figure 4.6. The astrometric solution was based on the USNO-A2.0 (Hipparcos-based) catalog. The error in the relative astrometry is dominated by the uncertainty between the optical and radio reference frames, which is $\sim 0''.4$ (90% confidence limit; Deutsch, 1999). The near-IR identification is a marginally resolved $K = 18.3 \pm 0.3$ object at the geometric midpoint of the radio lobes, but the North-Eastern extension of the western radio lobe suggests that the extended $K = 19.4 \pm 0.3$ object $3''.5$ North of the midpoint between the radio lobes might well be related to this object. Higher resolution and deeper radio data will be needed to clarify the radio-optical morphology, and if the companion object should be considered part of the main galaxy or not. In the R -band image obtained with the ESO 3.6m telescope (see Chapter 3), we marginally detect the northern object, but do not detect the southern object down to $R = 24$, classifying this object as an ERO with $R - K > 5$.

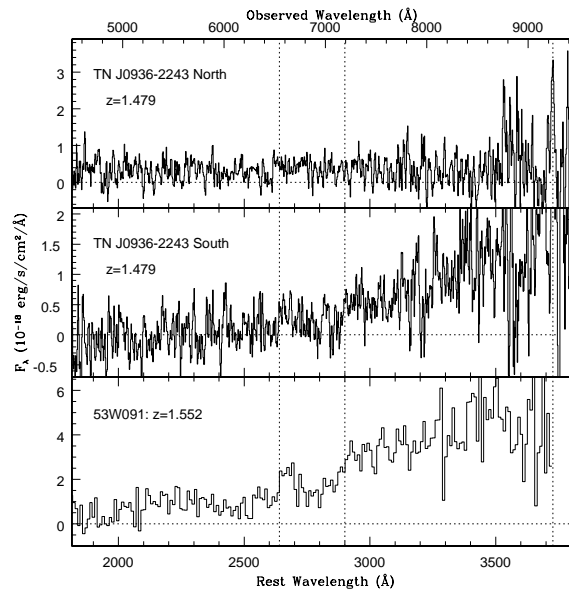


Figure 4.7: The top and middle panels show the spectra of the northern and southern components of TN J0936–2243. Vertical dotted lines indicate the wavelengths of the 2640 Å and 2900 Å breaks and [O II] λ 3727. For reference, we show the spectrum of LBDS 53W091 from Spinrad et al. (1997).

We obtained an LRIS spectrum with the slit passing through the two near-IR objects, as indicated in figure 4.6.

The spectrum of the fuzzy northern object (Fig. 4.7, top panel) shows a weak, relatively flat continuum with a single emission line at 9240 Å, while the southern object (Fig. 4.7, middle panel) shows a very red object, but no convincing emission lines. If we interpret the emission line in the northern object as [OII] λ 3727 Å, and assume the same $z = 1.479$ for the southern object, the latter displays the 2640 Å and 2900 Å continuum breaks. We therefore assume both objects are components of the same source, or companion objects.

The spectrum of the southern component closely resembles the old, red galaxies LBDS 53W091 at $z = 1.55$ (Spinrad et al., 1997, Fig. 4.7, bottom panel) and LBDS 53W069 at $z = 1.69$ (Dunlop, 1999). TN J0936–2243 is $\sim 3\times$ brighter than LBDS 53W091 (which has $S_{1412} = 22.1$ mJy and $\Theta < 3''.7$; Windhorst, van Heerde & Katgert 1984), has a similar spectral index, and is twice as large. However, LBDS 53W069 ($S_{1412} = 3.7$ mJy and $\Theta < 5''.1$) is ~ 20 times fainter at 1.4 GHz than TN J0936–2243. While a deeper spectrum would be needed to measure the exact

Table 4.8: Quasars identified from our USS sample

Source	z	S_{1400} mJy	α_{radio}	LAS ''	R^a	m_R mag	m_K^b mag	$\alpha_{optical}$	Identification
WN J0717+4611	1.462	108	-1.30	6.2	0.6	21.6	16.8±0.5	-3.9	WN J0717+4611
WN J0923+4602	0.727	12	-1.49	21.6	3.6	18.3	>16	...	RX J09232+4602
WN J1124+3228	1.525	39	-1.31	219	3.6	17.4	15.7±0.2	-1.9	FIRST J1124+3228
WN J2313+4053	2.99	11	-1.50	18.8	...	-2.2	WN J2313+4053

^a R is the radio core-to-lobe flux density ratio.

^b Determined from Lick Gemini observations or from 2MASS (Jarrett et al., 2000).

REFERENCES: RX J09232+4602: Wu, Bade, & Beckmann (1999); FIRST J1124+3228: White et al. (2000)

strengths of the 2640 Å and 2900 Å breaks in the southern component, the comparison with LBDS 53W091 suggests that the break is of similar magnitude or larger, implying an age of the stellar population of $\gtrsim 3$ Gyr. Further evidence for an old age comes from the very red $R - K$ color.

The identification of TN J0936–2201 with the southern $K = 18.3$ component puts this object on the main trend in the Hubble $K - z$ relation at $z = 1.479$. If the diffuse northern component is part of the same physical system, the total magnitude could even mount to $K = 18.0$ in an 8'' diameter aperture. Because the radio luminosity of TN J0936–2201 is not particularly weak ($L_{365} = 9.4 \times 10^{36}$ erg s⁻¹ Hz⁻¹), and no strong contribution from AGN emission is seen in the spectrum, this argues against a significant direct contribution from a non-stellar AGN dominated component to the K-band magnitudes (Eales et al., 1997; Lacy, Bunker, & Ridgway, 2000).

4.4.4 Quasars

Since the initial literature search in Chapter 2, two more sources in our USS sample have been identified as quasars according to the literature. We list these sources together with two quasars presented in this chapter in table 4.8. We fitted the continuum slope α_{opt} from line-free regions of the optical spectra ($f_\nu \propto \nu^{\alpha_{opt}}$) and measured the radio core-to-lobe flux density ratio R for three objects. Our R values are only rough approximations, based on 1.4 GHz or 4.8 GHz maps; deeper and higher resolution radio maps are needed to confirm the high core-dominance in these quasars. We find that the three measured optical spectral indices are steeper than the median $\alpha_{opt} \simeq -1.0$ found from the MRC quasar sample (Baker et al., 1999).

We note that the quasars in our sample are at slightly higher redshifts, and probably contain much steeper spectrum radio cores than the $\alpha_{core} \sim 0$ of the MRC quasars (Kapahi et al., 1998b). The radio morphology of our sources (see Chapter 7) shows much more diffuse radio lobes than the more classic FR II morphologies of the MRC quasars (see Kapahi et al., 1998b). Such diffuse lobes could easily be over-resolved in the high-frequency radio maps used to construct our USS sample (which are of $\sim 5\times$ higher resolution than the low frequency maps). This missing flux would tend to over-estimate the steepness of the derived spectral index, and add sources with such morphologies in an USS sample.

4.5 Conclusions

We have determined new redshifts of 49 USS sources, 33 of which are part of our new sample of USS sources (Chapter 2). Considering only the spectra from this main USS sample, one third are radio galaxies at $z > 3$, showing the high efficiency of our sample in finding very high redshift radio galaxies, when combined with a near-IR identification campaign. The K -band images allow the preferential selection of the faintest objects, which on the basis of the Hubble $K-z$ diagram are expected to have the highest redshifts. This combined USS and faint K -band magnitude selection technique explains why we find similar numbers of sources from $z = 0$ to $z = 4$ from our sample, despite the expected decrease in the fraction of the most distant and luminous radio galaxies in a sample with a ten times lower flux limit than previous efforts.

We have also found four quasars from our USS sample, of which at least three have very red optical continuum slopes, suggesting that such red quasars have been missed by previous quasar samples.

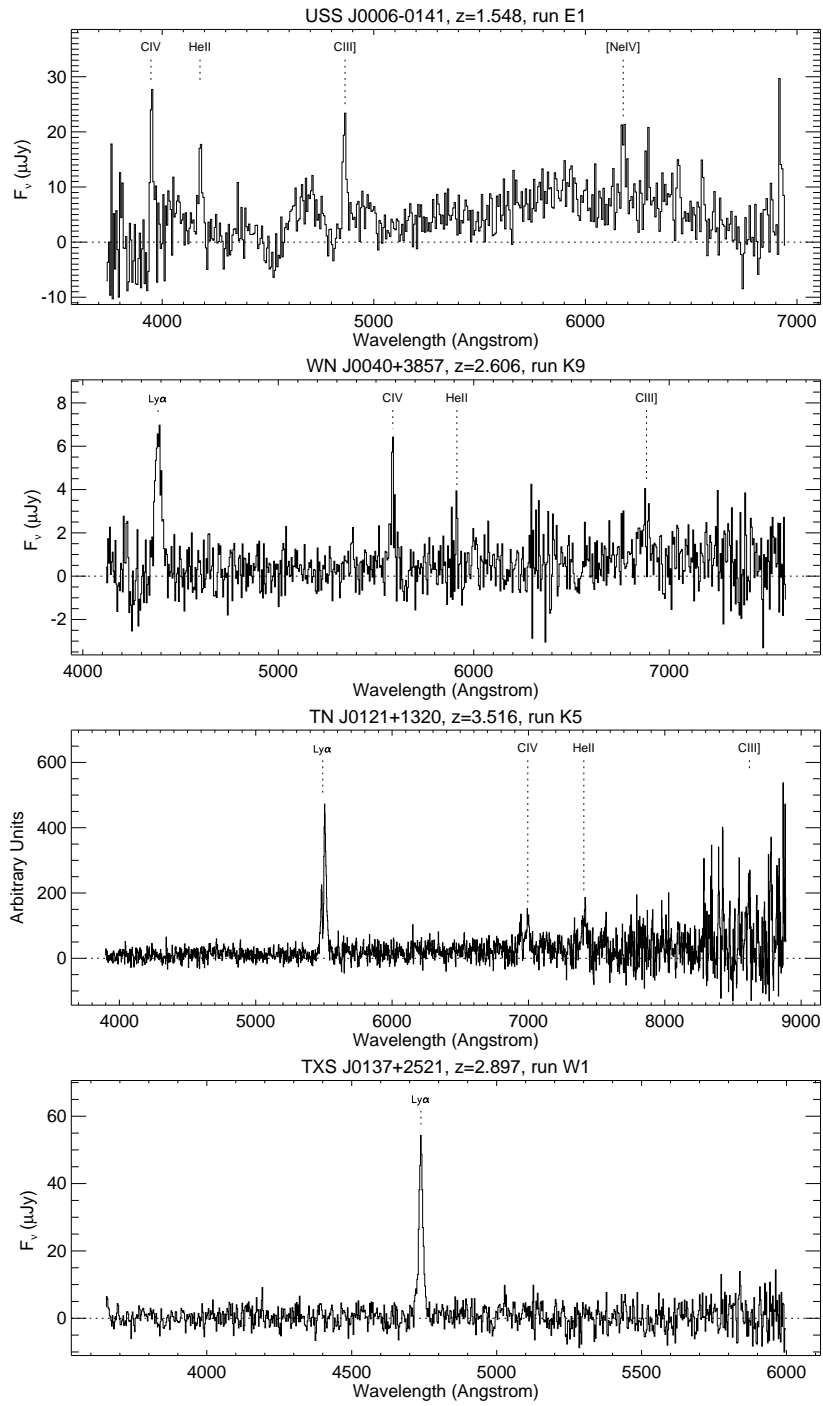
We also find five sources without distinctive emission or absorption features. We exclude the possibility that these are stars or BL Lacs. Possible identifications include (i) radio galaxies with faint emission lines in the “redshift desert” at $1.5 \lesssim z \lesssim 2.3$, (ii) radio galaxies with an obscured AGN, which are dominated by a stellar continuum observed with insufficient S/N, and (iii) pulsars.

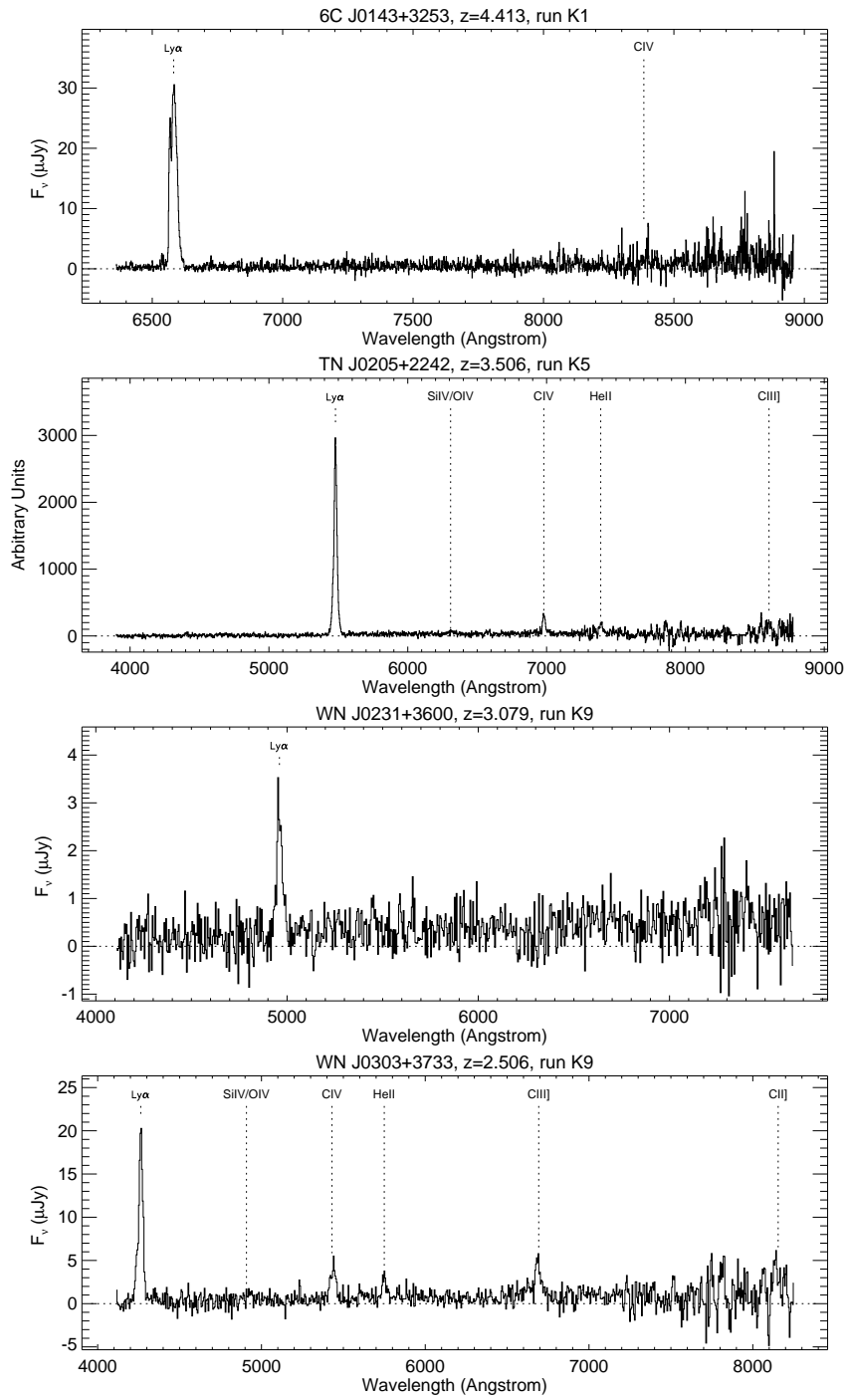
Three objects with $K \sim 20-21$ did not yield any optical continuum or line emission, even after 50–90 min integrations with the Keck telescope. These objects are possible $z > 7$ targets.

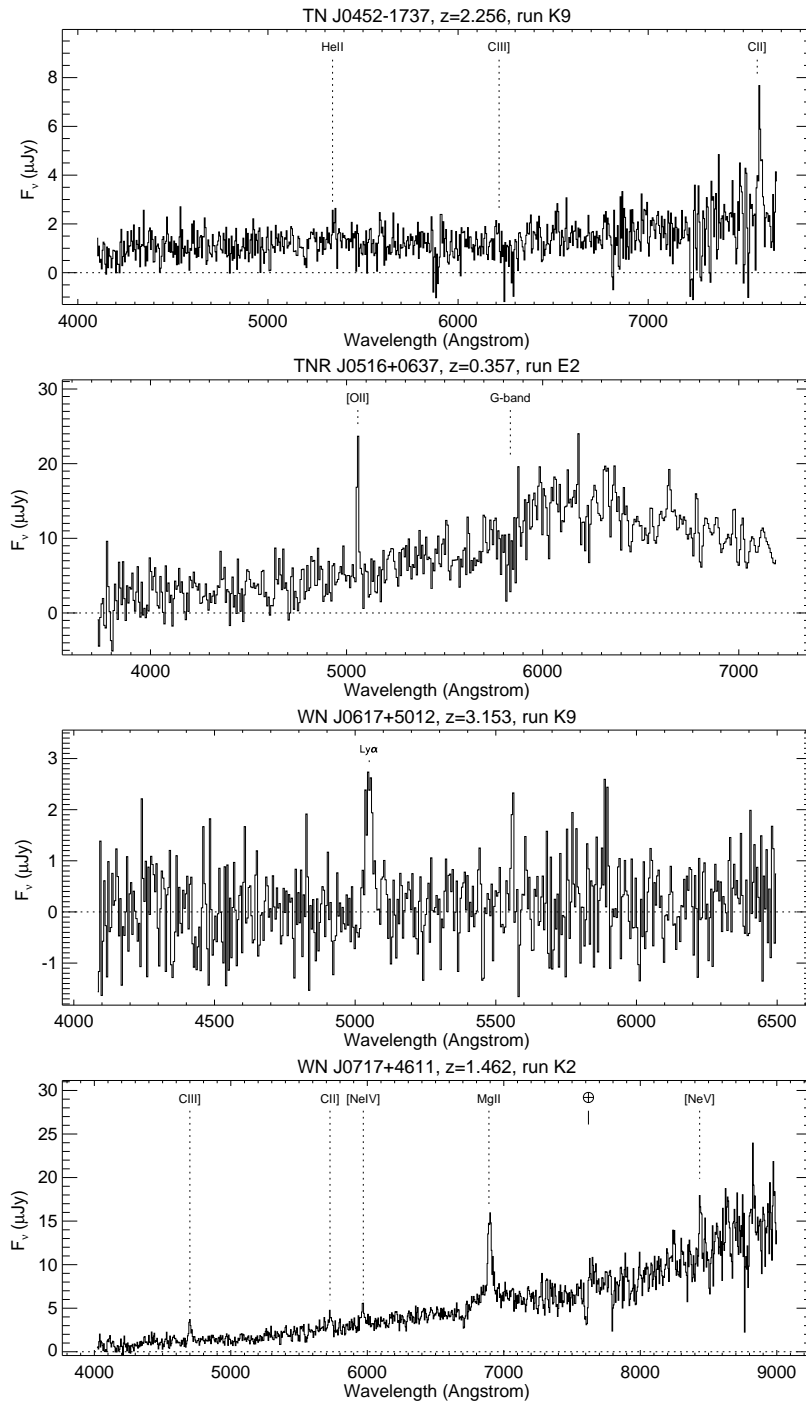
This chapter increases the number of known $z > 2$ radio galaxies to 143 (including 27 at $z > 3$, 6 at $z > 4$, and 1 at $z > 5$). In Chapter 8, we use these new emission line data to perform a statistical analysis of the emission line regions of radio galaxies from $z = 0$ to $z = 5.19$.

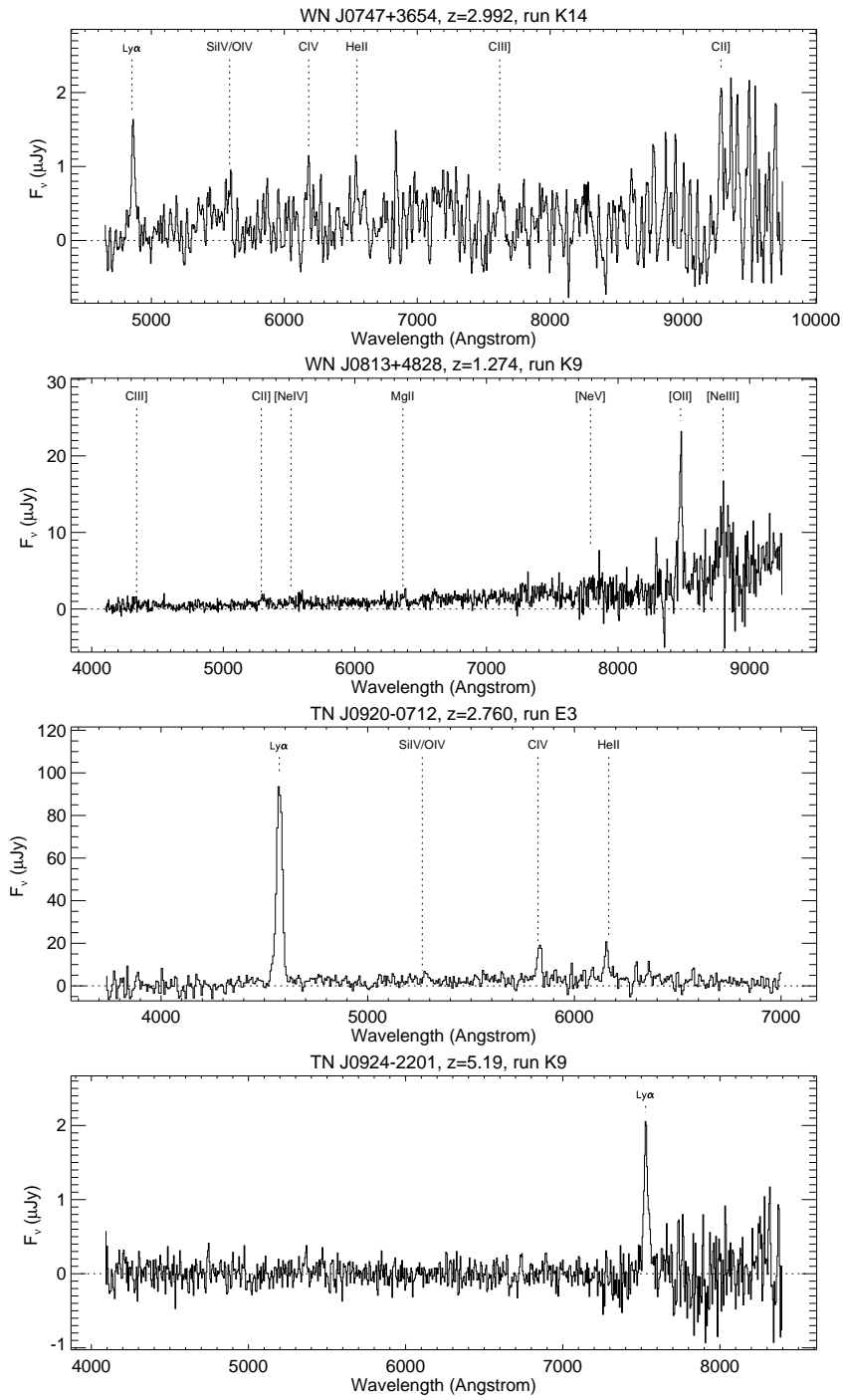
Acknowledgements

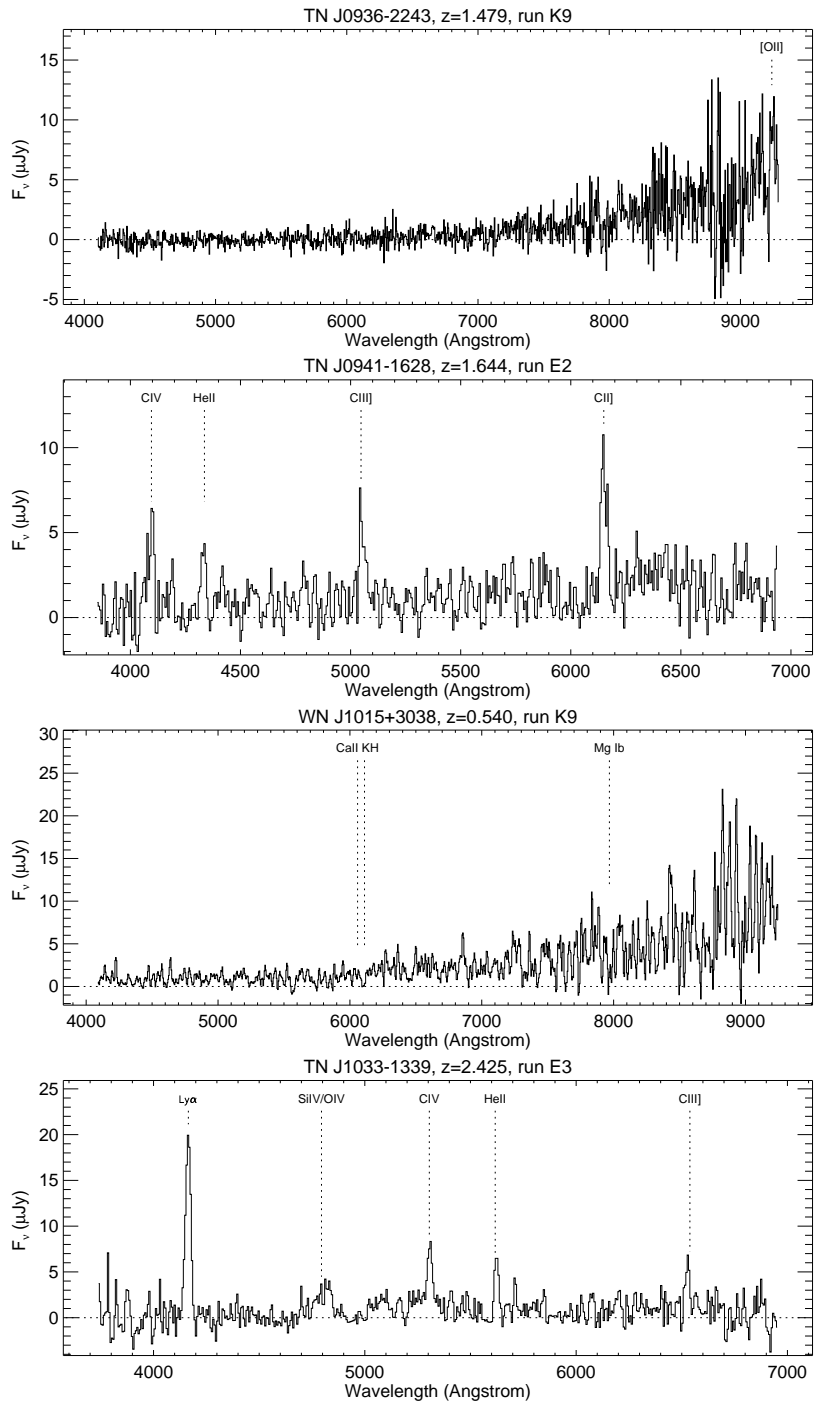
We are grateful for the excellent help provided by the staff of the Lick, Keck, ESO, and WHT telescopes. We thank Arjun Dey for his help during one of the Keck runs, Sally Laurent-Muehleisen and Nahum Arav for useful discussions, Mike Brotherton for providing the electronic version of the FIRST J1124+3228 quasar, and Hy Spinrad for his comments on the manuscript. This publication makes use of data products from the Two Micron All Sky Survey and of the NASA/IPAC Extragalactic Database (NED). The work by CDB, WvB, WdV and SAS at IGPP/LLNL was performed under the auspices of the U.S. Department of Energy by University of California Lawrence Livermore National Laboratory under contract No. W-7405-Eng-48. This work was supported in part by the Formation and Evolution of Galaxies network set up by the European Commission under contract ERB FMRX-CT96-086 of its TMR programme.

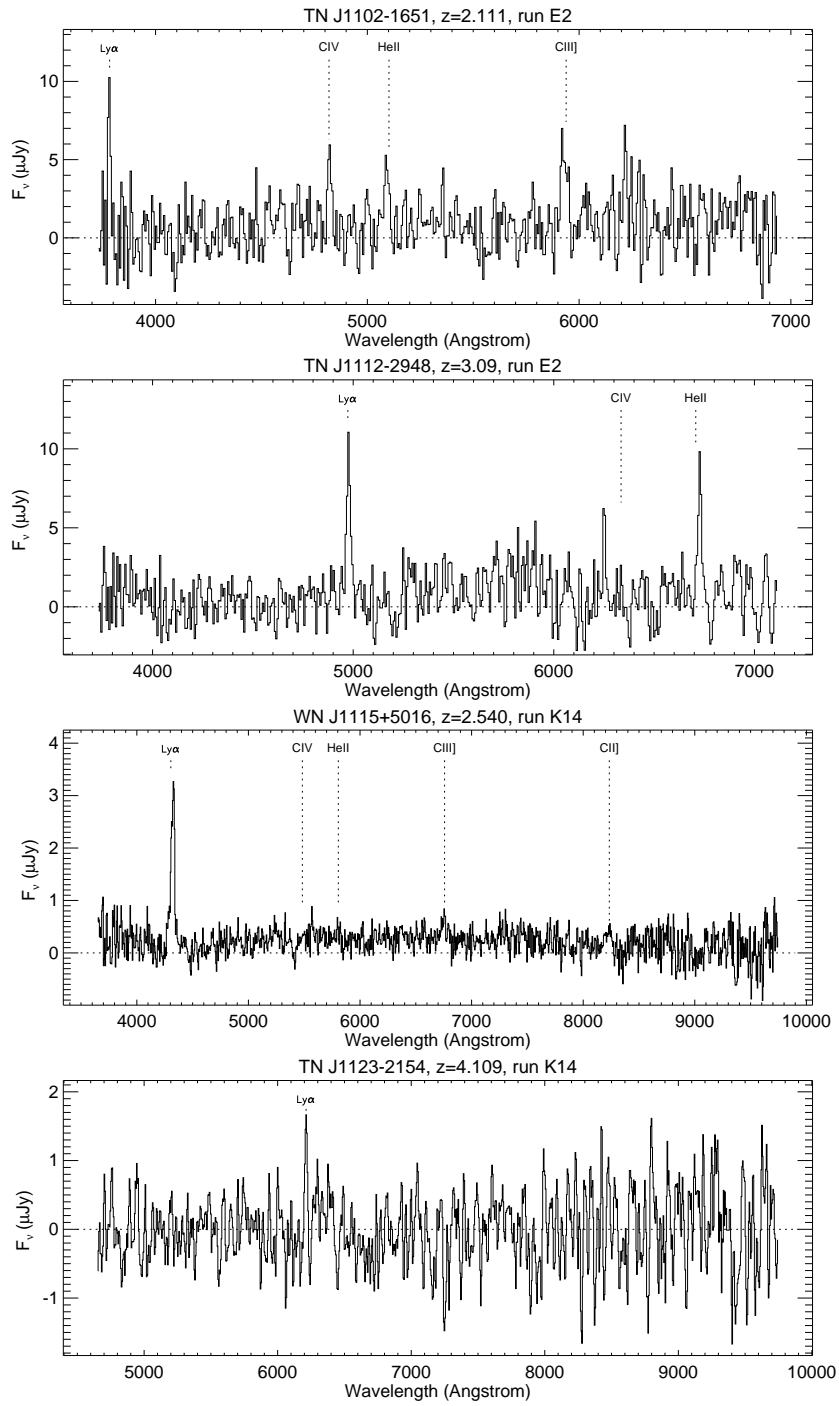


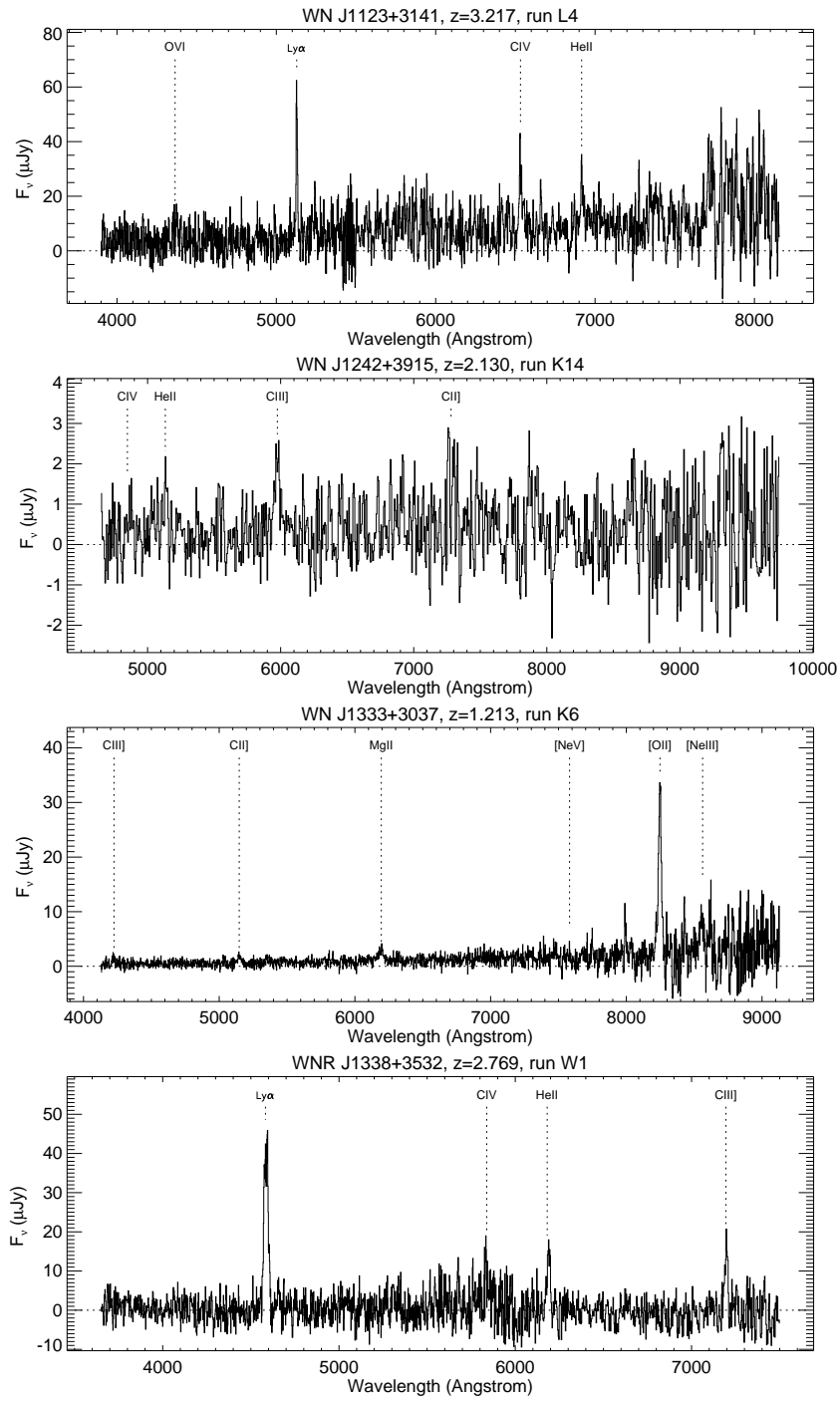


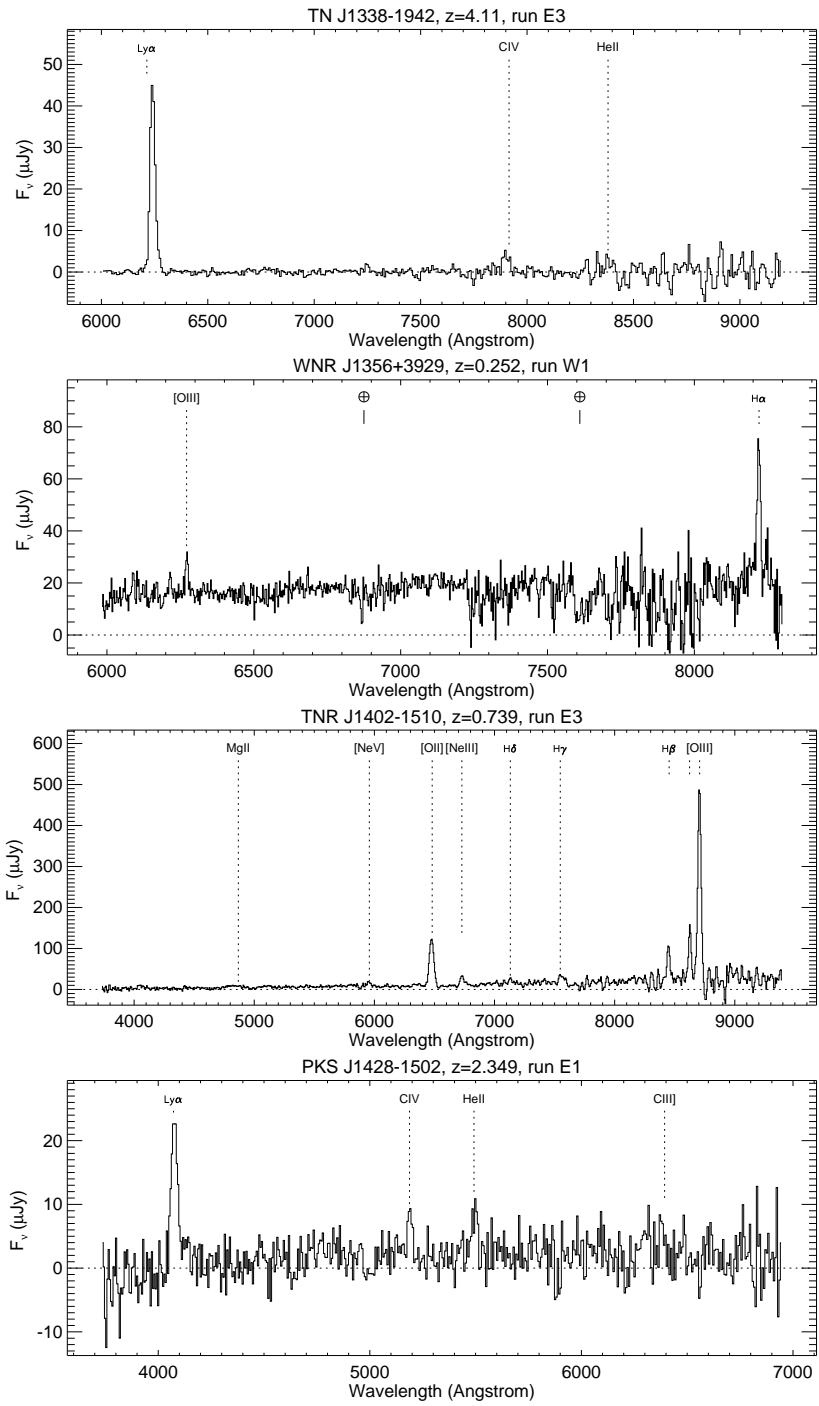


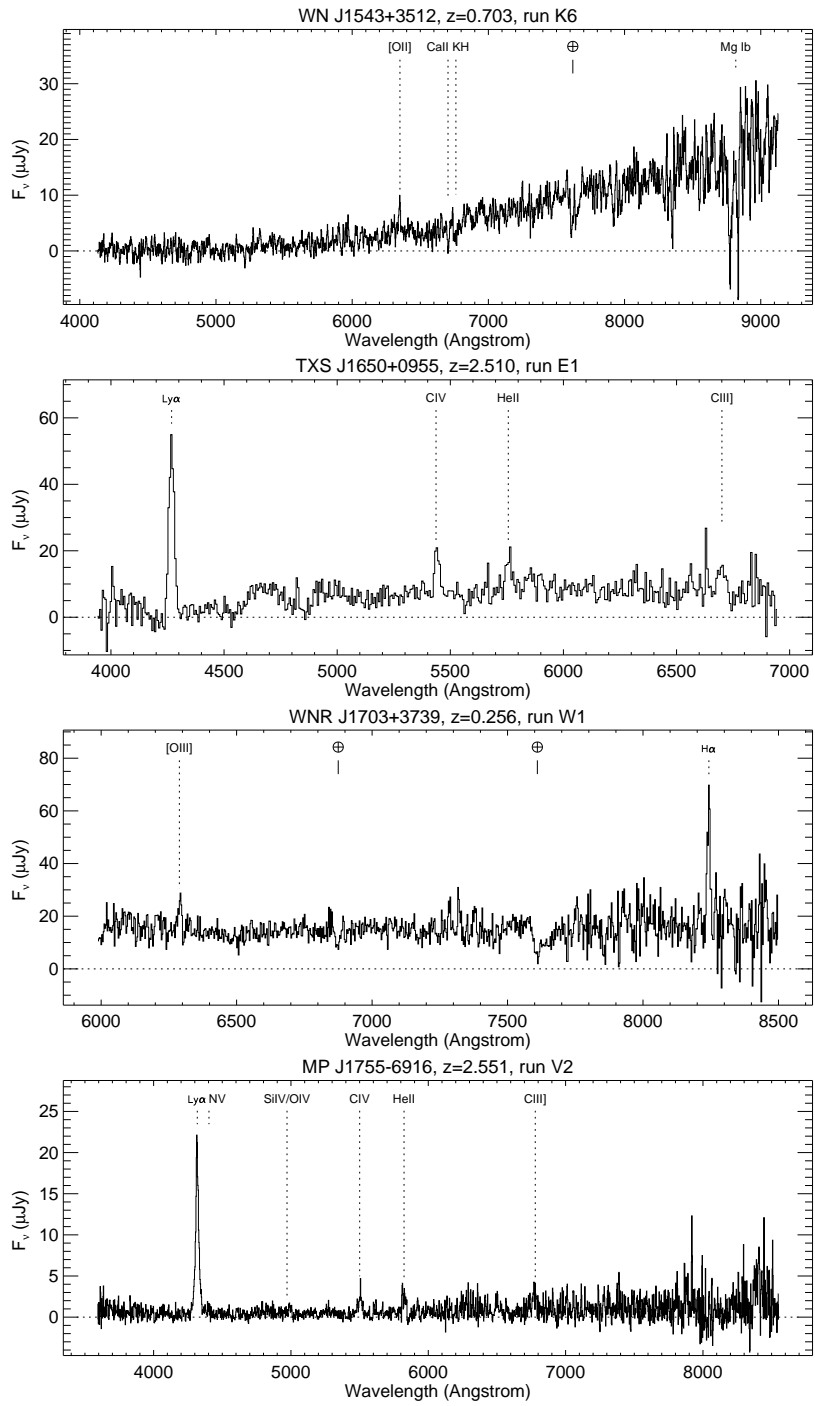


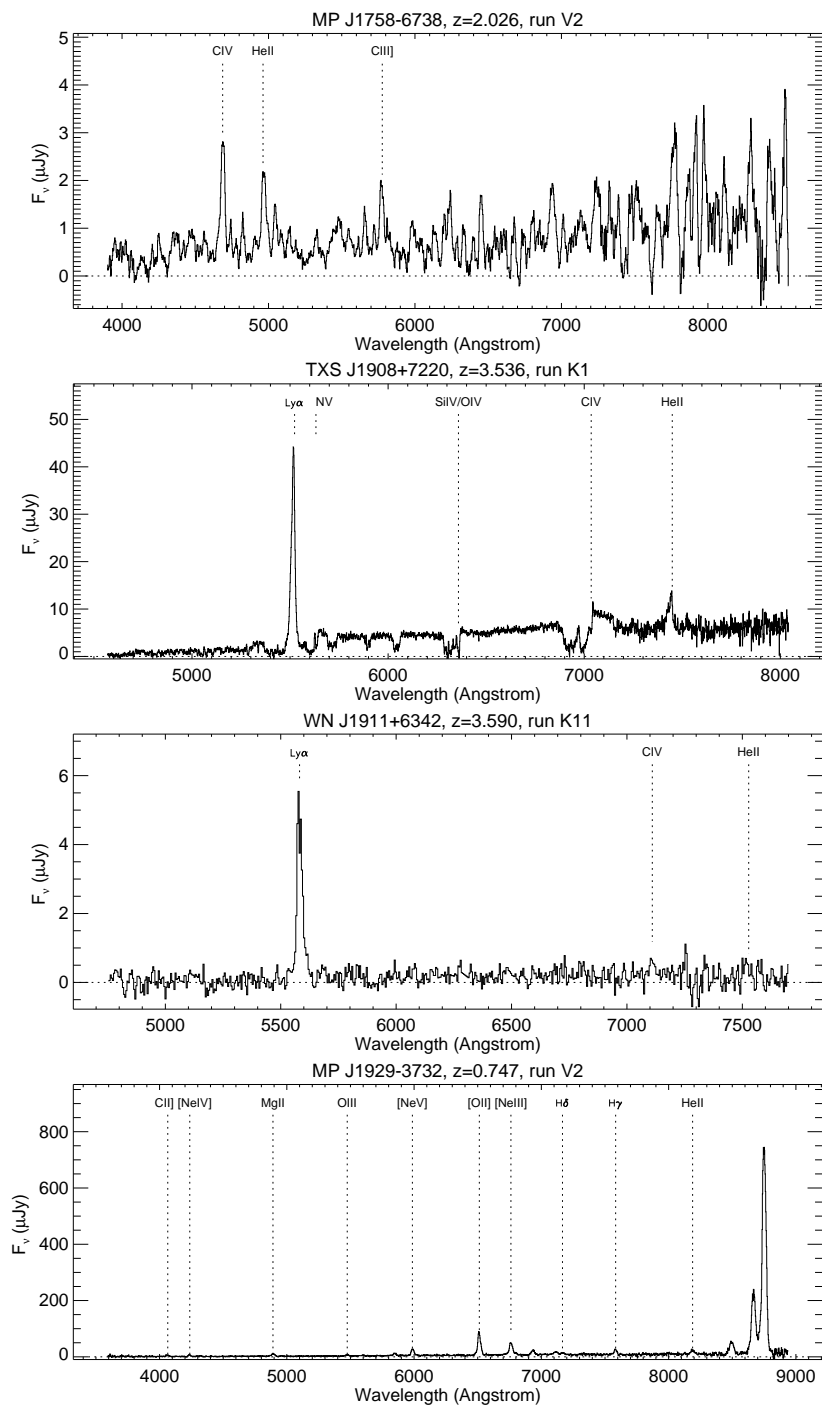


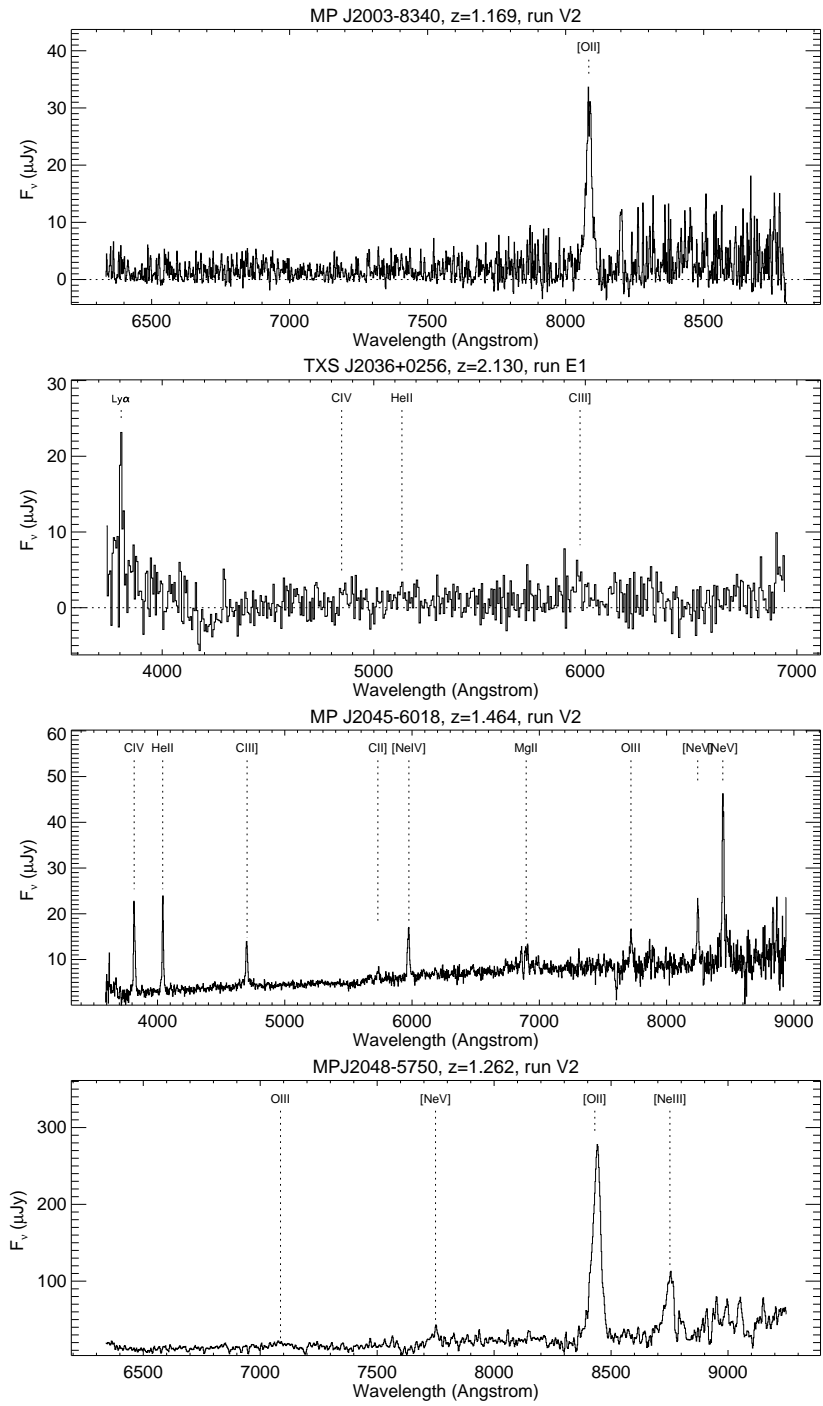


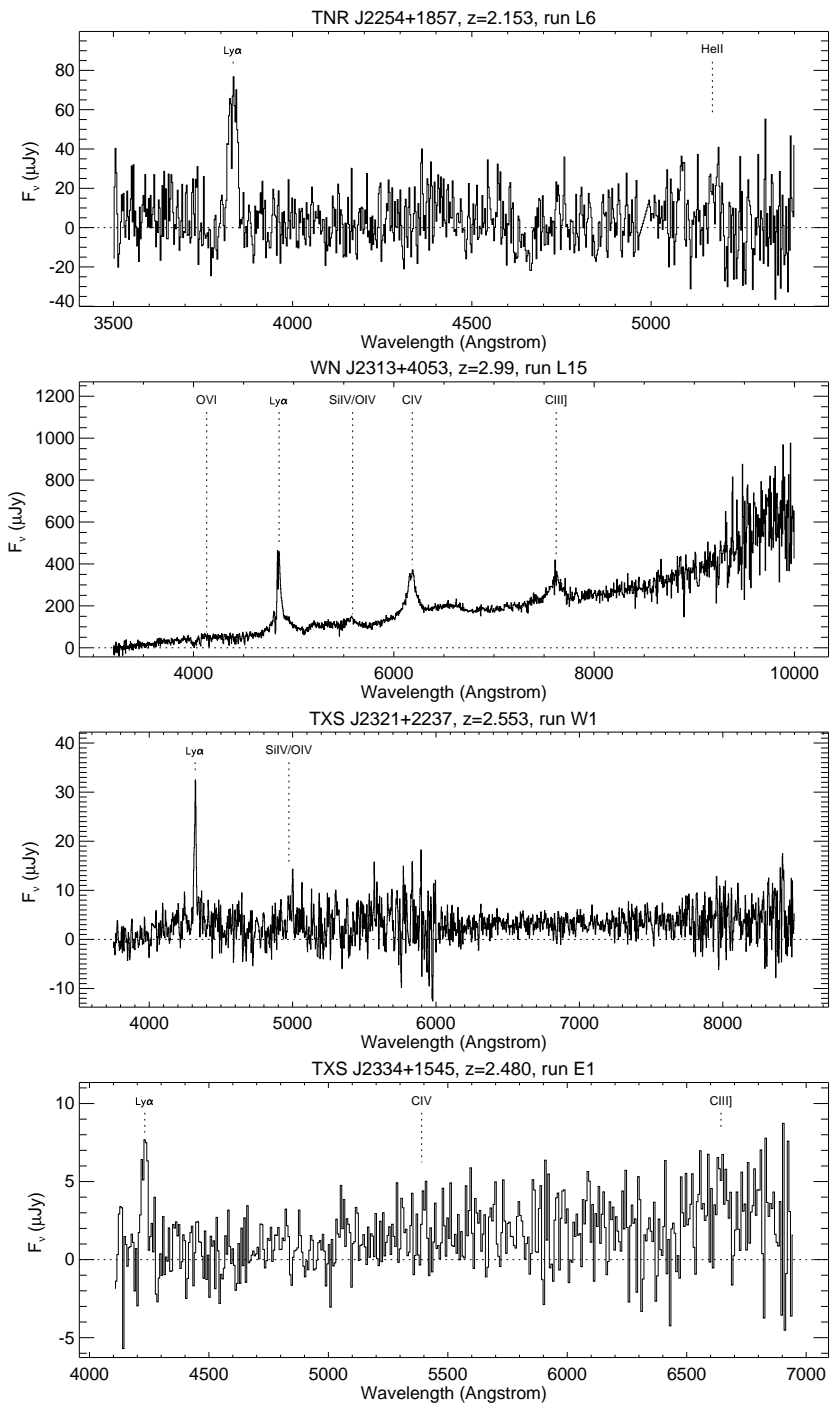












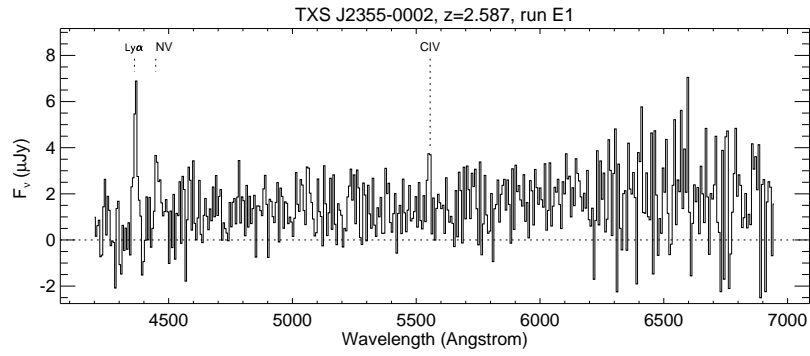


Figure 4.8: Spectra of sources from the WN/TN/MP USS samples with prominent features indicated. The positions of the vertical dotted lines indicate the predicted observed wavelength of the lines at the redshift quoted on top of each individual spectrum, and not the wavelength of the fitted peak. Differences between the feature and the dotted line thus show velocity shifts of the lines. The source name, redshift, and observing run (see table 4.3) are shown on top of each spectrum. Telluric OH absorption is indicated by \oplus .

A Radio Galaxy at $z = 5.19$

W. van Breugel, C. De Breuck, S. A. Stanford, D. Stern, H. Röttgering,
& G. Miley 1999, *ApJ*, 518, L61

Abstract

We report the discovery of the most distant known AGN, the radio galaxy TN J0924–2201 at $z = 5.19$. The radio source was selected from a new sample of ultra-steep spectrum (USS) sources, has an extreme radio spectral index $\alpha_{365}^{1400} = -1.63$, and is identified at near-IR wavelengths with a very faint, $K = 21.3 \pm 0.3$ object. Spectroscopic observations show a single emission line at $\lambda \sim 7530 \text{ \AA}$ which we identify as Ly α . The K -band image, sampling rest-frame U -band, shows a multi-component, radio-aligned morphology, typical of lower-redshift radio galaxies. TN J0924–2201 extends the near-IR Hubble, or $K - z$, relation for powerful radio galaxies to $z > 5$, and is consistent with models of massive galaxies forming at even higher redshifts.

5.1 Introduction

How did the first objects form after the Big Bang? In hierarchical cosmologies (e.g., Turner, 1998), the first gravitationally bound systems may have been stars and small star-forming systems which merge to form galaxies in large dark matter halos. Arising from the end products of stellar evolution and mergers, central black holes could grow to become extremely massive. However, it is not clear how this process would work at very high redshifts, where little time is available. It has been suggested that primordial black holes may form well before their host galaxies (Loeb, 1993). In any case, accretion events fueling massive black holes are thought to manifest themselves as active galactic nuclei (AGN; e.g., Rees, 1984). Due to their extreme

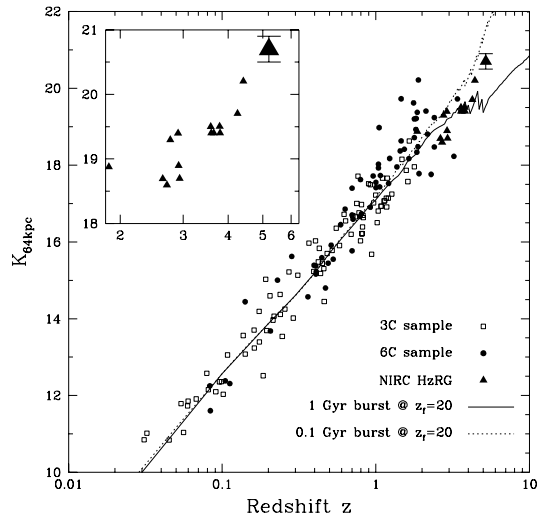


Figure 5.1: Hubble $K - z$ diagram. Filled triangles are Keck measurements of HzRGs from van Breugel et al. (1998), the large triangle is TN J0924–2201, and all other photometry is from Eales et al. (1997). Magnitudes are aperture-corrected to a 64 kpc metric diameter using $H = 65 \text{ km s}^{-1} \text{ Mpc}^{-1}$ and $\Omega = 0.30$, for which TN J0924–2201 has $K = 20.7 \pm 0.3$. Two stellar evolution models from Bruzual & Charlot (1999), normalized at $z < 0.1$, are plotted, assuming parameters as shown.

luminosity, AGN are convenient beacons for exploring these formative, ‘Dark Ages’ of our Universe.

Extragalactic radio sources have played an important role in identifying active galaxies at high redshifts. The most distant known *galaxies* have consistently been radio-selected until only very recently. In this Letter we report the discovery of a radio galaxy at $z = 5.19$. At this redshift it is the most distant known AGN, surpassing even quasars for the first time in 36 years. Throughout this chapter we use $H_0 = 65 h_{65} \text{ km s}^{-1} \text{ Mpc}^{-1}$, $\Omega_M = 0.3$, and $\Lambda = 0$. For these parameters, $1''$ subtends $7.0 h_{65}^{-1} \text{ kpc}$ at $z = 5.19$ and the Universe is only 1.08 Gyr old, corresponding to a lookback time 91.1% of the age of the Universe.

5.2 Source Selection

The most efficient method to find high-redshift radio galaxies (HzRGs) is to combine two well-known techniques. The first is to select radio sources with ultra-steep spectra (USS) at radio wavelengths, or very red ‘radio color’ (e.g., Chambers, Miley, & van Breugel, 1990). Most powerful radio galaxies have radio spectral energy distributions

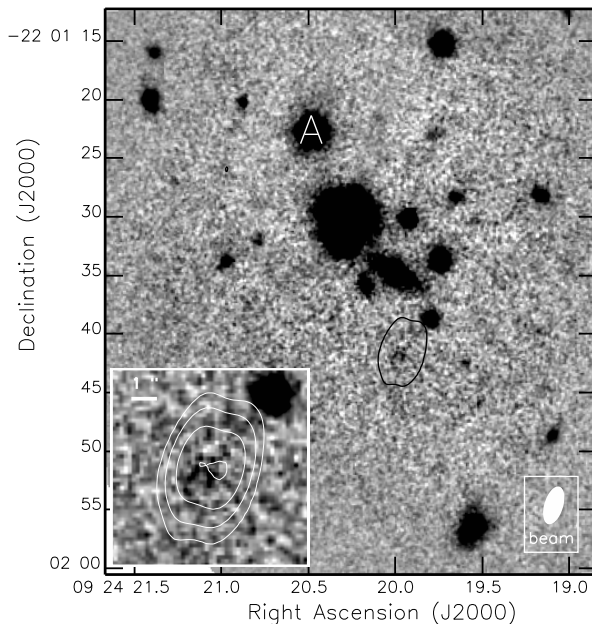


Figure 5.2: Keck/NIRC K -band image of TN J0924–2201, with radio contours superposed. Star ‘A’, offset from the HzRG by $\Delta\alpha = 7''.2$ (E) and $\Delta\delta = 18''.7$ (N), was used for blind-offsetting for the spectroscopic observations.

which steepen with frequency. Therefore, at fixed observing frequencies more distant sources exhibit steeper spectra (e.g., van Breugel et al., 1999b).

A second selection criterion relies upon the magnitude–redshift relationship at infrared wavelengths, or $K - z$ Hubble diagram, for powerful radio galaxies (Figure 5.1). At low redshifts ($z < 1$), powerful radio galaxies are uniquely associated with massive galaxies. The well-behaved $K - z$ diagram suggests that such galaxies can be found through near-IR identification. This has been confirmed by the discovery of many $3 < z < 4.4$ radio galaxies which approximately follow the $K - z$ relationship, even to the highest redshifts and despite significant morphological evolution (van Breugel et al., 1998).

Using several new, large radio surveys we constructed a USS sample ($S_\nu \propto \nu^\alpha$; $\alpha_{365}^{1400} < -1.30$; Chapter 2) which is much larger, more accurate, and goes to fainter flux density limits than previous such samples. TN J0924–2201, with $\alpha_{365}^{1400} = -1.63 \pm 0.08$, is among the steepest sources of the sample. VLA observations at 4.85 GHz show the source is a slightly resolved $1''.2$ double with $S_{4850} = 8.6 \pm 0.5$ mJy centered at $\alpha_{J2000} = 09^h 24^m 19^s.92$, $\delta_{J2000} = -22^\circ 01' 41''.5$ (Figure 5.2).

Table 5.1: Spectroscopic Measurements of TN J0924–2201

UT Date	1998 Dec 19	1998 Dec 20
z	5.202 ± 0.002	5.188 ± 0.001
λ	7539.2 ± 1.9	7522.9 ± 1.5
$F_{Ly\alpha}$	$[10^{-17} \text{ erg cm}^{-2} \text{ s}^{-1}]$	3.4 ± 0.6
$F_{\lambda}^{\text{cont}}$	$[10^{-21} \text{ erg cm}^{-2} \text{ s}^{-1} \text{ \AA}^{-1}]$	3.3 ± 5.7
$W_{Ly\alpha}^{\text{obs}}$	$[\text{\AA}]$	> 2760
$\text{FWHM}_{Ly\alpha}$	$[\text{km s}^{-1}]$	$710 - 1550$
	1574 ± 192	1474 ± 106

5.3 Observations

We obtained K_s images of TN J0924–2201 using (NIRC; Mathews & Soifer, 1994) at the Keck I telescope. We integrated for 32 minutes on UT 1998 April 18 in photometric conditions with $0''.5$ seeing, and again for 32 minutes on UT 1998 April 19 through light cirrus with $0''.6$ seeing. The observing procedures, calibration, and data reduction techniques were similar to those described by van Breugel et al. (1998). The final image comprising 3840 s of on–source integration is shown in Figure 5.2. Using circular apertures of $2''.1$ diameter, encompassing the entire object, we measure $K = 21.15$ for night 1, and 21.45 for night 2. We estimate that $K = 21.3 \pm 0.3$. If TN J0924–2201 is at $z = 5.19$ (§5.4), then redshifted [O II] at $\lambda = 2.307\mu\text{m}$ would be included in the K_s passband and some of the K–band flux might be due to line emission.

We obtained spectra of TN J0924–2201 through a $1''.5$ wide, $3'$ long slit using LRIS (Oke et al., 1995) at the Keck II telescope. Both nights were photometric with $0''.6$ seeing and the integration times were 5400 s on UT 1998 December 19 (position angle 0°) and 4400 s on UT 1998 December 20 (position angle 180°). The observations used the 150 lines mm^{-1} grating ($\lambda_{\text{blaze}} \approx 7500 \text{ \AA}$; $\Delta\lambda_{\text{FWHM}} \approx 17 \text{ \AA}$), sampling the wavelength range 4000 \AA to $1\mu\text{m}$. Between each 1800 s exposure, we reacquired offset star A (see Fig. 5.2), performed $20''$ spatial shifts to facilitate removal of fringing in the reddest regions of the spectra, and blind offset the telescope to return TN J0924–2201 within the slit. We calculated the dispersion utilizing a NeAr lamp spectrum taken immediately subsequent to the observations (RMS variations of 0.50 \AA), and adjusted the zero point according to telluric emission lines. Final wavelength calibration is accurate to 1 \AA . The spectra were flux-calibrated using observations of Feige 67 and Feige 110 obtained on each night and were corrected for foreground Galactic extinction using a reddening of $E_{B-V} = 0.0168$ determined from the dust maps of Schlegel, Finkbeiner & Davis (1998).

We find a strong, single emission line at $\lambda \sim 7530 \text{ \AA}$ which shifts by $\approx 16 \text{ \AA}$ between the two nights. (Figure 5.3; Table 5.1). The cause of the line offset is unclear, though it may be related to problems LRIS was experiencing with slippage in the movable

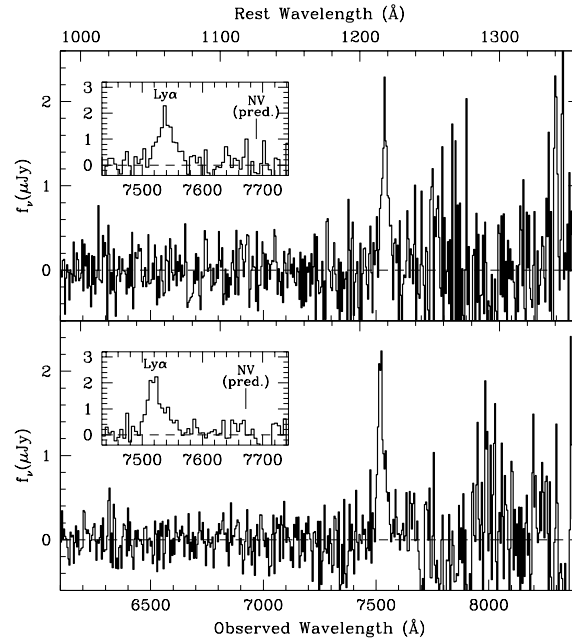


Figure 5.3: Keck spectra of TN J0924–2201. Top panel is night 1, bottom is night 2. Spectra were extracted using a $1''.5 \times 1''.5$ aperture. Inserts illustrate the emission line morphology, which is attenuated on the blue edge for night 2. The predicted wavelength of N V λ 1240 emission is indicated.

guider at the time of the observations. The relative brightnesses of other sources on the slit vary between each 1800 s observation, indicating that despite our precautions of reacquiring the target after each exposure, guider slippage must have caused some variations in telescope offsetting. These slight pointing changes may have caused the slit to sample different regions of spatially–extended, line–emitting gas. We note that TN J0924–2201 indeed shows two separate components at K (Figure 5.2), and emission–line regions of HzRGs are known to be kinematically complex (Chambers, Miley, & van Breugel, 1990; van Ojik et al., 1997).

Line parameters are measured with a Gaussian fit to the emission line and a flat (in F_λ) fit to the continuum (Table 5.1). Equivalent width values were derived from a Monte Carlo analysis using the measured line flux and continuum values with errors, subject to the constraint that both are > 0 . For UT 1998 Dec 19, when no continuum was reliably detected, we quote the 90% confidancy limit, $W^{\text{obs}} > 2760 \text{ \AA}$. For UT 1998 Dec 20, when continuum was marginally detected, we quote the 90% confidancy interval, $W^{\text{obs}} = 710 - 1550 \text{ \AA}$.

Table 5.2: Physical parameters of HzRGs

Name	z	$L_{\text{Ly}\alpha}^{\dagger}$	L_{365}^{\dagger}	α_{365}^{1400}	$W_{\text{Ly}\alpha}^{\text{rest}}$ (Å)	$\text{FWHM}_{\text{Ly}\alpha}$ (km s^{-1})	Θ^{\S} (kpc)	Reference
TN J0924–2201	5.19	1.3	7.5	–1.63	>115	1500	8	This chapter
6C 0140+326	4.41	11	1.3	–1.15	...	1500	19	Rawlings et al. (1996)
8C 1435+63	4.25	3.2	11	–1.31	670:	1800	28	Spinrad et al. (1995)
TN J1338–1942	4.13	20	2.3	–1.31	>700:	1300	37	Chapter 6
4C 41.17	3.798	12	3.3	–1.25	100:	1400	99	Dey et al. (1997b)
4C 60.07	3.79	16	4.1	–1.48	150	2900:	65	Röttgering et al. (1997)

[†] Ly α luminosity in units of $10^{-43} \text{erg s}^{-1}$

[‡] Radio power at 365 MHz in units of $10^{-36} \text{erg s}^{-1}$

[§] Radio largest angular size

5.4 Redshift Determination

As discussed by Dey et al. (1998) and Weymann et al. (1998) for two $z > 5$ Ly α -emitting field galaxies, a solitary, faint emission line at red wavelengths is most likely to be either low-redshift [O II] or high-redshift Ly α . Similar arguments are even more persuasive for HzRGs because of their strong, rich emission line spectra. For example, if the line at $\approx 7530 \text{ \AA}$ were [O II] at $z = 1.020$ then composite radio galaxy spectra (McCarthy, 1993; Stern et al., 1999a) should have shown C II] at 4699 \AA with $\approx 40 - 70\%$ the strength of [O II], and Mg II at 5653 \AA with $\approx 20 - 60\%$ the strength of [O II]. Similar arguments rule out identifying the emission line with H α at $z = 0.147$ or [O III] at $z = 0.504$, since in these cases even stronger confirming lines should have been seen.

The large equivalent widths also argue against identifying the emission line with [O II] at $z = 1.020$, implying $W_{[\text{OII}]}^{\text{rest}} > 1370 \text{ \AA}$ (night 1) and $350 < W_{[\text{OII}]}^{\text{rest}} < 770 \text{ \AA}$ (night 2). Radio galaxy composites typically have rest-frame [O II] equivalent widths of $\approx 130 \text{ \AA}$ (McCarthy, 1993; Stern et al., 1999a), though active galaxies with extreme $W_{[\text{OII}]}^{\text{rest}}$ are occasionally observed ($W_{[\text{OII}]}^{\text{rest}} \approx 750 \text{ \AA}$; Stern et al., 2000b). The equivalent width of TN J0924–2201 is more typical of high-redshift Ly α which is often observed with rest-frame values of several $\times 100 \text{ \AA}$ in HzRGs (Table 5.2). We also note that the observations from the second night show that Ly α is attenuated on the blue side, presumably due to associated and intervening hydrogen gas, as is commonly observed in HzRGs (e.g., van Ojik et al., 1997; Dey, 1997a) and normal star-forming galaxies at $z > 5$ (e.g., Dey et al., 1998).

Finally, the faint K -band magnitude of TN J0924–2201 conforms to the extrapolation of the $K - z$ diagram to $z > 5$ (Figure 5.1). Identifying the emission line with [O II] would imply a severely underluminous HzRG (3 – 4 mag). We therefore conclude that the most plausible identification of the emission line in TN J0924–2201 is with Ly α at a (mean) observed wavelength of 7530 \AA and $z = 5.19$. Table 5.1 gives the dereddened emission-line fluxes.

5.5 Discussion

Among all known $z \gtrsim 3.8$ HzRGs, TN J0924–2201 is fairly typical in radio luminosity, equivalent width and velocity width (Table 5.2). But this source has the steepest radio spectrum, consistent with the $\alpha - z$ relationship for radio galaxies (e.g., Röttgering et al., 1997). TN J0924–2201 also has the smallest linear size, perhaps indicating that the source is relatively young and/or embedded in a denser environment compared to the other HzRGs, commensurate with its large velocity width (van Ojik et al., 1997) and very high redshift. Together with 8C 1435+63, TN J0924–2201 appears underluminous in $\text{Ly}\alpha$, which might be caused by absorption in a relatively dense cold and dusty medium. Evidence for cold gas and dust in some of the most distant HzRGs has been found from sub-mm continuum and CO-line observations of 8C 1435+63 and 4C 41.17 (e.g., Ivison et al., 1998a).

Our observations of TN J0924–2201 extend the Hubble $K - z$ diagram for powerful radio galaxies to $z = 5.19$, as shown in Figure 5.1, where simple stellar evolution models are shown for comparison. Despite the enormous k -correction effect (from U_{rest} at $z = 5.19$ to K_{rest} at $z = 0$) and strong morphological evolution (from radio-aligned to elliptical structures), the $K - z$ diagram remains a powerful phenomenological tool for finding radio galaxies at extremely high redshifts. Deviations from the $K - z$ relationship may exist (Eales et al. 1997; but see McCarthy 1998), and scatter in the $K - z$ values appears to increase with redshift.

The clumpy, radio-aligned U_{rest} morphology resembles that of other HzRGs (van Breugel et al., 1998; Pentericci et al., 1999a). If the continuum is dominated by star light, as appears to be the case in the radio-aligned $z = 3.798$ HzRG 4C 41.17 (Dey et al., 1997b), then $M(U) = -24.4$ for TN J0924–2201 and we derive a SFR of $\sim 200 M_{\odot} \text{ yr}^{-1}$, assuming a Bruzual & Charlot (1999) GISSEL stellar evolution model with metallicity $Z = 0.008$, no extinction, and a Salpeter IMF. This SFR value is highly uncertain due to the unknown, but competing, effects of extinction and [O II] emission-line contamination, but not unreasonable. It is 2.5 times *less* than in 4C 41.17, which has $M(U) = -25.2$ using the same aperture (Chambers, Miley, & van Breugel, 1990). TN J0924–2201 may be a massive, active galaxy in its formative stage, in which the SFR is boosted by induced star formation (e.g., Dey et al., 1997b). For comparison other, ‘normal’ star forming galaxies at $z > 5$ have 10 – 30 times lower SFR ($\sim 6 - 20 M_{\odot} \text{ yr}^{-1}$; Dey et al., 1998; Weymann et al., 1998; Spinrad et al., 1998).

Recent $z \sim 3$ and $z \sim 4$ Lyman-break galaxy observations have suggested a possible divergence of star formation and AGN activity at high redshift (Steidel et al., 1999), contrary to what was previously thought (e.g., Haehnelt, Natarajan & Rees, 1998). However, if starbursts and AGN are closely coupled, as suggested to explain the class of quasar-powered ultra-luminous infrared galaxies (Sanders & Mirabel, 1996), then young AGN may inhabit especially dusty, obscured galaxy systems. To obtain a proper census of the AGN population at the very highest redshifts therefore requires samples which avoid optical photometric selection and extinction bias, such as our

cm-wavelength/K-band radio galaxy sample.

We conclude by noting, as emphasized by Loeb (1993), that if massive black holes form in a hierarchical fashion together with their host galaxies, then this process must be quick and efficient, as available timescales are short: at $z = 5.19$ the Universe is only 1 Gyr old. It is unclear how this could be done and other models, where ‘primordial’ massive black holes form soon after the Big Bang and *prior* to the beginning of galaxy formation, may require additional investigation.

Acknowledgements

We thank G. Puniwai, W. Wack, R. Goodrich and R. Campbell for their expert assistance during our observing runs at the W.M. Keck Observatory, and A. Dey, J. Graham and H. Spinrad for useful discussions. The work by W.v.B., C.D.B. and S.A.S. at IGPP/LLNL was performed under the auspices of the US Department of Energy under contract W-7405-ENG-48. W.v.B. also acknowledges support from NASA grant GO 5940, and D.S. from IGPP/LLNL grant 98-AP017.

VLT Spectroscopy of the $z=4.11$ Radio Galaxy
TN J1338–1942

C. De Breuck, W. van Breugel, D. Minniti, G. Miley, H. Röttgering,
S. A. Stanford, & C. Carilli 1999, *A&A*, 352, L51

Abstract

We present optical, infrared and radio data of the $z = 4.11$ radio galaxy TN J1338–1942, including an intermediate resolution spectrum obtained with FORS1 on the VLT Antu telescope. TN J1338–1942 was the first $z > 4$ radio galaxy to be discovered in the southern hemisphere and is one of the most luminous Ly α objects in its class. The Ly α and rest-frame optical emission appear co-spatial with the brightest radio hotspot of this very asymmetric radio source, suggesting extremely strong interaction with dense ambient clouds.

The Ly α is spatially extended by $\sim 4''$ (30 kpc), has an enormous rest-frame equivalent width, $W_{\lambda}^{rest} = 210 \pm 50 \text{ \AA}$, and has a spectral profile that is very asymmetric with a deficit towards the blue. We interpret this blue-ward asymmetry as being due to absorption of the Ly α photons by cold gas in a turbulent halo surrounding the radio galaxy and show that the required neutral hydrogen column density must be in the range $3.5 - 13 \times 10^{19} \text{ cm}^{-2}$. The two-dimensional spectrum indicates that the extent of the absorbing gas is comparable (or even larger) than the $4''$ (30 kpc) Ly α emitting region.

The VLT observations are sufficiently sensitive to detect the continuum flux both blue-ward and red-ward of the Ly α emission, allowing us to measure the Ly α forest continuum break (Ly α 'discontinuity', D_A) and the Lyman limit. We measure a $D_A = 0.37 \pm 0.1$, which is ~ 0.2 lower than the values found for quasars at this redshift. We interpret this difference as possibly due to a bias towards large D_A introduced in high-redshift quasar samples that are selected on the basis of specific optical colors. If such a bias would exist in optically

selected quasars, – and even in samples of Lyman break galaxies –, then the space density of both classes of object will be underestimated. Furthermore, the average HI column density along cosmological lines of sight as determined using quasar absorption lines would be overestimated. Because of their radio-based selection, we argue that $z > 4$ radio galaxies are excellent objects for investigating D_A statistics.

6.1 Introduction

Within standard Cold Dark Matter scenarios the formation of galaxies is a hierarchical and biased process. Large galaxies are thought to be assembled through the merging of smaller systems, and the most massive objects will form in over-dense regions, which will eventually evolve into the clusters of galaxies (Kauffmann et al., 1999). It is therefore important to find and study the progenitors of the most massive galaxies at the highest possible redshifts.

Radio sources are convenient beacons for pinpointing massive elliptical galaxies, at least up to redshifts $z \sim 1$ (Lilly & Longair, 1984; Best, Longair & Röttgering, 1998a). The near-infrared ‘Hubble’ $K - z$ relation for such galaxies appears to hold up to $z = 5.2$, despite large K -correction effects and morphological changes (Lilly & Longair, 1984; van Breugel et al., 1998; Chapter 5). This suggests that radio sources may be used to find massive galaxies and their likely progenitors out to very high redshift.

While optical, ‘color-dropout’ techniques have been successfully used to find large numbers of ‘normal’ young galaxies (without dominant AGN) at redshifts surpassing those of quasars and radio galaxies (Weymann et al., 1998), the radio and near-infrared selection technique has the additional advantage that it is unbiased with respect to the amount of dust extinction. High redshift radio galaxies (HzRGs) are therefore also important laboratories for studying the large amounts of dust (Dunlop et al., 1994; Ivison et al., 1998a) and molecular gas (Papadopoulos et al., 2000), which are observed to accompany the formation of the first forming massive galaxies.

Using newly available, large radio surveys we have begun a systematic search for $z > 4$ HzRGs to be followed by more detailed studies of selected objects. In this Letter, we present deep intermediate resolution VLT/FORS1 spectroscopy of TN J1338–1942 which, at $z = 4.11$, was the first $z > 4$ radio galaxy discovered in the southern hemisphere (De Breuck et al., 1999), and is one of the brightest and most luminous Ly α objects of its class.

In §6.2, we describe the discovery and previous observations of TN J1338–1942. In §6.3 we describe our VLT observations, and in §6.4 we discuss some of the implications of our results. Throughout this paper we will assume $H_0 = 65 \text{ km s}^{-1} \text{ Mpc}^{-1}$, $q_0 = 0.15$, and $\Lambda = 0$. At $z = 4.11$, this implies a linear size scale of 7.5 kpc/arcsec .

6.2 Source selection and previous observations

The method we are using to find distant radio galaxies is based on the empirical correlation between redshift and observed spectral index in samples of low-frequency selected radio sources (e.g., Carilli et al., 1999). Selecting radio sources with ultra steep spectra (USS) dramatically increases the probability of pinpointing high- z radio galaxies, as compared to observing radio galaxies with more common radio spectra. This method, which can to a large extent be explained as a K-correction induced by a curvature of the radio spectra, has been shown to be extremely efficient (e.g., Chambers, Miley, & van Breugel, 1990; Chapter 5).

We constructed such a USS sample ($\alpha_{365\text{MHz}}^{1.4\text{GHz}} < -1.30$; $S_\nu \propto \nu^\alpha$; Chapter 2), consisting of 669 objects, using several radio catalogs which, in the southern hemisphere, include the Texas 365 MHz catalog (Douglas et al., 1996) and the NVSS 1.4 GHz catalog (Condon et al., 1998).

As part of our search-program we observed TN J1338–1942 ($\alpha_{365\text{MHz}}^{1.4\text{GHz}} = -1.31 \pm 0.07$) with the ESO 3.6m telescope in 1997 March and April (De Breuck et al., 1999). The radio source was first identified by taking a 10 minute R -band image. Followup spectroscopy then showed the radio galaxy to be at a redshift of $z = 4.13 \pm 0.02$, based on a strong detection of $\text{Ly}\alpha$, and weak confirming C IV and He II. At this redshift its derived rest-frame low frequency (178 MHz) radio luminosity is comparable to that of the most luminous 3CR sources.

More detailed radio information was obtained with the VLA at 4.71 GHz and 8.46 GHz on 1998 March 24, as part of a survey to measure rotation measures in HzRGs (Pentericci et al., 2000a). We detect two radio components ($S_{4.7\text{GHz}}^{\text{NW}} = 21.9$ mJy; $S_{4.7\text{GHz}}^{\text{SE}} = 1.1$ mJy) separated by $5''.5$ in the field of the radio galaxy (Fig. 6.1). The bright NW component has a very faint radio companion ($S_{4.7\text{GHz}}^{\text{C}} = 0.3$ mJy) at $1''.4$ to the SE. Our present observations show that all components have very steep radio spectra with $\alpha_{4.7\text{GHz}}^{8.5\text{GHz}}(\text{NW}) \sim -1.6$, $\alpha_{4.7\text{GHz}}^{8.5\text{GHz}}(\text{SE}) \sim -1.8$, and $\alpha_{4.7\text{GHz}}^{8.5\text{GHz}}(\text{C}) \sim -1.0$. The proximity and alignment of such rare USS components strongly suggests that they are related and part of one source. While further observations over a wider frequency range would be useful to confirm this, for now we conclude that TN J1338–1942 is a very asymmetric radio source, and identify component C at $\alpha_{2000} = 13^{\text{h}}38^{\text{m}}26^{\text{s}}10$ and $\delta_{2000} = -19^\circ42'31''.1$ with the radio core. Such asymmetric radio sources are not uncommon (e.g., McCarthy, van Breugel & Kapahi, 1991a), and are usually thought to be due to strong interaction of one of its radio lobes with very dense gas or a neighboring galaxy (e.g., Feinstein et al., 1999).

We also obtained a K -band image with the Near Infrared Camera (NIRC; Mathews & Soifer, 1994) at the Keck I telescope on UT 1998 April 18. The integration time was 64 minutes in photometric conditions with $0''.5$ seeing. Observing procedures, calibration and data reduction techniques were similar to those described by van Breugel et al. (1998). Using a circular aperture of $3''$, encompassing the entire object, we measure $K = 19.4 \pm 0.2$ (we do not expect a significant contribution from emission lines at the redshift of the galaxy). In a 64 kpc metric aperture, the magnitude is

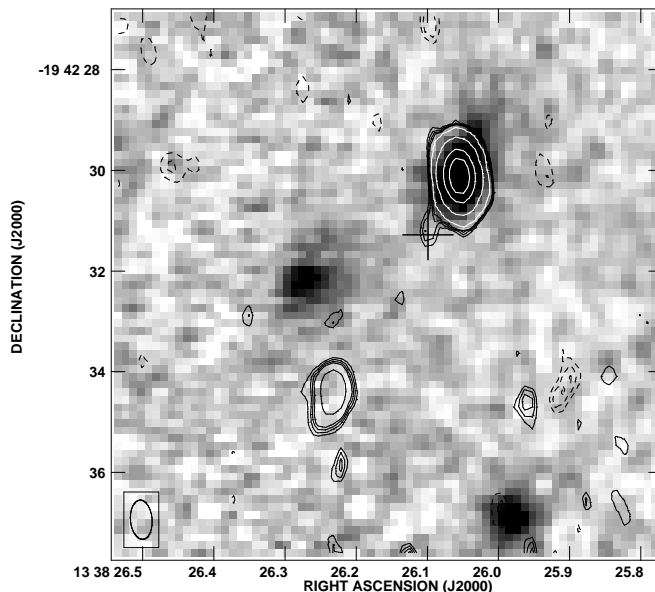


Figure 6.1: 4.85 GHz VLA radio contours overlaid on a Keck K -band image. The cross indicates the position of the likely radio core at 8.5 GHz, which appears offset from the galaxy by $1''.4$ ($\sim 4\sigma$) along the radio axis. Contour levels are -0.23 , -0.17 , -0.12 , 0.12 , 0.15 , 0.17 , 0.20 , 0.35 , 1.45 , 5.8 , and 29 mJy/beam

$K_{64} = 19.2 \pm 0.3$, which puts TN J1338–1942 at the bright end, but within the scatter, of the $K - z$ relationship (van Breugel et al., 1998).

We determined the astrometric positions in our $5' \times 5'$ R -band image using the USNO PMM catalog (Monet et al., 1998). We next used the positions of nine stars on the R -band image in common with the Keck K -band to solve the astrometry on the $1' \times 1'$ K -band image. The error in the *relative* near-IR/radio astrometry is dominated by the absolute uncertainty of the optical reference frame, which is $\sim 0''.4$ (90% confidence limit; Deutsch, 1999). In Figure 6.1, we show the overlay of the radio and K -band (*rest-frame* B -band) images. The NW hotspot coincides within $0''.035$ of the peak of the K -band emission, while some faint diffuse extensions can be seen towards the radio core and beyond the lobe. The positional difference between the peak of the K -band emission and the radio core is $1''.4$ ($\sim 4\sigma$), which suggests that the AGN and peaks of the K -band and $\text{Ly}\alpha$ emission may not be co-centered.

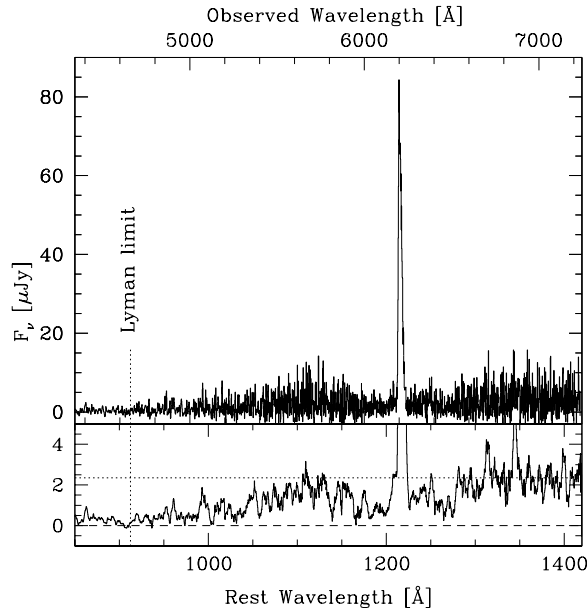


Figure 6.2: VLT spectrum of TN J1338–1942. The lower panel has been boxcar smoothed by a factor of 15 to better show the shape of the Ly α forest and the Lyman limit. The horizontal dotted line is the extrapolation of the continuum at $1300\text{\AA} < \lambda_{rest} < 1400\text{\AA}$, and the vertical dotted line indicates the position of the $\lambda_{rest} = 912\text{\AA}$ Lyman limit.

6.3 VLT observations

Because of the importance of TN J1338–1942 as a southern laboratory for studying HzRGs, we obtained a spectrum of this object with high signal-to-noise and intermediate spectral resolution with FORS1 on the ANTU unit of the VLT on UT 1999 April 20. The purpose of these observations was to study the Ly α emission and UV-continuum in detail.

The radio galaxy was detected in the acquisition images ($t_{\text{int}} = 2 \times 60$ s; $I = 23.0 \pm 0.5$ in a $2''$ aperture). We used the 600R grism with a $1''.3$ wide slit, resulting in a spectral resolution of 5.5\AA (FWHM). The slit was centered on the peak of the K -band emission at a position angle of 210° North through East. To minimize the effects of fringing in the red part of the CCD, we split the observation into two 1400 s exposures, while offsetting the object by $10''$ along the slit between the individual exposures. The seeing during the TN J1338–1942 observations was $\sim 0''.7$ and conditions were photometric.

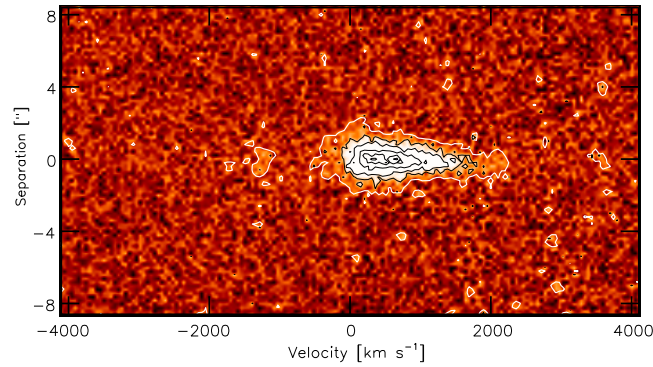


Figure 6.3: Two dimensional FORS1 spectrum of the Ly α region. Note the strong, 1400 km s $^{-1}$ wide depression in the blue half.

Data reduction followed the standard procedures using the NOAO IRAF package. We extracted the one-dimensional spectrum using a 4'' wide aperture, chosen to include all of the Ly α emission. For the initial wavelength calibration, we used exposures of a HeArNe lamp. We then adjusted the final zero point of the wavelength scale using telluric emission lines. The flux calibration was based on observations of the spectrophotometric standard star LTT2415, and is believed to be accurate to $\sim 15\%$. We corrected the spectrum for foreground Galactic extinction using a reddening of $E_{B-V} = 0.096$ determined from the dust maps of Schlegel, Finkbeiner & Davis (1998). In Figure 6.2 we show the observed one dimensional spectrum and in Figure 6.3 the region of the two-dimensional spectrum surrounding the Ly α emission line. Most notable is the large asymmetry in the profile, consistent with a very wide (~ 1400 km s $^{-1}$) blue-ward depression. Following previous detection of Ly α absorption systems in HzRGs (Röttgering et al., 1995b; van Ojik et al., 1997; Dey, 1999) we shall interpret the blue-ward asymmetry in the Ly α profile of TN J1338–1942 as being due to foreground absorption by neutral hydrogen.

The rest-frame equivalent width of Ly α in TN J1338–1942, $W_{\lambda}^{\text{rest}} = 210 \pm 50$ Å, is twice as high as in the well-studied radio galaxy 4C 41.17 ($z = 3.80$; Dey et al., 1997b). The large Ly α luminosity ($L_{\text{Ly}\alpha} \sim 4 \times 10^{44}$ erg s $^{-1}$ after correction for absorption) makes TN J1338–1942 the most luminous Ly α emitting radio galaxy known.

Following Spinrad et al. (1995), we measure the continuum discontinuity across the Ly α line, defined as $[\langle F_{\nu}(1250 - 1350\text{Å})/F_{\nu}(1100 - 1200\text{Å}) \rangle] = 1.56 \pm 0.24$. Similarly, for the Lyman limit at $\lambda_{\text{rest}} = 912\text{Å}$, we find $[\langle F_{\nu}(940 - 1000\text{Å})/F_{\nu}(850 - 910\text{Å}) \rangle] = 2.2 \pm 0.5$, though this value is uncertain because the flux calibration at the edge of the spectrum is poorly determined.

The presence of these continuum discontinuities further confirm our measured redshift. However, the redshift of the system is difficult to determine accurately because our

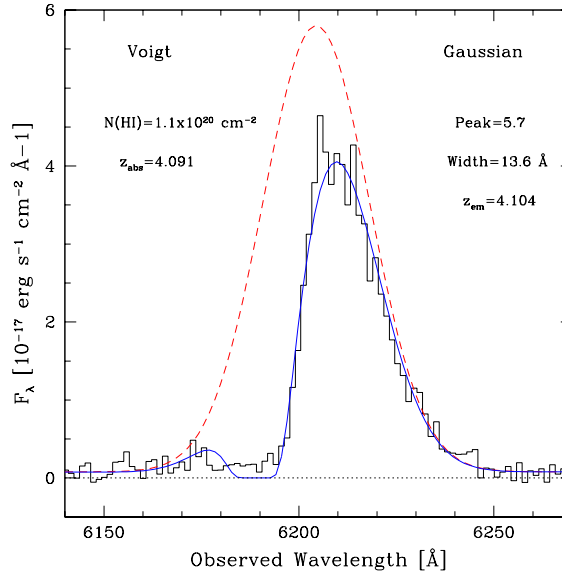


Figure 6.4: Part of the spectrum around the Ly α line. The solid line is the model consisting of a Gaussian emission profile (dashed line) and a Voigt absorption profile with the indicated parameters.

VLT spectrum does not cover C IV or He II. Furthermore, since the Ly α emission is heavily absorbed, it is likely that the redshift of the peak of the Ly α emission (at $6206 \pm 4 \text{ \AA}$, $z = 4.105 \pm 0.005$) does not exactly coincide with the redshift of the galaxy. We shall assume $z = 4.11$.

6.4 Discussion

TN J1338–1942 shares several properties in common with other HzRGs but some of its characteristics deserve special comment. Here we shall briefly discuss these.

6.4.1 Ly α emission

Assuming photoionization, case B recombination, and a temperature of $T = 10^4$ K we use the observed Ly α emission to derive a total mass ($M(\text{HII})$) of the HII gas (e.g., McCarthy et al., 1990b) using $M(\text{HII}) = 10^9 (f_{-5} L_{44} V_{70})^{1/2} M_{\odot}$. Here f_{-5} is the filling factor in units of 10^{-5} , L_{44} is the Ly α luminosity in units of 10^{44} ergs s^{-1} , and V_{70} is the total volume in units of 10^{70} cm^3 . Assuming a filling factor of 10^{-5}

(McCarthy et al., 1990b), and a cubical volume with a side of 15 kpc, we find $M(\text{HII}) \approx 2.5 \times 10^8 M_{\odot}$. This value is on the high side, but well within the range that has been found for HzRGs (e.g., van Ojik et al., 1997).

Previous authors have shown that gas clouds of such mass can cause radio jets to bend and decollimate (e.g., van Breugel et al., 1985; Lonsdale & Barthel, 1986; Barthel & Miley, 1988). Likewise, the extreme asymmetry in the TN J1338–1942 radio source could well be the result of strong interaction between the radio-emitting plasma and the Ly α gas.

6.4.2 Ly α absorption

Our spectrum also shows evidence for deep blue-ward absorption of the Ly α emission line. We believe that this is probably due to resonant scattering by cold HI gas in a halo surrounding the radio galaxy, as seen in many other HzRGs (c.f., Röttgering et al., 1995b; van Ojik et al., 1997; Dey, 1999). The spatial extent of the absorption edge as seen in the 2-dimensional spectrum (Fig. 6.3) implies that the extent of the absorbing gas is similar or even larger than the $4''$ (30 kpc) Ly α emitting region.

To constrain the absorption parameters we constructed a simple model that describes the Ly α profile with a Gaussian emission function and a single Voigt absorption function. As a first step, we fitted the red wing of the emission line with a Gaussian emission profile. Because the absorption is very broad, and extends to the red side of the peak, the parameters of this Gaussian emission profile are not well constrained. We adopted the Gaussian that best fits the lower red wing as well as the faint secondary peak, 1400 km s^{-1} blue-wards from the main peak. The second step consisted of adjusting the parameters of the Voigt absorption profile to best match the sharp rise towards the main peak. The resulting model (shown along with the parameters of both components in Figure 6.4) adequately matches the main features in the profile. We varied the parameters of both components, and all acceptable models yield column densities in the range $3.5 \times 10^{19} - 1.3 \times 10^{20} \text{ cm}^{-2}$.

The main difference between our simple model and the observations is the relatively flat, but non-zero flux at the bottom of the broad depression. This flux is higher than the continuum surrounding the Ly α line, indicating some photons can go through (i.e., a filling factor less than unity) or around the absorbing cloud. If the angular size of absorber and emitter are similar, the size of the absorber is $R_{\text{abs}} \sim 10 \text{ kpc}$. The total mass of neutral hydrogen then is $2 - 10 \times 10^7 M_{\odot}$, comparable to or somewhat less than the total mass of HII.

6.4.3 Continuum

Following Dey et al. (1997b), and assuming that the rest frame UV continuum is due to young stars, one can estimate the star-formation rate (SFR) in TN J1338–1942 from the observed rest-frame UV continuum near 1400 \AA . From our spectrum we estimate that $F_{1400} \sim 2 \mu\text{Jy}$, resulting in a UV luminosity $L_{1400 \text{ \AA}} \sim 1.3 \times 10^{42} \text{ erg s}^{-1} \text{ \AA}^{-1}$

and implying a SFR between $90 - 720 h_{65}^{-2} M_{\odot} \text{ yr}^{-1}$ in a $10 \times 30 \text{ kpc}^2$ aperture. These values are similar to those found for 4C 41.17. In this case detailed HST images, when compared with high resolution radio maps, strongly suggested that this large SFR might have been induced at least in part by powerful jets interacting with massive, dense clouds (Dey et al., 1997b; van Breugel et al., 1999b; Bicknell et al., 2000). The co-spatial Ly α emission-line and rest-frame optical continuum with the brightest radio hotspot in TN J1338–1942 suggests that a similar strong interaction might occur in this very asymmetric radio source.

The decrement of the continuum blue-wards of Ly α (Fig. 6.2) due to the intervening HI absorption along the cosmological line of sight is described by the “flux deficit” parameter $D_A = \langle 1 - \frac{f_{\nu}(\lambda_{1050-1170})_{\text{obs}}}{f_{\nu}(\lambda_{1050-1170})_{\text{pred}}} \rangle$ (Oke & Korycanski, 1982). For TN J1338–1942 we measure $D_A = 0.37 \pm 0.1$, comparable to the $D_A = 0.45 \pm 0.1$ that Spinrad et al. (1995) found for the $z = 4.25$ radio galaxy 8C 1435+64 (uncorrected for Galactic reddening). This is only the second time the D_A parameter has been measured in a radio galaxy.

The decrement described by D_A is considered to be extrinsic to the object toward which it has been measured, and should therefore give similar values for different classes of objects at the same redshift. Because they have bright continua, quasars have historically been the most popular objects to measure D_A . For $z \sim 4.1$, quasars have measured values of $D_A \sim 0.55$ (e.g., Schneider, Schmidt, & Gunn, 1991a, 1997). Similar measurements for color selected Lyman break galaxies do not yet exist.

Other non-color selected objects, in addition to radio galaxies, which do have reported D_A measurements are serendipitously discovered galaxies ($z = 5.34, D_A > 0.70$, Dey et al., 1998) and narrow-band Ly α -selected galaxies ($z = 5.74, D_A = 0.79$, Hu, McMahon, & Cowie, 1999). Because of their larger redshifts these galaxy values can not directly be compared with those of quasars ($z_{\text{max}} = 5.0, D_A = 0.75$, Songaila et al., 1999). However, they seem to fall slightly ($\Delta D_A \sim -0.1$) below the theoretical extrapolation of Madau (1995) at their respective redshifts, which quasars do follow rather closely. This is also true for the two radio galaxies ($\Delta D_A \sim -0.2$) at their redshifts. Thus it appears that non-color selected galaxies, whether radio selected or otherwise, have D_A values which fall below those of quasars.

Although, with only two measurements, the statistical significance of the low radio galaxy D_A values is marginal, the result is suggestive. It is worthwhile contemplating the implications that would follow if further observations of $z > 4$ radio galaxies and other objects selected without an optical color bias confirmed this trend. Given that optical color selection methods (often used to find quasars, and Lyman break galaxies) favour objects with large D_A values, it is perhaps not surprising that non-color selected $z > 4$ objects might have lower values of D_A . Consequently, quasars and galaxies with low D_A values might be missed in color-based surveys. This then could lead to an underestimate of their space densities, and an overestimate of the average HI columns density through the universe.

Radio galaxies have an extra advantage over radio selected quasars (e.g., Hook &

McMahon, 1998), because they very rarely contain BAL systems (there is only one such example, 6C 1908+722 at $z = 3.537$; Dey, 1999). Such BAL systems are known to lead to relatively large values of D_A , indicating that part of the absorption is not due to cosmological HI gas, but due to absorption within the BAL system (Oke & Korycanski, 1982). A statistically significant sample of $z > 4$ radio galaxies would therefore determine the true space density of intervening HI absorbers.

6.5 Conclusions

Because of its enormous Ly α luminosity and strong continuum, its highly asymmetric and broad Ly α profile, and its very asymmetric radio/near-IR morphology TN J1338–1942 is a unique laboratory for studying the nature of $z > 4$ HzRGs. It is particularly important to investigate the statistical properties of similar objects by extending the work begun here to a significant sample of $z > 4$ HzRGs. The VLT will be a crucial facility in such a study.

Acknowledgements

We thank the referee, Hy Spinrad, for his comments, which have improved the paper. We also thank Remco Slijkhuis for his help in using the ESO archive, and Mỹ Hà Vuong for useful discussions. The W. M. Keck observatory is a scientific partnership between the University of California and the California Institute of Technology, made possible by the generous gift of the W. M. Keck Foundation. The National Radio Astronomy Observatory is operated by Associated Universities Inc., under cooperative agreement with the National Science Foundation. The work by C.D.B., W.v.B., D.M. and S.A.S. at IGPP/LLNL was performed under the auspices of the US Department of Energy under contract W-7405-ENG-48. DM is also supported by Fondecyt grant No. 01990440 and DIPUC.

Discovery of an Ultra-Steep Spectrum, Highly Polarized
Red Quasar at $z = 1.462$

C. De Breuck, M. S. Brotherton, H. D. Tran, W. van Breugel, &
H. Röttgering 1998, *AJ*, 116, 13

Abstract

We report the discovery of WN J0717+4611, a highly polarized red quasar at $z = 1.462$, selected from a sample of faint ($S_{1400} > 10$ mJy) ultra steep spectrum ($\alpha_{1400}^{327} < -1.3$; $S \propto \nu^\alpha$) radio sources. VLA observations at 4.85 GHz show that the radio source is dominated by a 21 mJy core. Using the Keck telescopes, we obtained spectra with a combined wavelength range covering 4000 Å to 1.6 μm , and spectropolarimetric observations between 4000 Å and 9000 Å. We identify WN J0717+4611 as a quasar based on broad emission of Mg II $\lambda 2799$ (FWHM $\simeq 11,000$ km s $^{-1}$), a stellar R_S -band Lick image and the high luminosity of the object ($M_B = -24.2$). The optical linear polarization is wavelength-independent at 15% in both the continuum and the emission lines, with the polarization angle orthogonal to the radio jet axis. We argue that the polarization mechanism is scattering of quasar light by surrounding small dust grains or electrons. WN J0717+4611 appears highly reddened for a core-dominated quasar.

7.1 Introduction

The tight correlation in the Hubble $K - z$ diagram of the parent galaxies of luminous radio sources suggests that high redshift radio galaxies (HzRGs) may be used to study the formation and evolution of massive ellipticals (Lilly, 1989; Eales et al., 1997; van Breugel et al., 1998). HzRGs have now been found out to redshifts of ~ 4.5 , which is presumably close to the time they underwent their first burst of star formation. As a result of various vigorous search campaigns, ~ 20 HzRG are now known at $z > 3$.

Virtually all of these have been found by identifying sources with ultra-steep ($\alpha \lesssim -1$) radio spectra (Chambers et al., 1996a; Rawlings et al., 1996; Röttgering et al., 1997, , Chapter 2). Although this ultra-steep spectrum (USS) search technique has now been proven the most effective way of finding HzRGs, no uniform large-area search could be done because the radio surveys used to construct the samples were either not sensitive enough, or had limited sky coverage. During the past years, several new, deep all-sky radio surveys have become available: the Faint Images of the Radio Sky at Twenty Centimeters at 1.4 GHz (FIRST; Becker et al., 1995), the Westerbork Northern Sky Survey at 325 MHz (WENSS; Rengelink et al., 1997), and the NRAO VLA Sky Survey at 1.4 GHz (NVSS; Condon et al., 1998). These allow for the first time a major survey of faint radio sources with extreme spectral index properties.

We have used these new surveys to define a sample of USS sources, for further optical identification and spectroscopic studies (see De Breuck et al., 1998 for a summary). Our sample includes sources with radio flux densities $\sim 10\times$ fainter than previous large USS searches (Chambers et al., 1996a; Röttgering et al., 1997). Subsequent optical imaging and spectroscopy of our sample indicates that 2/3 of the USS sources with $R < 24$ are radio galaxies with redshifts $z > 2$. We will report in detail on these results in forthcoming papers.

In this paper, we present the discovery and follow-up observations of one of our USS sources, WN J0717+4611 at $z = 1.462$. This source was selected for a special study because of its strong core-dominated FR II morphology (Faranoff & Riley, 1974) and a bright stellar $R_S = 21.6$ identification. Such a combination of properties is unique in our USS sample, and its bright compact optical identification is reminiscent of 6C 1908+722, a $R = 21$ radio galaxy at $z = 3.515$ with a broad absorption line (BAL) system (Dey, 1997a).

Our Keck optical spectropolarimetry observations do not reveal such a BAL system, but, in combination with the IR-spectroscopy that was originally obtained to study the age of the stellar population by means of the strength of the 4000 Å-break, it shows evidence for a highly polarized red quasar. We argue that the polarization is caused by scattering and not by synchrotron radiation, as in most highly polarized quasars (Cohen et al., 1997). The spectral properties of the polarized light indicates that the red color of WN J0717+4611 is strong evidence for dust obscuration, which has been one of the prime explanations for the red quasars (e.g., Webster et al., 1995), although other mechanisms, like a host galaxy or synchrotron contribution, have also been proposed (e.g., Benn et al., 1998).

We describe the radio and optical imaging, IR spectroscopy, and optical spectropolarimetry in §7.2, and present the results in §7.3. We discuss the classification, the origin of the high polarization, and compare WN J0717+4611 with possibly related objects in §7.4, and present our conclusions in §7.5. Throughout the paper, we use $H_0 = 50 \text{ km s}^{-1} \text{ Mpc}^{-1}$, $q_0 = 0$ and $\Lambda = 0$. At $z = 1.462$, changing these values to $H_0 = 65 \text{ km s}^{-1} \text{ Mpc}^{-1}$, $q_0 = 0.1$, would reduce size and distance by 30%, which would not affect our conclusions.

Table 7.1: Radio Data

Catalog	Frequency (MHz)	Flux density ^a (mJy)	Resolution	Reference
WENSS	327	724 ± 15	$54'' \times 78''$	Rengelink et al. (1997)
TEXAS	365	553 ± 82^b	$20'' \times 28''$	Douglas et al. (1996)
B3	408	510 ± 60	$2'.6 \times 4'.8$	Ficarra et al. (1985)
NVSS	1400	105 ± 10	$45'' \times 45''$	Condon et al. (1998)
GB6	4850	24 ± 12	$3'.7 \times 3'.3$	Gregory et al. (1991)
VLA (total)	4860	36.9 ± 0.3	$0''.43 \times 0''.39$	This chapter
VLA (lobes)	4860	15.7 ± 0.3	$0''.43 \times 0''.39$	This chapter
VLA (core)	4860	21.2 ± 0.3	$0''.43 \times 0''.39$	This chapter

^a Errors quoted are 3σ

^b This source has an environment flag “C”, indicating that the fringe amplitudes were affected by surrounding sources (see Douglas et al., 1996 for details)

7.2 Observations and data reduction

7.2.1 Radio Observations

Table 7.1 summarizes the radio flux density measurements for WN J0717+4611. Our USS sample includes all sources with $\alpha_{1400}^{327} < -1.3$, determined from the WENSS 327 MHz and NVSS 1.4 GHz radio surveys. Both these surveys have comparable resolutions of $54''$ and $45''$, respectively, minimizing missing flux problems in the spectral index determination. WN J0717+4611 has a spectral index of $\alpha_{1400}^{327} = -1.31$ which satisfies the above selection criterion. For a full discussion of the sample and selection techniques, see Chapter 2.

To determine the radio morphology and accurate astrometry for optical identification, we obtained snapshot VLA observations of our USS sample on 1996 October 28 with the A-array. As part of this program, WN J0717+4611 was observed for 5 minutes at a frequency of 4.86 GHz at $0''.4$ resolution. We used standard data reduction techniques in the NRAO *ATPS* package, including phase-only self-calibration. 3C 286 was the primary flux calibrator; the difference between the predicted and observed flux of the other observed flux calibrator (3C 48) indicates that our flux calibration is accurate to within 2%. The final map (Fig. 7.1) has an rms noise level of $86 \mu\text{Jy}$, and shows an FR II morphology with an unusually bright core, located at $\text{RA(J2000)} = 7^{\text{h}}17^{\text{m}}58^{\text{s}}.48$, $\text{DEC(J2000)} = +46^{\circ}11'38''.9$. The southern lobe is edge-brightened and about a factor of 2 brighter than its northern, more diffuse, counterpart. To check the structure of these lobes and to improve the sensitivity to detect low-brightness structures, we also mapped the source using only the core for self-calibration, and limiting the UV-coverage to half the maximum range. All maps show the same morphology seen in Figure 7.1.

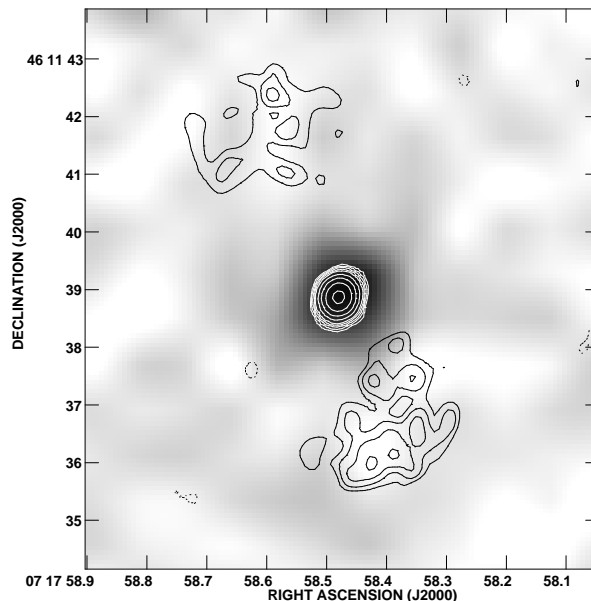


Figure 7.1: Greyscales: R_S -band Lick image; Contours: VLA 4.86 GHz image. Contour levels are $-0.26, 0.26, 0.37, 0.52, 0.73, 1.0, 1.5, 2., 2.9, 4.1, 5.8, 8.3, 11.7$ and $16.5 \text{ mJy beam}^{-1}$.

7.2.2 Lick Identification and Spectroscopy

R_S -band (Djorgovski, 1985) imaging and long-slit spectroscopic observations were made with the KAST double-beam imaging spectrograph (Miller & Stone, 1994) on the Lick 3m telescope on 1996 November 11, under photometric conditions and a seeing of $1''.3$. We determined the astrometric solution of the image with the *AIPS* task XTRAN, using coordinates of 8 stars detected on the POSS plates. The resulting astrometric accuracy is $\sim 1''$. A stellar $R_S = 21.6 \pm 0.3$ object was detected at the location of the radio core (Fig. 7.1). A 20-minute spectrum was taken with a $2''$ slit oriented east-west, centered on the object, and using a dichroic that splits the light at 5500 \AA . We used a 452/3306 grism and a 300/7500 grating in the blue and red arm resulting in a dispersion of 2.54 \AA/pix (resolution $\sim 6 \text{ \AA FWHM}$) and 4.6 \AA/pix (resolution $\sim 8 \text{ \AA FWHM}$), respectively, covering a continuous wavelength range from 3500 \AA to $10,000 \text{ \AA}$. The spectrum (not shown) shows a weak continuum in the red and no continuum and a single narrow line in the blue at 3816 \AA . We initially assumed this line to be $\text{Ly}\alpha$ from a radio galaxy at $z = 2.138$, because of the absence of $\text{H}\beta$ and $[\text{O III}] \lambda\lambda 4959, 5007$ if the identification would be $[\text{O II}] \lambda 3727$. The Keck optical spectrum (see below) showed that the correct identification of this line is $\text{C IV } \lambda 1549$.

7.2.3 Keck Infrared Spectroscopy

A low-resolution IR spectrum was obtained on 1996 November 29 using the Near Infra-Red Camera (NIRC; Mathews & Soifer, 1994) at the 10m Keck I telescope. The gr150 grism was used in combination with the JH -filter. The dispersion was $\sim 50 \text{ \AA}/\text{pix}$, and the slit width was $1''.275$, resulting in a resolution of 190 \AA (FWHM). Conditions during the observations were photometric, but the seeing was variable. To achieve good sky-subtraction, we used ten 5-minute exposures, while shifting the object along the slit. The first six exposures had poor seeing, and were discarded. The 5 minute integrations were slightly too long under these variable atmospheric conditions, resulting in saturated sky lines between 1.45 and $1.6 \mu\text{m}$.

To remove dark counts and sky emission, we subtracted the average of the two bracketing exposures from each observation. We divided the resulting frames by the normalized domeflat, and removed the residual sky emission by subtracting a low-order fit along the spatial direction. We then shifted the four remaining good frames and combined them, while masking out the bad pixels determined from the domeflats.

For wavelength calibration, we initially used the dispersion formula listed for the gr150 grism in the NIRC manual. This was further refined by assuming the redshift determined from spectropolarimetric observations (§7.2.4), and shifting the $H\beta$ line by 120 \AA (60% of resolution) to match this redshift.

We observed HD 56605 (an A3 star to minimize intrinsic spectral features), immediately after WN J0717+4611. These observations were reduced in the same manner as our primary target. After extraction of the 1-dimensional spectra, WN J0717+4611 was divided by HD 56605 to correct for atmospheric absorption. HD 56605 was also used for absolute flux calibration, under the assumptions that it has a main sequence color $V - J = +0.15$, a blackbody temperature $T_{eff} = 9000\text{K}$ (Johnson, 1966), and $V = 8.0$ (SIMBAD database).

The flux-calibrated spectrum matches up well with the optical spectrum described below, confirming the reliability of the flux calibration and the photometric conditions during both runs.

7.2.4 Keck Spectropolarimetry

The spectropolarimetric observations were made on 1996 December 9 at the 10m Keck II telescope using the Low Resolution Imaging Spectrometer (LRIS; Oke et al., 1995) in conjunction with the polarimeter (Cohen et al., 1997). The observations were split into four 15-minute exposures, each at a different orientation of the waveplate at angles of 0° , 45° , 22.5° , and 67.5° (see Goodrich et al., 1995 for details). The 300 l mm^{-1} grating blazed at 5000\AA combined with the $1''$ wide slit resulted in a resolution of $\sim 10\text{\AA}$ (FWHM). The dispersion was $2.5 \text{ \AA}/\text{pix}$, yielding a spectral coverage from 4015 \AA to 9005 \AA . No order blocking filter was used, since second order contamination from the blue is negligible, as the spectrum is very red. Atmospheric conditions were photometric, but the seeing was poor and variable (up to $1''.5$), making

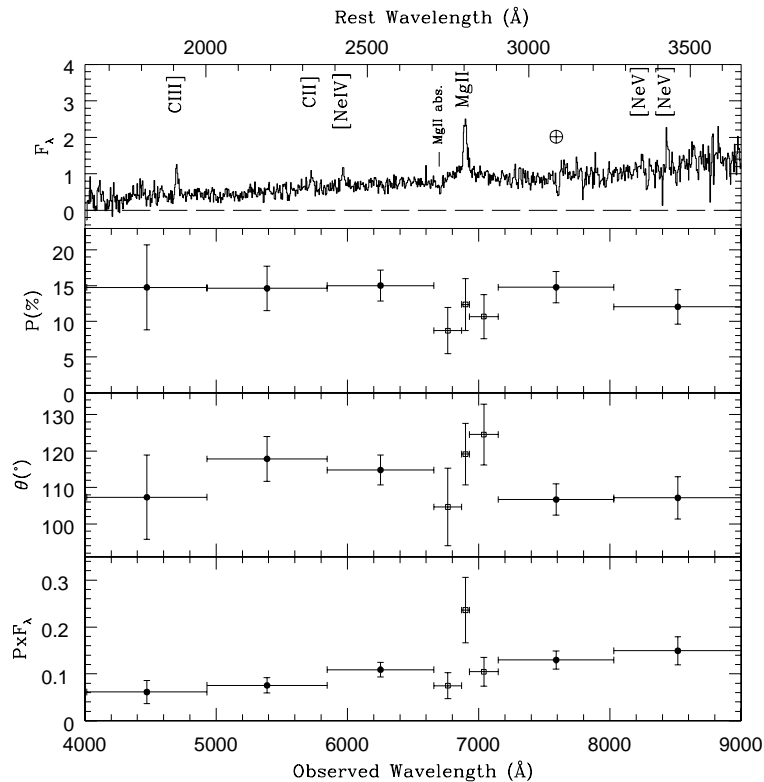


Figure 7.2: The wavelength dependence of the total flux density F_λ units, percentage of polarization P , polarization angle θ , and polarized flux $P \times F_\lambda$ for WN J0717+4611 measured in a $6'' \times 1''$ aperture. F_λ and $P \times F_\lambda$ are in units of $10^{-18} \text{ erg s}^{-1} \text{ cm}^{-2} \text{ \AA}^{-1}$. P , θ and $P \times F_\lambda$ are measured in bins: horizontal bars indicate the bin widths, and vertical bars indicate 1σ errors. The region that has been incompletely corrected for telluric A band absorption is denoted by \oplus . Within the errors, the continuum polarization is constant across the spectrum ($P \approx 15\%$), and similar to that of the emission lines.

the spectrophotometry with the $1''$ slit unreliable.

The observations were reduced using the NOAO IRAF package and SuperMONGO routines developed by Dey et al. (1996), based on the method described by Miller et al. (1988). The flux calibration was performed using the standard star Feige 34 (Massey et al., 1988). The polarization measured from this unpolarized star was $< 0.15\%$ at all wavelengths, validating our polarimetric calibration. Our polarimetric results are presented in Figure 7.2. The faint continuum necessitated binning of the Stokes Q and U data into $\sim 1000 \text{ \AA}$ bins to improve S/N. To check the validity of this result, we used different bin sizes, which were all consistent with the results shown in Figure 7.2.

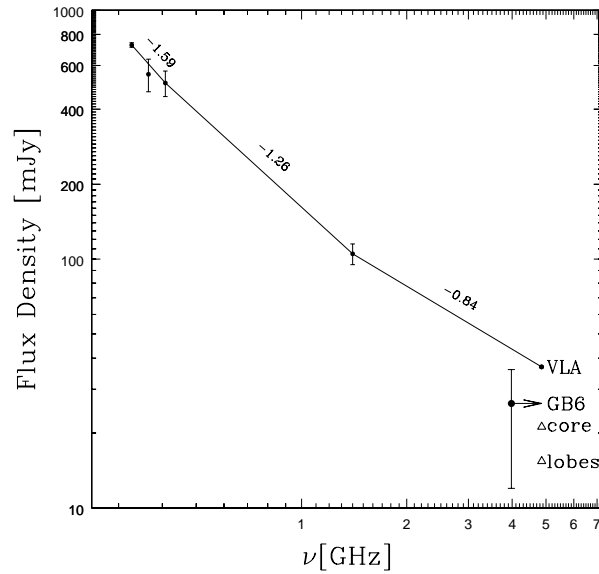


Figure 7.3: Flux density plotted against frequency for the radio data given in Table 7.1. The dots indicate the total emission, and the triangles the emission from the core and lobes separately. For clarity, the 4.85 GHz GB6 flux has been shifted. Note the flattening of the spectral index with frequency and the excess core emission in our VLA data.

We corrected the spectrum for telluric A and B absorption (due to O_2) using an atmospheric transmission curve made by dividing the flux calibrated spectrum of Feige 34 by a model spectrum interpolated over the A and B bands. The atmospheric conditions during the target and standard star observations were similar, but there was a significant difference in airmass between Feige 34 (1.1) and WN J0717+4611 (~ 1.5). The B band coincides with the narrow-line part of the Mg II $\lambda 2799$ region. We estimate that the residual error after B band correction is $\sim 20\%$ and this could significantly affect our measurement of the width and strength of the narrow component. The broad component of Mg II $\lambda 2799$ is not affected by the B band, as it is three times broader than the B band.

7.3 Results

The radio-spectrum (Fig. 7.3) flattens with increasing frequency, with the spectral index changing from $\alpha = -1.59$ between 327 MHz and 408 MHz to $\alpha = -0.84$ between 1.4 GHz and 4.85 GHz. This suggests an increasing contribution with frequency of a flat spectrum component, probably the core.

Table 7.2: Line Measurements

Instrument ^a	Line	λ_{rest} (Å)	λ_{obs} (Å)	z_{em}	F_{int} ^b	FWHM ^c (km s ⁻¹)	W_{λ}^{rest} (Å)
KAST	C IV	1549.1	3816 ± 2	1.463	30.2 ± 4.0	1200 ± 400	28 ± 12
LRIS	C III]	1908.7	4700 ± 2	1.462	0.9 ± 0.1	1200 ± 300	6 ± 1
LRIS	C II]	2326.8	5726 ± 2	1.461	0.4 ± 0.1	1200 ± 400	3.2 ± 0.4
LRIS	[Ne IV]	2425.0	5968 ± 2	1.461	0.6 ± 0.1	1000 ± 300	2.8 ± 0.4
LRIS	Mg II(narrow)	2799.1	6900 ± 2	1.465	2.0 ± 0.4	1300 ± 300	13 ± 1
LRIS	Mg II(broad)	2799.1	6900 ± 1	1.465	4.6 ± 0.4	11000 ± 500	13 ± 1
LRIS	Mg II(abs.)	2799.1	6703 ± 1	1.395 ^d	...	2000 ± 300	-7 ± 1
LRIS	[Ne V] λ 3426	3345.9	8242 ± 3	1.463	0.5 ± 0.3	800 ± 400	1.2 ± 0.4
LRIS	[Ne V] λ 3426	3426.0	8437 ± 2	1.463	0.7 ± 0.3	600 ± 300	1.2 ± 0.4
NIRC	[Ne III] λ 3869	3868.8	9500 ± 50
NIRC ^e	Hβ	4861.3	11940 ± 30	...	11 ± 5	...	45 ± 10
NIRC ^e	[O III]	4959.5	12230 ± 30	...	18 ± 5	...	70 ± 15
NIRC ^e	[O III]	5006.8	12350 ± 30	...	53 ± 5	...	220 ± 15
NIRC	Hα	6562.8	16265 ± 50

^a KAST = KAST on Lick 3m, 2''slit; LRIS = LRIS on Keck II, 1''slit;

NIRC = NIRC JH filter + gr150 grism on Keck I, 1''275 slit.

^b In units of 10⁻¹⁶ erg s⁻¹ cm⁻², and corrected for Galactic reddening using the Cardelli et al. (1989) extinction curve with A_V=0.24.

^c Deconvolved with the instrumental resolution (5.5Å for KAST; 10Å for LRIS).

^d Absorption line system with a blue velocity shift of 8500 km s⁻¹.

^e FWHM unresolved with the 4600 km s⁻¹ resolution.

The combined total intensity spectrum from the Lick and Keck observations (Fig. 7.4) shows 11 emission lines and a red continuum with $\alpha_{opt} = -1.6$ ($F_{\lambda} \propto \lambda^{\alpha_{opt}}$). We used the SPECFIT package inside IRAF to fit the different components of the spectrum, and present the measurements in Table 7.2. The average redshift of WN J0717+4611 is $z = 1.462 \pm 0.001$. We do not detect any significant velocity shifts among the narrow emission lines. The Mg II λ2799 line appears to have a ~ 350 km s⁻¹ redshift relative to the other lines, but this can be accounted for by using a higher multiplication factor for the atmospheric B band correction, as suggested by the residuals at the A band and the higher airmass of the object. All emission lines except Mg II λ2799 show only a narrow (FWHM ~ 1200 km s⁻¹) component. In Mg II λ2799, we detect 3 components: a narrow (FWHM = 1200 km s⁻¹) component, a broad (FWHM = 11,000 km s⁻¹) component, and an intervening foreground absorption system blueshifted by 8500 km s⁻¹ at $z = 1.395$ (Fig. 7.2).

A comparison of the smoothed version of the Lick spectrum and the Keck total intensity optical spectrum shows a close agreement in both continuum slope and level, suggesting that (i) conditions during both nights were photometric, (ii) the continuum emission from the object originates from an area that is $\lesssim 1''$, and (iii) the object is not highly variable in the optical on timescales of ~ 1 month. The overlay also explains why we did not previously detect the Mg II λ2799 in the Lick spectrum: the stronger atmospheric B band absorption at Lick Observatory reduced the amplitude of this line to $\sim 1\sigma$.

The low resolution and large errors in the wavelength calibration of the IR spectrum make it impossible to determine the velocity shifts of the lines. The [Ne III] λ 3869 λ3869 and Hα lines are both detected at the edges of the spectrum, but the fluxes and widths of both lines are highly uncertain. The only two lines in a reliable part of the

IR spectrum are $H\beta$ and the [O III] $\lambda\lambda 4957, 5007$ doublet. However, at $z = 1.462$, the separation between $H\beta$ and [O III] $\lambda 4959$ is 240 \AA — barely resolved with our 190 \AA resolution. We therefore used the IR spectrum only to confirm the redshift and constrain the reddening of the continuum.

We detect a percentage polarization of $15 \pm 3\%$ and a polarization angle of $110^\circ \pm 10^\circ$, both constant with wavelength within the uncertainties. The polarization angle is orthogonal to line connecting the hotspots with the radio core. The percentage polarization and polarization angle are similar in the emission lines and the continuum.

7.4 Discussion

Since the object was not at the initially assumed redshift, the IR spectroscopy and optical spectropolarimetry were not appropriate to detect a 4000 \AA -break nor a C IV BAL system. However, this data showed that this object is a red quasar with a highly polarized optical continuum, which we will argue in the context of Unified Models, presents evidence for scattering by dust or electrons.

7.4.1 Classification

We classify WN J0717+4611 as a quasar because:

1. We detect a broad component (FWHM $\simeq 11,000 \text{ km s}^{-1}$) underlying the narrow Mg II $\lambda 2799$ emission line (Fig. 7.2).
2. The Lick R_S -band image shows a stellar ($\lesssim 1''3$) $R_S \simeq 21.6$ object coinciding with the radio core.
3. The absolute magnitude $M_B = -24.2$ is brighter than the $M_B = -23$ cutoff used by Véron & Véron (1996) to classify stellar objects as quasars. The M_B has been calculated assuming a constant power law with index $\alpha_{opt} = -1.6$ without line-contamination correction, but has not yet been corrected for Galactic or intrinsic reddening, and should therefore be interpreted as a lower limit on the luminosity.
4. Of the 28 objects in our USS sample for which we have already obtained images and spectra, only three are quasars on the basis of broad lines (including WN J0717+4611). All three have an unresolved, $R \sim 21$ core identification, while the other 25 are radio galaxies which show an extended, $R \gtrsim 23$ optical counterpart.

As mentioned in §7.3, the object did not show any optical variability within a timescale of ~ 1 month. WN J0717+4611 is not an optical violently variable (OVV; Januzzi et al., 1993), as most highly polarized quasars are (Januzzi et al., 1993). Further reasons to exclude WN J0717+4611 from being an OVV are the extremely steep

radio spectrum (Gear et al., 1994), and the rejection of the synchrotron mechanism as the explanation of the high polarization (§7.4.2).

The radio emission from WN J0717+4611 is strongly core-dominated, and we derive a rest-frame 12 GHz radio-core to lobe ratio $R \simeq 0.6$ (Orr & Browne, 1982; Wills & Brotherton, 1995). Baker & Hunstead (1995; hereafter BH95) have classified radio-loud quasars based this core dominance parameter, and constructed composite spectra for different values of R . One of the main results was that both the strength of the Fe line complex near Mg II $\lambda 2799$ and the amount of reddening increase with decreasing core dominance (smaller R). This can be understood in the context of the AGN unification model (e.g., Antonucci et al., 1993a), in which the fainter radio cores are thought to be central AGNs that are only modestly Doppler boosted since their jets are at relatively large angles of the line of sight. As a result, such quasars are thought to experience a higher reddening by the dusty torus surrounding the AGN (Baker, 1997). On the basis of the core-dominance and the classification of BH95, we would statistically expect relatively strong Fe-lines, and low reddening. This is contrary to what is observed, and in fact, a much better similarity (Fig. 7.4) is found when comparing our combined optical–IR spectrum with the average spectrum of Compact Steep Spectrum (CSS) radio sources by BH95.

In the top panel of Figure 7.4, we show the observed spectra, corrected for Galactic reddening with an $A_V = 0.25$ [value as listed in the NED database, determined from Burstein & Heiles (1982) and using the Cardelli et al. (1989) extinction curve]. We subsequently dereddened this spectrum with an $A_V = 1.2$ to match to CSS composite, assuming an SMC-type extinction curve (Prevot et al., 1984) at the redshift of the quasar. We used the SMC type law rather than the Galactic, because no 2200 Å dust feature was obvious (Bonatto et al., 1996). The resulting spectrum, presented in the bottom panel of Figure 7.4 shows a close resemblance with the BH95 composite CSS spectrum. However, the physical size of the radio lobes of WN J0717+4611 is 92 kpc, which is significantly larger than the commonly accepted maximum size of 20 kpc for CSS sources (e.g., Sanghera et al., 1995). Why then do we see this resemblance? BH95 suggest a significant reddening might explain the extremely red continuum in CSS sources compared to the more core-dominated quasars. A straightforward interpretation of the resemblance of WN J0717+4611 to the CSS composite would therefore be high reddening by dust in both. Similarly, high amounts of reddening have been seen in other radio-loud quasars (e.g., IRAS 13349+2438, Wills et al., 1992; PKS 1610–771, Courbin et al., 1997; 5C7.195, Willot et al., 1997), and have been proposed to hide a significant population of quasars (Webster et al., 1995).

7.4.2 The Origin of the Polarization

We consider the four most common mechanisms that can produce the observed polarization.

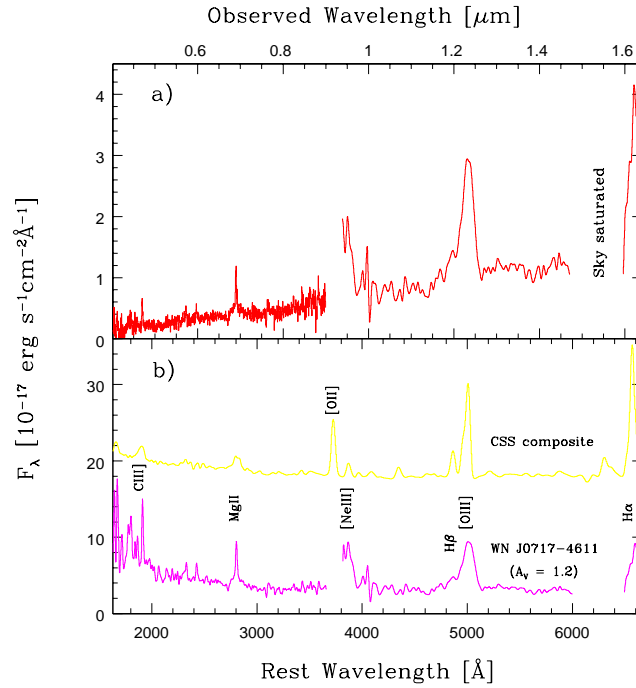


Figure 7.4: (a) Optical and IR spectra of WN J0717+4611, corrected for Galactic reddening with $A_V=0.24$, using the Cardelli et al. (1989) extinction curve. The flux calibration at both ends of the IR spectrum is highly uncertain, and the region between 1.47 and 1.60 μm is not usable because of saturation by sky lines. b) Top spectrum: Composite CSS spectrum compiled by Baker & Hunstead (1995), arbitrarily shifted vertically. Bottom spectrum: the spectra in a) dereddened with a local $A_V = 1.2$ at $z = 1.462$, using an SMC extinction law. Note that the [O II] $\lambda 3727$ line falls just between our optical in IR spectra.

1. **Optical synchrotron emission:** A significant contribution to the continuum polarization by optical synchrotron emission can be excluded because the degree of polarization and polarization angle of the narrow emission lines (which cannot be caused by synchrotron radiation) are similar to those in the continuum, implying a common non-synchrotron origin.
2. **Transmission through aligned dust grains:** Another possible polarization mechanism is transmission of nuclear light through aligned dust grains. However, the high 15% polarization, and the flat shape of the wavelength dependence cannot be fit with a Serkowski law (Serkowski et al., 1975). Furthermore, in our Galaxy, the amount of interstellar polarization is related to the amount of interstellar reddening by $P_{max} < 9 \times E(B - V)\%$, which would imply an $A_V > 5$ in WN J0717+4611, much higher than observed.

For similar reasons, the polarization cannot be due to a foreground screen in our own Galaxy: the observed $E(B - V) = 0.1$ and at the Galactic latitude of WN J0717+4611 ($b \sim 24^\circ$) no polarization at the 15% level has been detected (Serkowski et al., 1975).

3. **Scattered AGN light by dust or electrons:** The most likely mechanism is scattering by dust or electrons. The mean polarization angle of 110° is perpendicular to the line connecting the 2 hotspots through the core. This is just what is expected in the AGN unification model, where we would be observing continuum emission from the AGN being scattered within the cone containing the radio jets. Both the high level and the wavelength-independence of the polarization can be explained with scattering by electrons or small ($2\pi a/\lambda \ll 1$) dust grains (e.g., Wills et al., 1992).

7.4.3 Comparison with Other Quasars

Highly Polarized Quasars (HPQs) are defined as quasars with an optical polarization $P > 3\%$, independent of the polarization mechanism (e.g., Januzzi et al., 1993). Because these objects are rare, and the surveys used to find them were biased, no general properties of HPQs have been determined. We therefore briefly compare WN J0717+4611 with other HPQs in the literature that have similar characteristics. Another radio-loud HPQ that is not an OVV is OI 287 ($z = 0.445$; Goodrich & Miller, 1988; Antonucci et al., 1993b). This object has a continuum polarization of 8.2%, independent of wavelength. However, its polarization properties are different from WN J0717+4611: OI 287 has narrow emission lines that are consistent with being unpolarized, but the broad $H\beta$ does show polarization, while in WN J0717+4611 the emission lines are polarized at the same level as the continuum. Furthermore, the polarization angle of the continuum is parallel to the radio structure, while it is orthogonal in WN J0717+4611. Hence it has been suggested (Goodrich & Miller, 1988) that OI 287 has a thin obscuring disk between the NLR and BLR. In the case of WN J0717+4611, the obscuring torus seems to be large and encompass also the NLR.

An object that is very similar to WN J0717+4611 in its optical properties is 3CR 68.1 ($z = 1.228$; Brotherton et al., 1998). 3CR 68.1 is also an HPQ that is neither an OVV nor BALQSO. The optical polarization is also caused by scattering, as in WN J0717+4611, and it is also an extremely red quasar. In the context of the unified schemes, it is argued that 3CR 68.1 is seen under a dusty, highly inclined view. The radio properties are very different from WN J0717+4611 however, as 3CR 68.1 is an extremely lobe-dominated source ($R \sim 4 \times 10^{-4}$) with the weakness of its core possibly due to free-free absorption. We interpret WN J0717+4611 as a less inclined object than 3CR 68.1, but with a similar amount of dust obscuration and scattered light.

The object that is perhaps most similar to WN J0717+4611 is 5C 7.195 ($z = 2.034$;

Willot et al., 1998). Its radio structure also shows a core-dominated FR-II morphology and has a steep radio spectrum. Similarly, the optical object is unresolved, and its spectrum can be fitted by a quasar spectrum reddened by $A_V = 1.1$. The quasar nature is also supported by the detection of broad H α . As Willot et al. (1998) remark, a significant number of these red quasars could easily have been classified as radio galaxies, as the underlying broad lines require good seeing and high S/N measurements. WN J0717+4611 is a perfect example: without the high-quality Keck spectrum, we would have classified this object as a radio galaxy.

7.5 Conclusions

Our main observational results for WN J0717+4611 are:

- 1) The radio source has a core-dominated FR II morphology, with a total size of ~ 90 kpc and an ultra-steep spectrum with an integrated spectral index $\alpha_{1400}^{327} = -1.31$. The radio spectrum flattens with increasing frequency, presumably because of an increasing contribution from a flatter spectrum core.
- 2) The optical object is a quasar because it is stellar, has broad Mg II $\lambda 2799$ emission with (FWHM $\simeq 11,000$ km s $^{-1}$), and is very luminous with $M_B = -24.2$.
- 3) The object appears exceptionally reddened for its core-dominance of $R \simeq 0.6$, compared to the statistical results of BH95. When dereddened with an $A_V = 1.2$, it matches well with the composite CSS quasar spectrum, which is already more reddened than the core-dominated quasar composite.
- 4) We detect a wavelength-independent 15% optical polarization, which is similar in both continuum and emission lines. The polarization angle is orthogonal to the radio axis, which, in the context of the unified models of quasars and radio galaxies, is consistent with scattering due to small dust grains or electrons located in the cone containing the radio jet.

We have compared WN J0717+4611 with other HPQs and red quasars in the literature, and found no object that shares all observational characteristics. 5C1.195 (Willot et al., 1998) seems to be a very similar object, and it was discovered in a similar way, indicating more of these objects may be found from radio-selected samples. The presence of a significant population of (highly) reddened quasars at cosmological redshifts is currently subject to considerable debate (Webster et al., 1995; Benn et al., 1998). While our observations of a single object do not bear any statistical significance on the size of this population, they do show that highly reddened, dusty quasars do indeed exist.

Acknowledgements

We thank Arjun Dey, Adam Stanford and Dan Stern for providing the Keck data and their advise on the data reduction, Andrea 'Grapes' Cimatti and Chris O'Dea for useful discussions, and Jo Baker for providing the composite Molonglo quasar spectra. The W.M. Keck Observatory is a scientific partnership between the University of

California and the California Institute of Technology, made possible by a generous gift of the W.M. Keck foundation. The VLA is a facility of the National Radio Astronomy Observatory, which is operated by Associated Universities Inc. under cooperative agreement with the National Science Foundation. This research has made use of the NASA/IPAC Extragalactic Database (NED) which is operated by the Jet Propulsion Laboratory, California Institute of Technology, under contract with the National Aeronautics and Space Administration. Work performed at the Lawrence Livermore National Laboratory is supported by the DOE under contract W7405-ENG-48.

A Statistical Study of Emission Lines from High Redshift Radio Galaxies

C. De Breuck, H. Röttgering, G. Miley, W. van Breugel, & P. Best
2000, *A&A*, in press

Abstract

We have compiled a sample of 165 radio galaxies from the literature to study the properties of the extended emission line regions and their interaction with the radio source over a large range of redshift $0 < z < 5.2$. For each source, we have collected radio (size, lobe distance ratio and power) and spectroscopic parameters (luminosity, line width and equivalent width) for the four brightest UV lines. We also introduce a parameter $A_{\text{Ly}\alpha}$ measuring the asymmetry of the Ly α line, assuming the intrinsic redshift of the line is the same as that for the He II λ 1640 line, and show that this parameter is a good measure of the amount of absorption in the Ly α line.

Using these 18 parameters, we examine the statistical significance of all 153 mutual correlations, and find the following significant correlations: (i) Ly α asymmetry $A_{\text{Ly}\alpha}$ with radio size D and redshift z , (ii) line luminosity with radio power, (iii) line luminosities of Ly α , C IV, He II and C III] with each other, and (iv) equivalent widths of Ly α , C IV, He II and C III] with each other. We interpret the correlation between redshift and $A_{\text{Ly}\alpha}$ as an increase in the amount of HI around radio galaxies at $z > 3$. The almost exclusive occurrence of HI absorption in small radio sources could indicate a denser surrounding medium or a low density region not yet pressurized by the radio source, as suggested by Binette et al. (2000). Correlations (ii) to (iv) provide evidence for a common energy source for the radio power and total emission line luminosity, as found in flux density-limited samples of radio sources.

The luminosity of the Ly α line relative to the other emission lines and the continuum shows a strong increase at $z \gtrsim 3$, coincident with the increase in the

amount of associated HI absorption. This indicates an increased abundance of hydrogen, both ionized and neutral, which may well be the reservoir of primordial hydrogen from which the galaxy is forming. This metallicity evolution is also seen in the nitrogen abundance, which shows a variation of more than an order of magnitude, with the $z > 3$ radio galaxies occupying only the $Z < 2Z_{\odot}$ region.

To examine the ionization mechanism of the extended emission line regions in HzRGs, we plot the UV emission line data in line-ratio diagnostic diagrams. The diagrams involving the high ionization C IV, He II and C III] lines seem to confirm previous results showing that AGN photo-ionization provides the best fit to the data. However, these models cannot fit the C II]/C III] ratio, which lies closer to the predictions for the highest velocity shock ionization models. We note that the C II] line is five times more sensitive to shock ionization than the high ionization UV lines, and show that a combination of shock and photo-ionization provides a better overall fit to the integrated spectra of HzRGs. A substantial contribution from shock ionization will show up first in shock sensitive lines like C II] or Mg II. We also confirm the findings of Best, Röttgering & Longair (2000b) that shock ionization occurs almost exclusively in small radio sources, and show that the angular size distribution can indeed explain the differences in three HzRG composite spectra. Because most HzRGs have radio sizes $\lesssim 150$ kpc, their integrated spectra might well contain a significant contribution from shock ionized emission.

8.1 Introduction

During the last two decades, high redshift radio galaxies (HzRGs) have been used as probes of galaxy formation. Out to $z \sim 1$, they are uniquely identified with massive ellipticals (e.g., Lilly & Longair, 1984; Best, Longair & Röttgering, 1998a). There are strong indications that this is also true at higher redshifts, mostly based on the remarkably strong correlation in the Hubble $K - z$ diagram out to $z = 5.19$ (Lilly, 1989; Eales et al., 1997; van Breugel et al., 1998; Chapter 5). By studying radio galaxies over a large range of redshift, we can thus study the formation and evolution of massive galaxies.

The spectra of HzRGs are mostly dominated by characteristic extended emission lines, indicative of a halo of ionized gas. The most prominent line in these extended emission line regions is Ly α : the luminosity can reach $\sim 10^{45}$ erg s $^{-1}$ and the spatial extent can be up to ~ 150 kpc (e.g., van Ojik et al., 1996; Adam et al., 1997). This allows a detailed study of the kinematics of the gas, both close to the galaxy, where interactions with the radio jets can be studied, as well as at large distances from the AGN where the gas is still undisturbed and should trace the primordial distribution of the gas in these massive galaxies. Within the extent of the radio source, the high line velocity widths (~ 1500 km s $^{-1}$) and disturbed morphologies (e.g., Villar-Martín et al., 1999b; Bicknell et al., 2000) of the emission line gas indicate a strong interaction with the radio jets. This interaction is also obvious in statistical comparisons of the radio and

optical morphologies in $z \gtrsim 0.6$ radio galaxies: (i) the UV and optical emission is often aligned with the radio source (e.g., McCarthy et al., 1987; Chambers, Miley, & van Breugel, 1987), (ii) the radio and emission-line gas morphological asymmetries are strongly correlated (McCarthy, van Breugel & Kapahi, 1991a), and (iii) the rest-frame U - or B -band morphology depends on radio size (Best, Longair & Röttgering, 1996).

The bright Ly α emission profiles frequently show narrow absorption caused by neutral HI in the HzRG (van Ojik et al., 1997). This HI absorption seems to occur almost exclusively in small radio sources, prompting van Ojik et al. to suggest that the HI absorption indicates a dense intergalactic region which confines the radio source. However, the detection of highly ionized C IV $\lambda\lambda$ 1549 absorption in 0943–242 at $z = 2.93$ suggests that the absorption is located further out in a low-metallicity gas shell (Binette et al., 2000), providing us with a new tool to probe the outer regions of forming massive galaxies.

The radio power and emission line luminosities are found to be correlated (e.g., McCarthy, 1993; Willott et al., 1999), indicating that the central AGN is the common energy source for both. The most likely mechanisms for the transformation of this AGN energy into emission line luminosity are photo-ionization by an anisotropic UV source and shock excitation. Because the ionizing spectra of these mechanisms are quite different, they will lead to differences in the emission line spectra, which can be used to determine the dominating source of ionization. Such studies using UV line ratio diagrams suggest that the main ionizing mechanism in HzRGs is nuclear photo-ionization (e.g., Villar-Martín, Tadhunter & Clark, 1997; Allen, Dopita & Tsvetanov, 1998, hereafter VM97 and ADT98). However, a recent study of $z \sim 1$ radio galaxies finds that shock ionization is important in most of the smaller (< 150 kpc) sources (Best, Röttgering & Longair, 2000b, hereafter BRL00). Because the radio sources in HzRGs generally have sizes < 150 kpc, this is in apparent contradiction with the results of VM97 and ADT98 (unless there is a drastic change in the ionization mechanism between $z \sim 1$ and $z \gtrsim 2$).

From the above, it is clear that the properties of the gas in HzRGs can provide an important diagnostic to study various processes in forming massive galaxies, such as star formation, chemical enrichment of the interstellar matter, and the influence of the AGN through shocks or photo-ionization. Detailed observations of several representative individual galaxies (such as 4C 41.17; Chambers, Miley, & van Breugel, 1990; Dey et al., 1997b; Bicknell et al., 2000) can be used to determine the relative importance of these mechanisms, but these should be complemented with a search for statistical relations between the emission line properties and other radio properties of a large sample of HzRGs. Such a study for $z \lesssim 2.5$ radio galaxies (Baum & McCarthy, 2000) finds systematically larger line widths and velocity field amplitudes at $z > 0.6$ than at lower redshifts, but remains inconclusive on the origin: gravitational or due to jet-cloud interactions.

To allow such a statistical study over a continuous redshift range $z = 0$ to $z = 5.2$, we have compiled from the literature the emission line properties of a large sample of radio

Table 8.1: Radio surveys used to construct our sample of radio galaxies.

Survey	Flux density	Spectral index	Angular size	n_{spec}	Reference
3C	$S_{178} > 10$ Jy	none	none	15	Laing, Riley & Longair (1983)
BRL	$S_{408} > 8$ Jy	none	none	39	BRL99
MRC	$S_{408} > 0.95$ Jy	none	none	19	McCarthy et al. (1996)
B2 1 Jy	$1 < S_{408} < 2$ Jy	none	none	3	Allington-Smith (1982)
6C/7C/8C	varies ^b	none	none	7	Lacy et al. (1999)
6C*	$0.96 < S_{151} < 2.00$ Jy	$\alpha_{4850} < -0.981$	$\Theta < 15''$	2	Blundell et al. (1998)
WN/TN	$S_{1400} > 10$ mJy	$\alpha_{151} < -1.30$	$\Theta < 1'$	34	Chapter 2
USS	varies ^c	$\alpha < -1.0^c$	none	30	Röttgering et al. (1994)
MG	$S_{5000} > 50$ mJy	$\alpha_{4800} < -0.75$	$\Theta < 10''$	14	Stern et al. (1999a)

^a n_{spec} is the number of sources with spectroscopic redshifts.

^b The Cambridge surveys listed in Table 1 of Lacy et al. (1999) consist of five sub-samples, each having different flux density limits.

^c The USS sample of Röttgering et al. (1994) consists of nine sub-samples, each with different flux density and spectral index limits. See Table 4 of Röttgering et al. (1994) for details.

galaxies, together with relevant radio properties. In this paper, we first describe the compilation of our HzRG sample (§8.2), and then go on to discuss the determination of the different radio and spectroscopic parameters (§8.3). In §8.4, we perform a statistical analysis of correlations between these parameters, taking the sometimes strong selection effects into account. In §8.5, we use diagnostic line-ratio diagrams to examine the ionization mechanisms in HzRG, and we discuss the implications of our results for the nature of HzRGs in §8.6. We present our conclusions in §8.7.

Throughout, we shall assume $H_0 = 50$ km s⁻¹Mpc⁻¹, $q_0=0.5$, and $\Lambda = 0$, unless otherwise stated, but our results do not depend on the adopted cosmology. We shall abbreviate the emission lines as follows: N V for N V λ 1240, C IV for C IV $\lambda\lambda$ 1549, He II for He II λ 1640, C III] for C III] λ 1909, C II] for C II] λ 2326, Mg II for Mg II λ 2800, [O II] for [O II] λ 3727, and [O III] for [O III] λ 5007.

8.2 Sample selection

Table 8.1 lists nine samples designed to find HzRGs. The surveys can be divided into two classes: (i) several large flux density-limited surveys such as the 3CR (Spinrad et al., 1985), BRL99 sample (Best, Röttgering & Lehnert, 1999), MRC (McCarthy et al., 1996), and 6C, 7C and 8C surveys (e.g., Lacy et al., 1999); (ii) several “filtered” surveys, which have been designed to find the highest redshift objects. For the latter, the radio spectral index is most often used (ultra steep spectrum sources, e.g., Chapter 2), sometimes in combination with an angular size upper limit (e.g., Blundell et al., 1998). Alternatively, the filter consists of a flux density interval centered around the peak in the source counts around 1 Jy (e.g., Allington-Smith, 1982).

These two types of samples are complementary, in the sense that the complete surveys can provide information on the entire range of values of the parameters that were used as a high redshift filter (usually spectral index or radio size), while the filtered samples can extend the radio power and redshift coverage of the un-filtered samples. For example, the addition of data from filtered surveys partially compensates for the Malmquist bias in the flux density-limited surveys (see Fig. 8.1). We therefore com-

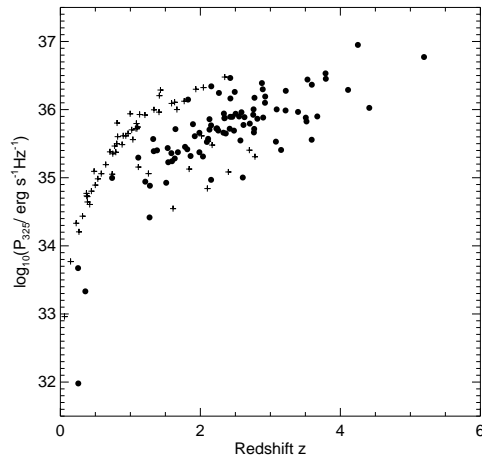


Figure 8.1: Radio power at 325 MHz against redshift. Sources from un-filtered surveys are plotted with + signs, and sources from samples with spectral index and/or radio size filters are plotted as filled circles. Note the tight correlation at $z < 1$ due to the flux density limited 3C survey, and the filtered surveys that fill up the lower power regions at $1 < z < 4$.

piled spectroscopic data on HzRGs from the samples listed in Table 8.1, augmented with four sources from other small surveys. We shall concentrate on radio galaxies at $z > 2$, because above this redshift, the brightest UV lines ($\text{Ly}\alpha$, C IV, He II, and C III]) can be observed with ground based optical spectrographs.

Of the 145 known $z > 2$ radio galaxies, 78 have published spectroscopic parameters including line fluxes, equivalent widths, and line widths. In order to fully investigate redshift dependence, we consider also spectroscopic data for the $z < 2$ sources from the samples that provided sources at $z > 2$. Our final sample contains a similar number of sources at $z < 2$ and at $z > 2$ (Fig. 8.2). From Figure 8.1, we can see that we indeed include sources at $z \gtrsim 2$ with radio powers that are more than an order of magnitude lower than in the un-filtered samples. In appendix A, we list all 165 sources.

8.3 Determination of source parameters

We now describe the radio and spectroscopic parameters from the literature papers and some derived quantities, as listed in Table 8.A.

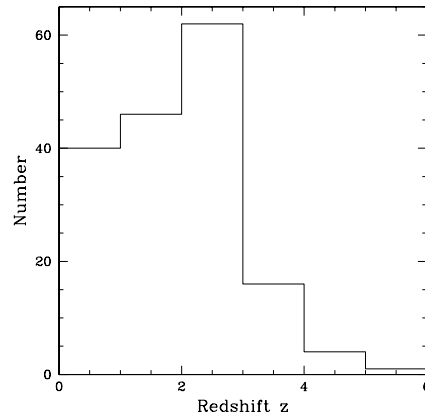


Figure 8.2: Redshift distribution of the sample of $z > 2$ radio galaxies with spectroscopic data, and the lower redshift extension.

8.3.1 Radio parameters

Radio power

In order to obtain a uniform measurement of the radio flux densities, we determined the low frequency radio flux density from the 325 MHz WENSS ($\delta > +28^\circ$; Rengelink et al., 1997) or the 365 MHz Texas radio survey ($-35^\circ < \delta < +28^\circ$; Douglas et al., 1996), and the 1.4 GHz radio flux density from the NVSS (Condon et al., 1998). This procedure finds radio flux densities for 88% of the sources in our HzRG sample. Of the 19 missing sources, one (USS 0529-549) lies outside the area covered by the surveys and one (VLA J123642+621331) is too faint to be detected in any of the three surveys. The remaining sources have not been detected in the incomplete Texas catalogue. Because no other deep large area radio surveys at frequencies below 325 MHz or above 1.4 GHz exist¹, we could not correct for the spectral curvature when performing a K-correction in the calculation of the rest-frame mono-chromatic radio power. Because the radio spectra of HzRGs are predominantly concave, neglecting this spectral curvature will generally lead to an over-estimation of the radio power of the highest redshift sources. Neglecting a spectral curvature of $\Delta\alpha = 0.4$ between rest and observed frequency at $z = 5$ will overestimate the radio power up to a factor of two. From the spectral curvature in a large USS sample (Figure 2.9), we expect only 30% of the sources in our radio galaxy sample to have more spectral curvature, while all our sources are at lower redshifts. We therefore believe that our rest-frame radio powers are accurate to within a factor of two.

¹The Cambridge 6C, 7C and 8C surveys only cover areas of the sky at $\delta > 30^\circ$, 20° and 60° , respectively (Hales, Baldwin & Warner, 1993; Riley, Waldram & Riley, 1999; Rees, 1990), while the Texas surveys covers $\delta > -35^\circ$ (Douglas et al., 1996).

Radio size

To compile the data on the projected radio sizes, we generally took the largest separation between the components of the radio source from the same reference as the spectroscopy data (listed in appendix A). For the sources of Röttgering et al. (1997), we used the radio sizes from Röttgering et al. (1994), for the MRC/1 Jy sample of McCarthy et al. (1996) the sizes are from Kapahi et al. (1998a), and for the MG sample of Stern et al. (1999a), the sizes are from Lawrence et al. (1986).

Radio lobe distance ratio Q

Carilli et al. (1997) and Pentericci et al. (2000a) have obtained 4.7 GHz and 8.2 GHz VLA observations of 64 HzRGs. For the objects for which they identified a radio core, we measured the radio lobe distance ratio Q from their 8.2 GHz contour plots². We also measured the Q values in the sample of Best, Röttgering & Lehnert (1999), and took published values for 3CR galaxies from Best et al. (1995) and McCarthy, van Breugel & Kapahi (1991a). For small and faint sources this parameter is difficult to determine, which limits the possibility to examine the dependency of Q, especially at the highest redshifts, where the radio size of the sources in our sample is smaller.

Other radio parameters

We considered to use the lobe flux density ratio R (e.g., McCarthy, van Breugel & Kapahi, 1991a), which could provide a rough indication of orientation effects. However, too few published high resolution radio data are available at present to perform a statistically significant study of the correlations involving this parameter.

8.3.2 Spectroscopic parameters

Line fluxes

We used published line fluxes throughout this paper (see Appendix A for references). The apertures used to extract the one-dimensional spectra were generally chosen to include all the flux of the most spatially extended emission line. The spread in aperture sizes and depths of the spectra will give rise to an increased scatter when comparing line luminosities from different samples. Some objects were observed under non-photometric conditions, and so we only include these sources for line-ratio studies. We have also determined 5σ upper limits to the flux of N V in 45 objects. Because line ratios are least sensitive to uncertainties in the relative flux calibration, we shall emphasise studies involving line ratios at the expense of studies involving detailed kinematics of the emission lines, which can only be determined from the brightest line, i.e., Ly α .

²Q is defined by McCarthy, van Breugel & Kapahi (1991a) as the ratio of the distance from the radio core to the more distant radio hotspot divided by the distance from the radio core to the closer of the radio hotspot.

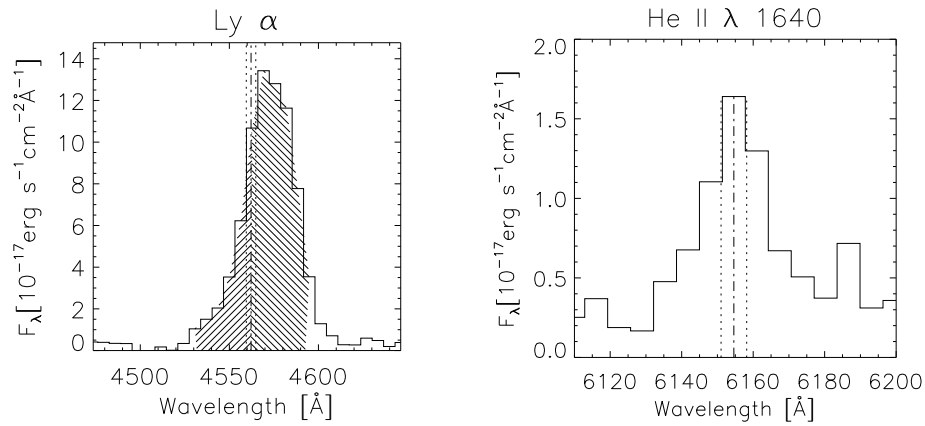


Figure 8.3: Example of the determination of the Ly α asymmetry parameter $A_{\text{Ly}\alpha}$. The right panel shows the position of the He II line (dash-dotted line) determined by a Gaussian fit with the uncertainties indicated by dotted lines. The left panel shows the position of the peak of Ly α as predicted from the He II fit, with the errors indicated. The left and right hatched areas indicate the 2000 km/s intervals used to calculate the flux on both sides of the assumed systemic redshift. The $A_{\text{Ly}\alpha}$ derived from this spectrum is $A_{\text{Ly}\alpha} = -0.49$, with the range of uncertainties going from -0.58 to -0.39 .

Ly α asymmetry

The Ly α emission in HzRGs often shows absorption profiles caused by HI surrounding the radio galaxy, (e.g., van Ojik et al., 1997; Röttgering et al., 1995b; Dey, 1999; Chapter 6). This absorption preferentially occurs on the blue side of the emission line, which leads to a characteristic triangular shape of the Ly α line in two dimensional spectra. Such asymmetries in Ly α are often also observed in other objects with strong Ly α emission at very high redshift (e.g., Dey et al., 1998), and might also have a contribution from intervening HI absorbers along the cosmological line of sight.

While high resolution spectroscopy of these Ly α lines allows one to determine characteristics of the HI absorber (Röttgering et al., 1995b; van Ojik et al., 1997), this is rarely possible with their discovery spectra, which have typical resolutions of a few hundred. To derive some information on the HI absorption from these low-resolution spectra, we therefore introduce a parameter which measures the relative flux on the blue and red sides of the assumed systemic redshift. Because absorption near the maximum of the Ly α emission can shift the observed peak of the profile by as much as 500 km s^{-1} (Röttgering et al., 1997), we have to use other emission lines to determine the systemic redshift. The only other strong lines in HzRGs observed simultaneously with Ly α are C IV, He II, and C III]. From these, He II is the most appropriate line to use, because unlike C IV, He II is not a resonant line, so the profile should be less affected by absorption.

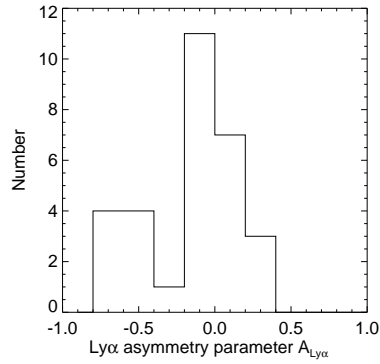


Figure 8.4: Distribution of the Ly α asymmetry parameter $A_{Ly\alpha}$. Note the preference for blue-ward absorption (negative $A_{Ly\alpha}$ values).

We obtained one-dimensional spectra from the samples of Röttgering et al. (1997), Stern et al. (1999a), and from Chapter 4. In 31 objects, the quality of the spectrum was sufficient to allow Gaussian fitting of the He II line. We cannot exclude the possibility that this criterion introduces some selection effects, as it preferentially includes objects with strong He II emission, although almost all the objects observed with Keck/LRIS are included, regardless of their He II flux. We approximated the error in the position of the peak of the Ly α line as the quadratic sum of the error in the He II Gaussian fit and the error in the wavelength calibration, the latter being approximated as a quarter of the dispersion of appropriate spectrum (the resolution of the different spectra varies from $\sim 10\text{\AA}$ to $\sim 25\text{\AA}$).

We define the Ly α asymmetry parameter

$$A_{Ly\alpha} \equiv \frac{F_{blue} - F_{red}}{F_{blue} + F_{red}},$$

where F_{blue} is the flux within 2000 km s^{-1} blue-ward of the systemic Ly α wavelength and F_{red} is the flux within 2000 km s^{-1} red-ward of the systemic Ly α wavelength (see Fig. 8.3 for an example). Because in the lowest resolution spectra, these 2000 km s^{-1} intervals often include only a few dispersion elements (pixels) of the spectrogram, we include only the percentage of the flux in the lowest and highest bin that lies within the 2000 km s^{-1} interval. A value of $A_{Ly\alpha} = -1$ means total absorption of the flux on the blue side, a completely symmetrical profile has $A_{Ly\alpha} = 0$, and positive $A_{Ly\alpha}$ values indicate absorption on the red side. We calculated the range of allowed $A_{Ly\alpha}$ values from the error in the predicted systemic wavelength of Ly α . Because the peak sometimes falls on a steep side of the observed Ly α profile, this can lead to asymmetric errors in $A_{Ly\alpha}$. We excluded three sources where the range in $A_{Ly\alpha}$ was larger than 1.5 due to their large uncertainties. We could accurately determine the $A_{Ly\alpha}$ parameter for 25 HzRGs. The distribution (Fig. 8.4) shows a strong peak around $A_{Ly\alpha} = 0$

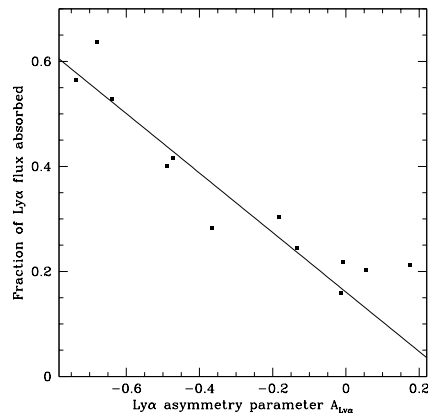


Figure 8.5: The fraction of Ly α flux absorbed plotted against the Ly α asymmetry parameter (see text for details). Note that no more than 65% gets absorbed, and that the asymmetry parameter is a good measure of the total amount of absorption, as indicated by the linear fit.

(no asymmetry) and a secondary peak around $A_{Ly\alpha} = -0.6$ (blue absorption), but no sources with strong red-ward absorption. This is consistent with the trend seen from high resolution spectroscopy, where the median velocity of the HI absorbers is blue-shifted by 100 km s^{-1} with respect to the peak emission redshift (van Ojik et al., 1997).

For 12 HzRGs, the resolution and signal to noise of the Ly α profile was sufficient to extrapolate over the absorption profiles while fitting the emission with a single Gaussian profile (see Chapter 6 for an example). In cases where the profile is clearly non-Gaussian, we also included a Voigt function. We again used the He II redshift to predict the peak position of the Gaussian Ly α emission (in two cases a variation of $1\text{--}2\text{\AA}$ provided a better fit, which is consistent with the wavelength calibration errors). We varied the peak flux and FWHM of the Gaussian until we obtained a good fit on one side of the profile. We use these crude Gaussian models to determine how much flux was emitted before the HI absorption (integrating out to three times the FWHM of the Gaussian fit). We used this total flux to calculate an approximate fraction of the Ly α flux that is absorbed. Figure 8.5 compares this fraction with $A_{Ly\alpha}$. As expected, we find a strong correlation indicating that (i) our $A_{Ly\alpha}$ parameter is a good approximation of the absorbed flux and (ii) that even in the most asymmetric profiles, the observed Ly α flux is only diminished by $\sim 50\%$, although we cannot exclude the possibility that sources with higher absorption fractions are missing from the samples because they are too weak to be detected. A limitation of our method is that it is insensitive to absorption which is centered near the peak of the emission, but such cases are rather rare (van Ojik et al., 1997).

For two of the highest redshift HzRGs where He II falls outside the optical window, we use the fit in Figure 8.5 to calculate the approximate $A_{\text{Ly}\alpha}$ value. This is particularly important if we want to study the redshift evolution of $A_{\text{Ly}\alpha}$. As a final note, it should be stressed that this procedure provides only a rough measure of the Ly α kinematics. The main goal of the $A_{\text{Ly}\alpha}$ parameter is to examine the existence of strong trends with redshift, or parameters of the radio source. A detailed study of the kinematics is impossible with these low-resolution data, and is beyond the scope of this chapter.

8.4 Correlations between parameters

8.4.1 Selection effects

The main problems we encounter when searching for correlations between the different parameters in our sample of HzRGs are the selection effects resulting from the search techniques used to find them and technical limitations of the spectrographs. A well known example of the first effect is the Malmquist bias in flux density limited samples. As discussed in §8.2, the addition of several filtered surveys with lower flux density limits alleviated this bias, especially at $2 < z < 4$, the range we shall concentrate on (Fig. 8.1). However, comparisons with $z < 2$ radio galaxies will still be strongly affected by Malmquist bias.

More subtle selection effects are due to the wavelength-dependent sensitivity of the optical spectrographs. Weak emission line objects could well have been escaped detection at certain redshifts where the brightest lines are not observable. For example, fewer sources are known in the $1.5 \lesssim z \lesssim 2$ “redshift desert” where [O II] λ 3727 has shifted out of the optical window and Ly α has not yet entered, and the redshift will have to be based on weaker lines like C IV, He II C III] or C II] (e.g., Stern et al., 1999a). At very high redshift ($z > 3$), weaker lines red-ward of Ly α will shift to wavelengths where measurement is difficult due to fringing of the CCD and bright OH sky-lines (e.g., Osterbrock & Martel, 1992). This should have only a limited effect on the line ratio diagnostics, because the spectra of $z > 3$ radio galaxies are generally of higher quality than those at $2 < z < 3$: the highest redshift spectra were usually obtained with larger aperture telescopes, or the integration time was extended to search for confirming lines.

8.4.2 Statistical tests

Most previous studies have each concentrated on specific correlations between a few specified parameters in HzRGs. Here, we shall examine correlations between all of our measured parameters. Some apparent correlations between two parameters might be due to the correlation of one or both of these parameters with a third parameter (either by selection effects or by a real correlation). As argued by Macklin (1982), the statistical test that de-couples such dependent correlations, while retaining as much information as possible, is the Spearman partial rank correlation coefficient. We shall

apply this test to determine if some correlations are not due to selection effects in one or both of the parameters.

In the first approximation, we simply exclude lower or upper limits from this analysis. For most parameters, this will not have a serious effect on the results, because less than 5% of the data are lower or upper limits. However, 12% of the linear sizes are upper limits, and an even higher percentage of the equivalent widths are lower limits (from 11% for $W_{\text{HeII}}^{\text{rest}}$ to 35% for $W_{\text{Ly}\alpha}^{\text{rest}}$). To treat these limits, or “censored data”, in a statistically meaningful manner with minimal loss of information, a class of statistical methods called “survival analysis” has been developed (e.g., Isobe, Feigelson & Nelson, 1986). To test the correlations involving radio size and equivalent widths with survival analysis methods, we shall use the ASURV software package Isobe & Feigelson (1990); Lavalley, Isobe & Feigelson (1992), which is incorporated into the NOAO reduction package IRAF. Three different correlation tests within ASURV are of importance to this work: Cox’s hazard model, generalized Kendall’s τ , and generalized Spearman’s ρ . We shall take the variables as correlated if all three of these models give significance levels³ >95%. One of the deficiencies of survival analysis for astronomical purposes is that upper limits are assumed to be precisely known. Especially the lower limits to the equivalent widths are very uncertain due to the extreme faintness of the continuum emission. Survival analysis is not as effective in handling dependent correlations in the way the Spearman partial rank analysis can. We shall therefore only use survival analysis to check whether the addition of censored data changes the significance of a correlation which was found from our previous analysis.

8.4.3 Spearman rank analysis

To investigate every possible dependent correlation, we first calculated the Spearman rank correlation coefficient and the associated significance levels for all 153 possible combinations of source parameters in our HzRG sample. The results are presented in appendix B. The correlation coefficients and number of available parameters are tabulated in the lower left half of the Table, and the significance levels in the upper right half. We also calculated these values for a $H_0 = 65 \text{ km s}^{-1} \text{ Mpc}^{-1}$, $q_0 = 0.15$ cosmology, but this changed the values of the correlation coefficients by less than 0.1.

We find 33 correlations with significance levels >99%, and 10 additional which are between 95% and 99% significant. These correlations are:

- Redshift z with radio size D , radio power P_{325} , radio spectral index α and line luminosity L_{CIV} , L_{HeII} or L_{CIII} .
- Radio spectral index α with radio size D .
- Radio spectral index α with radio power P_{325} .

³Note that for consistency with previous statistical work on HzRGs, by significance level we mean the significance level of the correlation, and not the probability of the null hypothesis (no correlation) being true, which is generally used in survival analysis.

- Radio spectral index α with line luminosity (increasingly stronger correlation for weaker emission lines).
- Radio spectral index α with equivalent width of C IV, He II and C III].
- Radio size D with Ly α asymmetry $A_{\text{Ly}\alpha}$, and L_{HeII} .
- Radio lobe distance ratio Q with equivalent width $W_{\text{Ly}\alpha}^{\text{rest}}$ and $W_{\text{HeII}}^{\text{rest}}$.
- Radio power P_{325} and P_{1400} with all four line luminosities.
- Line luminosities of Ly α , C IV, He II and C III] with each other.
- Ly α luminosity with both Ly α equivalent width $W_{\text{Ly}\alpha}^{\text{rest}}$ and Ly α line width $\Delta v_{\text{Ly}\alpha}$.
- Equivalent widths of Ly α , C IV, He II and C III] with each other.
- Equivalent widths of fainter lines (He II and C III]) with line widths of Ly α and to a lesser extent fainter lines.

We shall now examine if some of these correlation are due to selection effects, dependent correlations with other parameters, or are removed if sources with upper/lower limits are included.

8.4.4 Correlations influenced or caused by selection effects

Radio size and power vs. redshift

The dependence of radio size D on redshift z and radio power P_{325} has been examined by a number of authors (e.g., Neeser et al., 1995; Blundell, Rawlings, & Willott, 1999a). The range of often contradictory results is due to several selection effects (e.g., in selection frequency) in the samples used to examine this correlation. Our sample of radio galaxies is too inhomogeneous and incomplete to address this question. For example the Malmquist bias in radio power (Fig. 8.1) will dominate the $P_{325} - z$ correlation. For $z > 2$, the probability that z and P_{325} are uncorrelated drops from 1.15×10^{-21} to 1.6×10^{-4} , indicating the Malmquist bias is strongly decreased, but not removed (see Fig. 8.1). While part of the correlation might be due to an underlying real correlation (e.g., between z and D), we consider the effect of the selection effects too large and will not examine the significance of these relations.

Radio spectral index vs. radio size and radio power

In some samples designed to find HzRGs, the radio size D has been used as an additional “high redshift filter” in combination with a spectral index cutoff. This will lead to selection effects in the redshift-spectral index relation, masking a possible real correlation.

The relation between spectral index and radio power is not independent, because we used the spectral index to calculate the rest-frame radio power of our sources.

Radio spectral index vs. line luminosity and equivalent width

The luminosities of the UV emission lines and rest-frame equivalent widths appear to be correlated, with the weakest line (C III]) showing the strongest correlation.

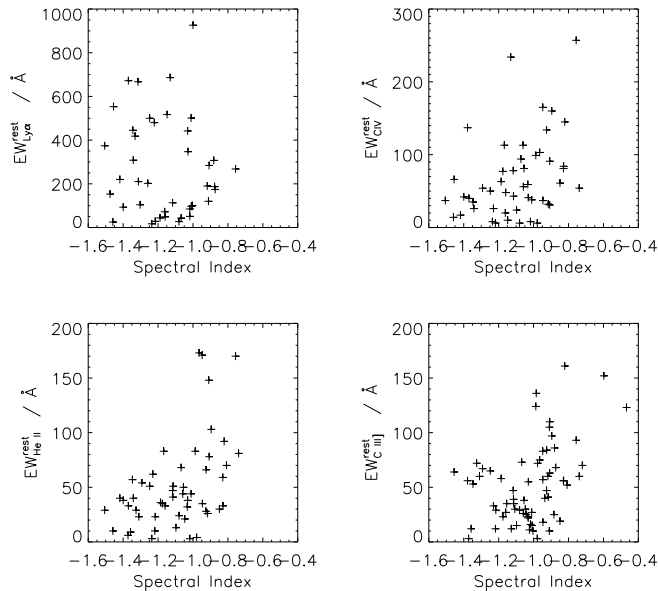


Figure 8.6: Rest-frame equivalent width plotted against radio spectral index. Note that the trend for redder lines (He II and C III] is more offset towards flatter spectral indices than for the blue lines (Ly α and C IV). This arises because at higher redshift (i.e., steeper spectral index) the bluest lines either shift into less sensitive parts of the observable window, where they can only be detected if they have high equivalent widths.

However, due to the way we constructed our sample of radio galaxies, the sources with the flattest spectral indices are all at relatively low redshift ($z \lesssim 2$). Because the line luminosities are strongly correlated with redshift (see next section), we only find the low-luminosity lines in the low-redshift flattest spectrum sources of our sample.

The apparent correlation between radio spectral index and rest-frame equivalent width is also influenced by subtle redshift selection effects: the increasingly bluer lines will only be detected at higher redshifts due to the fixed wavelength range of the optical spectrographs. At the lowest redshifts, these lines will be in the bluest, least sensitive part of the CCD, and they will only be detected when they have a high equivalent width. This effect is obvious in Fig. 8.6: the apparent correlation between rest-frame equivalent width and spectral index seems to shift towards flatter spectral indices in the redder lines, which are only observed in the lower redshift sources which have flatter radio spectral indices.

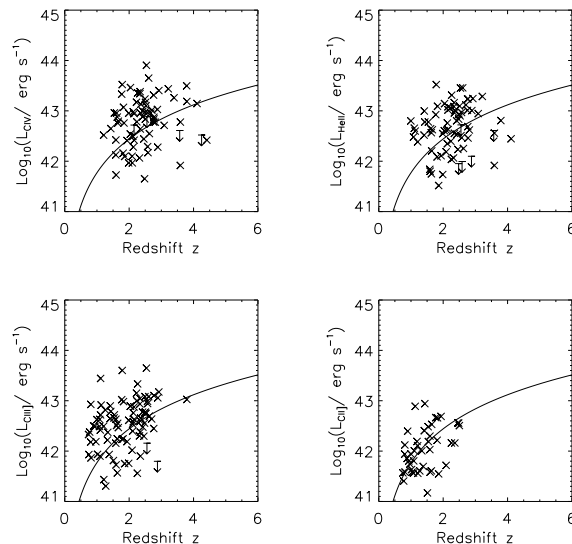


Figure 8.7: Emission line luminosity for C IV, He II, C III] and C II] plotted against redshift. The plotted line indicates the luminosity as a function of redshift at which a line with an emission line flux of $1.0 \times 10^{-16} \text{erg s}^{-1} \text{cm}^{-2} \text{\AA}^{-1}$, near the detectability of 3-4m class telescopes, would be detected. Note that the higher wavelength lines are increasingly weaker, and lie closer to the detection limit. The lack of sources below this limit leads to an artificial redshift dependence of the line luminosity.

Emission line luminosity vs. redshift

The apparent correlation between line luminosity and redshift z is a less known selection effect. The correlation is weak or absent for $\text{Ly}\alpha$, but increasingly stronger for C IV, He II, and C III]. The reason for this is obvious in Figures 8.7 and 8.8, where we plot the emission line luminosities against redshift together with a curve which denotes the luminosity corresponding to an emission line with a flux of $1.0 \times 10^{-16} \text{erg s}^{-1} \text{cm}^{-2} \text{\AA}^{-1}$, which is close to the minimum detectable level of most of the observations. We clearly find a line-luminosity redshift degeneracy, as found for the radio powers. This degeneracy becomes more pronounced as the lines become weaker. The $\text{Ly}\alpha$ line is generally an order of magnitude brighter than the other UV lines. In addition, the two highest redshift radio galaxies have very weak $\text{Ly}\alpha$ (TN J0924–2201 at $z = 5.19$ and VLA J123642+621331 at $z = 4.42$; Chapter 5; Waddington et al., 1999), and have been detected at flux levels an order of magnitude fainter than what has been attempted for the other lines. The lines red-ward of $\text{Ly}\alpha$ are increasingly fainter, and lie much closer to the detection limit, and will therefore more easily be missed.

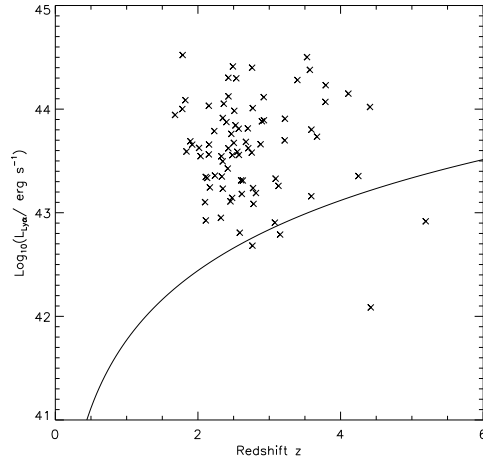


Figure 8.8: Emission line luminosity for Ly α plotted against redshift. The line indicates a line with an emission line flux of $1.0 \times 10^{-16} \text{ erg s}^{-1} \text{ cm}^{-2} \text{ \AA}^{-1}$, near the detectability of 3-4m class telescopes. Note that there is no artificial redshift dependence, as for the lines in Figure 8.7.

Variable		Percentage Censored	Significance		
Independent	Dependent		Cox	Kendall	Spearman
$L_{\text{Ly}\alpha}$	$W_{\text{Ly}\alpha}^{\text{rest}}$	36%	34.71%	85.00%	81.36%
L_{CIV}	$W_{\text{CIV}}^{\text{rest}}$	18%	99.92%	99.78%	99.65%
L_{HeII}	$W_{\text{HeII}}^{\text{rest}}$	11%	99.51%	99.25%	99.31%
$L_{\text{CIII]}}$	$W_{\text{CIII]}}^{\text{rest}}$	10%	70.19%	98.29%	97.85%

Table 8.2: Results of survival analysis on the correlations between line luminosity and equivalent width. The significance indicates the probability a correlation is detected.

Emission line luminosity vs. equivalent width

The correlations between the equivalent width and line luminosities are also dominated by selection effects, namely the difficulty to detect objects with weak emission line fluxes and high equivalent widths. These sources probably do exist, as the objects for which there are lower limits to the equivalent widths frequently have low line luminosities. When we apply survival analysis models to the complete dataset (Table 8.2), we find that the correlations with Ly α and C III] are no longer significant. Given that both the detections and lower limits to the equivalent widths in these weak lines are highly uncertain, we interpret these correlations as too uncertain to be trustworthy.

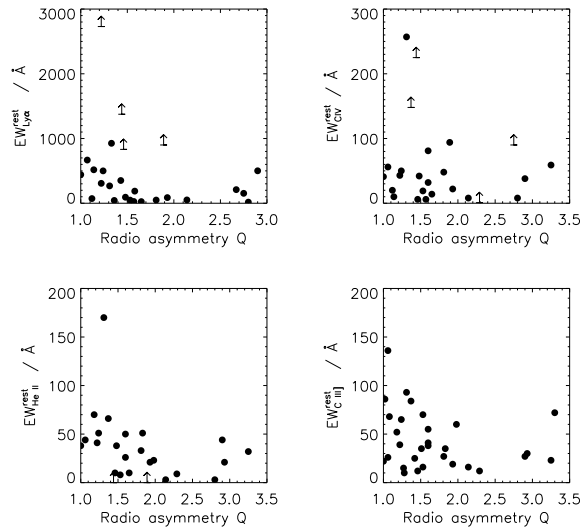


Figure 8.9: Equivalent widths of the strong UV lines plotted against radio lobe distance ratio Q .

$\text{Ly}\alpha$ line width vs. equivalent width of He II and C III]

A final correlation which we consider dominated by selection effects is the correlation of equivalent widths of fainter lines (He II and C III) with line widths of $\text{Ly}\alpha$. When the two sources with $\Delta v_{\text{Ly}\alpha} > 3000 \text{ km s}^{-1}$ are not considered, the significance of these correlations drops to $< 95\%$. Such sources probably have a broad component detected in $\text{Ly}\alpha$, but not in the weaker lines.

8.4.5 Possible correlations

A few parameters, for which limited data exist appear to show correlations. One set of such correlations are those between the radio lobe distance ratio Q and rest-frame equivalent widths of the UV lines. From the plots of these four correlations (Fig. 8.9), we find that there is a dearth of highly asymmetric radio sources with large equivalent widths.

One possible explanation of this effect can be found in the observing techniques used to determine the redshifts of HzRGs. In some objects where the correct identification of the host galaxy is uncertain, the spectroscopic slit will be positioned such as to increase the chances to detect strong line emission which can be used to determine the redshift. Most often, this means that the slit is aligned with the radio emission. In relatively symmetrical sources with a slight bending of the radio lobes, this could mean that the slit will not be perfectly centered on the host galaxy. In highly asymmetric

Variables	Number	r_{PL}	$r_{PL,z}$	σ
$P_{325}, L_{Ly\alpha}$	67	0.35 (0.38)	0.37 (0.38)	3.06 (3.14)
P_{325}, L_{CIV}	64	0.40 (0.28)	0.29 (0.28)	2.40 (2.27)
P_{325}, L_{HeII}	61	0.35 (0.24)	0.25 (0.24)	1.94 (1.91)
$P_{325}, L_{CIII]}$	79	0.47 (0.30)	0.31 (0.30)	2.78 (2.68)
$P_{325}, L_{CII]}$	42	0.68 (0.73)	0.70 (0.70)	5.29 (5.39)
P_{325}, L_{MgII}	30	0.62 (0.65)	0.56 (0.56)	3.25 (3.26)

Table 8.3: Spearman partial rank correlation analysis for the correlations between radio power P_{325} , line luminosity of the bright UV lines and redshift. r_{PL} is the Spearman rank coefficient of the radio power and line luminosity, and $r_{PL,z}$ is the Spearman partial rank coefficient, taking the selection effects with redshift into account. σ is the significance of the partial rank correlation, which is equivalent to the deviation from a unit variance normal distribution if no correlation is present. Values in brackets are for a $H_0 = 65 \text{ km s}^{-1} \text{ Mpc}^{-1}$, $q_0=0.15$ cosmology.

sources, the slit will be more often centered near the presumed optical identification, which will increase the chance that host galaxy continuum emission is included, and lead to a lower equivalent width. Based on only ~ 20 sources, we therefore consider this correlation suggestive. A sample of radio galaxies observed in a consistent way would be needed to fully examine the significance of this correlation.

8.4.6 Probable correlations

Line luminosities and equivalent widths

We find that the line luminosities of the four bright UV lines are all strongly correlated with each other. We also find a similar result for the rest-frame equivalent widths. This indicates that the different emission lines in HzRGs are powered by the same mechanism. We shall discuss this further in §8.5.

Radio power vs. emission line luminosity

To examine the correlation between radio power and emission line luminosity, we use the Spearman partial rank coefficient, including redshift as the third parameter, and thus taking the Malmquist bias of both parameters into account. Table 8.3 presents the results of this analysis. Figure 8.10 shows graphical representations of the correlations.

Table 8.3 shows that the selection effects with redshift have only a minor influence on the correlation between the radio powers and Ly α C II] and Mg II luminosity, but do artificially strengthen the correlations with C IV, He II, and C III]. This is because the radio power - redshift degeneracy becomes less pronounced, or absent at $z > 2$, where the UV lines shift into the optical spectroscopy window, and because

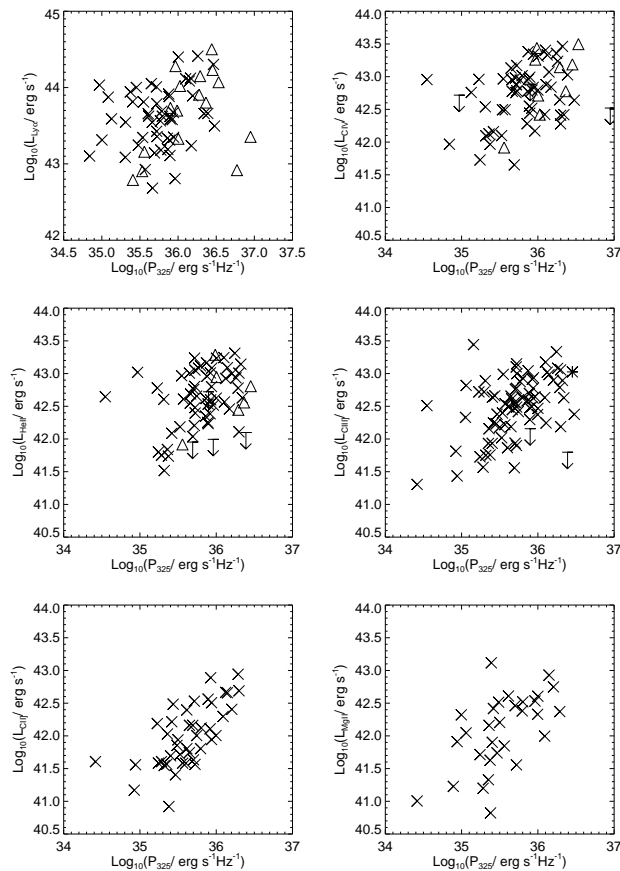


Figure 8.10: Line luminosity for Ly α , C IV, He II, C III] C II] and Mg II plotted against radio power at 325 MHz. Crosses represent sources at $z < 3$, triangles those at $z > 3$.

of the increasingly more important redshift selection effects with weaker emission lines, as discussed in §8.4.3. We have examined this correlation using the radio power at 325 MHz and 1.4 GHz, and found only minor differences, with the P_{325} yielding slightly stronger correlations. We prefer to use the P_{325} because the higher frequency might have a larger contribution from a Doppler boosted core (see e.g., Blundell, Rawlings, & Willott, 1999a).

We find a $\gtrsim 2\sigma$ probability that the correlations between radio power and line luminosity are not due to their mutual correlations with redshift. We shall discuss this further in §8.6.2.

x, y	Number	r_{xy}	$r_{xy,z}$	σ
$D, A_{\text{Ly}\alpha}$	25	-0.60(-0.59)	-0.64(-0.64)	3.48 (3.44)
$A_{\text{Ly}\alpha}, z$	25	0.33(0.33)	0.41(0.09)	2.02 (2.06)

Table 8.4: Spearman partial rank correlation analysis for the correlations between radio size D , Ly α asymmetry $A_{\text{Ly}\alpha}$, and redshift z . r_{xy} is the Spearman rank coefficient, and $r_{xy,z}$ is the the Spearman partial rank coefficient, taking the selection effects with the third parameter into account. σ is the significance of the partial rank correlation, as in Table 8.2. Values in brackets are for a $H_0 = 65 \text{ km s}^{-1} \text{ Mpc}^{-1}$, $q_0=0.15$ cosmology.

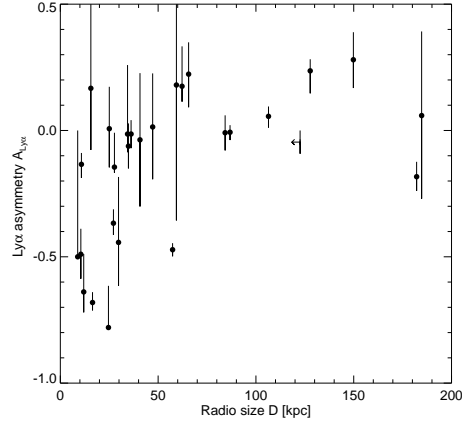


Figure 8.11: Ly α asymmetry parameter $A_{\text{Ly}\alpha}$ plotted against radio size. Error bars reflect the uncertainty in the wavelength calibration and fitting of the He II line, and need not be symmetrical. Note that strong blue Ly α absorption only occurs in smaller radio sources.

Ly α asymmetry vs. Radio size, and vs. redshift

The Spearman rank analysis (appendix B) indicates that there is an anti-correlation between radio size and Ly α asymmetry $A_{\text{Ly}\alpha}$ with a confidence level of 99.86%. We perform a Spearman partial rank analysis, because of the possibility of this arising artificially from the correlation between redshift and radio size D .

From this analysis (Table 8.4), we find that $A_{\text{Ly}\alpha}$ appears to be correlated with radio size and redshift independently. From Figure 8.11, we see that all seven HzRGs with $A_{\text{Ly}\alpha} > 0.3$ have radio sizes $D < 60$ kpc. This confirms the results of van Ojik et al. (1997), who found from high resolution spectroscopy that HI absorption preferentially occurs in radio galaxies smaller than 50 kpc.

The correlation with redshift is less significant, but we lack sufficient data at $z > 3$, because our method requires the detection of the He II line, which starts shifting out of the optical band at these redshifts. However, Dey (1999) shows Ly α velocity profiles of four $z > 3.5$ radio galaxies with the redshift predicted from He II or C III] indicated,

which all show strong blueward absorption. His results are not only consistent with the $A_{\text{Ly}\alpha}$ – D trend, but also show stronger absorption for the $z > 4$ radio galaxies, as is also seen in TN J1338–1942 at $z = 4.11$ (Chapter 6). We discuss this result further in §8.6.4.

8.4.7 Summary of correlation analysis

After consideration of all selection effects, we find 22 real correlations, viz.

- Radio size D and redshift z with Ly α asymmetry $A_{\text{Ly}\alpha}$.
- UV line luminosity with radio power (8 correlations).
- Line luminosities of Ly α , C IV, He II and C III] with each other (6 correlations).
- Equivalent widths of Ly α , C IV, He II and C III] with each other (6 correlations).

8.5 Emission line ratios

The relative intensities of emission lines provide a valuable tool to examine the physical state of the extended emission line gas in HzRGs. The (rest-frame) UV emission lines from different elements (mainly hydrogen, carbon, helium, and nitrogen) and the three ionization states of the carbon lines (C II], C III], and C IV) can distinguish between different ionization mechanisms, and in some cases provide information on the relative abundance of these elements.

An efficient way to compare the data with model predictions is to use line-ratio diagrams. For HzRGs, the rest-frame optical lines which are normally used for such studies have shifted to the near-IR, and we have to use the rest-frame UV-lines that have shifted into the optical. VM97 and ADT98 have used line ratios involving the C IV, He II, C III] and C II] lines to compare HzRG spectra (from Röttgering et al., 1997) with the predictions from photo-ionization and shock models. Our HzRG sample contains almost three times as many sources as the samples in VM97 and ADT98: 58 sources have simultaneously observed C IV, He II, and C III] lines, with redshifts $1.2 < z < 3.8$, radio sizes $D < 365$ kpc, and radio powers $34.5 < \log(P_{325}) < 36.5$. In this section, we shall examine the dependence of the line ratios on these parameters, and on the physical parameters determined from the shock and photo-ionization models. Because we have seen in §8.4.4 that all of these parameters have an artificial redshift dependence, we shall first disentangle the mutual dependences of the line ratios on these parameters. After introducing the theoretical models, we shall compare the data with the range of model predictions, and examine the ratios involving Ly α and two rest-frame optical lines determined from near-IR spectroscopy.

8.5.1 HzRG UV line ratios

In §8.4.4, we found an increasing dependence of the C IV, He II, C III] and C II] line luminosities with redshift. This selection effect will also affect the line ratios. To

Line ratio	#	z			D			P_{325}		
		r_{rz}	$r_{rz,DP}$	σ	r_{rD}	$r_{rD,zP}$	σ	r_{rP}	$r_{rP,zD}$	σ
Ly α / C IV	41	-0.13	-0.06	-0.34	0.11	0.08	0.47	-0.09	-0.05	-0.33
Ly α / He II	32	-0.24	-0.06	-0.30	0.15	0.16	0.83	-0.35	-0.32	-1.71
Ly α / C III]	27	-0.19	-0.20	-0.93	-0.16	-0.23	-1.10	-0.19	-0.17	-0.81
C IV / He II	48	-0.10	-0.13	-0.87	-0.05	-0.08	-0.53	0.02	0.08	0.51
C IV / C III]	43	0.08	0.09	0.55	-0.01	-0.00	-0.01	-0.05	-0.06	-0.40
C IV / C II]	11	0.19	0.15	0.38	0.28	0.53	1.45	-0.74	-0.80	-2.71
C III] / He II	45	-0.24	-0.25	-1.65	0.03	-0.03	-0.15	0.03	0.09	0.57
C II] / He II	14	0.32	0.19	0.57	-0.63	-0.65	-2.31	0.31	0.58	1.97
C II] / C III]	29	-0.41	0.08	0.37	0.69	0.60	3.39	0.03	-0.08	-0.39

Table 8.5: Spearman partial rank correlation analysis for the correlations between nine UV line ratios and redshift z , radio size D , and radio power P_{325} . r_{rz} is the Spearman rank correlation coefficient between the line ratio r of the lines in the first column and z , while $r_{rz,DP}$ is the Spearman partial rank coefficient of that correlation, taking the possible correlations with D and P_{325} into account. σ is the significance of the partial rank correlation, as in Table 2. The last six columns similarly examine the correlations with radio size and radio power.

properly examine the trends involving line ratios, we used a four-parameter Spearman partial rank analysis (Table 8.5).

We find that only one of the correlations with more than 20 elements has more than 2σ significance, indicating that redshift, radio size or power do not have a strong influence on most emission line ratios. The only one of these correlations that is significant is the one between the C II]/C III] ratio and radio size D , which BRL00 reported as evidence that small sources in their sample of 14 3CR galaxies at $z \sim 1$ are ionized by shocks and larger sources by photo-ionization. Our sample, which includes all their sources, is twice as large, but only adds relatively small sources with $D < 150$ kpc. The Spearman partial rank analysis shows that the highest probability of correlation of C II]/C III] is indeed with D , and not with z or P_{325} . The results of BRL00 were not strongly affected by selection effects, because their 3CR subsample has a limited redshift range $0.7 < z < 1.2$. The addition of six upper limits to the radio size (Fig. 8.12) is consistent with the C II]/C III] - D correlation because no sources > 50 kpc with C II] stronger than C III] are found.

Stern et al.(1999; hereafter S99) reported a possible correlation between the C IV/C III] ratio and radio power. We find no evidence for a correlation of C IV/C III] with P_{325} , eventhough S99 used 25 of our 43 data points. This partly due to the exclusion of five sources (of which three are from S99) with only upper limits to the radio size. These three excluded sources are the only ones where C III] is stronger than C IV. If we retain these five sources and replace their upper limits to the radio size by detections⁴, we find a Spearman partial rank coefficient $r_{rP,zD} = 0.22$ and significance level $D_{rP,zD} = 1.35$. Further differences are caused by our different determination of the radio power (§8.3.1.1). It is clear that a larger and better defined sample with multi-frequency radio data to determine the radio power and deep spectroscopy to break the artificial redshift dependence of the line luminosities is needed to examine

⁴As discussed in §8.4.2, we cannot use survival analysis on dependent variables.

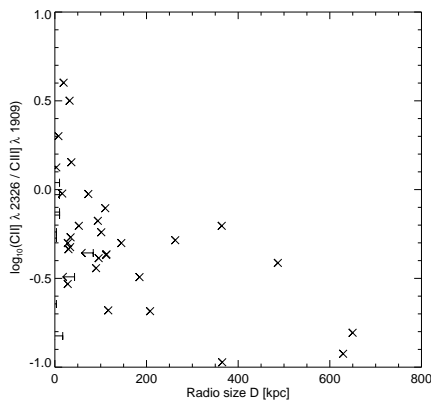


Figure 8.12: The C II]/C III] ratio plotted versus radio size. Note the absence of large sources with strong C II].

whether the C IV/ C III] line ratio is correlated with redshift, radio size, or radio power.

To summarize, the only strong correlation between the UV line ratios and radio properties is a dependence of the C II]/C III] ratio on radio size D . We find no evidence that the radio power and ionization state are correlated.

8.5.2 Shock and photo-ionization models

Of great importance in the study of the nature of the extended emission line regions in HzRGs is the mechanism responsible for producing the observed ionization state. The most likely mechanisms include photo-ionization from a central AGN, and shock ionization from the radio jets propagating through the interstellar medium. In this section, we describe three theoretical models that can predict the line ratios for these processes.

To calculate the predictions from shock ionization, we use the models of Dopita & Sutherland (1996; hereafter DS96). Their models consist of two components: (i) a down-stream shock component, dominated by the radiative cooling of the gas behind the shock, and (ii) an up-stream precursor component, dominated by the photo-ionization by the radiation from the shocked gas. Their models assume solar metallicities, and present a grid of model predictions for shock velocities in the range $150 < v < 500 \text{ km s}^{-1}$, and for values of the magnetic parameter $0 < B/\sqrt{n} < 4\mu\text{G cm}^{3/2}$, with B the pre-shock transverse magnetic field and n the pre-shock number density. This magnetic parameter controls the effective ionization parameter in the down-stream emitting component of the shock since at high shock velocities, the transverse magnetic field limits the compression caused by the shock through a balance of the magnetic pressure of the cloud and the ram pressure of the shock. Future

versions of these models extend the shock velocities out to 1000 km s^{-1} , and will include non-solar metallicities (Bicknell et al., 2000; Sutherland, private communication). To derive the He II $\lambda 1640$ fluxes (not included in the tables of DS96) from the He II $\lambda 4686$ fluxes that are provided, we assume a ratio of 9 (e.g., MacAlpine et al., 1985). Note that the shock+precursor models of ADT98 do not include this factor for the precursor component so that their He II $\lambda 1640$ values are underestimated by a factors of $\sim 1 - 6$ (Allen, private communication), whilst VM97 plotted the shock and precursor models separately, which is inappropriate for HzRG spectra, since these are spatially integrated over both the shock and precursor gas.

For the photo-ionization models, VM97 use the MAPPINGS I code developed by Binette, while ADT98 use the MAPPINGS II code developed by Sutherland. The differences between the two model predictions are minor for the relevant range of parameters. We use CLOUDY version C94 (Ferland, 1996), and also find very similar results, providing another independent consistency check with the results of VM97 and ADT98. We calculate the model spectra for the same range of parameters as ADT98 to facilitate comparison between the predictions of the different codes. We assume solar metallicities, and an ionizing continuum which is a power law spectrum ($\phi_\nu \propto \nu^\alpha$) with lower and higher energy cutoffs of 0.01 Ryd and 100 Ryd (1.36 keV), but the models do not depend strongly on the exact values of these limits. We calculate spectra for a power law spectral index $\alpha = -1.5$ which provides a better fit in the low redshift Seyfert spectra (e.g., Evans et al., 1999), and for $\alpha = -1.0$, which VM97 find to match the HzRG data better. For the hydrogen density, we used a value of $n = 100$, as commonly used for the extended emission line regions (e.g., McCarthy et al., 1990b) and a high density value of $n = 1000 \text{ cm}^{-3}$. We vary the ionization parameter⁵ U from 0.001 to 0.1 in steps of 0.5 dex to cover the entire range of observed line ratios.

Binette, Wilson & Storchi-Bergmann (1996; hereafter B96) present an alternative photo-ionization sequence by considering emission from two distinct cloud populations. In their model, the light from the photo-ionizing source first passes through a population of matter-bounded (optically thin) clouds, and subsequently strikes ionization-bounded (optically thick) clouds located further outwards. They produce a sequence by varying the the parameter $A_{M/I}$, defined as the ratio of the solid angle subtended by the matter-bounded clouds to the solid angle subtended by the ionization-bounded clouds. They keep the power law spectral index of the ionizing continuum incident at the matter-bounded clouds constant at $\alpha = -1.3$ and the ionization parameter constant at $U_{MB} = 0.04$. By adding this ionization-bounded component, B96 solve several shortcomings of the classical photo-ionization models, like the inability to produce strong high excitation UV lines for reasonable values of U inferred from the optical lines. Because the $A_{M/I}$ models require that the ionizing

⁵Defined as $U = (cn)^{-1} \int_{\nu_0}^{\infty} (\phi_\nu d\nu)/h\nu$, with ϕ_ν the monochromatic ionizing energy flux impinging on the cloud, ν_0 the ionizing potential of hydrogen, n the total gas density at the front face of the cloud, c the speed of light, and h Planck's constant.

continuum incident on the ionization-bounded clouds first has to be “filtered” by the matter-bounded clouds, the values of $A_{M/I}$ cannot strictly be less than unity. However, if the matter-bounded clouds are obscured along the line of sight, we can observe apparent $A_{M/I} < 1$ values.

8.5.3 Comparison with the observations

Figure 8.13 reproduces three diagnostic diagrams from VM97 and ADT98, showing the C IV, He II, and C III] lines, and a Carbon-only plot from ADT98, showing the ratios of C IV, C III], and C II].

Shock models

From the left panels in Figure 8.13, we find that the present shock or shock+precursor models cannot explain the ratios involving C IV, He II, and C III], while roughly half of the HzRGs in the Carbon-only plot coincide with the highest shock velocity (500 km s^{-1}) models. In the plots without C II], the least discrepant predictions are the highest shock velocity shock+precursor models. The disturbed kinematics of the emission line gas indicate that shocks with velocities $> 500 \text{ km s}^{-1}$ are probably occurring in HzRGs (Bicknell et al., 2000), so it will be of great interest to compare the data with higher shock velocity models (Sutherland et al., in preparation). Preliminary results indicate that the existing models cannot be simply extrapolated (Allen, private communication). Moreover, the DS96 shock models have only been calculated for solar metallicities, which are unlikely to be correct in the extended emission line regions at the highest redshifts (§8.6.3 Binette et al., 2000). Lower metallicities will lead to less efficient cooling and raise the temperature in the precursor area, leading to stronger emission. We conclude that the present shock models can only reproduce the C II] vs. C III] ratio, but that extensions of the present models to higher shock velocities and lower metallicities will be needed to fully determine the importance of this ionization mechanism.

Pure photo-ionization

From the right panels in Figure 8.13, we find that pure photo-ionization provides good fits to the C IV/He II and C IV/C III] ratios, and a reasonable fit to the C III]/He II ratio, but fails to explain the C II]/C III] ratio. In the plots without C II] the majority of the data-points are bracketed by the models with power law spectral indices of the incident ionizing continuum of $\alpha = -1$ and $\alpha = -1.5$. In the plot involving C II] the $\alpha = -1$ model provides the least discrepant predictions. All plots suggest ionization parameters $-2.5 \lesssim \log_{10}(U) \lesssim -2$ for the $\alpha = -1$ models and $-2 \lesssim \log_{10}(U) \lesssim -1.5$ for the $\alpha = -1.5$ models.

The poor fit in the Carbon-only plot indicates that the different ionization stages of Carbon originate from distinct regions in the galaxies. The fact that the $A_{M/I}$

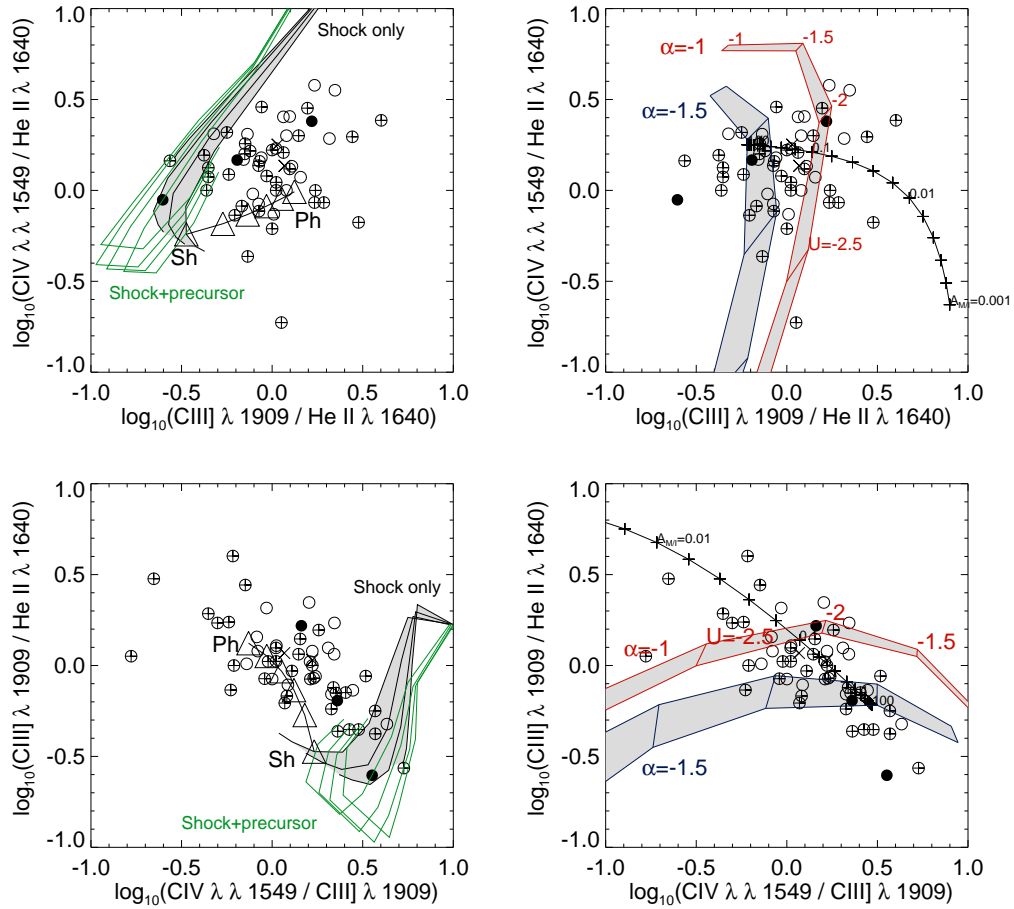


Figure 8.13: Line ratio diagnostic diagrams for C IV, He II, C III], and C II]. The left panels show the shock (shaded grid) and shock+precursor (unshaded grid) models. Shock velocity increases along the lines from 150 km s^{-1} at the top or right to 500 km s^{-1} at the end of the curves, which show four values of the magnetic parameter $0 < B/\sqrt{n} < 4 \mu\text{G cm}^{3/2}$. The sequence shown by open triangles represents a composite model of a pure shock model with $B/\sqrt{n} = 4 \mu\text{G cm}^{3/2}$, $v = 400 \text{ km s}^{-1}$ and a photo-ionization model with power-law spectral index $\alpha = -1.0$, hydrogen density $n = 100 \text{ cm}^{-2}$ and ionization parameter $\text{Log}_{10}(U) = -2.25$. The triangles represent different fractions of each model in steps of 20% (see text for details).

The right panels show the photo-ionization models. We show four photo-ionization sequences, with the values of $\text{log}_{10}(U)$ every 0.5 dex. The top shaded grid represents two models with power law spectral index $\alpha = -1$, the bottom grid models are for $\alpha = -1.5$. The boundaries of the shaded sequences are models for a hydrogen density $n = 100$ (left or bottom) and $n = 1000$ (top or right). The single curve is the $A_{M/I}$ sequence of B96, with values $0.01 < A_{M/I} < 100$ and tickmarks every 0.2 dex.

The data are repeated in both panels. Open circles represent sources at $z < 2$, circled + signs at $2 < z < 3$, and filled circles at $z > 3$. The asterisks represent the two nearby Seyfert galaxies observed by Evans et al. (1999).

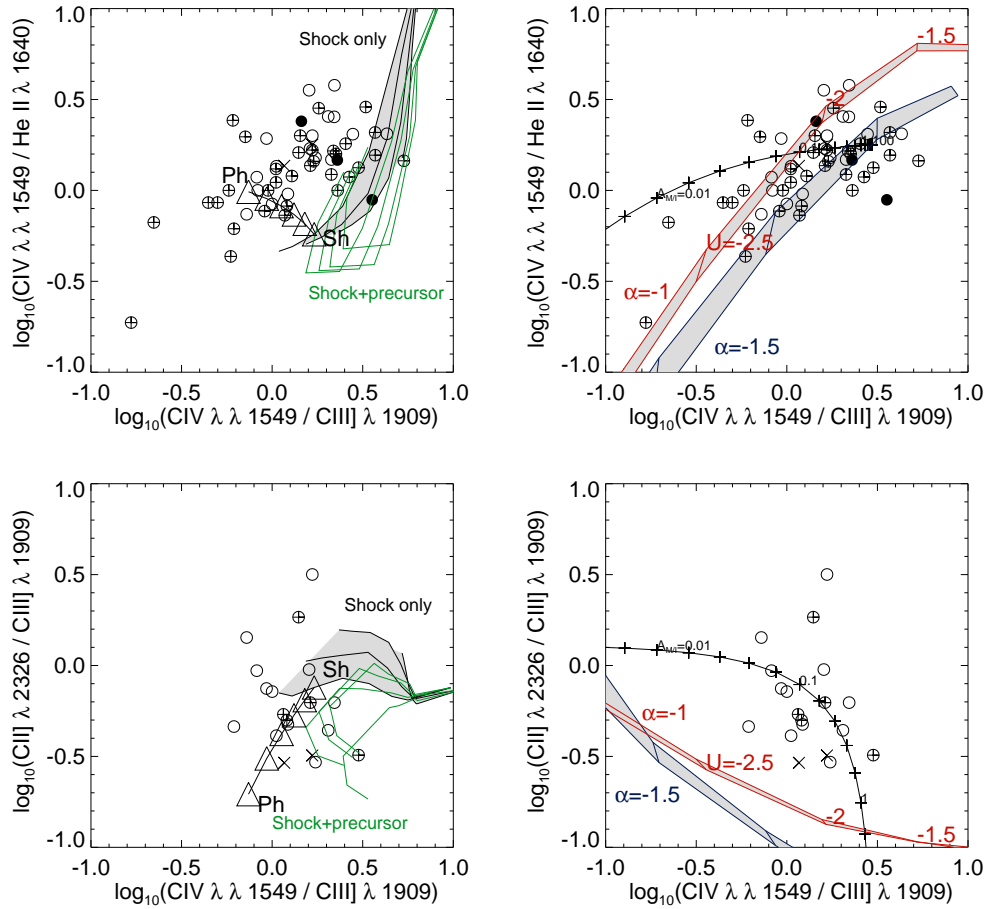


Figure 8.13: continued.

sequence provides the best fit in this diagram (see below) is consistent with this idea, as in this model we observe simultaneously emission from clouds with different incident ionizing radiation. We return to this in §8.6.1.

$A_{M/I}$ sequence

The predictions for the $A_{M/I}$ sequence in the models of B96 provide good fits to the data, but fails to reproduce the sometimes large spread of the points. This could be solved by changing the dust content, metallicity, spectral index or ionization parameter U_{MB} of the ionizing continuum incident on the matter-bound clouds,

or by internal reddening⁶. A value of $A_{M/I} \sim 0.1$ seems to best fit the data in all four diagrams, although the scatter ranges from $A_{M/I} \sim 0.02$ to $A_{M/I} \gtrsim 100$. A value of $A_{M/I} \sim 0.1$ means that as much as 90% of the matter-bounded clouds has to be obscured along the line of sight. In low redshift Seyferts, B96 and Evans et al. (1999) found values of $A_{M/I}$ slightly higher than unity provided the best fit to the data. If the $A_{M/I}$ sequence is the correct ionization mechanism model, the matter-bounded clouds would be much more obscured at higher redshift, or more obscured in radio galaxies than in Seyferts.

A possible way to obscure these regions could be preferential obscuration by dust. Dust masses up to $10^9 M_{\odot}$ have been detected in HzRGs (e.g., Archibald et al., 2000). If these large amounts of dust are located near the central parts of HzRGs, they could lead to obscuration of either the matter-bounded or ionization-bounded clouds. There are six radio galaxies in our sample with solid submm detections which also have published C IV, He II and C III] measurements (4C41.17, Chini & Krügel 1994, Dunlop et al. 1994; MG J1019+0534, Cimatti et al. 1998a; 4C24.28, 4C28.58 and 4C48.48, Archibald et al. 2000; TN J0121+1320, Reuland et al., in preparation). These six sources are not preferentially located in any part of the diagrams, and do not fall in the low $A_{M/I}$ region. We conclude that dust obscuration of the matter-bounded clouds is an unlikely explanation of the very low $A_{M/I}$ values. A variation of the $A_{M/I}$ sequence by changing the ionization parameter or power law spectral index incident on the matter-bounded clouds would be required to explain the high obscuration of the matter-bounded clouds and the observed scatter with these models.

Summary of comparison with the data

To summarize, we find that using only the line-ratio diagrams involving C IV, He II, and C III], the pure photo-ionization models provide the best fit to the HzRG data, but these models clearly fail to reproduce the observed C II]/ C III] ratio, which can be well fit by high shock velocity models. The models that use a combination of matter-bounded and ionization-bounded clouds seem to provide a reasonable fit to all four lines, but the spread of the points does not seem to follow the $A_{M/I}$ sequence, and suggests other parameters dominate the intrinsic differences in the ionization levels of the individual HzRGs. However, the combination of at least two zones with different ionization continua seems to be required to explain the emission line ratios in C IV, He II, C III], and C II].

In the remainder of this section, we shall compare these model predictions with some less commonly used emission line ratios. In §8.6.1, we shall return to the multiple zone ionization mechanisms.

⁶Galactic reddening will be negligible because most HzRGs have been identified from samples avoiding the Galactic plane, and some of the spectra in the literature have been corrected for reddening.

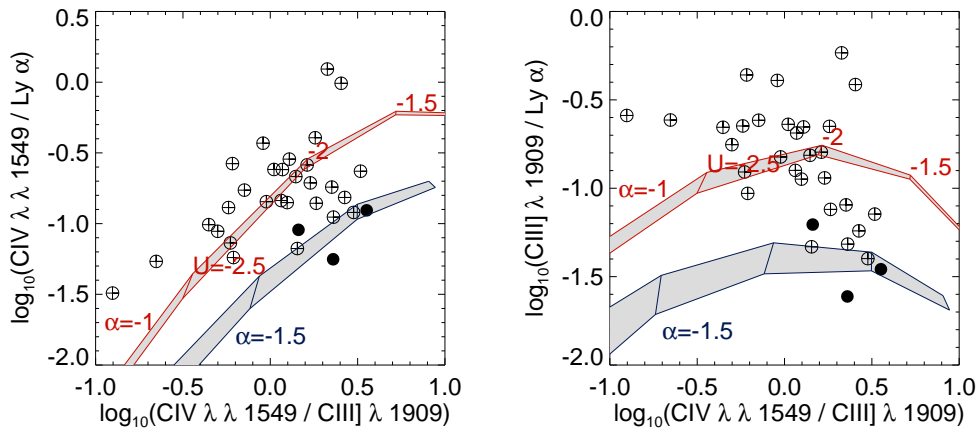


Figure 8.14: Line ratio diagnostic diagrams for Ly α , C IV and C III]. Models are as in Figure 8.13. Note the systematical over-luminosity of Ly α at $z > 3$ (filled circles).

8.5.4 Diagnostic diagrams with Ly α

In almost all HzRGs, the brightest UV line is Ly α . This line has not been frequently used in diagnostic line-ratio diagrams, because it is highly sensitive to resonance scattering inside and around the excited clouds, and to absorption by dust.

Villar-Martín, Binette & Fosbury (1996) have examined the effects of resonance scattering and dust on UV lines in HzRG. They found that cases where the Ly α emission is weak relative to the other UV lines can better be explained by geometrical (viewing angle) effects rather than by large amounts of dust, which would also affect the other UV lines, notably C IV. Another factor affecting the total flux in Ly α is absorption by associated HI. In §8.3.2.2, we saw that this HI absorption will reduce the total flux of the Ly α line by no more than 60%, which in most cases will not completely destroy the diagnostic value of the Ly α flux for line ratios. In this section, we shall therefore first compare the observed ratios involving Ly α with the values of the photo-ionization models found from the other UV lines, and then consider the geometrical and dust effects.

Figure 8.14 presents two diagnostic diagrams with line-ratios of Ly α , C IV, and C III]. We find that the simple photo-ionization model with a power law spectral index $\alpha = -1$ provides a good fit to the data in both diagrams. The range of the ionization parameter $-2.5 < \log_{10}(U) < -2$ is consistent with the values found from the diagrams in Fig. 8.13. Contrary to the diagrams in Fig. 8.13, the $\alpha = -1.5$ models do not provide a good fit to the data, because they overestimate the Ly α flux. This might be due to geometrical effects: changing the viewing angle from front to back illuminated Ly α can increase the C IV/Ly α ratio by almost an order of magnitude (see Fig. 7 of

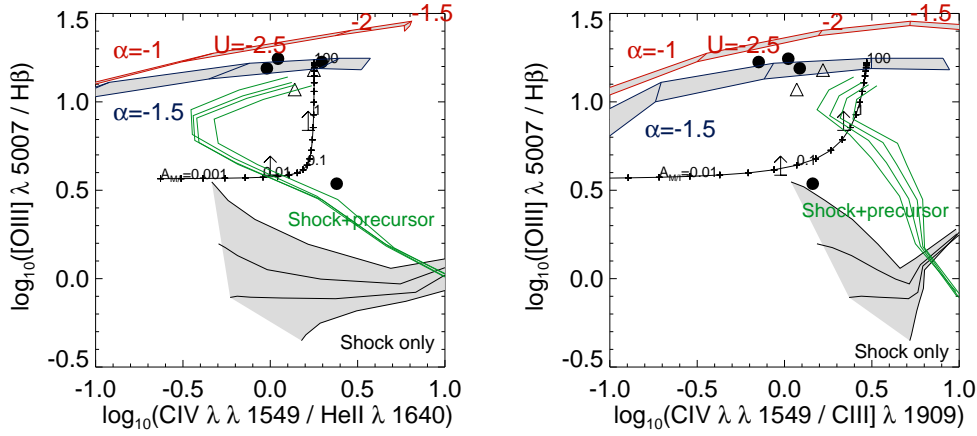


Figure 8.15: Optical-UV line ratio diagnostic diagrams. Dots and lower limits are HzRG data, and open triangles are the Seyfert galaxies NGC 5643 and NGC 5728 (Evans et al., 1999). Models are as in Figure 8.13.

Villar-Martín et al.(1996). We therefore do not take this better fit as evidence for a flatter spectral index of the incident ionizing continuum.

Some individual HzRGs have highly discrepant $\text{Ly}\alpha/\text{C IV}$ and $\text{Ly}\alpha/\text{C III]$ ratios. Both under- and over-luminous $\text{Ly}\alpha$ occurs. Dust extinction has been proposed as an explanation for under-luminous $\text{Ly}\alpha$ in the two most discrepant objects in our HzRG sample, TX 0211–122 at $z = 2.34$ (van Ojik et al., 1994) and MG J1019+0534 at $z = 2.765$ (Dey, Spinrad & Dickinson, 1995; Cimatti et al., 1998a). The $\text{Ly}\alpha$ in these objects is a factor of ~ 3 lower compared to the best fitting photo-ionization models and the bulk of the other HzRGs. However, in two objects with equally large amounts of dust, 4C 41.17 at $z = 3.8$ and TN J0121+1320 at $z = 3.516$, the $\text{Ly}\alpha$ is a factor ~ 3 brighter than the models and the mean of the other HzRGs. TN J0205+2242 at $z = 3.506$ does not have a large dust mass detected, while it is also $\sim 4\times$ over-luminous in $\text{Ly}\alpha$. We conclude that there is no strong correlation between the detection of a large global dust mass and an anomalously low $\text{Ly}\alpha$ flux. If dust obscuration is an important process in suppressing the $\text{Ly}\alpha$ luminosity, it would have to be a localized process, but this would be hard to achieve, given the large extent of the $\text{Ly}\alpha$ emission. High resolution $\text{Ly}\alpha$ imaging, combined with sensitive imaging of the IR-dust emission (with ALMA) would be needed to examine this in more detail. Metallicity differences and geometrical effects probably play a more important role than dust obscuration in the destruction of $\text{Ly}\alpha$. The most remarkable observation from Figure 8.14 is that three of the seven HzRGs with over-luminous $\text{Ly}\alpha$ in the $\text{C III]}/\text{Ly}\alpha$ versus $\text{C IV}/\text{C III]$ plot are at $z > 3$. We shall return to this in §8.6.3.

8.5.5 UV-optical diagnostic diagrams

In HzRGs, the rest-frame optical emission lines which are commonly used in line ratio diagnostic diagrams at low redshift, are redshifted into the near-IR. It has been a big technological challenge to obtain near-IR spectra of HzRGs with 2-4m telescopes, but recently, near-IR spectroscopy of HzRGs has become feasible with the advent of efficient near-IR spectrographs on 8-10m class telescopes (e.g., Larkin et al., 2000). It is to be expected that more near-IR spectroscopy of HzRGs will be available soon. To date, a total of 15 $z > 2$ radio galaxies have published near-IR spectra obtained with the 3.8m UKIRT and 2.2m UH telescopes (Eales & Rawlings, 1993; Iwamuro et al., 1996; Evans, 1998), and recently the first near-IR spectrum obtained with NIRSPEC at Keck was published (Larkin et al., 2000). As shown by ADT98, a diagnostic diagram of the optical [O III] to $H\beta$ versus the UV C IV/He II or C IV/C III] line ratios can separate the shock and shock+precursor models. Such diagrams have the added advantage that they are relatively insensitive to the effects of dust extinction, as the ratios are determined from lines close in wavelength. In four objects (3C 256, MRC 2025-218, 4C 40.36 and 4C 41.17), $H\beta$ was detected as well as [O III], and two more objects (USS 0828+193 and 4C 48.48) have lower limits to the [O III] to $H\beta$ ratio. The uncertainties in these points will be higher than in the optical spectroscopy because of the low signal-to-noise ratio and resolution of the near-IR spectroscopy.

Figure 8.15 reproduces the line-ratio diagrams from ADT98 with the five HzRG data points added. We also compare the HzRG data with combined HST and ground-based spectroscopy of two low-redshift Seyferts (Evans et al., 1999). The most firm conclusion from Figure 8.15 is the exclusion of the pure shock models. Only 4C 41.17 falls in a region of the plot that cannot be explained by pure photo-ionization models, but the $H\beta$ detection is marginal (Eales & Rawlings, 1993). The other detection and the lower limits are consistent with the Seyfert points, and fall in a region where the simple photo-ionization models overlap with the highest values of the $A_{M/I}$ sequence and the high shock velocities of the shock+precursor models. A comparison with the range of parameter values of the UV diagnostic diagrams suggests that the simple photo-ionization models have more consistent values than the $A_{M/I}$ sequence, because the weak $H\beta$, if confirmed by higher S/N observations, requires a higher fraction of matter-bounded clouds than the UV diagrams suggest. Alternatively, the highest shock velocity (500 km s^{-1}) predictions of the shock+precursor models can also explain most of the points in Figure 8.15. This again would require an extension of these models to higher shock velocities to fully examine the importance of this ionization mechanism in HzRGs.

To summarize, the comparison of the UV and optical line-ratios excludes the pure shock models, and is consistent with the high shock velocity shock+precursor models and the high values of the $A_{M/I}$ sequence. Pure photo-ionization models with a power-law spectral index $\alpha = -1$ and ionization parameter $U \sim 0.01$ seem to provide the most consistent fit to HzRG spectra. Future near-IR spectroscopy of HzRGs will be required to differentiate more unambiguously between these models.

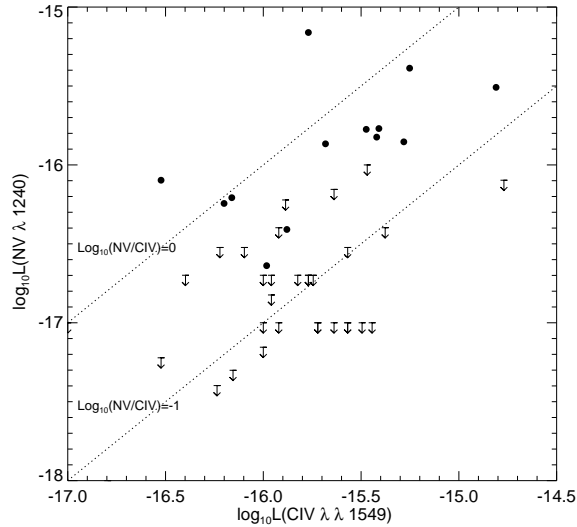


Figure 8.16: N V/ flux plotted C IV flux. The diagonal lines indicate constant N V/C IV ratios. Note that there is no strong clustering of the upper limits at high or low C IV fluxes, which would lead to an artificial correlation in the N V/C IV ratios.

8.5.6 Nitrogen overabundance

In the majority of HzRGs, the N V line was not detected. There are, however, several exceptions where N V is strong, and even a few cases where it is as bright as Ly α (e.g., van Ojik et al., 1994). Neither shock ionization nor variations of the densities or ionization parameters in the photo-ionization models are able to produce such strong N V emission (Villar-Martín et al., 1999c). The most likely explanation is that N V is over-abundant compared to the other species in HzRGs (van Ojik et al., 1994). Fosbury et al. (1998, 1999) found that HzRGs follow a close correlation in a N V/He II vs. N V/C IV diagram which is parallel to the relation defined by the broad line regions of quasars (Hamann & Ferland, 1993). These authors showed that this sequence can be explained by a large variation of the metallicity (from $Z \sim Z_{\odot}$ to $Z \gtrsim 10Z_{\odot}$) caused by rapid chemical evolution in a stellar population composed of massive stars. The parallel sequence defined by the extended emission line regions in HzRGs suggests that we also observe such a metallicity variation on much larger scales than the small central broad line region (Fosbury et al., 1999). Vernet et al. (1999) found that the radio galaxy sequence is best modeled with a metallicity sequence in which the nitrogen abundance increases quadratically, while the other elements increase linearly.

Figure 8.17 presents the N V/He II vs. N V/C IV diagram with all the points from

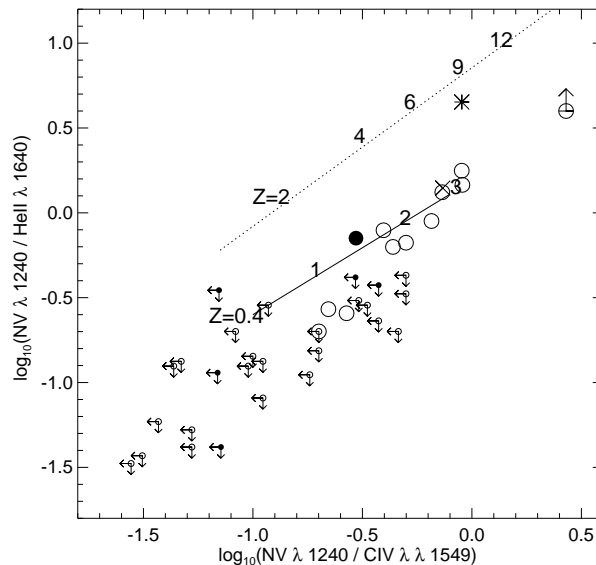


Figure 8.17: N V/He II vs. N V/C IV. Radio galaxies at $z < 3$ and $z > 3$ are represented with open and filled symbols, respectively. The dotted line represents the metallicity sequence defined by quasars (Hamann & Ferland, 1993), with the numbers along the line representing the metallicity in solar units. The solid line represents a metallicity sequence with quadratic N enhancement ($U=0.035$, power law spectral index $\alpha = -1.0$) from Vernet et al. (1999). The starburst galaxy IRAS F10214+4724 (Serjeant et al., 1998) is indicated with a cross and the hyper-luminous, gravitationally lensed object SMM J02399-0136 (Villar-Martín et al., 1999c) is indicated by a star. Note that the $z > 3$ objects seem to fall preferentially in the low metallicity region of the sequence.

our HzRG sample, of which two thirds have only upper limits for N V. The inclusion of such a large number of upper limits could lead to redshift selection effects. We believe this is a major problem in our sample, as N V is only observable over a limited redshift interval ($z \gtrsim 2$), and the highest redshift objects have been observed longer or with larger aperture telescopes. This is also obvious in the flux-flux diagram of the N V and C IV lines, which shows a constant spread of the detections and upper limits on C IV flux.

Using survival analysis, we find that the probability that the N V/C IV and N V/He II ratios are correlated with redshift is $< 35\%$, while the ratios are strongly correlated with each other (the generalized Spearman rank correlation coefficient is $r = 0.95$, significance level $> 99.99\%$). The extension of the radio galaxy sequence to both sides in Fig. 8.17 suggests that the nitrogen abundance shows an even larger variation than the $Z = 0.4Z_{\odot}$ to $Z = 3Z_{\odot}$ sequence proposed by Vernet. The most extreme source

in our sample is TXS J2353–0002 (Chapter 4), which has N V emission that is more than twice as luminous as C IV and undetected He II emission, at least four times weaker than N V.

Eventhough there is no statistical significance for a correlation between the N V/C IV ratio and redshift within the $2 \lesssim z \lesssim 4.4$ redshift interval we can observe both these lines, it is clear from Figure 8.17 that none of the $z > 3$ radio galaxies occupy the high metallicity end of the diagram. Moreover, the limits from the VLT and Keck spectra on the N V of TN J1338–1942 at $z = 4.11$ and 6C 0140+326 at $z = 4.41$ are quite strong (N V/C IV < 0.07), and suggest the $z > 4$ galaxies have even lower metallicities. It appears that the metallicities in the extended emission line regions of HzRGs show large variations, from values well below solar to several times solar. The highest metallicities only occur in $z \lesssim 3$ radio galaxies, while the most distant objects generally have sub-solar metallicities.

8.6 Discussion

8.6.1 Simultaneous shock and photo-ionization

From the diagnostic diagrams of the UV line ratios, and the combined UV and optical line ratios in §8.5, we found that the line-ratios involving C IV, He II, and C III] can best be explained by photo-ionization models, whilst the C II] to C III] ratio is better fitted by shock models with high shock velocities. Models that invoke a variation in the ratio of matter-bounded and ionization-bounded clouds provide a more consistent fit to all the UV line-ratios, although the large scatter of the data around the model predictions does not appear to follow the $A_{M/I}$ sequence.

We find that within the ranges of emission line fluxes measured in our HzRG sample, neither redshift, nor radio luminosity are important causes of this scatter. The radio size D also does not appear to influence the emission lines, with the notable exception of the C II]/C III] ratio. This was interpreted by BRL00 in a C II]/C III] versus [Ne III] λ 3869/[Ne V] λ 3426 diagram as evidence that the ionization mechanism in smaller radio sources is shocks, while the larger sources are photo-ionized. However, the only object from their sample that also has a published C IV flux, 3C 324, lies in the shock+precursor region in their diagram, but cannot be explained by any of the shock models in our diagrams involving the C IV, He II, and C III] lines (Fig. 8.13). The fluxes of these three lines in 3C 324 are very similar, putting the object consistently on the photo-ionization sequence with $\alpha = -1.0$, and $\log_{10} U \approx -2.2$ in all three plots involving these lines.

We interpret this apparent inconsistency as an indication that the integrated spectra of this, and most likely also other HzRGs, are a composite of differently ionized areas. The lower ionization state C II] line is much more sensitive to shock ionization than the other UV lines: in the shock ionization models of DS96, the C II] flux is similar to the C III] flux, while in the pure photo-ionization models, C II] is $\sim 5\times$ weaker than

C III]. An increasingly more dominant shock-ionized area will thus manifest itself first through brighter low-excitation lines such as C II]. We can now also understand why the $A_{M/I}$ sequence provides a much better fit to the Carbon-only plot than the pure photo-ionization models: from Table 2 of B96, we find that $25\times$ more C II] is produced in the matter-bounded clouds than in the ionization-bounded clouds; the addition of the ionization-bounded clouds could mimic the addition of a more dominant shock component.

To examine this idea of a mixture of shock and photo-ionized gas in the integrated spectra in more detail, we have over-plotted a sequence of the fraction of shock to photo-ionization on the line-ratio diagrams in Figure 8.13. We picked the pure photo-ionization model with $n = 100 \text{ cm}^{-3}$, $\alpha = -1.0$ and $\log U = -2.25$, and added a contribution of the shock model with $v = 400 \text{ km s}^{-1}$ and $B/\sqrt{n} = 4\mu\text{G cm}^{3/2}$ in steps of 20%. This approach is likely to be a serious oversimplification, because we expect a range of parameters for both photo-ionization and shock models, but it might be a reasonable approach in a single object, such as 3C 324. A 40% shock contribution, in this object would provide an excellent fit in the Carbon-only plot, while it will not shift the predicted ratios in the other diagrams by as much. The C II]/C III] and C III]/He II ratios show the largest variation when the fraction of shock ionization is increased, with the C II] flux increasing faster towards the shock models than the He II flux. A varying shock contribution might well explain some of the scatter observed in the diagrams of Figure 8.13. Assuming that the $\alpha = -1.0$ pure photo-ionization sequence is the most representative, the scatter in all diagrams always seems to fall along the side of the sequence pointing towards the (high shock velocity) shock models. Because the C II] line is the most sensitive to shock ionization, most points in the Carbon-only plot do not fall on the photo-ionization sequence, but closer to the shock models.

Another effect which could raise the C II]/C III] ratio is differential extinction. For a single, central photo-ionizing source (the AGN), the ionization parameter U of a cloud located closer to the source will be higher than for the same cloud located further out. If the higher excitation photo-ionized gas is more centrally located than the lower excitation gas, it will be more subject to extinction. However, the C II]/C III] ratio is not very sensitive to changes in the ionization parameter U for an ionizing continuum with an $\alpha = -1.0$ power law spectrum. For example, to change the ionization parameter from $\log U = -2.0$ to $\log U = -2.5$ we need to move three times further out from the AGN, while the C II]/C III] ratio only changes by a factor of two. We consider it very unlikely that this effect can be dominant, and so we neglect it.

The above findings could undermine the diagnostic value of the different line-ratio diagrams. If the integrated HzRG spectra are a composite of different regions, we should not necessarily try to fit all lines with a single model. Photo-ionization remains the main process in HzRGs, but using only high excitation lines, we cannot exclude shock ionization, like VM97 and ADT98 did. The high excitation diagrams, which include lines that are insensitive to shock ionization, can be used to determine the

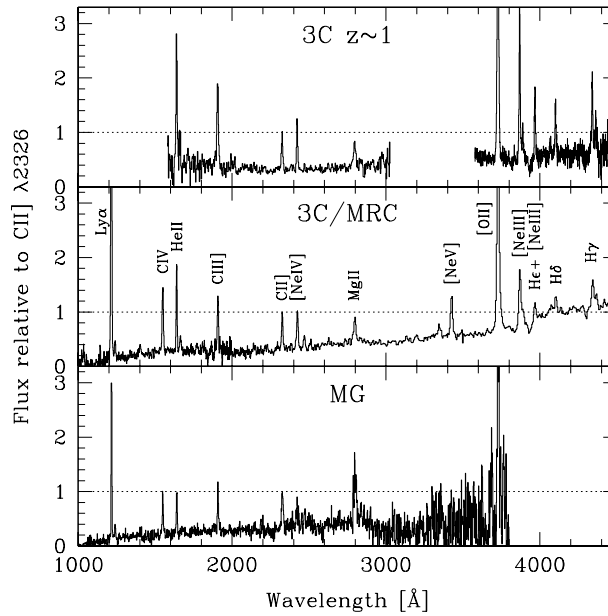


Figure 8.18: Composite spectra from 3C sources at $z \sim 1$ (Best, Röttgering & Longair, 2000a), the 3C and MRC samples (McCarthy & Lawrence, 2000) and the MG (Stern et al., 1999a). All spectra have been normalized to the C II] λ 2326 line. The 3C galaxies in the top panel have the largest radio sizes, while the MG galaxies in the bottom panel the have smallest. This is clearly reflected in the dominance of the C II] line compared to the C IV, He II and C III] lines.

best fitting parameters of the photo-ionization model, which can then subsequently be used in the diagram which include lines that are more sensitive to shock ionization, such as C II], to estimate the relative contribution of shock ionization.

The study of BRL00 has shown that significant shock contributions only occur in sources with radio sizes $\lesssim 150$ kpc. Because only 15% of the $z > 2$ galaxies in our HzRG sample have radio sizes > 150 kpc (and only 6% > 200 kpc), the contribution of shock ionization in HzRGs might well be important. There is also further kinematical and morphological evidence for the presence of shocks in HzRGs. At relatively low redshifts ($z \lesssim 1$), the line widths in radio galaxies are $\lesssim 500$ km s $^{-1}$ and can also be explained by gravitational origins (Baum & McCarthy, 2000). However, at $z \gtrsim 2$, the line widths of the UV lines are ~ 1500 km s $^{-1}$, which is more easily explained by acceleration due to the passage of a bow shock associated with the expansion of the radio source, although different processes might also play a role, such as (i) infall of material from large distances, (ii) large scale outflows of companion Lyman break galaxies, or (iii) bipolar outflows produced by super-winds (Villar-Martín, Binette & Fosbury, 1999a). In some objects at low redshift (e.g., van Breugel et al., 1985;

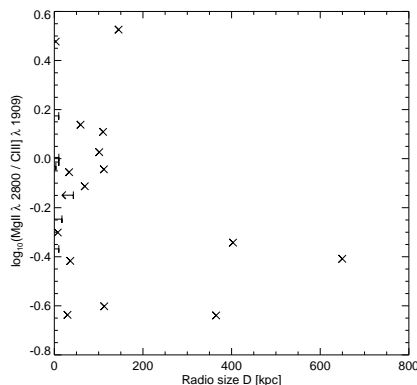


Figure 8.19: The Mg II/C III] ratio plotted versus radio size. Note the absence of large sources with strong Mg II.

Villar-Martín et al., 1999b) and at high redshift (Bicknell et al., 2000), there is also morphological evidence for the interaction of the radio jet with the ambient gas.

The presence of a significant percentage of shock ionized gas in the integrated spectra of HzRGs would explain the poor fit of the pure photo-ionization models to the C II]/C III] ratio (Fig. 8.13). Because of the lack of sources with radio sizes >150 kpc, we do not find a population of pure photo-ionization sources like BRL00 do. The radio size - ionization mechanism relation can also explain the different line ratios in three published composites of HzRGs (Fig. 8.18). The MG sample of S99, which has an angular size cutoff $\theta < 10''$, contains more sources with relatively strong C II] lines. The C II]/C III] ratio in the MG composite spectrum of S99 is $1.6\times$ stronger than the ratio in the 3C/MRC composite of McCarthy & Lawrence (2000), which does not have an explicit angular size cutoff. This can be easily interpreted if the MG sample contains more sources with important contributions of shock ionization. On the other end, a composite spectrum of 14 3CR galaxies at $0.7 < z < 1.25$ (Best, Röttgering & Longair, 2000a) contains more larger radio sources, and should therefore be the most representative composite of the photo-ionization in HzRGs, at least at $z \sim 1$. The C II]/C III] ratio in this composite is 0.3, which is indeed much closer to the pure photo-ionization models.

We can also use Fig. 8.18 to identify other emission lines that could be sensitive to shock ionization. The only obvious candidate line is Mg II, which has a constant ratio compared to C II] in the 3C($z \sim 1$) and 3C/MRC composites, and is very bright in the MG composite. However, the high luminosity in the MG composite is most likely due to the high selection frequency of the MG survey (5 GHz). At such frequencies, the sources will be more dominated by the flat spectrum radio core, and they will appear more like quasars, which have more prominent Mg II lines than radio galaxies, while their C II] lines is five times weaker than Mg II (see e.g., Boyle, 1990). Indeed, S99 showed that the Mg II/C III] ratio in the MG composite is similar to those in

quasar composites, and deep spectro-polarimetric observations of radio galaxies and ultra-luminous IR galaxies have revealed a scattered broad Mg II component (Tran et al., 1998, 2000).

The plot of the Mg II/C III] ratio versus radio size D in our sample (Fig. 8.19) looks remarkably similar to the C II]/C III] versus D plot (Fig. 8.12). The highest shock velocity models of DS96 indeed predict Mg II to be twice as strong as C III], while in a pure photo-ionization model with $n = 100 \text{ cm}^{-3}$, $\alpha = -1.0$ and $\log U = -2.25$, Mg II would be twice as faint as C III]. We can therefore also use the Mg II line to identify a strong shock contribution to the integrated HzRG spectrum, but should be aware that this line is much more subject to small contributions from obscured broad line regions than C II].

8.6.2 Emission-line luminosity - radio power correlations

In the previous section, we argued that the ionization mechanism in HzRGs is a composite of nuclear photo-ionization and shock ionization dominating the lower ionization lines. Both these processes are likely to be linked to the power of the central engine. To examine this dependence, we shall now consider the relation between the radio power and the emission line luminosity of the shock and photo-ionization sensitive lines.

In §8.4.6.2, we found that the UV line luminosities are weakly correlated with the radio power over ~ 2 orders of magnitude, with the strongest results for the C II] and Ly α luminosity. This should be compared with the strong correlation between the H α + [NII] or [O II] luminosity and radio power, which extends over nearly five orders of magnitude in radio power (e.g., Baum & Heckman, 1989; Rawlings & Saunders, 1991; McCarthy, 1993; Willott et al., 1999). This relation has prompted these authors to suggest a common energy source (the AGN) for the *total* emission line luminosity and radio power. To calculate the total line luminosity, they have taken the flux in one or two of the brightest lines (Ly α , [O II], [O III] or H α) and calculated the flux in the other lines using fixed line ratios. In HzRGs, the brightest line is Ly α , which can represent up to 1/3 of the total narrow line luminosity (assuming the line ratio from the composite of McCarthy 1993). We can thus use Ly α to calculate the total line luminosity, but this line has the disadvantage that it is highly influenced by resonant scattering and geometrical effects (e.g., Villar-Martín, Binette & Fosbury, 1996), which will cause the total line flux to be underestimated by a varying amount. The weaker correlation with the fainter high ionization lines can be explained by measurement errors and an intrinsic scatter caused by differences in the relation due to different accretion rates, environmental effects, or time variability of the AGN which reaches the narrow-line regions and radio lobes at different times (see Willott et al. 1999 for a detailed discussion).

The fact that the radio power does not correlate with the line ratios (Table 8.5), but does correlate with the individual UV lines, suggests that in the majority of HzRGs, the total emission line luminosity is dominated by one of the ionization processes

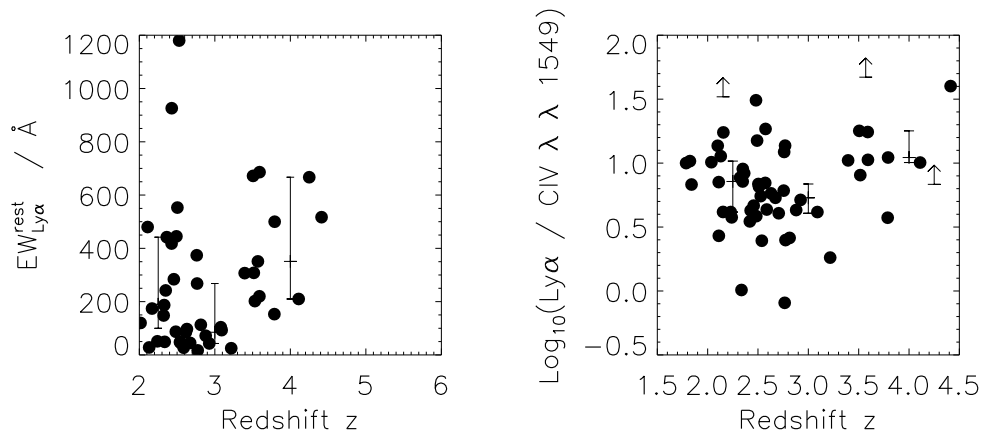


Figure 8.20: $\text{Ly}\alpha$ equivalent width (left panel) and $\text{Ly}\alpha/\text{C IV}$ ratio (right panel) as a function of redshift. Overplotted in each plot are three bins in redshift: $z < 2.5$, $2.5 < z < 3.5$, and $z > 3.5$. The tickmarks on each bin are the 25 percentile level, median and 75 percentile levels. Note that the $z > 3.5$ bin is always higher than the lower redshift bins, suggesting a higher $\text{Ly}\alpha$ flux at the highest redshifts.

(shocks or AGN photo-ionization), and this process has a common energy source with the radio power. Alternatively, it is possible that both mechanisms depend equally strong on radio power.

It is remarkable that the shock ionization dominated C II] line luminosity has the strongest correlation with radio power (see Table 8.3). This suggests that in more luminous radio sources, the shock ionized regions become more prominent. However, the range in radio power in our HzRG sample is still limited, and deeper spectra of less radio-luminous radio galaxies are needed to confirm this trend.

8.6.3 The independent behavior of $\text{Ly}\alpha$

In §8.5.4, we found that radio galaxies with relatively over-luminous $\text{Ly}\alpha$ emission occur more often at $z > 3$ than at lower redshifts. The correlation over the entire redshift range $2.0 < z < 4.4$ is not very strong, and from Table 8.5, we find that it is not stronger than the correlation with radio size or radio power. However, the rest-frame $\text{Ly}\alpha$ equivalent width also increases at $z \gtrsim 3$. Figure 8.20 plots the relative intensity of $\text{Ly}\alpha$ compared with the continuum (\equiv equivalent width; this measure takes some account of absorption by dust), and with C IV. We find that at $z \gtrsim 3$, $\text{Ly}\alpha$ is roughly twice as strong compared to both the continuum and C IV than at $z \lesssim 3$. We see similar trends in the ratios with He II and C III], but we have too few data points to make a significant claim. This effect cannot be entirely due to selection effects, as HzRGs with weaker $\text{Ly}\alpha$ could still have been detected (see Figure 8.7).

We interpret the over-luminous $\text{Ly}\alpha$ as spectroscopic evidence for the youth of radio

galaxies at $z \gtrsim 3$. At these redshifts, the radio sources found from flux density-limited surveys are inevitably young (Blundell & Rawlings, 1999b). It is therefore conceivable that they are still surrounded by large halos of primordial hydrogen from which the galaxy is formed and which trace the over-dense region that harbours the AGN. The Ly α halos at $z \gtrsim 3$ are often very extended (e.g., van Ojik et al., 1996), so we may be witnessing the first epoch of star formation in primordial material. The very frequent occurrence of large amounts of HI absorption in the Ly α profiles of the highest redshift radio galaxies (§8.4.6.3) also indicates a larger amount of HI surrounding the radio galaxy. As such, the lower abundance of helium and metals at $z \gtrsim 3$ suggests metallicity evolution with redshift in forming massive galaxies. This would be consistent with our findings on the metallicity derived from the N V/C IV ratio (§8.5.6) and the recent results of Binette et al. (2000), who found strong evidence from co-spatial Ly α and C IV associated absorption that the material in the outer halo must have a much lower metallicity ($Z \sim 0.01Z_{\odot}$) than the more centrally located emitting material.

At $z \lesssim 3$, the radio galaxies become more relaxed, and even the outer parts have experienced chemical enrichment through massive starbursts caused by the infall of the surrounding material on the central (proto-)galaxy, or by the passage of the radio jets. This picture is consistent with the change in rest-frame optical morphology seen in a sample of HzRGs observed in K -band by van Breugel et al. (1998). At $z \gtrsim 3$, their morphologies are clumpy and radio-aligned, while at $z \lesssim 3$, they often have well organized elliptical profiles, much like their low redshift counterparts.

8.7 Conclusions

We have compiled a sample of 165 HzRG, half of which are at $z > 2$. From this sample, we have shown that:

- The different UV line luminosities and equivalent widths are strongly correlated, indicating that the narrow line region gets most of its energy from a common energy source. The UV line luminosities also appear to be correlated with radio power, suggesting a common energy source and either a dominating ionization mechanism or two mechanisms that increase equivalently with radio power. However, the shock ionization sensitive C II] line appears to be more strongly correlated than the photo-ionization dominated lines, suggesting the more powerful radio sources can ionize a larger amount of gas by means of shock ionization.
- Using the systematic redshift determined from the He II line, we introduce a parameter $A_{\text{Ly}\alpha}$ measuring the asymmetry in the Ly α emission line due to HI absorption. We find that the absorption occurs most frequently at the blue side, and mainly in sources with smaller radio sizes and at higher redshift. The higher HI absorption could trace a denser surrounding medium which can confine the radio source more (van Ojik et al., 1997), or it could reveal an low density region that has not yet been pressurized by the passage of a radio jet (Binette et al., 2000).

- We confirm the results from Fosbury et al. (1998, 1999), who found that HzRGs occupy a sequence in a N V/C IV vs. N V/He II diagram which is parallel to the metallicity sequence defined by the BLR in quasars. The inclusion of upper limits to the N V flux further extends this sequence to much lower metallicities. The $z > 3$ objects occupy the lower metallicity part of this sequence.
- For $z \gtrsim 3$, Ly α becomes over-luminous with respect to both the continuum and the other emission lines. We interpret this as indicating an increasing hydrogen abundance with redshift and evidence that the highest redshift radio galaxies tend to be in an earlier stage of their formation epoch, still surrounded by the reservoir of primordial hydrogen from which the galaxy is forming.
- Pure photo-ionization models with an ionizing continuum of power law spectral index -1.0 provide better fits to the line ratios involving C IV, He II, and C III] than shock models, but cannot explain the C II]/C III] ratio. A combination of shock and photo-ionization in the integrated HzRG spectra can better explain the observed ratios, because the C II] line is $\sim 5\times$ more sensitive to shocks than photo-ionization. Such a shock ionization component will not be seen in high excitation line ratios, where the photo-ionization will dominate. Diagnostic line-ratio diagrams consisting of only high excitation lines will therefore fail to detect contributions of shock ionization.
- The UV line ratios are not correlated with redshift, radio size, or radio power, with one exception: high C II]/C III] ratios only occur in small radio sources ($\lesssim 150$ kpc). This confirms the results of BRL00, who found that the high C II]/C III] ratios can be explained by shock ionization, but occur only in small radio sources, where the radio size is comparable to the extent of the emission lines regions. The C II]/C III] ratio in HzRGs requires the addition of a component of shock ionized gas to the integrated HzRG spectra. This is consistent with the generally small radio sizes and high line widths observed. A composite spectrum of HzRGs with small radio sizes (MG) indeed shows a higher contribution of lines sensitive to shock ionization (C II], Mg II) than composites based on larger radio sources (3C, MRC).
- Within the shock ionization models, the highest shock velocity models provide the best fit to the HzRG spectra. An expansion of these models to higher shock velocities and lower metallicities is needed to determine the full contribution of shock ionization to the integrated HzRG spectra.

Acknowledgements

We thank Daniel Stern for providing electronic versions of the MG spectra, and Pat McCarthy for allowing us to use the 3C/MRC composite spectrum. We also thank Mark Allen, Montse Villar-Martín, and Emmanuel Moy for useful discussions. The work by C.D.B. and W.v.B. at IGPP/LLNL was performed under the auspices of the US Department of Energy by University of California Lawrence Livermore National Laboratory under contract W-7405-ENG-48. This work was supported in part by the Formation and Evolution of Galaxies network set up by the European Commission under contract ERB FMRX-CT96-086 of its TMR programme.

Appendix A Radio galaxy sample

Table 8.A: Radio galaxy sample

Source	z	LAS ^a	Q ^b	Log(F_{395}) erg/s/Hz	Log(F_{1400}) erg/s/Hz	$A_{Ly\alpha}^c$	Ly α	N V	Line Flux 10^{-16} erg/cm ² /s			C II]	Ref.
									C IV	He II	C III]		
USS 0003-019	1.541	3.3	...	35.23	34.48	5.90	3.90	3.40	1.00	DB
BRL 0016-129	1.589	3.5	...	36.09	35.51	1.60	...	2.60	1.20	BRL
MG 0018+0940	1.586	<1.2	...	35.36	34.84	0.81	0.42	0.87	0.65	Ste
MRC 0030-219	2.168	<0.3	...	35.48	34.93	McI
6C 0032+412	3.670	3.0	...	35.90	35.16	Lac
WN J0040+3857	2.606	1.4	...	35.00	34.14	-0.13	...	<0.20	DB
MG 0046+1102	1.813	<1.2	...	35.42	34.79	0.65	0.55	0.79	0.74	Ste
3C 22.0	0.935	24.6	1.2	35.62	35.04	6.06	1.25	B00
BRL 0056-172	1.019	17.0	...	35.70	35.05	1.40	0.70	BRL
BRL 0101-128	0.387	16.0	...	34.64	34.17	BRL
TN J0121+1320	3.516	0.3	...	35.83	34.97	DB
MG 0122+1923	1.595	<1.2	...	35.24	34.77	0.32	0.38	0.32	0.23	Ste
BRL 0125-143	0.372	15.0	1.7	34.77	34.24	BRL
BRL 0128-264	2.348	33.0	...	36.48	35.81	<0.15	1.10	...	0.60	...	BRL
BRL 0132+079	0.499	9.0	...	34.89	34.43	BRL
TXS J0137+2521	2.897	6.9	...	35.88	35.16	<0.13	DB
MRC 0140-257	2.616	3.4	...	35.77	35.13	Mc4
6C 0140+326	4.413	2.6	1.1	36.03	35.30	<0.01	0.16	Raw
MRC 0152-209	1.920	1.0	...	35.61	35.03	Mc4
MRC 0156-252	2.016	8.3	...	35.61	35.04	McI
USS 0200+015	2.229	5.1	...	35.72	34.97	-0.04	...	<0.40	4.20	3.20	4.00	...	Röt
TN J0205+2242	3.506	2.7	...	35.88	35.01	DB
MRC 0203-209	1.258	12.0	...	35.06	34.47	6.70	...	McI
USS 0211-122	2.336	16.2	1.8	35.94	35.21	0.24	...	4.10	5.60	3.10	2.20	...	Röt
USS 0214+183	2.130	5.9	1.6	35.71	35.04	3.00	1.80	1.80	...	Röt
BRL 0219+082	0.266	155.0	...	34.21	33.75	BRL
WN J0231+3600	3.079	14.8	...	35.53	34.70	0.06	...	<0.05	DB
WN J0303+3733	2.504	4.4	...	35.94	35.02	-0.01	...	<0.20	1.50	...	1.30	0.70	DB
MG 0311+1532	1.986	5.1	...	35.37	34.81	0.34	0.20	0.21	...	Ste
BRL 0310-150	1.769	<10.0	...	36.12	35.60	10.20	4.00	5.00	2.20	BRL
MRC 0316-257	3.130	7.6	McI
MRC 0324-228	1.894	9.6	...	35.79	35.13	Mc4
MRC 0349-211	2.329	7.2	1.6	35.66	35.11	Mc4
USS 0355-037	2.153	11.8	...	35.77	34.99	<0.30	2.70	3.70	2.30	...	Röt
BRL 0357-163	0.584	7.0	...	35.06	34.51	BRL
MRC 0406-244	2.427	7.3	...	36.46	35.62	Mc4
USS 0417-181	2.773	3.7	2.8	36.17	35.39	-0.14	...	<0.10	1.20	0.50	Röt
USS 0448+091	2.037	22.4	...	35.31	34.64	<0.40	1.20	1.40	2.70	...	Röt
TN J0452-1737	2.256	2.4	...	35.69	34.82	0.30	0.40	DB
4C 60.07	3.788	16.0	2.8	36.53	35.60	<0.10	2.70	Röt
TN J0516+0637	0.357	1.3	...	33.33	32.53	DB
BRL 0519-208	1.086	<2.0	...	35.80	35.15	6.00	0.90	BRL

Source	z	LAS ^a	Q ^b	Log(P_{325})	Log(P_{1400})	$A_{Ly\alpha}^c$	Ly α	N V	C IV	Line Flux He II	C III]	C II]	Ref.
USS 0529-549	2.575	<16.0	-0.05	7.40	<0.20	0.40	0.90	1.80	...	R δ t
WN J0617+5012	3.153	3.4	...	35.41	34.54	...	0.80	<0.10	DB
4C 41.17	3.792	20.0	1.2	36.45	35.66	...	14.60	0.39	1.32	0.55	0.91	...	R δ t
B3 0731+438	2.429	10.8	1.3	36.16	35.53	...	31.00	Mc3
B3 0744+464	2.926	1.9	1.4	36.19	35.56	...	12.00	Mc3
USS 0748+134	2.419	13.2	...	35.72	34.97	...	6.30	<0.20	1.80	1.50	1.40	...	R δ t
WN J0813+4828	1.274	0.9	...	34.42	33.52	0.20	0.40	DB
USS 0828+193	2.572	...	1.2	35.55	34.84	-0.06	13.30	<0.10	1.90	1.90	2.00	...	R δ t
BRL 0850-206	1.337	13.0	...	36.00	35.40	2.10	0.90	BRL
BRL 0851-142	1.665	7.0	...	36.00	35.47	3.40	2.30	1.60	...	BRL
4C 12.32	2.468	15.0	13.00	GK
USS 0857+036	2.814	4.0	...	35.87	35.16	-0.44	2.60	<0.10	1.00	0.70	R δ t
B2 0902+34	3.395	5.0	1.2	35.97	35.41	...	21.00	...	2.00	Lil
3C 217.0	0.898	13.1	3.3	35.61	34.99	6.79	5.34	B00
TN J0920-0712	2.760	1.4	...	36.00	35.05	-0.49	44.00	<0.10	3.60	3.00	DB
TN J0924-2201	5.195	1.2	...	36.77	35.74	...	0.35	<0.01	DB
TN J0941-1628	1.644	1.9	...	35.71	34.87	3.20	0.90	DB
3C 226.0	0.818	31.8	1.3	35.60	34.96	2.00	1.90	DB
USS 0943-242	2.923	3.7	...	36.10	35.36	-0.37	20.10	1.70	3.90	2.70	1.94	1.00	B00
MG 1019+0534	2.765	2.2	1.3	35.66	35.19	-0.68	0.84	0.23	1.04	0.85	2.30	...	R δ t
TN J1033-1339	2.427	2.0	...	35.89	35.02	0.17	9.80	<0.10	2.30	0.80	0.49	...	Ste
BRL 1039+029	0.535	6.4	...	34.98	34.56	DB
3C 247.0	0.749	13.9	1.5	35.35	34.89	BRL
TN J1102-1651	2.111	3.0	...	35.57	34.72	-0.78	2.70	<0.20	1.00	1.30	2.73	1.18	B00
3C 252.0	1.104	56.7	2.0	35.74	35.04	6.16	3.56	1.38	DB
TN J1112-2948	3.090	9.1	1.5	36.00	35.12	0.22	2.90	<0.05	0.70	1.20	B00
USS 1113-178	2.239	10.3	2.1	35.72	35.08	...	6.40	<0.20	1.70	0.70	2.80	...	DB
3C 256.0	1.824	4.0	2.9	36.15	35.51	...	54.20	1.40	5.23	5.47	4.28	2.03	R δ t
WN J1123+3141	3.217	25.8	1.6	35.99	35.06	-0.18	6.20	<1.00	3.40	2.40	Sim
USS 1138-262	2.156	11.4	1.5	36.34	35.57	...	13.90	<0.30	0.80	1.30	DB
BRL 1138+015	0.443	5.2	...	34.80	34.39	R δ t
MG 1142+1338	1.279	<0.4	...	34.88	34.50	BRL
BRL 1140-114	1.935	3.9	...	36.30	35.60	1.00	0.50	0.60	1.90	Ste
B2 1141+354	1.781	11.0	...	35.45	34.82	...	47.00	0.80	...	BRL
3C 265.0	0.810	78.8	1.5	35.80	35.07	22.78	3.56	AS
4C 26.38	2.608	23.0	...	36.28	35.07	8.90	5.70	2.40	...	B00
B2 1230+349	1.533	11.0	...	35.44	34.85	3.00	2.00	R δ t
6C 1232+39	3.220	8.0	...	36.28	35.48	...	10.00	AS
VLA J123642+621331	4.424	0.2	0.07	AS
USS 1243+036	3.570	7.0	1.4	23.50	<0.50	B00
MG 1251+1104	2.322	<1.2	2.31	<0.06	0.30	0.30	0.52	...	R δ t
3C 280.0	0.997	13.7	1.2	35.94	35.43	10.76	1.50	Ste
BRL 1303+091	1.409	8.0	2.9	35.96	35.30	7.17	...	B00
BRL 1307+000	0.419	60.0	1.1	34.61	34.13	3.50	...	BRL

Source	z	LAS ^a	Q^b	$\text{Log}(P_{325})$	$\text{Log}(P_{1400})$	$A_{Ly\alpha}^c$	Ly α	N V	C IV	Line Flux	He II	C III]	C II]	Ref.
WN J1333+3037	1.213	0.4	...	34.94	33.65	0.30	0.40	DB
WN J1338+3532	2.769	11.6	...	35.72	34.97	-0.01	17.80	<0.60	1.30	...	3.00	2.20	...	DB
TN J1338-1942	4.110	1.4	2.7	36.29	35.46	-0.50	10.10	<0.07	1.00	0.20	DB
3C 289.0	0.967	10.6	1.1	35.65	35.09	2.81	1.01	E00
BRL 1344-078	0.384	<10.0	...	34.72	34.15	BRL
4C 24.28	2.879	7.0	1.1	36.39	35.65	...	7.30	6.90	1.70	Röt
WN J1356+3929	0.253	1.6	...	33.67	32.86	DB
BRL 1354+013	0.819	33.0	BRL
USS 1357+007	2.673	4.6	Röt
MG 1401+0921	2.093	3.5	...	35.53	34.92	-0.06	9.10	<0.20	1.70	DB
TN J1402-1510	0.739	15.9	...	35.00	34.38	0.41	0.50	0.17	Ste
3C 294.0	1.786	14.5	1.4	DB
USS 1410-001	2.363	23.5	1.0	35.65	35.00	0.06	155	3.10	15.50	15.50	18.60	Mc2
BRL 1411-057	1.094	47.0	1.4	35.72	35.06	...	28.00	1.68	3.36	2.52	1.12	0.36	...	Cim
BRL 1422-297	1.632	<10.0	...	36.11	35.57	4.30	...	1.10	BRL
USS 1425-148	2.349	10.7	...	35.88	35.28	-0.01	20.70	<0.70	2.30	2.30	1.00	DB
8C 1435+635	4.250	4.3	1.1	36.95	36.12	...	1.50	Spi
USS 1436+157	2.538	4.7	1.5	-0.01	42.00	<0.80	17.00	6.00	9.40	Röt
BRL 1436-167	0.146	<12.0	...	33.77	33.29	BRL
BRL 1509+015	0.792	7.2	1.4	35.37	34.87	BRL
USS 1545-234	2.755	6.3	1.9	35.92	35.24	0.01	6.70	<0.20	1.10	1.80	Röt
3C 324.0	1.208	11.1	1.7	35.92	35.34	3.67	2.70	3.47	1.43	...	E00
USS 1558-003	2.527	7.7	0.18	14.90	<0.10	2.70	1.70	1.20	Röt
BRL 1602-174	2.043	37.0	3.2	36.32	35.67	10.00	4.80	2.70	BRL
BRL 1602-288	0.482	61.0	1.0	35.09	34.48	BRL
BRL 1602-093	0.109	290.0	BRL
BRL 1603+001	0.059	11.0	...	32.96	32.22	BRL
BRL 1621-115	0.375	<20.0	...	34.73	34.25	BRL
3C 340.0	0.775	44.7	1.1	35.47	34.84	7.08	0.75	...	E00
BRL 1628-268	0.166	93.0	BRL
BRL 1643+022	0.095	7.1	1.3	BRL
TXS J1650+0955	2.510	19.4	0.28	20.90	<0.10	3.20	2.70	1.20	DB
BRL 1649-062	0.236	85.0	DB
WN J1703+3739	0.256	30.1	...	31.98	31.41	Röt
USS 1707+105	2.349	21.7	4.30	<0.10	...	0.90	DB
3C 352.0	0.806	12.3	1.6	35.50	34.84	0.20	E00
3C 356.0	1.079	73.4	...	35.72	35.04	4.33	4.41	0.52	...	E00
BRL 1732-092	0.317	45.0	...	34.44	34.00	BRL
8C 1736+650	2.400	17.0	...	35.08	34.24	...	18.00	L99
7C 1740+6640	2.100	<0.5	...	34.84	34.50	...	4.10	...	0.30	L99
7C 1758+6719	2.700	45.0	...	35.40	34.69	...	12.00	0.80	L99
7C 1802+6456	2.110	26.0	...	35.54	34.76	...	7.10	...	1.00	...	0.80	L99
8C 1803+661	1.610	36.0	...	34.55	33.93	5.30	2.60	1.90	L99
3C 368.0	1.132	8.5	2.0	35.93	35.10	5.11	10.57	9.98	...	E00

Source	z	LAS ^a	Q ^b	Log(F_{325})	Log(P_{1400})	$A_{Ly\alpha}$ ^c	Ly α	N V	C IV	Line Flux		C III]	C II]	Ref.
										He II	C III]			
7C 1805+6332	1.840	14.0	...	35.13	34.47	...	17.00	...	2.50	L99	
7C 1807+6719	2.780	1.9	...	35.31	34.78	...	2.10	0.70	L99	
4C 40.36	2.265	20.0	...	36.24	35.42	6.20	5.60	5.90	...	Röt	
BRL 1859-235	1.430	4.2	...	36.29	35.68	3.40	4.60	4.70	6.70	BRL	
TXS J1908+7220	3.530	14.4	...	36.44	35.64	...	32.00	<0.20	DB	
WN J1911+6342	3.590	1.8	...	35.56	34.66	-0.64	1.40	<0.03	0.08	0.08	DB	
BRL 1912-269	0.226	48.0	1.1	34.33	33.57	BRL	
BRL 1920-077	0.648	23.0	...	35.19	34.62	BRL	
4C 48.48	2.343	17.0	1.1	35.87	35.20	6.10	3.70	2.80	...	Röt	
MRC 2025-218	2.630	5.1	...	35.89	35.25	...	4.00	0.62	0.69	0.35	0.97	...	VM99	
TXS J2036+0256	2.130	3.1	...	35.86	35.09	0.01	6.80	<0.30	0.60	0.70	1.20	...	DB	
MG 2037-0011	1.512	<0.4	...	34.93	34.63	0.44	0.10	Ste	
MG 2058+0542	1.381	<0.4	...	35.40	35.02	0.41	Ste	
MRC 2104-242	2.491	21.8	...	36.26	35.41	...	57.00	<3.80	3.80	1.90	2.66	...	VM99	
4C 23.56	2.483	47.0	1.9	8.00	1.36	2.08	1.52	1.28	0.80	Cim	
MG 2109+0326	1.634	<1.2	...	35.28	34.71	0.32	0.21	0.23	Ste	
MRC 2115-253	1.114	1.7	...	35.16	34.45	0.14	0.24	0.15	Mc1	
MG 2121+1839	1.860	6.3	...	35.32	34.73	0.53	1.60	Ste	
BRL 2120-166	0.882	14.0	...	35.49	34.86	BRL	
MG 2144+1928	3.582	8.5	...	36.37	35.65	-0.47	6.15	<0.04	0.58	0.35	Ste	
USS 2202+128	2.706	3.4	1.4	35.79	35.10	...	7.70	<0.10	1.90	2.40	Röt	
3C 441.0	0.708	26.0	3.1	35.38	34.82	0.30	B00	
MRC 2224-273	1.679	0.4	...	35.37	34.72	...	47.00	Mc4	
MRC 2247-232	1.326	9.3	...	35.57	35.01	1.50	...	Mc4	
USS 2251-089	1.986	4.5	1.4	35.66	35.07	3.30	1.30	1.50	...	Röt	
TN J2254+1857	2.153	2.7	...	34.97	34.15	...	33.00	<1.00	...	3.20	DB	
MRC 2303-253	0.740	18.6	...	35.05	34.35	7.00	...	Mc1	
MG 2308+0336	2.457	35.89	35.32	-0.74	2.93	0.57	0.63	0.39	0.45	0.83	Ste	
BRL 2318-166	1.414	<5.0	...	36.20	35.52	7.80	6.20	2.00	BRL	
MRC 2318-244	1.113	25.0	1.1	35.29	34.74	Mc4	
TXS J2321+2237	2.553	8.1	...	35.90	35.14	0.17	8.10	<0.20	DB	
BRL 2322-052	1.188	7.8	1.80	BRL	
TXS J2334+1545	2.480	6.4	...	35.69	34.98	...	3.10	<0.10	0.10	...	0.80	...	DB	
BRL 2347-026	1.036	<2.0	...	35.56	35.03	0.60	BRL	
TXS J2351+1034	1.334	2.2	...	35.39	34.60	DB	
4C 28.58	2.891	28.0	2.3	36.30	35.44	0.30	1.60	1.80	...	Röt	
TXS J2355-0002	2.587	33.8	1.6	35.96	35.28	...	1.30	0.80	0.30	DB	

^a Radio largest angular size, see §8.3.1.2

^b Radio lobe distance ratio, see §8.3.1.3

^c Ly α asymmetry, see §8.3.2.2

REFERENCES: AS=Allington-Smith et al. (1988); BRL=Best, Röttgering & Lehnert (1999); B00=Best, Röttgering & Longair (2000a);

Cim=Cimatti et al. (1998b); DB=Chapter 4; GK=Gopal-Krishna et al. (1995); Lac=Lacy et al. (1994); L99=Lacy et al. (1999);

Lil=Lilly (1988); Mc1=McCarthy et al. (1990a); Mc2=McCarthy et al. (1990b); Mc3=McCarthy (1991b); Mc4=McCarthy et al. (1991c);

Raw=Rawlings et al. (1996); Röt=Röttgering et al. (1997); Sim=Simpson et al. (1999); Spi=Spinrad et al. (1995); Ste=Stern et al. (1999a);

VM99=Villar-Martin et al. (1999c); Wad=Waddington et al. (1999)

References

- Abell, G., Corwin, H., & Olowin, R. 1989, *ApJS*, 70, 1
- Adam, G., Rocca-Volmerange, B., Gérard, S., Ferruit, P., & Bacon, R. 1997, *A&A*, 326, 501
- Allen, M., Dopita, M., & Tsvetanov, Z. 1998, *ApJ*, 493, 571 (ADT98)
- Allington-Smith, J. 1982, *MNRAS*, 199, 611
- Allington-Smith, J., Spinrad, H., Djorgovski, S., & Liebert, J. 1988, *MNRAS*, 234, 1091
- Andernach, H., Verkhodanov, O. & Verkhodanova, N. 2000, *IAU Symp.* 199, in press, astro-ph/0001473
- Antonucci, R. 1993, *ARA&A*, 31, 473
- Antonucci, R., Kinney, A., & Hurt, T. 1993, *ApJ*, 414, 506
- Appenzeller, I., Stahl, O., Kiesewetter-K., S., Kudritzki, R., Nicklas, H., & Rupprecht, G. 1997, in: *The early universe with the VLT*, ed. J. Bergeron, Springer, Heidelberg, New York, p. 35
- Archibald, E., Dunlop, J., Hughes, D., Rawlings, S., Eales, S., & Ivison, R. 2000, *MNRAS*, in press, astro-ph/0002083
- Baade, W., & Minkowski, R. 1954, *ApJ*, 119, 206
- Bade, N. et al. 1998, *A&AS*, 127, 145
- Baker, J., & Hunstead, R. 1995, *ApJ*, 452, L95 (BH95)
- Baker, J. 1997, *MNRAS*, 286, 23
- Baker, J., Hunstead, R., Kapahi, V., & Subrahmanya, C. 1999, *ApJS*, 122, 29
- Barger, A., Cowie, L., Mushotzky, R., & Richards, E., 2000, *AJ*, submitted, astro-ph/0007175
- Barthel, P., & Miley, G. 1988, *Nature*, 333, 319
- Barthel, P. 1989, *ApJ*, 336, 606
- Baum, S. & Heckman, T. 1989, *ApJ*, 336, 702
- Baum, S. & McCarthy, P. 2000, *AJ*, in press, astro-ph/0002329
- Becker, R., White, R., & Edwards, A. 1991, *ApJS*, 75, 1
- Becker, R., White, R., & Helfand, D. 1995, *ApJ*, 450, 559
- Benn, C., Rowan-Robinson, M., McMahon, R., Broadhurst, T., & Lawrence, A. 1993, *MNRAS*, 263, 98
- Benn, C., Vigotti, M., Carballo, R., Gonzales-Serrona, J., & Sanchez, S. 1998, *MNRAS*, 295, 451
- Bennett, A. 1962, *MNRAS*, 68, 163
- Best, P., Bailer, D., Longair, M. & Riley, J. 1995, *MNRAS*, 275, 1171
- Best, P., Longair, M. & Röttgering, H. 1996, *MNRAS*, 280, L9
- Best, P., Longair, M., & Röttgering, H. 1998a, *MNRAS*, 295, 549
- Best, P., Röttgering, H. & Lehnert, M. 1999, *MNRAS*, 310, 223 (BRL99)
- Best, P., Röttgering, H. & Longair, M. 2000a, *MNRAS*, 311, 1
- Best, P., Röttgering, H. & Longair, M. 2000b, *MNRAS*, 311, 23 (BRL00)
- Bicknell, G., Sutherland, R., van Breugel, W., Dopita, M., Dey, A., & Miley, G. 2000, *ApJ*, in press, astro-ph/9909218
- Binette, L., Wilson, A. & Storchi-Bergmann, T. 1996, *A&A*, 312, 365 (BWS96)

- Binette, L., Kurk, J., Villar-Martín, M & Röttgering, H. 2000, A&A, in press, astro-ph/0002210
- Blumenthal, G., & Miley, G. 1979, A&A, 80, 13
- Blundell, K., Rawlings, S., Eales, S., Taylor, G., & Bradley, A 1998, MNRAS, 295, 265
- Blundell, K., Rawlings, S., & Willott, C. 1999, AJ, 117, 677
- Blundell, K., Rawlings, S., & Willott, C. 1999a, AJ, 117, 677
- Blundell, K., & Rawlings, S. 1999b, Nature, 399, 330
- Bonatto, C., Bica, E., Pastoriza, M., & Alloin, D. 1996, A&AS, 118, 89
- Boyle, B. J. 1990, MNRAS, 243, 231
- Bremer, M. Rengelink, R., Saunders, R., Röttgering, H. J. A., Miley, G., & Snellen, I. 1998, in *Observational Cosmology with the New Radio Surveys*, ed. M. N. Bremer, N. Jackson, & I. Pérez-Fournon (Dordrecht: Kluwer), p. 165
- Brotherton, M. S., Wills, B., Dey, A., van Breugel, W., & Antonucci, R. 1998, ApJ, 501, 110
- Bruzual, A., & Charlot, S. 1999, personal communication
- Burstein, D., & Heiles, C. 1982, AJ, 87, 1165
- Cardelli, J., Clayton, G., & Mathis, J. 1989, ApJ, 345, 245
- Carilli, C., Röttgering, H., van Ojik, R., Miley, G., & van Breugel, W. 1997, ApJS, 109, 1
- Carilli, C., Harris, D., Pentericci, L., Röttgering, H., Miley, G., & Bremer, M. 1998, ApJ, 494, L143
- Carilli, C., Röttgering, H., Miley, G., Pentericci, L., & Harris, D. 1998, in 'The Most Distant Radio Galaxies', ed. H. Röttgering, P. Best, & M. Lehnert (Amsterdam: KNAW), p. 123
- Carter, D. et al. 1994, *ISIS Users' Manual*
- Carter, D., & Bridges, T. 1995, *WHT Prime Focus and Auxiliary Port Imaging Manual*
- Casali, M., & Hawarden, T. 1992, JCMT-UKIRT Newsletter, 4, 33
- Chambers, K., Miley, G., & van Breugel, W. 1987, Nature, 329, 604
- Chambers, K., Miley, G., & van Breugel, W. 1990, ApJ, 363, 21
- Chambers, K., Miley, G., van Breugel, W., & Huang, J.-S. 1996a, ApJS, 106, 215
- Chambers, K., Miley, G., van Breugel, W., Bremer, M., Huang, J.-S., & Trentham, N 1996b, ApJS, 106, 247
- Chini, R., & Krügel, E. 1994, A&A, 288, L33
- Cimatti, A., di Serego-Alighieri, S., Fosbury, R., Salvati, M., & Taylor, D. 1993, MNRAS, 264, 421
- Cimatti, A., Freudling, W., Röttgering, H., Ivison, R., & Mazzei, P. 1998a, A&A, 329, 399
- Cimatti, A., di Serego Alighieri, S., Vernet, J., Cohen, M., & Fosbury, R. 1998b, ApJ, 499, L21
- Cohen, M., Vermeulen, R., Ogle, P., Tran, H., & Goodrich, R. 1997, ApJ, 484, 201
- Coleman, P., & Condon, J. 1985, AJ, 90, 8
- Collins, C., Guzzo, L., Nichol, R., & Lumsden, S. 1995, MNRAS, 274, 1071
- Condon, J., Anderson, E., & Broderick, J. 1995, AJ, 109, 2318
- Condon, J., et al. 1998, AJ, 115, 1693
- Courbin, F., Hutsemékers, D., Meylan, G., Magain, P., & Djorgovski, S. 1997, A&A, 317, 656
- Cowie, L., et al. 1994a, ApJ, 432, L83
- Cowie, L., et al. 1994b, ApJ, 434, 114
- Cowie, L., & Hu, E. 1998, AJ, 115, 1319
- Crawford, C. et al. 1995, MNRAS, 274, 75
- Daddi, E. et al. 2000, A&A, in press, astro-ph/0005581
- De Breuck, C., van Breugel, W., Röttgering, H., & Miley, G. 1998, in *Observational Cosmology with the New Radio Surveys*, ed. M. Bremer et al. (Dordrecht: Kluwer), p. 185
- De Breuck, C., van Breugel, W., Röttgering, H., Miley, G., & Carilli, C. 1998, in "Looking Deep in the Southern Sky", ed. R. Morganti & W. Couch (Berlin Heidelberg: Springer), p. 246

- de Ruiter, H., Willis, A., & Arp, H. 1977, *A&A*, 28, 211
- Deutsch, E. 1999, *AJ*, 118, 1882
- Dey, A., Spinrad, H., & Dickinson, M. 1995, *ApJ*, 440, 515
- Dey, A., Cimatti, A., van Breugel, W., Antonucci, R., & Spinrad, H. 1996, *ApJ*, 465, 157
- Dey, A. 1997, in *Proc. Mass Ejection from Active Galactic Nuclei*, ed. N. Arav, I. Schlossman & R. Weymann 1997a, *ASP Conf. Series*, 128, 35
- Dey, A., van Breugel, W., Vacca, W., & Antonucci, R. 1997b, *ApJ*, 490, 698
- Dey, A., Spinrad, H., Stern, D., Graham, J., & Chaffee, F. 1998, *ApJ*, 498, L93
- Dey, A., Graham, J., Ivison, R., Smail, I., Wright, G., & Liu, M. 1999a, *ApJ*, 519, 610
- Dey, A. 1999b, in "The Most Distant Radio Galaxies", ed. H. Röttgering, P. Best & M. Lehnert (Amsterdam: KNAW), p. 19
- Dickinson, M., in *Proc. STScI May 1997 Symposium "The Hubble Deep Field,"* eds. M. Livio, S. Fall and P. Madau (Cambridge: Cambridge Univ. Press), p. 218
- Dickinson, et al. 2000, in preparation
- Dickson, R., Tadhunter, C., Shaw, M., Clarck, N., & Morganti, R. 1995, *MNRAS*, 273, L29
- Djorgovski, S. 1985, *PASP*, 97, 1119
- Dopita, M., & Sutherland, R. 1996, *ApJS*, 102, 161 (DS96)
- Douglas, J., Bash, F., Bozyan, F., Torrence, G., & Wolfe, C. 1996, *AJ*, 111, 1945
- Dunlop, J., & Peacock, J. 1990, *MNRAS*, 247, 19
- Dunlop, J., & Peacock, J. 1993, *MNRAS*, 263, 936
- Dunlop, J., Hughes, D., Rawlings, S., Eales, S., & Ward, M. 1994, *Nature*, 370, 347
- Dunlop, J., Peacock, J., Spinrad, H., Stern, D., & Windhorst, R. 1996, *Nature*, 381, 581
- Dunlop, J. 1999, in *Proc. KNAW colloquium 'The Most Distant Galaxies'*, ed. P. Best, H. Röttgering, & M. Lehnert, p. 71
- Eales, S., & Rawlings, S. 1993, *ApJ*, 411, 67
- Eales, S., Rawlings, S., Law-Green, D., Cotter, G., & Lacy, M. 1997, *MNRAS*, 291, 593
- Elston, R., Rieke, G., & Rieke, M. 1988, *ApJ*, 331, L77
- Evans, A. 1998, *ApJ*, 498, 553
- Evans, I., Koratkar, A., Allen, M., Dopita, M., & Tsvetanov, Z. 1999, *ApJ*, 521, 531
- Fan, X. et al. 1999, *ApJ*, 526, L57
- Fan, et al. 2000, *AJ*, submitted, astro-ph/0005414
- Faranoff, B., & Riley, J. 1974, *MNRAS*, 167, 31
- Feinstein, C., Macchetto, F., Martel, A., Sparks, W., & McCarthy, P. 1999, *ApJ*, 526, 623
- Ferland, G. 1996, *Hazy: A Brief Introduction to CLOUDY*, Univ. of Kentucky Dept. of Phys. and Astron. Internal Report
- Ficarra, A., Grueff, G., & Tomassetti, G. 1985, *A&AS*, 59, 255
- Filippenko, A. 1982, *PASP*, 94, 715
- Fosbury, R. et al. 1998, in *NICMOS and the VLT: A New Era of High Resolution Near Infrared Imaging and Spectroscopy*, ESO Conference and Workshop Proceedings 55, W. Freudling and R. Hook eds., p. 190
- Fosbury, R. et al. 1999, in *ESO conference on Chemical Evolution from Zero to High Redshift*, ESO astrophysics symposia, J. Walsh & M. Rosa eds., in press, astro-ph/9901115
- Fosbury, R. 2000, in "proceedings of the SPIE International Symposium on 'Astronomical Telescopes and Instrumentation'", in press, astro-ph/0005275
- Frater, R., Brooks, J., & Whiteoak, J. 1992, *JEEE*, Australia, 12, 2, p. 103
- Gear, W. K., Stevens, J. A., Hughes, D. H., Lichtfield, S. J., Robson, E. I., Teräsanta, H., Valtaoja, E., Steppe, H., Aller, M. F., & Aller, H. D. 1994, *MNRAS*, 267, 167
- Giovannini, G., Tordi, M. & Feretti, L. 1999, *New Astronomy*, 4, 141

- Goodrich, R. W., & Miller, J. S. 1988, *ApJ*, 331, 332
- Goodrich, R. W., Cohen, M. H., & Putney, A. 1995, *PASP*, 107, 179
- Gopal-Krishna, Giraud, E., Melnick, J., & Della Valle, M. 1995, *A&A*, 303, 705
- Gregg, M., Becker, R., White, R., Helfand, D., McMahon, R. & Hook, I. 1996, *AJ*, 112, 407
- Gregory, P., & Condon, J. 1991, *ApJS*, 75, 1011
- Griffith, M. & Wright, A. 1993, *AJ*, 105, 1666
- Griffith, M. & Wright, A., Burke, B., & Ekers, R. 1994, *ApJS*, 90, 179
- Griffith, M. & Wright, A., Burke, B., & Ekers, R. 1995, *ApJS*, 97, 347
- Hales, S., Baldwin, J., & Warner, P. 1993, *MNRAS*, 263, 25
- Haehnelt, M., Natarajan, P. & Rees, M. 1998, *MNRAS*, 300, 817
- Hamann, F., & Ferland, G. 1993, *ApJ*, 418, 11
- Heckman, T., O’Dea, C., Baum, S., & Laurikainen, E. 1994, *ApJ*, 428, 65
- Helfand, D., Schnee, S., Becker, R., White, R., & McMahon, R. 1999, *AJ*, 117, 1568
- Hill, R. et al. 1997, *ApJ*, 486, L99
- Hook, I., & McMahon, R. 1998, *MNRAS*, 294, 7L
- Hornschemeier, A., et al. 2000, *ApJ*, in press, astro-ph/0004260
- Hu, E., McMahon, R., & Cowie, L. 1999, *ApJ*, 522, L9
- Hubble, E., & Humason, M. 1931, *ApJ*, 74, 43
- Hughes, D., Dunlop, J., & Rawlings, S. 1997, *MNRAS*, 289, 766
- Isobe, T., Feigelson, E., & Nelson, P. 1986, *ApJ*, 306, 490
- Isobe, T. & Feigelson, E. 1990, *BAAS*, 22, 917
- Iverson, R. et al. 1998a, *ApJ*, 494, 211
- Iwamuro, F., Oya, S., Tsukamoto, H., & Maihara, T. 1996, *ApJ*, 466, L67
- Januzzi, B. T., Smith, P. S., & Elston, R. 1993, *ApJS*, 85, 265
- Jarrett, T., Chester, T., Cutri, R., Schneider, S., Skrutskie, M., & Huchra, J. 2000, *AJ*, in press, astro-ph/0004318
- Jarvis, M., Rawlings, S., Willot, C., Blundell, K., Eales, S., & Lacy, M. 1999, *ASP Conf. Ser.* 193: The Hy-Redshift Universe: Galaxy Formation and Evolution at High Redshift, p. 90
- Jedrzejewski, R. 1987, *MNRAS*, 226, 747
- Johnson, H. L. 1966, *ARA&A*, 4, 193
- Kapahi, V., Athreya, R., van Breugel, W., McCarthy, P., & Subrahmanya, C. 1998a, *ApJS*, 118, 275
- Kapahi, V., et al. 1998b, *ApJS*, 118, 327
- Kaplan, D., Condon, J., Arzoumanian, Z., & Cordes, J. 1998, *ApJS*, 119, 75
- Kaplan, D., Cordes, J., Condon, J., & Djorgovski, S. 2000a, *ApJ*, 529, 859
- Kaplan, D., Cordes, J., & Condon, J. 2000b, *ApJS*, 126, 37
- Kauffmann, G., & Charlot, S. 1998, *MNRAS*, 297, L23
- Kauffmann, G., Colberg, J., Diaferio, A., & White, S. 1999, *MNRAS*, 303, 188
- Kauffmann, G., & Haehnelt, M. 2000, *MNRAS*, 311, 576
- Kellermann, K., Pauliny-Toth, I., & Williams, P. 1969, *ApJ*, 157, 1
- Komissarov, S., & Gubanov, A. 1994, *A&A*, 285, 27
- Kormendy, J., & Richstone, D. 1995, *ARA&A*, 33, 581
- Krolik, J., & Chen, W. 1991, *AJ*, 102, 1659
- Kurk, J., Röttgering, H., Pentericci, L., & Miley, G. 1999, in “Clustering At High Redshift”, *ASP Conf. Series*, ed. A. Mazuer & O. Le Fevre, in press, astro-ph/9910257
- Kurk, J., et al. 2000, *A&A*, 358, L1
- Lacy, M., Hill, G., Kaiser, M.-E., & Rawlings, S. 1993, *MNRAS*, 263, 707

- Lacy, M., et al. 1994, MNRAS, 271, 504
- Lacy, M., Rawlings, S., Hill, G., Bunker, A., Ridgway, S., & Stern, D. 1999, MNRAS, 308, 1096
- Lacy, M., Bunker, A., & Ridgway, S. 2000, AJ, in press, astro-ph/0003290
- Laing, R., Riley, J., & Longair, M. 1983, MNRAS, 204, 151
- Large, M., Mills, B., Little, A., Crawford, D., & Sutton, J. 1981, MNRAS, 194, 693
- Larkin, J., et al., ApJ, in press, astro-ph/0002335
- Laurent-Muehleisen, S., Kollgaard, R., Feigelson, E., Brinkmann, W., & Siebert, J. 1999, ApJ, 525, 127
- Lavalley, M., Isobe, T., & Feigelson, E. 1992, ASP Conf. Ser. 25: Astronomical Data Analysis Software and Systems I, 1, 245
- Lawrence, C., et al. 1986, ApJS, 61, 105
- Le Fevre, O., Deltorn, J., Crampton, D., & Dickinson, M. 1996, ApJ, 471, L11
- Lemaître, G. 1927, Ann. Soc. Sci. Bruxelles, 47A, 49
- Lemaître, G. 1931, MNRAS, 91, 483
- Leyshon, G., & Eales, S. 1998, MNRAS, 295, 10
- Lilly, S., & Longair, M. 1984, MNRAS, 211, 833
- Lilly, S. 1988, ApJ, 333, L161
- Lilly, S. 1989, ApJ, 340, 77
- Loeb, A. 1993, ApJ, 403, 542
- Lonsdale, C., & Barthel, P. 1986, ApJ, 303, 617
- Lorimer, D., Yates, J., Lyne, A., & Gould, D. 1995, MNRAS, 273, 411
- MacAlpine, G., Davidson, K., Gull, T., & Wu, C. 1985, ApJ, 294, 147
- Machalski, J. & Ryś, S. 1981, A&A, 99, 388
- Macklin, J. 1982, MNRAS, 199, 1119
- Madau, P. 1995, ApJ, 441, 18
- Magorrian, J., et al. 1998, AJ, 115, 2285
- Manning, C., Stern, D., Spinrad, H., & Bunker, A. 2000, ApJ, 537, 65
- Martel, A. et al. 1998, AJ, 115, 1348
- Martin, C., Halpern, J., & Schiminovich, D. 1998, ApJ, 494, L211
- Massey, P., Strobel, K., Barnes, J. V., & Anderson, E. 1988, ApJ, 328, 315
- Matthews, T., Morgan, W., & Schmidt, M. 1964, ApJ, 140, 35
- Mathews, K., & Soifer, B., 1994, in Proc. Infrared Astronomy with Arrays: The Next Generation, ed. I. McClean (Dordrecht: Kluwer), p. 239
- McCarthy, P., van Breugel, W., Spinrad, H., & Djorgovski, S. 1987, ApJ, 321, L29
- McCarthy, P., Kapahi, V., van Breugel, W., & Subrahmanya, C. 1990a, AJ, 100, 1014
- McCarthy, P. et al. 1990b, ApJ, 365, 487
- McCarthy, P., van Breugel, W., & Kapahi, V. 1991a, ApJ, 371, 478
- McCarthy, P. 1991b, AJ, 102, 518
- McCarthy, P., van Breugel, W., Kapahi, V., & Subrahmanya, C. 1991c, AJ, 102, 522
- McCarthy, P. 1993, ARA&A, 31, 639
- McCarthy, P., Kapahi, V., van Breugel, W., Persson, S., Atheya, R., & Subrahmanya, C. 1996, ApJS, 107, 19
- McCarthy, P. 1998, in proc. "KNAW colloquium: High Redshift Galaxies", (Kluwer: Dordrecht), p. 5
- McCarthy, P. & Lawrence, C. 2000, in preparation
- McLean, I. et al. 1993, Proc. SPIE, 1946, 513
- McLure, R. & Dunlop, J. 2000, MNRAS, in press, astro-ph/9908214

- Miller, J. & Stone, R. 1994, Lick Observatory Technical Report No. 66
- Miller, J., Robinson, L., & Goodrich, R. 1988, in *Instrumentation for Ground-Based Astronomy*, ed. L. Robinson (New York: Springer), p. 157
- Minkowski, R. 1960, *ApJ*, 132, 908
- Monet, D. et al. 1998, USNO-SA2.0, (U.S. Naval Observatory, Washington DC)
- Mushotzky, R., Cowie, L., Barger, A., & Arnaud, K. 2000, *Nature*, 404, 459
- Napier, P., Thompson, A., & Ekers, R. 1983, *Proc. IEEE*, 71, 1295
- Nasuti, F., Mignani, R., Caraveo, P., & Bignami, G. 1996, *A&A*, 314, 849
- Neeser, M., Eales, S., Law-Green, J., Leahy, J. & Rawlings, S. 1995, *ApJ*, 451, 76
- Nelson, K. 1995, MPh thesis, Cambridge University
- Odehahn, S. & Aldering, G. 1996, Private communication to NED.
- Oke, J., & Korycanski, D., *ApJ*, 255, 11
- Oke, J. et al. 1995, *PASP*, 107, 375
- Oort, M., Katgert, P., Steeman, F., & Windhorst, R. 1987, *A&A*, 179, 41
- Oort, M. 1988, *A&A*, 193, 5
- Orr, M., & Browne, I. 1982, *MNRAS*, 200, 1067
- Osterbrock, D. E. 1989, *Astrophysics of Gaseous Nebulae and Active Galactic Nuclei* (Mill Valley, CA: Univ. Sci.)
- Osterbrock, D. & Martel, A. 1992, *PASP*, 104, 76
- Owen, F., & Laing, R. 1989, *MNRAS*, 238, 357
- Owen, F., Condon, J., & Ledden, J. 1983, *AJ*, 88, 1
- Papadopoulos, P., Röttgering, H., van der Werf, P., Guilloteau, S., Omont, A., Tilanus, R., and van Breugel, W. 2000, *ApJ*, 528, 626
- Pascarelle, S., Windhorst, R., Keel, W., & Odehahn, S. 1996, *Nature*, 383, 45
- Pedani, M., & Grueff, G. 1999, *Å*, 350, 368
- Pentericci, L. et al. 1999a, *A&A*, 341, 329
- Pentericci, L. 1999b, PhD thesis, Universiteit Leiden
- Pentericci, L., van Reeve, W., Carilli, C., Röttgering, H., & Miley, G. 2000a *A&AS*, in press, astro-ph/0005524
- Pentericci, L., et al. 2000b, *ApJ*, submitted
- Pentericci, L., et al. 2000c, *A&A*, submitted
- Perryman, M., & ESA 1997, *The Hipparcos and Tycho catalogues*, Noordwijk: ESA Publications Division, ESA SP Series 1200
- Persson, S., Murphy, D., Krzeminski, W., Roth, M., & Rieke, M. 1998, *AJ*, 116, 2475
- Postman, M., & Lauer, T. 1995, *ApJ*, 440, 28
- Prevot, M., Lequeux, J., Prevot, L., Maurice, E., & Rocca-Volmerange, B. 1984, *A&A*, 132, 389
- Pursimo, T. et al. 1999, *A&AS*, 134, 50
- Rawlings, S., Eales, S., & Warren 1990, *MNRAS*, 243, 14P
- Rawlings, S. & Saunders, R. 1991, *Nature*, 349, 138
- Rawlings, S., Lacy, M., Blundell, K., Eales, S., Bunker, A., & Garrington, S. 1996, *Nature*, 383, 502
- Rawlings, S., Blundell, K., Lacy, M. & Willot, C. 1998, in *Observational Cosmology with the New Radio Surveys*, ed. M. Bremer, N. Jackson, & I. Pérez-Fournon (Dordrecht: Kluwer), p. 171
- Rees, M. 1984, *ARA&A*, 22, 471
- Rees, N. 1990, *MNRAS*, 244, 233
- Rengelink, R., et al. 1997, *A&A*, 124, 259
- Rengelink, R. 1998, Ph.D. thesis, Universiteit Leiden.
- Richards, E., Kellermann, K., Fomalont, E., Windhorst, R., & Partridge, R. 1998, *AJ*, 116, 1039

- Riley, J., Waldram, E., & Riley, J. 1999, MNRAS, 306, 31
- Röttgering, H., Lacy, M., Miley, G., Chambers, K., & Saunders, R., A&AS, 108, 79
- Röttgering, H., Miley, G., Chambers, K., & Machetto, F. 1995a A&AS, 114, 51
- Röttgering, H., Hunstead, R., Miley, G., van Ojik, R., & Wieringa, M. 1995b, MNRAS, 277, 389
- Röttgering, H., van Ojik, R., Miley, G., Chambers, K., van Breugel, W., & de Koff, S. 1997, A&A, 326, 505
- Röttgering, H., de Bruyn, G., & Pentericci, L. 1999, The Most Distant Radio Galaxies, Ed. H. Röttgering, P. Best, & M. Lehnert. 1999, 113
- Sanders, D. & Mirabel, F. 1996, ARA&A, 34, 749
- Sanghera, H., Saikia, D., Lüdke, E., Spencer, R., Foulsham, P., Akujor, C., & Tzioumis, A. 1995, A&A, 295, 629
- Savaglio, S., Benetti, S., & Pasquini, L. 1997, EFOSC1 Operating Manual
- Schlegel, D., Finkbeiner, D., Davis, M. 1998, ApJ, 500, 525
- Schneider, D., Schmidt, M., & Gunn, J. 1991a, AJ, 101, 2004
- Schneider, D., Schmidt, M., & Gunn, J. 1991b, AJ, 102, 837
- Schneider, D., Schmidt, M., & Gunn, J. 1997, AJ, 144, 36
- Serjeant, S., et al. 1998, MNRAS, 298, 321
- Serkowski, K., Mathewson, D., & Ford, V. 1975, ApJ, 196, 261
- Shakhbazian, R. 1973, Astrofizika, 9, 495
- Sheppard, M., 1997, in ASP Conference Series, Vol 125, Astronomical Data Analysis Software and Systems VI, ed. G. Hunt & H. E. Payne (San Francisco: Astron. Soc. of the Pacific), 77
- Simpson, C. et al. 1999b, ApJ, 525, 659
- Simpson, C., Rawlings, S., & Lacy, M. 1999a, MNRAS, 306, 828
- Simpson, C., Ward, M., Wall, J. 2000, MNRAS, in press, astro-ph/0007475
- Smail, I., Hogg, D., Yan, L., & Cohen, J. 1995, ApJ, 449, L105
- Smail, I. et al. 1999, MNRAS, 308, 1061
- Songaila, A., Cowie, L., Hu, E., & Gardner, J. 1994, ApJS, 94, 461
- Songaila, A., Hu, E., & Cowie, L. 1999, ApJ, in press, astro-ph/9908321
- Spinrad, H., Djorgovski, S., Marr, J., & Aguilar, L. 1985, PASP, 97, 932
- Spinrad, H., Dey, A., & Graham, J. 1995, ApJ, 438, 51
- Steidel, C., Gialalisco, M., Pettini, M., Dickinson, M., & Adelberger, K. 1996, ApJ, 462, L17
- Spinrad, H. et al. 1997, ApJ, 484, 581
- Spinrad, H., et al. 1998, AJ, 116, 2617
- Steidel, C., Pettini, M., & Hamilton, D. 1995, AJ, 110, 2519
- Steidel, C., Adelberger, K., Gialalisco, M., Dickinson, M., & Pettini, M. 1999, ApJ, 519, 1
- Stern, D., et al. 1999a, AJ, 117, 1122 (S99)
- Stern, D., & Spinrad, H. 1999b, PASP, 111, 1475
- Stern, D., et al. 2000a, ApJ, 533, L75
- Stern, D., Bunker, A., Spinrad, H., & Dey, A. 2000b, ApJ, 537, 73
- Stoche, J. et al. 1991, ApJS, 76, 813
- Tielens, A., Miley, G., & Willis, A. 1979, A&AS, 35, 153
- Tran, H., Cohen, M., Ogle, P., Goodrich, R., & di Serego Alighieri, S. 1998, ApJ, 500, 660
- Tran, H., Cohen, M., & Villar-Martín 2000, AJ, in press, astro-ph/0004383
- Turner, M. 1998, in "Axions '98", ed. P. Sikive (Nucl. Phys. Proc. B), in press, astro-ph/9811366
- van Breugel, W., Filippenko, A., Heckman, T., & Miley, G. 1985, ApJ, 293, 83
- van Breugel, W., Stanford, S. A., Spinrad, H., Stern, D., & Graham, J. 1998 ApJ, 502, 614

- van Breugel, W. et al. 1999a, in 'The Most Distant Radio Galaxies', ed. H. Röttgering, P. Best & M. Lehnert (Amsterdam: KNAW), p. 49
- van Breugel, W., De Breuck, C., Röttgering, H., Miley, G., & Stanford, A. 1999b, in "Looking Deep in the Southern Sky", ed. R. Morganti, Sydney, p. 236
- van Ojik, R., Röttgering, H., Miley, G., Bremer, M. N., Macchetto, F., & Chambers, K. 1994, A&A, 289, 54
- van Ojik, R. 1995, PhD thesis, Rijksuniversiteit Leiden
- van Ojik, R., Röttgering, H., Carilli, C., Miley, G., Bremer, M., & Machetto, F. 1996, A&A, 313, 25
- van Ojik, R., Röttgering, H., Miley, G., & Hunstead, R. W. 1997, A&A, 317, 358
- Verkhodanov O., Trushkin S., Andernach H., Chernenkov V. 1997, in "Astronomical Data Analysis Software and Systems VI", ed.: G. Hunt and H. Payne, ASP Conference Series, Vol. 125, p. 322-325.
- Vernet, J., Fosbury, R., Villar-Martín, M., Cohen, M., di Serego Alighieri, S., & Cimatti, A. 1999, in "The Hy redshift Universe", eds. A. Bunker & W. van Breugel, ASP Conf. Series, Vol. 193, p. 102
- Véron-Cetty, M. P., & Véron, P. 1996, ESO Sci. Rep., 17, 1
- Vigotti, M., GruEFF, G., Perley, R., Clark, B., & Bridle, A. 1989, AJ, 98, 419
- Villani, D., & di Serego Alighieri, S. 1999, A&AS, 135, 299
- Villar-Martín, M., Binette, L., & Fosbury, R. 1996, A&A, 312, 751
- Villar-Martín, M., Tadhunter, C., & Clark, N. 1997, A&A, 323, 21 (VM97)
- Villar-Martín, M., Binette, L., & Fosbury, R. 1999a, A&A, 346, 7
- Villar-Martín, M., Tadhunter, C., Morganti, R., Axon, D., & Koekemoer, A. 1999b, MNRAS, 307, 24
- Villar-Martín, M., Fosbury, R., Binette, L., Tadhunter, C., & Rocca-Volmerange, B. 1999c, A&A, 351, 47
- Voges, W., et al. 1999, A&A, 349, 389
- Waddington, I., Windhorst, R., Cohen, S., Partridge, R., Spinrad, H., & Stern, D. 1999, ApJ, 526, L77
- Webster, R., Francis, P., Peterson, B., Drinkwater, M., & Masci, F. 1995, Nature, 375, 469
- Weymann, R., Morris, S., Foltz, C., & Hewett, P. 1991, ApJ, 373, 23
- Weymann, R., et al. 1998, ApJ, 505, L95
- White, N., Giommi, P., & Angelini, L. 1994, IAU Circ., 6100, 1
- White, R., Becker, R., Helfand, D., & Gregg, M. 1997, ApJ, 475, 479
- White, R., et al. 2000, ApJS, 126, 133
- Wieringa, M., Ph. D. thesis, Rijksuniversiteit Leiden
- Wieringa, M., & Katgert, P. 1992, A&AS, 93, 399
- Williams, R., et al. 1996, AJ, 112, 1335
- Willot, C., Rawlings, S., Blundell, K., & Lacy, M. 1998, Proc. Radio Surveys Workshop, Tenerife Spain, ed. M. Bremer (Dordrecht: Kluwer), p. 209
- Willott, C., Rawlings, S., Blundell, K., & Lacy, M. 1999, MNRAS, 309, 1017
- Wills, B., et al. 1992, ApJ, 400, 96
- Wills, B., & Brotherton, M. S. 1995, ApJ, 448, L81
- Windhorst, R., van Heerde, G., & Katgert, P. 1984, A&AS, 58, 1
- Windhorst, R., Miley, G., Owen, F., Kron, R., & Koo, D. 1985, ApJ, 289, 494
- Witzel, A., Schmidt, J., Pauliny-Toth, I., & Nauber, U. 1979, AJ, 84, 942
- Wright, A., Griffith, M., Burke, B., & Ekers, R. 1994, ApJS, 91, 111
- Wright, A., Griffith, M., Troup, E., Hunt, A., Burke, B., & Ekers, R. 1996, ApJS, 103, 145
- Wu, X.-B., Bade, N., & Beckmann, V. 1999, A&A, 347, 63
- ZabuldoFF, A., Geller, M., Huchra, J., & Vogeley, M. 1993, AJ, 106, 1273

De zoektocht naar jonge sterrenstelsels

De elementaire bouwstenen van het heelal zijn sterrenstelsels. Deze bestaan uit vele miljard sterren die door zwaartekracht samengehouden worden. Eén van de belangrijkste vragen in de hedendaagse sterrenkunde is: hoe zijn deze sterrenstelsels ontstaan en geëvolueerd? Op het eerste gezicht lijkt deze vraag nogal moeilijk te beantwoorden, want de sterrenstelsels in de omgeving van ons eigen Melkwegstelsel lijken allen in een gevorderd stadium van hun evolutie te zijn. Deze sterrenstelsels in het nabije universum bevatten namelijk een aanzienlijk aantal sterren die al meer dan 10 miljard jaar oud zijn.

Het is echter mogelijk om jonge sterrenstelsels waar te nemen, door terug te kijken in de tijd. Dit kan omdat de snelheid van het licht eindig is (300 000 km/s), zodat het licht van ver afgelegen sterrenstelsels lang onderweg is om de Aarde te bereiken. Het licht van een sterrenstelsel dat zich op 100 000 000 000 000 000 000 (10^{23}) km bevindt zal dus 10 miljard jaar onderweg geweest zijn vooraleer het door telescopen op Aarde wordt waargenomen. Door steeds verder afgelegen sterrenstelsels waar te nemen kunnen we dus verder terugkijken in het verleden.

Het bepalen van de afstand tot een object is een apart vak in de sterrenkunde. Het is mogelijk om de afstanden van verafgelegen sterrenstelsels vrij nauwkeurig te bepalen, door gebruik te maken van de uitdeining van het heelal. Deze ontdekking werd omstreeks 1930 gedaan door de Amerikaanse astronoom Edwin Hubble. Hij stelde dat de verder weggelegen sterrenstelsels zich sneller van ons af bewegen dan degene die zich dichterbij ons in de buurt bevinden. Omgekeerd zullen de sterrenstelsels die zich sneller van ons verwijderen dus ook verder van ons afgelegen zijn. De omrekeningsfactor tussen snelheid en afstand die hiervoor gebruikt wordt (de zogenaamde Hubble constante) wordt gekalibreerd door de verwijderingssnelheid van objecten met bekende afstand te meten. Momenteel is deze waarde gekend met een nauwkeurigheid beter dan 20%.

Aangezien het heelal uitdeint, moet het in het verleden ook kleiner geweest zijn. Dit leidde tot de suggestie van de Belgische astronoom Georges Lemaître dat het heelal ook een begin moet gehad hebben. Dit begin van tijd en ruimte (de Oerknal of 'Big Bang'), was ongeveer 15 miljard jaar geleden. Deze leeftijd is afhankelijk van de exacte waarde van de Hubble constante. Door sterrenstelsels waar te nemen die op afstanden van 14 miljard lichtjaren staan, weten we zeker dat deze jonger dan

ongeveer 1 miljard jaar moeten zijn, aangezien geen enkel object ouder dan het heelal kan zijn. Door de studie van die extreem ver weg gelegen objecten kunnen we de vorming van sterrenstelsels waarnemen.

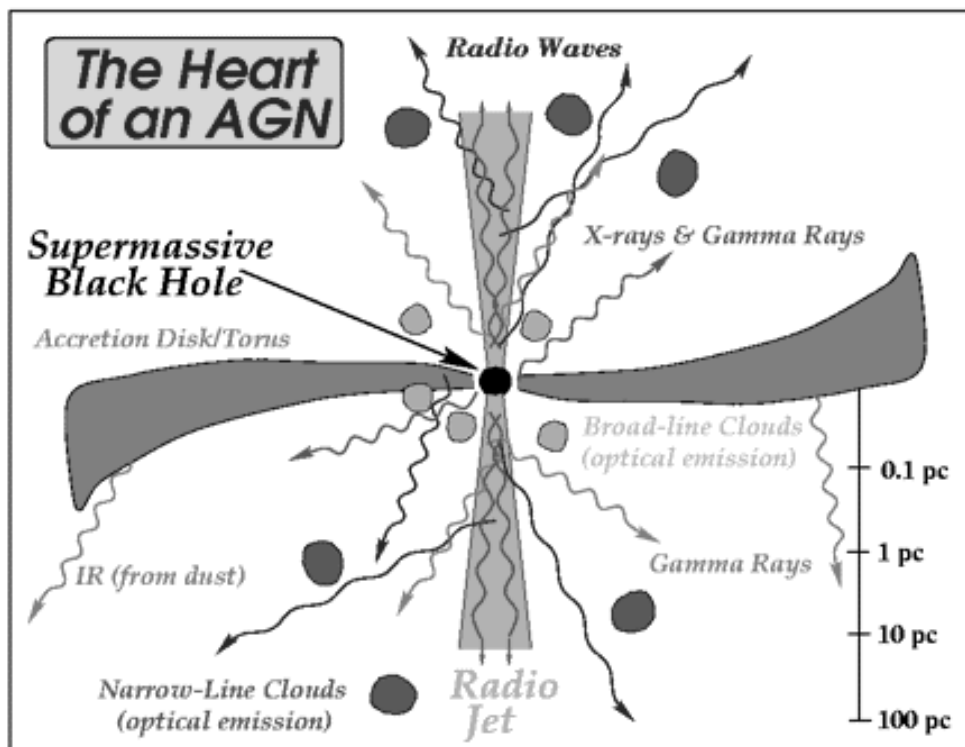
Om jonge sterrenstelsels waar te nemen moeten we dus sterrenstelsels trachten te vinden die zich zeer snel van ons af bewegen. Deze verwijderingssnelheid kan vrij nauwkeurig gemeten worden aan de hand van de roodverschuiving van emissie lijnen in het spectrum⁷ van een sterrenstelsel. Hoe meer de lijnen in het spectrum naar de rode kant verschuiven, hoe sneller het object zich van ons af beweegt. Deze verwijderingssnelheid is een direct gevolg van de uitdeining van het heelal: hoe verder het object is, hoe sneller dit gebied zich van ons lijkt te verwijderen. In werkelijkheid zijn het niet de objecten die zich van ons verwijderen, maar is het het heelal zelf dat groter wordt. Omdat het heelal uitdeint, wordt de golflengte van de straling die zich erdoor beweegt ook uitgerekt, waardoor het hele spectrum van een verafgelegen object naar de langere (=rode) golflengtes verschuift. In de praktijk worden de afstanden van sterrenstelsels uitgedrukt in eenheden van roodverschuiving z : het nabije universum bevindt zich op $z = 0$, terwijl een object op $z = 5$ zich op bijna 14 miljard lichtjaar bevindt (weerom is deze afstandswaarde afhankelijk van de exacte waarde van de Hubble constante). Hoge roodverschuiving is dus een synoniem voor grote afstand of jonge leeftijd.

Zware sterrenstelsels met centrale zwarte gaten

Tot voor kort was het selecteren van bronnen met radiostraling de meest efficiënte manier om sterrenstelsels op hoge roodverschuiving te vinden. De voornaamste reden hiervoor is dat er 5 tot 10 miljard jaar geleden veel meer sterrenstelsels waren met heel sterke radiostraling in vergelijking met het huidige (nabije) universum. Daardoor zijn de radio bronnen aan de hemel verder verwijderd dan de meest lichtsterke optische (zichtbare) bronnen. De oorsprong van deze sterke radiostraling is te vinden in de super-zware centrale zwarte gaten van deze sterrenstelsels. Een zwart gat is een extreem compact object dat zo zwaar is dat niets er uit kan ontsnappen, ook het licht niet. Alle materie die erdoor aangetrokken wordt, zal in een zogenaamde accretieschijf naar het zwart gat aangetrokken worden in een spiraalvormige baan. Bij dit proces wordt een grote hoeveelheid energie geproduceerd, waaronder ook radiostraling in de vorm van twee straalstromen of 'jets' (zie Figuur 1). De lichtsterkte van de radiobron is afhankelijk van de hoeveelheid materie die het zwart gat voedt: hoe zwaarder het sterrenstelsel, hoe meer gas er naar het zwart gat kan stromen om daarbij straling te produceren. Omdat we enkel de meest lichtsterke radiobronnen kunnen waarnemen tot op grote afstand, zijn deze radiobronnen ook de meest zware sterrenstelsels op deze afstand. Het heelal was vroeger compacter, waardoor de onderlinge afstand tussen de verschillende sterrenstelsels kleiner was. Op die manier konden er

⁷Een spectrum kan gemeten worden met een instrument dat aan de telescoop gekoppeld wordt; dit zal het licht dat door de telescoop komt verspreiden afhankelijk van hun golflengte (kleur), net zoals dit op Aarde in een regenboog gebeurt.

meer kleine sterrenstelsels opgeslokt worden door de zware sterrenstelsels. Door deze samensmelting van sterrenstelsels groeit de voorraad materie om het zwarte gat te voeden, waardoor het sterker zal gaan schijnen als een radiobron.



Figuur 1: Schematische voorstelling van de kern van een sterrenstelsel met een actieve kern (active galactic nucleus of AGN). De straling van de verschillende componenten wordt op verschillende golflengtes uitgezonden. De enige straling die tot op grote afstand van het zwarte gat kan waargenomen worden is afkomstig van de radio 'jets'. (Figuur overgenomen van <http://arise.jpl.nasa.gov/arise/blackholes/blackholes.html>.)

Door systematisch de roodverschuiving van radiobronnen te bepalen zijn steeds verder weg gelegen sterrenstelsels ontdekt. Bij het begin van mijn proefschrift in 1996 had het verst bekende sterrenstelsel een roodverschuiving van $z = 4.41$. De laatste jaren is een nieuwe generatie optische telescopen met een 4 keer grotere spiegeloppervlakte in gebruik genomen. De eerste, en ook de grootste van deze generatie is de Keck telescoop, waarvan er nu twee copies in gebruik zijn (zie Figuur 2). Met deze telescopen is het nu ook mogelijk om lichtzwakkere sterrenstelsels op hoge roodverschuiving te vinden, zonder daarvoor eerst de radiostraling waar te nemen. Deze waarnemingen zijn de laatste jaren heel intensief gedaan, zodat er nu al meer zeer ver weg staande

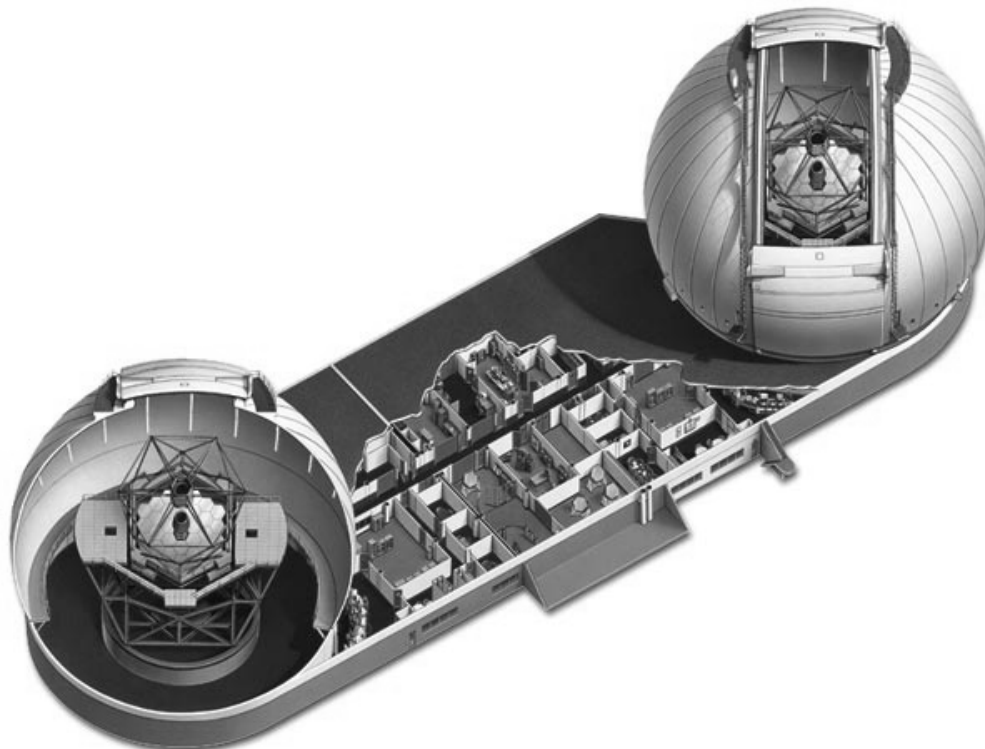
sterrenstelsels bekend zijn zónder dan mét sterke radiostraling. Er zijn met deze nieuwe techniek nu al sterrenstelsels gevonden tot op een roodverschuiving $z = 5.74$. Ondanks deze vernieuwde concurrentie is het nog steeds zeer belangrijk om te blijven zoeken naar radiobronnen op grote afstand, omdat deze de zwaarste, en ook de meest lichtsterke objecten zijn die we in het jonge heelal kunnen waarnemen. Ze zijn dan ook de sterrenstelsels die we het meest gedetailleerd kunnen bestuderen. Het is ook van belang om deze zware sterrenstelsels met hun centrale zwarte gaten te vergelijken met theoretische modellen over de vorming van sterrenstelsels. Het bestaan van een zwaar sterrenstelsel met een zwart gat op een roodverschuiving $z = 5$ betekent dat er maximaal 1 miljard jaar is om dit soort objecten samen te stellen. Verscheidene modellen voorspellen ook dat er zich rond de zwaarste sterrenstelsels heel wat kleinere sterrenstelsels bevinden. Door eerst de lichtsterke sterrenstelsels te vinden kunnen we dan ook in de buurt van zo'n sterrenstelsels zoeken naar andere, kleinere sterrenstelsels.

Het onderzoek beschreven in dit proefschrift

Een van de doelstellingen van dit proefschrift is het vinden van zware sterrenstelsels op hoge roodverschuiving aan de hand van hun radiostraling. Aangezien er tegenwoordig miljoenen radiobronnen bekend zijn, en het bepalen van de roodverschuiving veel waarneemtijd op grote telescopen vergt, is het onmogelijk om van al die radiobronnen de afstand te bepalen. Gelukkig is het mogelijk om een drastische selectie te maken uit deze bronnen aan de hand van hun radiostraling zelf, en zo de kans het op vinden van bronnen met een grote roodverschuiving aanzienlijk te vergroten. De techniek die wij hiervoor gebruiken wordt al 20 jaar met succes toegepast. Het komt er op neer bronnen te kiezen met een ultra steil radio spectrum (USS bronnen). Dit zijn bronnen die op lange radio golflengtes veel lichtsterker zijn dan op kortere. Door de 0.1% bronnen te selecteren met het grootste verschil (de steilste spectra), wordt de kans dat deze zich op hoge roodverschuiving bevinden sterk vergroot. Deze techniek werkt omdat de radio spectra van sterrenstelsels met sterke radiostraling meestal dezelfde vorm hebben (zie Figuur 1.1 voor een voorbeeld). Als een bron een hogere roodverschuiving heeft, schuift het hele spectrum zoals dat op Aarde waargenomen wordt op naar langere golflengtes. Omdat radio telescopen steeds op vaste golflengtes meten, zal er voor een bron op hogere roodverschuiving een steeds steiler gedeelte van het spectrum worden waargenomen.

In hoofdstuk 2 van dit proefschrift hebben wij een lijst van 669 USS bronnen samengesteld aan de hand van verschillende radio catalogi, die bij het begin van mijn onderzoek net beschikbaar waren. Samen bestrijken deze radio catalogi een groot gedeelte van de hemel. Die voornaamste catalogi die wij voor het samenstellen van onze USS lijst gebruikten zijn:

- De Westerbork Northern Sky Survey (WENSS) op een golflengte van 92cm. Deze werd waargenomen met de Westerbork Synthese Radio Telescoop, die zich in de Nederlandse provincie Drenthe bevindt.



Figuur 2: Een schematische voorstelling van de twee Keck telescopen die zich op de 4200m hoge vulkaan Mauna Kea in Hawai'i bevinden. Een aanzienlijk gedeelte van de waarnemingen beschreven in dit proefschrift zijn met deze telescopen gedaan. De hoofdspiegels bestaan elk uit 36 afzonderlijke segmenten en hebben een diameter van 10 meter.

- De NRAO VLA Sky Survey (NVSS) op een golflengte van 20cm, waargenomen met de Very Large Array, in de Amerikaanse staat New Mexico.
- De Faint Images of the Radio Sky at Twenty centimeters (FIRST), eveneens op 20cm waargenomen met de VLA.
- De Texas Survey op een golflengte van 82cm, waargenomen met een speciaal daarvoor ontworpen telescoop in de Amerikaanse staat Texas.

Vervolgens hebben wij 410 van deze USS bronnen meer in detail waargenomen met de VLA en Australia Telescope Compact Array. Met de resultaten van deze waarnemingen kunnen de posities nauwkeuriger bepaald worden, en ook een aantal bronnen uitgesloten worden die er uit zien als dichtbij staande radiobronnen.

Om de roodverschuiving van deze sterrenstelsels te bepalen moeten waarnemingen in

het optisch (zichtbaar) licht gedaan worden, want in het radio spectrum zijn geen sterke lijnen aanwezig waarmee de roodverschuiving kan gemeten worden. Hoofdstuk 3 beschrijft deze optische waarnemingen met 5 verschillende optische telescopen. Aan de hand van deze waarnemingen kunnen de sterrenstelsels geïdentificeerd worden van waaruit de radiostraling afkomstig is. Dit is niet eenvoudig omdat deze ver afstaande sterrenstelsels zeer zwak zijn in optisch licht. Daarvoor moet de positie aan de hemel nauwkeurig bekend zijn, zodat we met zekerheid kunnen bepalen welk van de objecten in de buurt van de radiobron de juiste identificatie is. Wanneer dit gelukt is kunnen we terug naar de telescoop gaan om met een spectrograaf de roodverschuiving proberen te bepalen van deze optische identificaties (Hoofdstuk 4). Omdat onze bronnen zo ver weg zijn, lijkt het licht dat ons bereikt ook heel zwak, en hebben we de allergrootste telescopen nodig om ze te kunnen detecteren (zoals de Keck, zie Figuur 2). In sommige gevallen volstaan zelfs de grootste telescopen niet, en kan de afstand nog niet bepaald worden. In totaal hebben we op deze manier roodverschuivingen bepaald voor 50 sterrenstelsels. Hieronder bevinden zich 10 op een roodverschuiving hoger dan 3, wat bijna een verdubbeling is van wat voorheen bekend was. Een directe vergelijking van de sterrenstelsels op dezelfde roodverschuiving die niet met een radio techniek gevonden zijn toont inderdaad aan dat onze radiobronnen duidelijk veel zwaarder en lichtsterker zijn (ook in het optisch golflengte gebied).

In Hoofdstuk 5 tot 7 gaan we iets dieper in op de waarnemingen van 3 speciale bronnen die wij ontdekt hebben. De meest in het oog springende bron is TN J0924–2201 (Hoofdstuk 5): dit is tot op heden de verst gekende radiobron in het universum op een roodverschuiving van $z = 5.19!$ Deze ontdekking toont aan dat er ongeveer 1 miljard jaar na de Oerknal al zeer zware zwarte gaten gevormd waren. De tweede verst verwijderde bron in onze lijst is TN J1338–1942 (Hoofdstuk 6). Aan de hand van een optisch spectrum genomen met de splinternieuwe ESO Very Large Telescope vinden wij aanwijzingen dat er zich rond dit sterrenstelsel heel wat neutraal waterstof bevindt, wat erop wijst dat het nog niet volledig gevormd is.

In hoofdstuk 8 brengen we al deze gegevens samen, en onderzoeken we welke invloed het zwart gat en de bijhorende radiobron hebben op het sterrenstelsel waarin zij zich bevinden. Omdat er nu sterrenstelsels gekend zijn binnen het hele roodverschuivingsbereik van $z = 5$ tot $z = 0$, kunnen we ook de evolutie in tijd onderzoeken. Het blijkt dat de zeer energierijke straling van de materie rond het zware centrale zwart gat het overige gas in het sterrenstelsel ioniseert, waardoor het gas in en om het sterrenstelsel zelf ook straling uit gaat zenden. Tegelijkertijd blijkt dat de enorme radio jets (zie Figuur 2) hieraan een belangrijke bijdrage leveren, wat voorheen nog wel eens verwaarloosd werd. We vinden ook aanwijzingen dat het gas rond de sterrenstelsels op de hoogste roodverschuivingen ($z > 3$) voornamelijk uit waterstof bestaat. In de sterrenstelsels op lagere roodverschuiving is het gas al verrijkt door stervormingsprocessen. Omdat het heelal direct na de Oerknal voornamelijk uit waterstof bestond, zou dit erop kunnen wijzen dat deze sterrenstelsels nog niet volledig gevormd zijn.

Curriculum Vitae

Op 3 februari 1973 ben ik geboren te Sint-Niklaas (België). Van 1986 tot 1991 volgde ik mijn middelbare school opleiding aan het Sint-Jozef-Klein-Seminarie te Sint-Niklaas, in de richting Latijn-Wiskunde. In 1991 kwam ik de opleiding Sterrenkunde aan de Universiteit Leiden volgen. Tijdens mijn doctoraalfase van deze opleiding heb ik eerst onderzoek verricht naar Synchrotron halos van spiraalstelsels, onder leiding van dr. Chris Carilli. Daarna heb ik de overdichtheid van bronnen uit de WENSS radio survey rondom Abell clusters onderzocht onder leiding van dr. Malcolm Bremer. In 1995 heb ik 2 maanden als zomerstudent doorgebracht bij NFRA in Dwingeloo (Drenthe), waar ik onder leiding van prof. dr. Ger de Bruyn radio-polarisatie waarnemingen van synchrotron halos gereduceerd heb, die genomen waren met de Westerbork Synthese Radio Telescoop. Tevens in 1995 bracht ik een werkbezoek aan dr. Chris Carilli in Cambridge (Massachusetts), volgde ik de Synthesis Imaging Summer School in Socorro (New Mexico), en bezocht de Young European Radio Astronomers Conference in Groningen, en de JIVE VLBI School in Dwingeloo.

In januari 1996 begon ik mijn promotieonderzoek onder leiding van prof. dr. George Miley, dr. Huub Röttgering, en dr. Wil van Breugel. Na 3 inleidende maanden in Leiden vertrok ik voor 3 jaar naar Livermore (Californië), waar ik als exchange graduate student werkte aan het Institute for Geophysics and Planetary Physics verbonden aan het University of California Lawrence Livermore National Laboratory. Deze uitwisseling maakte het mogelijk om de resultaten van 2 nieuwe radiosurveys te combineren, nl. de Westerbork Northern Sky Survey (gemaakt in Dwingeloo en Leiden) en de Faint Images of the Radio Sky at Twenty centimeters (gemaakt in Livermore). Ik heb de ik resultaten van dit onderzoek gepresenteerd op conferenties in Puerto de la Cruz (Tenerife, Spanje), Amsterdam, Sydney (Australië), en Asiago (Italië). Als onderdeel van dit onderzoek heb ik waarneemreizen gemaakt naar Lick Observatory (Californië, 15 maal), Keck Observatory (Hawaii, 6 maal), ESO La Silla (Chili, 3 maal), WHT op La Palma (2 maal), de VLA in Socorro en de Australia Telescope Compact Array in Narrabri (Australië).

Na mijn promotie zal ik als Marie Curie fellow verbonden zijn aan het Institut d'Astrophysique de Paris.

Acknowledgements

This project would not have been possible without the scientific and financial help from various people. First, I am grateful to the IGPP/LLNL for allowing me to spend more than three years in an ideal scientific environment, and to chase distant photons from radio to optical, and from Australia over Chile and La Palma to Hawaii. The relaxed working environment made me feel at home at IGPP right away. My gratitude goes out to Hien Tran and Mike Brotherton for our daily chats while eating lychee jellies, and to Andy Bunker, Daniel Stern, and David Alves for memorable excursions to The City and Berkeley. During numerous observing nights at Lick and Keck, Daniel Stern taught me all the Berkeley tricks to obtain spectra of invisible objects, while Adam Stanford solved all my K -band imaging problems.

We could start early with the optical and near-IR observations of our USS sample because Bob Becker and Jim Condon prioritized the observations of the FIRST and NVSS surveys towards the area covered by the WENSS.

Verder ben ik erkentelijk voor de hulp en het advies bij dit project van mijn collega's in Leiden, in het bijzonder Philip Best, Jaron Kurk en Arno Schoenmakers. Al mijn computer problemen werden deskundig opgelost door David Jansen en Erik Deul.

Mijn ouders hebben mijn studies steeds ten volle ondersteund, zowel financieel als mentaal, waarvoor ik hen heel dankbaar ben.